



UNIVERSITY OF LEEDS

Intensity fluctuations in Hurricane Irma (2017)

William Torgerson

Submitted in accordance with the requirements for the degree of
Doctor of Philosophy

The University of Leeds
School of Earth and Environment

31 October 2021

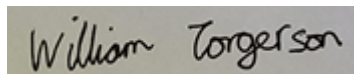
Intellectual Property

The candidate confirms that the work submitted is his own and that appropriate credit has been given where reference has been made to the work of others.

This copy has been supplied on the understanding that it is copyright material and that no quotation from the thesis may be published without proper acknowledgement.

© 2021 The University of Leeds, William Torgerson

Signed

A rectangular box containing a handwritten signature in black ink that reads "William Torgerson".

Acknowledgements

I would like to thank my supervisors: Dr Juliane Schwendike and Dr Andrew Ross for all their contributions to this research and continued support while writing this thesis. I would also like to thank my Met Office supervisor Dr Chris Short for his help and support in running the MetUM. In addition I would like to thank Emeritus professor Roger Smith for use of his balanced model and slab model scripts and helping to get them working.

I thank the Hurricane Research Division for providing dropsonde and flight level data.

I thank the Cooperative Institute for Meteorological Satellite Studies for making microwave imagery publicly available.

This work used Monsoon2, a collaborative High-Performance Computing facility funded by the Met Office and the Natural Environment Research Council.

This thesis was funded by the NERC DTP (grant code: NE/L002574/1) scholarship and CASE support from the Met Office.

Special thanks to my wonderful wife and to my parents for supporting me through this process.

List of Abbreviations

AAM Absolute angular momentum

BSA Beta skirt axisymmetrisation

CFL Courant–Friedrichs–Lewy

EWRC Eyewall replacement cycle

HUDRAT2 The revised Atlantic hurricane database

IR Infrared

MetUM Met Office Unified Model

MIMIC Morphed integrated microwave imagery

MPI Maximum potential intensity

MOGREPS-G Met Office Global and Regional Ensemble Prediction System

MSLP Mean sea level pressure

NHC National Hurricane Centre

NOAA National Oceanic and Atmospheric Administration

NWP Numerical weather prediction

PV Potential vorticity

RAL1-T Regional tropical science configuration

RI Rapid intensification

RMW Radius of maximum windspeed

S1,S2,S3 Strengthening phase one, two, and three

SATCON Satellite consensus algorithm

SE Sawyer–Eliassen

SEF Secondary eyewall formation

SST Sea surface temperature

TC Tropical cyclone

TPF Translating pressure fit

VHT Vortical hot tower

VRW Vortex Rossby wave

W1,W2,W3,W4 Weakening phase one, two, three, and four

WCF Wind centre fix

WRF The Weather Research and Forecasting model

Abstract

During a period of rapid intensification Hurricane Irma (2017) experienced two episodes of weakening that coincided with an expansion in the storm's radius of maximum wind speed. Such fluctuations in intensity can substantially alter the impacts of a storm, but are poorly understood. A modelling study was conducted using convection-permitting ensemble forecasts from the regional configuration of the Met Office Unified Model. The model was able to reproduce similar intensity fluctuations to those observed. The cause of the weakening was determined to be a balanced response to the diabatic heating and absolute angular momentum source associated with vortical hot tower like structures (VHTs) within the inner rainbands near the eyewall. The VHTs promoted boundary layer convergence and an unbalanced spin-up process which led to an increase in tangential wind speed outside of the eyewall and weakening at the radius of maximum wind resulting in the reorganisation of the eyewall. The intensity fluctuations were compared to a full eyewall replacement cycle that occurred later. The intensity fluctuations resemble a secondary eyewall formation event occurring close to the original eyewall, without the large region of suppressed convection typically seen in eyewall replacement cycles. The absence of this moat region results in a shorter period of weakening where the eyewall convection is disrupted but not replaced. The intensity fluctuations in Hurricane Irma differ from previously observed fluctuations, highlighting the need for further convection-permitting ensemble modelling case studies to determine the frequency, characteristics and impact of such fluctuations.

Contents

List of Figures	xiii
1 Introduction	1
2 Literature review	6
2.1 Understanding TC intensification through balanced dynamics	6
2.2 Limits of balanced axisymmetric theory: Unbalanced and asymmetric intensification	11
2.3 Rapid intensification	12
2.4 Eyewall replacement cycle	13
2.5 Intensity fluctuations	18
2.6 Intensity fluctuations in Hurricane Irma	19
2.7 Summary and unanswered questions	19
3 Methodology	21
3.1 Observational data	21
3.2 Numerical model setup	22
3.3 Diabatic tracers	24
3.4 TC centre and track finding methods	26
3.4.1 Simplex	26
3.4.2 Track finding methods	29
3.5 Vortex Rossby wave identification	32
3.6 Calculation of equivalent potential temperature (θ_e)	36
3.7 Summary	38

4	Model Evaluation	39
4.1	Synoptic overview	39
4.2	Intensity and tracks	41
4.3	Selection of a representative ensemble	44
4.4	Satellite observations	45
4.4.1	Comparison between model output and satellite imagery . . .	45
4.5	Radar imagery	46
4.5.1	Radar fractional skill score comparison	50
4.5.2	Radar RMW comparison	53
4.6	Flight-level wind analysis	53
4.7	Dropsonde data analysis	56
4.7.1	Preparing dropsonde data for comparison to model data . . .	56
4.7.2	Storm size comparison	64
4.7.3	Neighbourhood point analysis	64
4.8	Summary	69
5	Intensity fluctuations in Hurricane Irma (2017)	71
5.1	Introduction	71
5.2	Methodology	73
5.2.1	Calculation of a gradient wind	73
5.2.2	Calculation of maximum potential intensity	73
5.2.3	Slab boundary layer model setup.	74
5.2.4	Intensity fluctuations in observations	75
5.3	Results	75
5.3.1	Model simulation of intensity fluctuations	77
5.3.2	Environmental factors	80
5.3.3	PV Fourier decompositions	86
5.3.4	Barotropic structural changes	92
5.3.5	Convective structural changes	103
5.3.6	Unbalanced dynamics and the boundary layer	108
5.3.7	Composites over multiple ensemble forecasts	114
5.4	Discussion	117

5.5	Summary and conclusions	121
6	Intensity fluctuations: Balanced dynamics	124
6.1	Introduction	124
6.2	Methodology	127
6.2.1	Balanced Model	127
6.2.2	Regularization	130
6.2.3	Prognostic implementation of balanced model	132
6.3	Results	135
6.3.1	Secondary circulation	135
6.3.2	Secondary circulation budget	139
6.3.3	Balanced effect on the primary circulation	141
6.3.4	Prognostic runs	146
6.4	Discussion	152
6.5	Summary and conclusions	154
7	Eyewall replacement cycle and comparison with intensity fluctuations	156
7.1	Introduction	156
7.2	Results	157
7.2.1	Model evaluation	157
7.2.2	Secondary eyewall formation (SEF) dynamics	160
7.2.3	Comparison between eyewall replacement cycle and intensity fluctuations	170
7.3	Discussion	180
7.4	Summary and conclusions	184
8	Discussion and Conclusions	187
8.1	Summary of findings	188
8.1.1	Model evaluation	188
8.1.2	Analysis of intensity fluctuations during RI	189
8.1.3	Intensity fluctuations from a balanced perspective	191

8.1.4	Eyewall replacement cycle in Hurricane Irma (2017) and its link to intensity fluctuations	192
8.2	Implications	194
8.3	Limitations and future work	196

List of Figures

3.1	(a) Best track of Irma (black line) with points corresponding to the position of Irma on each date from 30 August 2017 to 13 September 2017. Orography (m) is shown in shading. The domain of the RA1T model is shown with the red rectangle. The two periods of RI are shown in yellow. The 18-ensemble tracks are displayed in grey with ensemble e15 shown in orange. Islands where landfall occurred are indicated by white dots and labels. (b) best track wind speed (black), the maximum surface wind of the ensembles initialised on 03 September 00 UTC with e15 highlighted in orange. Yellow lines indicate the two periods of RI.	25
3.2	Schematic of the simplex TC centre finding method used.	28
3.3	Ensemble member 0, T+36h, 10 m wind speed (shading) and MSLP (black contours) with scatter points showing an initial first guess for the algorithm (blue cross), MSLP (black cross), each point in the algorithm (grey dots) and the final point (red cross). A grey line shows the path centre of each simplex. The right panel shows a zoomed in version of the first. Contour intervals are 10 hPa for the left panel and 2 hPa for the right panel.	29
3.4	Comparison for the same time period and ensemble as Fig. 3.3 showing the difference between the storm-relative radial flow and the tangential flow in cylindrical coordinates using the MSLP centre (top) and the centre derived using the simplex method (bottom).	30

3.5	Comparison of the regional model ensemble member 0 track using MSLP and track derived with the simplex method.	30
3.6	Dropsondes (blue crosses), NHC interpolated best track (purple points), WC82 TC centre, TPF TC centre (black point with uncertainty cross), TPF implied RMW (thick orange line) and its standard error (thin orange lines) and TPF implied translation velocity (black arrow). Flights shown are (a,b): NOAA42 (01111A) flight occurring between 1911–0230UTC on 03 September t=0 is arbitrarily taken to be 22:22:52 the time at which dropsonde 4 hits the surface. (c,d): NOAA42 (01111A) flight occurring between 0959–1453 UTC on 05 September. t=0 is arbitrarily taken to be 12:35:10 roughly the time at which a dropsonde hits the surface and to coincide with a WC82 point.	33
3.7	Plot of p_{hol} showing p_e , RMW parameters as well as the implied pressure at the TC centre. Valid for (a): the NOAA42 (01111A) flight occurring between 19:11-02:30 UTC on 03 September (b): NOAA42 (01111A) flight occurring between 0959–1453 UTC on 05 September.	34
4.1	Storm tracks for Hurricane Irma (2017). The RA1T model (initialized 03 September 00 UTC) storm tracks are shown in red and the tracks from the global model are shown in blue. The grey line shows the IBTrACS best track and the black line shows the wind centre fix based track.	42
4.2	Average storm centre difference from the actual storm centre (wind centre fix centre) for both the global and regional model. The wind centre fix data was not available for the first 24 hours and, therefore, is not shown. One standard deviation either side of the mean is also shown. WCF data is unavailable before +21hours due to a paucity in dropsonde and flight data at this time.	42
4.3	(a) MSLP and (b) maximum surface wind speed as a function of run time for both the global (blue lines) and regional (red lines) simulations and NHC intensity (black line).	43

4.4	MSLP as a function of maximum surface wind speed for both the global and regional models, and NHC intensity for the simulation initialized on 03 September 00 UTC.	44
4.5	Regional model outgoing long wave radiation for 03 September 14 UTC (T+14 h) with visible/IR satellite for comparison.	47
4.6	Regional model outgoing long wave radiation for 04 September 14 UTC (T+38 h) with visible/IR satellite for comparison.	48
4.7	Regional model outgoing long wave radiation for 05 September 14 UTC (T+62 h) with visible/IR satellite for comparison.	49
4.8	Surface radar reflectivity (calculated from large scale rain rate) from the regional model initialized at 03 September 00 UTC. and flight level radar imagery for T+33h.	50
4.9	Fractional skill score composite for ensemble 15 valid for (a): T+9 h – T+24.3 h, (b) T+32.7 h – T+36.6 h, (c) T+57.3 h–T+61.1 h, (d) T+69.1 h–T+73.3 h.	51
4.10	Radar composite (left column) and model composite (right column) windspeed at 500 m height for ensemble 15 valid for (a),(b): T+21 h – T+24.3 h, (c),(d) T+32.7 h – T+37.6 h, (e),(f) T+57.3 h–T+61.1 h, (g),(h) T+69.1 h–T+73.3 h.	52
4.11	Comparison of the ensemble mean (left column) of wind speed to radar derived wind speed composite (right). Black lines show the height dependent RMW, black stipples show incomplete radar data (i.e. there is not data for all azimuthal angles). Valid for (a,b) T+21 h – T+24.3 h (c,d) T+32.7 h – T+37.6 h, (e,f) T+57.3 h–T+61.1 h, and (g,h) T+69.1 h–T+73.3 h.	54
4.12	Radar derived composite RMW (red line) as a function of height and regional model ensemble composite RMWs (grey lines) as a function of height for four different times.	55

4.13	Flight azimuthal wind (m s^{-1}) and virtual model flight azimuthal wind (calculated using interpolation from the relative TC centre) (m s^{-1}) as a function of distance from the storm centre for: (a) flight NOAA 42 (0111A) valid 19:11-02:30 UTC 03 September, (b) flight USAF 309 (0311A) valid 14:15-20:24 UTC 04 September, (c) flight NOAA 42 (0711A) valid 07:54-13:54 UTC 05 September.	57
4.14	Flight azimuthal wind speed (m s^{-1}) and virtual model flight azimuthal wind speed (m s^{-1}) for NOAA 42 (0211A).	58
4.15	Wind speed contour plot (m s^{-1}) with model storm centre (black point) and (a) original dropsonde location (point) and (b) adjusted dropsonde location.	60
4.16	Wind speed (m s^{-1}) vs pressure (hPa) for dropsonde (black) and (a) virtual dropsonde in MetUM (blue) with the standard deviation of neighbourhood points in the MetUM (pale blue). (a) Uncorrected virtual dropsonde, (b) virtual dropsonde corrected for the differing MetUM and observed RMW.	61
4.17	IR satellite derived TC size. Image produced by NOAA. Vertical lines added indicate the time period modelled.	64
4.18	‘Eyewall’ category on 04 September showing the dropsonde azimuthal (black line) and radial (red) wind with model neighbourhood (average of surrounding grid points) displaying the azimuthal (grey shading) and radial (red shading) wind.	65
4.19	As Fig. 4.18 with ‘Eye’ category dropsondes on 04 September.	66
4.20	As Fig. 4.18 with ‘Eyewall’ category dropsondes on 05 September.	67
4.21	As Fig. 4.18 with ‘Outer’ category dropsondes on 03 September.	68
5.1	Observed sea level pressure as a function of time based on SATCON, NHC forecaster assessed Best Track as well as direct dropsonde and flight measurements. The 96-hour period shown is the same as the simulation initialized on 03 September 00 UTC. Two notable weakening/stagnation periods during the rapid intensification are highlighted with the blue bands.	76

5.2	NOAA P3 flight radar (in dBZ) on (a) 05 September 0943 UTC and (b) 05 September 1232 UTC, colour enhanced infrared (IR) imagery (in ° C) on (c) 05 September 0945 UTC and (d) 05 September 1245 UTC and MIMIC microwave imagery (brightness temperature in K) for (e) 05 September 0945 UTC, (f) 05 September 1245 UTC. Upper row just before the start of the second blue bar in Fig. 5.1, lower row just after the start of the second blue bar in Fig. 5.1	77
5.3	Various model parameters (solid lines) and corresponding observations (dotted lines, where available) as a function of time. Details are given in the legend. Phases have been subjectively identified. Blue bands indicate weakening phases, and red bands indicate strengthening phases during the rapid intensification period. The individual strengthening and weakening phases have also been labelled (see top of plot). W stands for ‘weakening’, S stands for ‘strengthening’.	79
5.4	850–200mb vertical wind shear in 3 to 5 degree annulus from model TC centre as a function of time. Colour shading is total incoming short–wave radiation which allows easy identification of daytime (pale grey or white) or nighttime (darker grey). Thresholds defining weak, moderate, high or extreme (where TC development is impossible) are also based on Park et al. (2012).	81
5.5	Translation speed of the TC centre. Colour shading is total incoming short–wave radiation which allows easy identification of daytime (pale grey or white) or nighttime (darker grey). Thresholds defining the ideal development speed are based on Michaels et al. (2006).	83
5.6	Difference between MPI and actual minimum sea level pressure (left scale) and maximum surface wind speed (right scale). In both cases negative values represent actual storm intensities less than the MPI (i.e higher SLP or lower wind speed) and the zero line represents an intensity equal to the MPI. Colour shading is total incoming short–wave radiation which allows easy identification of daytime (pale grey or white) or nighttime (darker grey).	85

5.7	Mean PV field and azimuthal Wave 1, Wave 2 and Wave3+ frequency components for 1532m height level. Also shown are the intensity fluctuation phases, the RMW and $3\times$ RMW (the approximate theoretical stagnation radius).	87
5.8	PV (PVU, shaded) at 1532 m height for selected times and vertical velocity (1 m s^{-1} , black contour). The RMW is indicated by the dashed black line. A cross marks the centre of the TC. The data is output in 10-minute intervals, times are given to the nearest 0.1 hours.	89
5.9	Azimuthally averaged PV (PVU, shaded) as a function of radial distance and height for selected times. The RMW is indicated by the grey line. Also shown are the 1 m s^{-1} (black lines) and -1 m s^{-1} (dashed black lines) radial wind contours.	90
5.10	(a) Ratio of the low-level PV (depth averaged between 1052 m and 4062 m) at the centre of the TC to the maximum azimuthally averaged low level PV. (b) Maximum standard deviation of PV at 1532 m (black) and standard deviation of PV at 1532 m at the RMW (red). (c) Eccentricity of the ring fitted to the PV distribution at 1532 m. (d) Average barotropic conversion rate from the surface to 4062m averaged between 5 km and 70 km as a function of time. To smooth out high frequency noise a 1-h running mean is applied to 10-minute data. Weakening (blue) and strengthening (red) phases are also shown.	91

- 5.11 Change in PV over the past hour due to advection only (shaded PVU h⁻¹). Black line contours show the PV field in intervals of 5 PVU. Additionally, four sets of trajectories are shown for the following (r,z) points (black scatter points): (5 km, 1532 m), (15 km, 1532 m), (5 km, 782 m), and (15 km, 782 m). Purple lines and end scatter points represent the forward trajectory over the next hour while mustard lines and scatter points represent the backward trajectory over the previous hour. Each set of trajectories contains 8 points going back or forward with the same radial distance from the storm centre but with different azimuthal angles around the storm centre: from the east, northeast, north, northwest, west, southwest, south and southeast. The grey contours show vertical velocity in 0.25 m s⁻¹ intervals indicating the location of the inner eyewall. Yellow dashed line shows the -1 m s⁻¹ inflow contour. 94
- 5.12 Perturbation vertical velocity (m s⁻¹ shaded) (relative to the azimuthal mean), perturbation relative vorticity (10⁻³ s⁻¹ coloured line contours) shown at the same times as in Fig. 5.8. Heights shown are 2532 m for the red shades/lines, 4963 m for the grey shades/lines, 9934 m for the blue shades/lines. The centre of the TC is denoted by the cross and the RMW at 4963 m is indicated by the black dashed line. Black hatches represent regions where the maximum perturbation vertical velocity at any level exceeds 5 m s⁻¹. Yellow crosses show the locations of locally high perturbation relative vorticity at 4963 m to indicate the location of VHT like structures. 97
- 5.13 Colour shading shows the (a,c) mean and (b,d) eddy contributions to the tangential wind budget (see equation 5.2) in m s⁻¹ h⁻¹. Line contours show the average tangential wind tendency in 2 m s⁻¹ h⁻¹ intervals with dashed contours indicating negative tendencies. The top row shows the composite for W1 (averaged over the entire W1 phase) while the bottom row shows the composite for S1. The frictional term (not shown) also contributes a large positive tangential tendency in the boundary layer. 100

- 5.14 As with Fig. 5.13 but this time composites of no VHT activity (top row) and strong VHT activity (at least one VHT-like structure with ascent shading and vorticity contours at all three levels as in Fig. 5.12) (bottom row). Composites are created by averaging any times in the W1 and S1 combined period with no distinction between weakening and strengthening periods (45.5 hours to 57.5 hours) that either have no VHT activity (top row) or strong VHT activity (bottom row). . . . 101
- 5.15 Diabatic heating (shading, K h^{-1}), vertical velocity (line contours) in intervals of 0.5 m s^{-1} before and during the first weakening phase W1. Also shown as a grey line is the RMW. 105
- 5.16 Diabatic heating (K h^{-1}) for height 4963 m before and during the first weakening phase W1. Vertical velocity contours in intervals of 2 m s^{-1} . Yellow crosses indicate the location of the maximum local perturbation vertical velocity at the same level for any VHT like structures as determined by adapted criteria in Smith and Eastin (2010). 106
- 5.17 Left column shows azimuthally averaged agradient wind as a function of time (m s^{-1}) for (a), a radius of 35 km and (c) at the RMW. The right column shows, for the 35 km radius, the azimuthally averaged (b) tangential and (d) radial winds (m s^{-1}). The height of the lines are 12 m (blue), 102 m (green), 1902 m (orange) and 3002 m (red). Panels (a) and (c) also show the pressure gradient force (0.01 m s^{-2} , dashed lines) at selected levels. 109
- 5.18 Comparison of slab boundary layer model (left) with MetUM output (right) for agradient winds (top) and radial wind (bottom). For the slab boundary layer model the depth is taken to be 1202m whilst for the MetUM output the radial and agradient winds are averaged throughout the lowest 1202m. The yellow hatched zone in the left panels represents no data where the slab boundary layer model does not converge. 111

- 5.19 Left column shows, as a function of height and radius: the gradient wind (shading, left colourbar), the radial wind in intervals of 4 m s^{-1} with dashed lines indicating negative values, the tendency in tangential wind as small dots showing $+2 \text{ m s}^{-1} \text{ h}^{-1}$, large dots showing $+4 \text{ m s}^{-1} \text{ h}^{-1}$, line hatches showing $-2 \text{ m s}^{-1} \text{ h}^{-1}$ and cross hatches showing $-4 \text{ m s}^{-1} \text{ h}^{-1}$. Right column shows angular momentum (lines in units of $5 \times 10^{-5} \text{ m}^2 \text{ s}^{-1}$) and the secondary circulation as arrows in the plane of the cross section (with the boundary layer strong inflow omitted for clarity). The shading shows the contribution of the sum of the radial and vertical advection of angular momentum to the tangential wind budget. The colour scale used indicates which is the dominant term. If radial advection dominates over vertical advection then the blue/red shading is used and if vertical advection is dominant over radial advection then the green/purple scheme is used. For example green shading implies that the radial and vertical advection of angular momentum causes a negative tangential wind tendency and that the vertical term dominates. Also shown is RMW as the dashed grey line. The times shown in a,b are T+45, c,d, T+47.4 and e,f, T+49.8 (the first three panels in Fig. 5.12). A region of interest is denoted by the yellow ellipse. 113
- 5.20 Composite PV tendencies (PVU h^{-1} , shading) at 1532m across all weakening and strengthening phases in the six ensemble members with distinct fluctuations. Green dashed lines show the full range of RMWs at the same level. Hatching indicates regions where the average PV exceeds 30 PVU. Black circles show 25 km radial intervals. 115

- 5.21 Absolute angular momentum budget composites showing: (a) mean advection of angular momentum, and (b) eddy advection of angular momentum . Colour shading shows the difference in tangential wind tendency between the strengthening phase composite and the weakening phase composite in $\text{m s}^{-1}\text{h}^{-1}$. Line contours ($5 \text{ m s}^{-1}\text{h}^{-1}$ intervals, dashed lines imply negative values) show a composite of the contribution to tangential wind budget during all the strengthening phases (for example in subplot a at around 50 km there is a strongly positive tangential wind tendency from the mean term over all the strengthening phases). 116
- 5.22 Schematic outlining the proposed mechanism for the fluctuations modelled during the rapid intensification of Hurricane Irma during: (a,b) the end of a strengthening phase, (c,d) the middle of a weakening phase and (e,f) the start of the strengthening phase. Left column shows the horizontal structure of the storm including VHT-like structures (red), eyewall convection (grey) and regions of high PV (blue hatched). Right column shows the azimuthally averaged structure of the storm at each stage with arrows indicating the direction of the secondary circulation (larger arrows imply stronger flow). A red arrow in panel b indicates that the inflow is a balanced response to the VHT-like structure. A green arrow in d shows the direction of transport of high PV. In (b,d) the VHT-like structure is indicated by a 2nd cloud outside of the eyewall. 123
- 6.1 Comparison of (a) MetUM frictional AAM sink with (b) idealized mathematical AAM sink. Colour shading shows forcing in $\text{m s}^{-1}\text{h}^{-1}$ while line contours show the streamfunction of the secondary balanced response from this AAM sink only in $10^8 \text{ m}^2 \text{ s}^{-1}$ 129
- 6.2 Comparison of regularization methods showing non-elliptic regions after regularization in black. White regions have been successfully regularized. Input data from the MetUM from T+40 h. 132

6.3	Radial wind (m s^{-1} shading) and vertical velocity (0.5 m s^{-1} , contours) from the MetUM (left column) and the balanced model (middle column, with original MetUM F , and right column, with idealized F). RMW is indicated with the dotted grey line. Top row shows results at T+40 h, bottom row shows T+45.5 h.	136
6.4	As Fig. 6.3, but with top row showing results at T+47.5 h, bottom row showing T+50 h.	138
6.5	Radial wind (m s^{-1} , shading) and vertical velocity (0.5 m s^{-1} , thick line contours, 0.025 m s^{-1} and 0.125 m s^{-1} are also shown as thin line contours. Negative values are shown as dashed contours) from (a) diabatic heating, (b) eddy heating, (c) friction, (d) eddy AAM, (e) sum of all forcings, (f) MetUM secondary circulation, (g) MetUM secondary circulation minus the total balanced response (i.e. the unbalanced residual) for T+40 h.	142
6.6	As Fig 6.5 but for T+50 h.	143
6.7	Tangential wind tendency ($\text{m s}^{-1} \text{ h}^{-1}$, shading), AAM ($4 \times 10^5 \text{ m}^2 \text{ s}^{-1}$ contours), secondary circulation (arrows) from (a) diabatic heating, (b) eddy heating, (c) friction, (d) eddy AAM, (e) sum of all forcings, and (f) MetUM secondary circulation for T+45.5 h.	144
6.8	As fig. 6.7, but for T+50 h.	145
6.9	Full prognostic simulation with primary circulation (m s^{-1} , shading) and secondary circulation (arrows) with AAM ($8 \times 10^5 \text{ m}^2 \text{ s}^{-1}$, contours) at initialization and subsequent 2 hour periods. Also shown is the RMW (dashed grey line).	148
6.10	Prognostic simulations with heating forcing terms only. Lines show wind speed of simulations that have been initialized at different times (with MetUM forcings) with the same initial wind field. Dashed lines show the first 7 hours of the simulations which are deemed to be the model ‘spin-up’ period. The black solid line shows the average of all the simulations after the ‘spin-up’ period. Also indicated are the fluctuation phases which correspond to the MetUM forcings used at that time.	149

- 6.11 Prognostic simulation initialized with heating forcings beginning at T+28 h. Shown are composites over selected times with tangential wind tendency ($\text{m s}^{-1}\text{h}^{-1}$, shading) and secondary circulation (arrows) with AAM ($8 \times 10^5 \text{ m}^2 \text{ s}^{-1}$, line contours). Averaged diabatic heating forcings are shown with the purple contours showing values of 5 K h^{-1} and 20 K h^{-1} . Also shown is the RMW (dashed grey line). 151
- 6.12 Prognostic simulations with heating forcing terms only. Lines show wind speed of simulations that have been initialized with different constant heating forcings from the MetUM at each hour between T+42 h and T+49 h starting with the same initial wind field. Dashed lines show the first 7 hours of the simulations which are deemed to be the model ‘spin-up’ period. The solid line shows the simulations after the ‘spin-up’ period. 153
- 7.1 (a,c,e,g): Layer averaged (4062–7038 m) simulated vertical velocity (m s^{-1} , shading), (b,d,f,h): Microwave imagery at selected times within the eyewall replacement cycle. Times have been chosen such that they are relative to the approximate SEF stage in both the microwave and model data. These stages are: a,b Single spiral outer-rainband, c,d SEF, e,f outer eyewall becomes dominant, g,h remnant eye convection. 159
- 7.2 Wavenumber–2 PV for the eastern azimuth (shaded, PVU) at 1532 m. Vertical velocity (black line contours of 0.4, 0.8, 1.6, 3.2 m s^{-1}) along the same azimuthal angle and height. Also shown are the RMW for the same height (grey solid line) and $3 \times \text{RMW}$ as a proxy for the stagnation radius (purple solid line). The blue dashed line shows the trajectory of a hypothetical VRW propagating from the RMW at T+71 h using the VRW dispersion relation (equation 3.5). 162

- 7.3 Azimuthally averaged vertical velocity at 1532 m (shaded, m s^{-1}). Azimuthally averaged tangential wind acceleration (black line contours of 0.5 m s^{-1} intervals). Also shown are the RMW for the same height (thick grey solid line) and $3 \times \text{RMW}$ as a proxy for the stagnation radius (purple solid line). The dashed blue line shows the radial, time trajectory of a hypothetical VRW propagating from the RMW at T+71 h using the VRW dispersion relation (equation 3.5). 163
- 7.4 (a,c) Mean and (b,d) eddy terms (shaded, $\text{m s}^{-1} \text{ h}^{-1}$) of the tangential wind budget are shown. The tangential wind (line contours, 10 m s^{-1} intervals) and the RMW (grey dashed line) are also shown. 164
- 7.5 Tangential wind acceleration (shaded, m s^{-1}), tangential wind speed (line contours, 10 m s^{-1} interval) for selected times. Stippling shows regions where τ_{fil} is less than 30 minutes, and cross hatching shows regions where β is negative. 166
- 7.6 Agradient wind (shaded, m s^{-1}), tangential wind (black line contours, 5 m s^{-1} interval), and radial wind (orange line contours, 5 m s^{-1} interval, dashed lines imply an inflow) at 12 m height (a), and 552 m height (b). 168
- 7.7 Azimuthally averaged tangential wind tendency (shaded, m s^{-1} over 3 hours), three-hourly azimuthally averaged vertical velocity (black contours, $0.25, 0.5, 1 \text{ m s}^{-1}$ intervals and 1 m s^{-1} intervals thereafter) and wind in the plane of cross section (arrows) for selected periods prior and just after SEF. Arrow length in the vertical direction is scaled to be ten times longer than in the horizontal direction for the same flow speed. 169

- 7.8 Ratio of the low-level PV (depth averaged between 1052 m and 4062 m) at the centre of the TC to the maximum azimuthally averaged low level PV for: (a) ensemble member 10 of the 05 September 12 UTC simulation showing the full eyewall replacement cycle, (b) ensemble member 15 of the 03 September 00 UTC simulation showing the intensity fluctuations. In the case of (a) the vertical lines correspond to each of the four chosen times in Figure 7.3. In the case of (b) the weakening and strengthening phases are shown. 171
- 7.9 PV (PVU, shaded) at 1532 m height for selected times and vertical velocity (1 m s^{-1} , black contour). A black cross marks the centre of the TC. Black circles show radii in increments of 25 km. The data is output in 10-minute intervals, times are given to the nearest 0.1 hours. The top row is from ensemble member 10 of the 05 September 12 UTC simulation showing the full eyewall replacement cycle, the bottom row for ensemble member 15 of the 03 September 00 UTC simulation showing the intensity fluctuations. 173
- 7.10 Vertical velocity (m s^{-1} , shaded) and radial wind (0.1, 0.2, 0.5, 1, 2, 5, 10, 20, 50 m s^{-1} positive (solid) and negative (dashed) black contours). Panels a-d from ensemble member 10 of the 05 September 12 UTC simulation showing the full eyewall replacement cycle, panels e-h for ensemble member 15 of the 03 September 00 UTC simulation showing the intensity fluctuations. 175
- 7.11 Agradient wind (m s^{-1} , shaded), hourly tendency of the radial wind (0.5, 2, 5, 10 $\text{m s}^{-1} \text{ h}^{-1}$, positive (solid) and negative (dashed) yellow contours), tangential wind hourly tendency (0.5, 2, 5, 10 positive and negative $\text{m s}^{-1} \text{ h}^{-1}$, black contours). Panels a-d from ensemble member 10 of the 05 September 12 UTC simulation showing the full eyewall replacement cycle, panels e-h for ensemble member 15 of the 03 September 00 UTC simulation showing the intensity fluctuations. 177

7.12 Equivalent potential temperature (K, shaded), vertical velocity (0.1, 0.2, 0.5, 2, 5, 10 m s^{-1} positive (solid) and negative (dashed) black contours). Panels a-d from ensemble member 10 of the 05 September 12 UTC simulation showing the full eyewall replacement cycle, panels e-h for ensemble member 15 of the 03 September 00 UTC simulation showing the intensity fluctuations.	179
--	-----

Chapter 1

Introduction

Tropical cyclones (TCs) are high impact storms that frequent tropical regions on the Earth, including the North Atlantic region. TCs can bring extremely strong winds, heavy rains and storm surges when they impact coastal regions, such as the Caribbean islands or the Gulf of Mexico coastline. Some TCs intensify to hurricane strength (maximum wind speed higher than 33 m s^{-1}), with the potential to cause considerable damage to property and risk to life. TCs can suddenly intensify very quickly, a process which is known as rapid intensification (RI). RI is defined as the rate of intensity increase of at least 15.4 m s^{-1} per 24 hours (Kaplan et al., 2010). RI can be particularly dangerous if it occurs just before a storm makes landfall, as it can lead to stronger and more damaging winds than expected.

Numerical weather prediction (NWP) models are useful tools to help prepare for and mitigate against potential damage from these storms. Most NWP models are able to adequately forecast the track of TCs with reasonable accuracy (Heming et al., 2019). However, the intensity of TCs is handled relatively poorly by most NWP models (e.g. Courtney et al., 2019), with simulated mature storms being weaker than observed storms in most NWP models, although the advent of increasingly high resolution models has led to recent improvements in performance. NWP models are better at capturing mean sea level pressure (MSLP) compared to maximum wind speed, which is systematically underestimated (Heming, 2016). One recent improvement in intensity forecasts for TCs has come from the more extensive use

of convection-permitting forecasts, where convection is resolved explicitly.

One of the biggest challenges in weather forecasting is predicting when a TC will rapidly intensify. Most strong TCs undergo a period of RI (Kaplan and DeMaria, 2003). Although convection-permitting NWP models are capable of modelling some RI events, models still perform poorly when it comes to the timing of RI events (e.g. Short and Petch, 2018), indicating that the current understanding and representation of intensification processes prior to and during RI is likely to be incomplete. Being able to accurately predict the likelihood of an RI event is important as it can have a substantial impact on the potential damage a TC may cause, which in turn influences mitigation strategies.

Numerical weather prediction models also struggle to predict when RI will cease. In some cases RI is halted by the onset of an eyewall replacement cycle (EWRC), where a new eyewall develops outside the original eyewall before gradually contracting and replacing the original eyewall. Although there has been significant progress in recent years in understanding the physical processes and dynamics that govern EWRCs, NWP models still struggle to predict if and when they will occur. Improving the ability of NWP models to predict when an EWRC may occur is particularly useful since an EWRC occurring near land could alter the damage potential of the storm, on the one hand potentially preventing it from reaching a more intense state, but on the other hand expanding the radius of damaging winds to affect a bigger area.

Intensity fluctuations in TCs are alternating periods of strengthening and weakening that occur during the storm's lifetime. The fluctuations have practical implications, especially if they occur prior to landfall, as they could result in a storm that causes substantially more or less damage depending on whether it strengthens or weakens. As a result, there is a strong motivation to understand inner-core intensity fluctuations that occur with the intention of being able to predict their timing more precisely.

An EWRC is one form of intensity fluctuation that is capable of ending a period of RI, but there are also intensity fluctuations that can occur during RI. Nguyen et al. (2011) showed, in a modelling study, a different form of intensity fluctua-

tion, where Hurricane Katrina (2005) ‘vacillated’ between two disparate structures during its RI. These fluctuations caused the TC to briefly weaken or pause its intensification for a few hours before continuing to rapidly intensify. There have been comparatively few studies on so-called vacillation cycles (e.g. Hardy et al., 2021). As intensity fluctuations during RI are somewhat subtle fluctuations that occur over a period of hours, understanding them better requires intricate analysis over short time periods while the storm structure is rapidly changing. Convection-permitting model simulations are therefore needed to capture the rapid changes in intricate convective structures in the TC.

Hurricane Irma (2017) was chosen as a case study to investigate intensity fluctuations for several reasons. Firstly, it is a storm that underwent RI in an environment that stayed conducive to intensification throughout (warm sea surface temperatures, weak vertical wind shear, high mid-level moisture) and therefore limited the contribution the environment could have had on the intensity fluctuations. In addition, Irma was a fairly symmetric storm which allowed the fluctuations to be analysed without the complexity associated with an asymmetric TC.

A further advantage of selecting Hurricane Irma as a case study is that, in addition to the intensity fluctuations that occurred during RI, Irma underwent a full EWRC after the RI period. Therefore, a direct comparison can be made between these two different types of intensity fluctuations in the same storm, which may yield novel insights into both forms of fluctuations.

The overarching aim of the thesis is to understand the cause and development of the intensity fluctuations during RI and to explore if and how these fluctuations are related to other fluctuations, such as vacillation cycles and eye wall replacement cycles. In particular, what causes some TCs to develop these fluctuations and can they be predicted? In addition, the thesis will attempt to understand what complexities (such as asymmetries or boundary layer processes) are necessary to produce these types of intensity fluctuations. Previous papers on vacillation cycles mostly focused on Hurricane Katrina (2005), so this study provides the analysis of a new case with an understudied form of intensity fluctuation.

The specific questions addressed in this thesis are:

1. What structural changes occur during the course of the weakening and strengthening phases of the intensity fluctuations?
2. How well can a balanced dynamical paradigm explain the intensity fluctuations?
3. What causes the intensity fluctuations in Hurricane Irma (2017) to occur?
4. What are the differences and similarities between these intensity fluctuations in Hurricane Irma (2017) and vacillation cycles described in other storms?
5. What are the dynamical processes involved in the full EWRC in Hurricane Irma (2017) that occurred between 07 and 08 September?
6. Do intensity fluctuations exist on a spectrum between vacillation cycles and EWRCs?

In order to answer these questions, convection-permitting ensemble forecasts using the Met Office Unified model (MetUM) will be run and compared to observational data. An in-depth analysis will then be conducted into the model simulations to attempt to understand these fluctuations. The advantage of a modelling study is that structural changes that occur over short time periods can be diagnosed and linked to tangential wind weakening or strengthening in different parts of the storm. The use of ensemble forecasts allows the results to be generalized and gives some indication of how predictable these types of fluctuations are.

Understanding the intensity fluctuations that occurred during RI of Hurricane Irma (2017) builds on the current research on vacillation cycles and links the fluctuations to established paradigms of intensification such as the balanced dynamical framework. In particular, the thesis expands the understanding of the intensity fluctuations by providing a novel link between inner rainband convection and an unbalanced process in the boundary layer that destabilizes the eyewall structure during the intensity fluctuations. The thesis also breaks new ground by directly comparing the fluctuations to an EWRC occurring in the same storm. Linking two different types of intensity fluctuation in the same storm has not been done

before and provides valuable insight into the prerequisite conditions for both types of intensity fluctuation.

The thesis is organised as follows: Chapter 2 reviews the current literature on intensity fluctuations, introduces the relevant physics and intensification paradigms and notes the gaps that this research aims to bridge. Chapter 3 describes the methods and data used in the study including the MetUM model setup, observational data and any necessary diagnostic techniques used in the remainder of the thesis. Chapter 4 evaluates the MetUM's performance in simulating Hurricane Irma including the relevant period of RI by comparing the model output to observational data with the aim of justifying its use as a tool to understand the intensity fluctuations. Chapter 5 analyses these intensity fluctuations using the MetUM simulations in an attempt to explain their cause by examining the barotropic and convective structural changes as well as the role of unbalanced dynamics. Chapter 6 builds on the previous chapter by running a simplified balanced 'toy' model with the aim of understanding the extent to which the fluctuations can be described through the lens of balanced dynamics. Chapter 7 explores the differences and similarities of the intensity fluctuations with the EWRC while also providing some insight into the causes of the EWRC in Hurricane Irma. The findings are summarised in Chapter 8 and potential avenues of future research are suggested.

Chapter 2

Literature review

The aim of this chapter is to discuss the current literature on TC intensification and explain the relevance to the thesis and any gaps in the literature that the thesis aims to bridge. The chapter starts with a review of the axisymmetric balanced dynamical paradigm (section 2.1) which explains the basic concepts in TC intensification that form a foundation for understanding more complex inner core dynamics. This is extended in section 2.2 where the limits of this approach are explained and the role of the unbalanced boundary layer and asymmetrical processes such as vortex Rossby waves are discussed. With the groundwork for understanding intensification laid, the chapter then gives a summary of the current research into RI (section 2.3). The topic of eyewall replacement cycles is then discussed in section 2.4 in the context of intensity fluctuations that can occur in TCs that can cause RI to stop. Intensity fluctuations in general are then covered in section 2.5 with an emphasis on fluctuations occurring during RI. The specific case of intensity fluctuations in Hurricane Irma (2017) is then briefly looked at in section 2.6 before ending with a summary of the chapter (section 2.7).

2.1 Understanding TC intensification through balanced dynamics

Understanding how TCs intensify is an extensive area of research. There are many theories that describe how TCs intensify. For example Emanuel (1986) posits that

TCs spontaneously intensify in a positive feedback process where increasing wind speeds in a weak vortex lead to increased enthalpy fluxes from the sea surface. Another particularly popular intensification theory is known as the cooperative intensification paradigm initially developed by Ooyama (1969). This theory links intensification of a TC to its ability through deep convection to overcome frictional loss of energy near the surface, and is an example of a balanced axisymmetric theory.

To understand how TCs intensify, it has often been useful to consider the case of an idealised axisymmetric vortex in gradient wind and hydrostatic balance (e.g. Montgomery and Smith, 2014). Gradient wind balance is the condition where a parcel of fluid inside the vortex is balanced by the inward acting pressure gradient force and the outward acting centrifugal and Coriolis forces:

$$\frac{v^2}{r} + fv = \frac{1}{\rho} \frac{\partial p}{\partial r}, \quad (2.1)$$

where v is the azimuthal wind of the parcel, r is the radial distance from the centre of the storm, f is the Coriolis parameter ($f = 2\Omega \sin \varphi$ where Ω is the angular velocity of the Earth, φ is the latitude), ρ is the parcel density, and p is the pressure.

Hydrostatic balance constrains the vertical motion of fluid parcels whereby an upward buoyancy force determined by the pressure gradient is balanced by the downward gravitational force:

$$\frac{1}{\rho} \frac{\partial p}{\partial z} = -g, \quad (2.2)$$

where g is the acceleration due to gravity. A theoretical scale analysis done by Willoughby (1979) justified basing the understanding of intensification of TCs on the assumption of gradient wind and hydrostatic balance. The induction of a secondary (transverse) circulation can be thought of as a means to maintain the gradient wind balance in the presence of forcing which seeks to disrupt it. It is worth noting, however, that a ‘real’ TC is not in gradient wind balance in the boundary layer, which is a limitation to the theory that assumes a strict gradient wind balance

for the whole cyclone. By considering the case of the stationary vortex in gradient wind balance Eliassen (1951) was able to derive a partial differential equation, the Sawyer–Eliassen (SE) equation, that describes the response of absolute angular momentum (AAM) and heat sources on the secondary circulation. The solutions of this equation form a basis on which results from this study can be interpreted. There are many different forms of the SE with differing assumptions and levels of complexity. In Schubert and Hack (1982) the SE equation only accounts for diabatic heating sources, in Shapiro and Willoughby (1982) the effect of AAM sources is considered. The most general version of the SE equation does not invoke the Boussinesq approximation (neglecting variations in density except in the buoyancy term). A version of the SE equation, without the Boussinesq approximation was developed by Smith et al. (2005) and is outlined in Bui et al. (2009) who say this form of balance dynamics only assumes that “the flow is in hydrostatic and gradient wind balance”. This form of the SE equation is given below with similar notation as in Wang and Smith (2019):

$$\begin{aligned} \frac{\partial}{\partial r} \left(A \frac{\partial \psi}{\partial r} + \frac{B}{2} \frac{\partial \psi}{\partial z} \right) + \frac{\partial}{\partial z} \left(C \frac{\partial \psi}{\partial z} + \frac{B}{2} \frac{\partial \psi}{\partial r} \right) &= g \frac{\partial}{\partial r} (\chi^2 Q) + \frac{\partial}{\partial r} (c \chi^2 Q) - \frac{\partial}{\partial z} (\chi \xi \dot{V}), \\ A &= -g \frac{\partial \chi}{\partial z} \frac{1}{\rho r}, \\ B &= -\frac{\partial(\chi c)}{\partial z} \frac{2}{\rho r}, \\ C &= \left(\chi \xi (\zeta + f) + c \frac{\partial(\chi)}{\partial r} \right) \frac{1}{\rho r}, \end{aligned} \tag{2.3}$$

where $\chi = 1/\theta$ is the inverse of the potential temperature, g is the acceleration due to gravity, $c = v^2/r + fv$ is the sum of the centrifugal and Coriolis forces per unit mass, $\xi = f + 2v/r$ is twice the local absolute angular velocity, ζ is the vertical component of relative vorticity, Q is the forcing due to heating (diabatic heating and heating due to eddies), and \dot{V} is the forcing due to AAM (friction or eddy advection of AAM). The equation is written in terms of the streamfunction ψ , the gradient of which gives the secondary circulation:

$$u = -\frac{\partial \psi}{\partial z}, \quad w = \frac{\partial(r\psi)}{r\partial r}, \tag{2.4}$$

where w is the vertical velocity, and u is the radial velocity components of the induced secondary circulation. The SE equation written in this form has three spatially varying coefficients A , B , and C , which are directly proportional to the static stability (resistance to vertical motion), baroclinity (linked to the vertical shear) and inertial stability (resistance to radial motion) of the environment of the forcing.

The solutions to the SE equation, given in terms of the stream-function, for prescribed point heating sources are vertically orientated dipoles with the flow in each dipole moving in, up and out in a clockwise fashion on the outside and an anti-clockwise fashion on the inside. The strongest flow and the highest concentration of streamlines intersects with the heating source and the streamlines are usually near vertical here. For an AAM source the response is also a dipole, this time horizontally orientated with the streamlines pointing radially inward along the AAM source.

Most of the research since Eliassen (1951) has focussed on the effect of diabatic heating in TCs in relation to inertial stability. One example is that of Smith and Montgomery (2016) which builds on previous work by Schubert and Hack (1982) and others by considering the effect the inflow resulting from diabatic heating has on storm intensification. To understand the intensification of TCs it is necessary to consider the conservation of AAM, M :

$$v = \frac{M}{r} - \frac{1}{2}fr. \quad (2.5)$$

For an air parcel M is approximately materially conserved (i.e., $DM/Dt = 0$) above the boundary layer. Therefore, a parcel moving inward with decreasing r will have a compensatory increasing v in order to conserve M . The core region of TCs within the RMW has a high inertial stability whilst the outer region has a much lower inertial stability. A point heating source located just within the RMW will result in an asymmetrical response to the secondary circulation, in accordance with the dipolar solutions of the SE equation, with most of the streamlines outside the RMW in the radial direction and most of the streamlines inside the RMW in the vertical

direction. The result is a drawing in of AAM surfaces which in turn, as shown in equation 2.5, causes an increase in the tangential velocity, and forms a more intense TC.

By contrast, a heating source outside of the RMW causes outward motion within the high inertial stability region and thus causes the storm to expand and decrease in intensity. Schubert and Hack (1982), in particular, found that in intense storms the period of most RI was characterized by high core inertial stability compared to the environment. As storms intensify the principal heating source becomes confined to an annulus just inside the RMW and moves gradually outwards. When the heating source moves outside the RMW into a lower inertial stability region the storm stops intensifying. The formation of an eye causes the efficient heating to be located nearer to the RMW which acts to suppress further intensification.

Having diagnosed the secondary circulation, the effect of the balanced response, the tendency in the tangential wind, can be determined by differentiating equation 2.5 with respect to time, rewriting the tangential wind in terms of its material derivative ($\frac{dv}{dt} = u\frac{\partial v}{\partial r} + w\frac{\partial v}{\partial z} + \frac{\partial v}{\partial t}$), and noting that the AAM source $\frac{1}{r}\frac{\partial M}{\partial t}$ is given by $-\dot{V}$:

$$\frac{\partial v}{\partial t} = -u\frac{\partial v}{\partial r} - w\frac{\partial v}{\partial z} - \frac{uv}{r} - fu - \dot{V}. \quad (2.6)$$

Intensification of the TC driven only by the radial and vertical advection of AAM surfaces, as a consequence of a balanced dynamical response, as described by equations 2.3 and 2.4, is known as the balanced model of intensification. The balanced model of TCs is limited in explaining intensification as it is known that TCs are highly unbalanced in the upper-level outflow and boundary layer. For example, Smith and Montgomery (2015) point out that the observed maximum tangential wind speed occurs in the unbalanced boundary layer which would not be possible if TCs only intensified through the convergence of AAM from a purely balanced response. Despite these limitations, solving the SE is useful because it allows the contribution from balanced processes to be isolated from other intensification mechanisms.

2.2 Limits of balanced axisymmetric theory: Unbalanced and asymmetric intensification

A balanced axisymmetric framework despite being a useful conceptual model cannot explain many aspects of TC intensification. The boundary layer is known to be highly unbalanced, and even strong TCs in low wind shear environments are not perfectly symmetrical. To gain a complete understanding of TC intensification it is, therefore, necessary to understand how unbalanced dynamics and asymmetrical processes affect TC intensification.

The boundary layer spin-up mechanism, is explained in Montgomery and Smith (2018), and involves the role of the highly unbalanced boundary layer. If air parcels spiral inwards, towards a TC centre, fast enough to compensate for frictional AAM loss then an initially subgradient tangential wind in the boundary layer inflow may become supergradient, allowing the tangential wind within the boundary layer to be higher than the tangential wind above it. The unbalanced mechanism can also spin up the free vortex above the boundary layer through vertical transport of the high AAM air at the top of the boundary layer.

The axisymmetric theory does not fully explain the development of a TC, particularly during RI, due to the presence of asymmetric processes. These include the role of vortical hot towers (VHTs), which are local small, high relative vorticity and high vertical velocity regions within the eyewall. VHTs and their associated downdrafts can act to transport heat and AAM inwards to the eye prior to RI (Guimond et al., 2010) causing the storm to intensify by warming the eye and increasing the relative vorticity in the region of the VHTs. Persing et al. (2013) investigated the role of three-dimensional asymmetric dynamics on the intensification of a TC by comparing to a purely axisymmetric model configuration. It was found that the asymmetries in the convection generally lead to a weaker radial gradient of diabatic heating and retard intensification; however, sometimes locally intense convection can cause faster intensification through eddy processes than the axisymmetric case.

One other phenomenon not accounted for in the balanced, symmetric paradigm is vortex Rossby waves (VRWs) which are waves that propagate on the radial potential

vorticity (PV) gradients in TCs in a similar way to Rossby waves on planetary scale meridional vorticity gradients (Montgomery and Kallenbach, 1997). VRWs are capable of inducing barotropic instability within the eyewall which can affect the annular heating distribution and therefore impact on the intensity of the storm (Schubert et al., 1999).

A further complexity is the effect of vertical wind shear which can induce strong asymmetries in TCs. For example Leighton et al. (2018) showed that asymmetric intensification can become axisymmetric intensification if local subsidence and ascent cooperates with storm subsidence and ascent in the right quadrant. It has been suggested in Chan et al. (2019) that even though wind shear normally induces weakening it can, in some circumstances, not be detrimental to intensification.

2.3 Rapid intensification

Rapid intensification is an interesting context to apply theoretical understanding of intensification paradigms to, as it is still not well understood and hence is difficult to predict. Attempting to understand the inner core dynamics at play with the ultimate aim of predicting RI is, hence, a fertile area of new research.

One recurring feature of RI dynamics is the presence of VHTs or convective bursts which is another name for especially deep thunderstorms embedded within the central dense overcast of TCs. Guimond et al. (2010) described how subsidence from VHTs acted as a precursor to both axisymmetrisation of the eyewall and to RI which was also applied to a sheared storm in the case of Chen and Gopalakrishnan (2015) and Reasor et al. (2009). The role of convective bursts in initiating RI is explained in Wang and Wang (2014) and Harnos and Nesbitt (2016) as being a cause of increasing inertial stability in tandem with an axisymmetrisation of the eyewall. Given the apparent link between convective bursts and RI there have been attempts to predict RI by measuring the number or type of convective bursts that occur. McFarquhar et al. (2012) found that particularly strong convective bursts with vertical velocities exceeding the 99.9th percentile appeared just prior to RI whereas by contrast Rogers (2010) could not find a link between the onset of RI

and the number or type of convective burst but that RI was still linked to increased inertial stability near the eyewall. Hazelton et al. (2017) found that sudden short term intensification was associated with all forms of convective bursts including weak updraughts if they occurred inside the RMW. The radial location of the convective bursts were also found to be important in Rogers et al. (2013) where it was found that convective bursts inside the RMW promoted greater inward mass flux and mixing between the eyewall and eye.

Sitkowski and Barnes (2009) showed that this process of eyewall to eye mixing is an important precursor to RI. Barnes and Fuentes (2010) were able to show that a transfer of high entropy air from the TC eye is capable of triggering RI by enhancing ascent in the eyewall while promoting subsidence within the eye.

The symmetry of the TC is also relevant to the initiation of RI. Miyamoto and Takemi (2013) made clear the link between a more symmetrical storm and a more inertially stable core which creates a more conducive convective environment for intensification within the eyewall. It was observed in Rogers et al. (2016) that during RI there is a transition from a less symmetric to more symmetric structure in the diabatic heating. It is also possible for this axisymmetrisation process to be rapid, Callaghan (2017) showed that convection can be projected onto the mean field prior to RI beginning.

2.4 Eyewall replacement cycle

There can be many causes for the cessation of RI but one common cause is an eyewall replacement cycle, as shown for instance by Montgomery et al. (2014) in Hurricane Earl (2010). An eyewall replacement cycle is one of the most well studied forms of intensity fluctuations in TCs whereby a secondary outer eyewall forms at a greater radial distance than the original eyewall, gradually moves inwards and eventually replaces the original inner eyewall. The eyewall replacement cycle is associated with both an expansion of the tangential wind field and a weakening of the maximum tangential wind speed before resumption of intensification after the inner eyewall has been destroyed (Willoughby et al., 1982). Eyewall replacement cycles are common

in strong TCs, with seventy percent of major hurricanes undergoing an eyewall replacement cycle at least once in their lifetime (Kossin and Sitkowski, 2009). The expansion of the storm associated with the replacement can be destructive, by increasing the radius of gale force winds or increasing the probability of storm surge (Irish et al., 2008). A sudden eyewall replacement cycle just prior to landfall can be particularly destructive, hence the importance in understanding and predicting them.

Although there has been extensive research into the physics of eyewall replacement cycles, there is still not a consensus on any single preferred mechanism particularly for the secondary eyewall formation (SEF) event, where outer convection becomes organised into an axisymmetric ring with a local tangential wind maximum and can be considered to be an eyewall. For any given storm, multiple mechanisms may play a role for SEF and must, therefore, each be considered in turn.

One recently proposed mechanism given in Terwey and Montgomery (2008) is ‘beta skirt axisymmetrisation’ which borrows ideas originally applied in two-dimensional turbulent dynamics (such as Galperin et al., 2006) describing the ability of small eddies in the presence of a vorticity gradient to reorganise into large-scale jets in a process called anisotropic upscale cascading (energy being transferred from small to large scales). In the context of eyewall replacement cycles Terwey and Montgomery (2008) proposed that eddy turbulence from outer core convection could be axisymmetrised into a coherent low-level jet provided that there was a mean negative radial vorticity gradient (the beta skirt). Once the low-level jet became established, convection would organise at that radius due to a wind induced surface heat exchange positive feedback mechanism. In order for the eyewall replacement cycle to happen it is necessary for convection to occur in the beta skirt region. However, the radial distance of the SEF region needs to be large enough to occur outside of the filamentation zone which is characterised by a region of suppressed convection outside of the eyewall, where the characteristic time of shearing forces (filamentation time) is greater than the time taken for convection to develop, typically around 30 minutes. Qiu et al. (2010) were able to confirm the role of this mechanism by showing that vorticity anomalies from outer rainband convection that moved into the beta

skirt had an appropriately sized eddy velocity to be axisymmetrised into a vorticity ring.

Another mechanism that plays a role in SEF concerns VRWs. VRWs are convectively coupled, counter propagating vorticity perturbations, associated with spiral rainbands. The theory for VRWs was first formalised in Montgomery and Kallenbach (1997) who derived dispersion relations that describe their radial, vertical and azimuthal motion. The dynamics of VRWs were further studied in numerical simulations in Wang (2002). VRWs play an important role in the transport of AAM with the inward moving VRWs transporting AAM into the eye while the concomitant outward propagating waves transport AAM to a critical line (termed a ‘stagnation radius’ in Montgomery and Kallenbach, 1997) outside the eyewall where the radial group velocity of the waves asymptotes towards zero. In an observational analysis of Hurricane Elena (1985) Corbosiero et al. (2006) were able to show that coupled wave-1 and wave-2 radar reflectivity anomalies propagated at phase speeds consistent with the dispersion relation for VRWs and stopped at around three times the RMW, consistent with the stagnation radius. VRWs can contribute to SEF in several ways, firstly by promoting the development of spiral rainbands outside of the eyewall (e.g. Ruan et al., 2014) which can, through rainband induced radial convergence and unbalanced boundary layer dynamics, lead to SEF (Tyner et al., 2018). Secondly, VRWs directly contribute to SEF by accelerating the tangential wind through either wave-mean or wave-wave interactions described in Miller and Montgomery (2000). VRWs transferring vorticity outwards can also have the effect of expanding the beta skirt so it is able to aid SEF through a beta skirt axisymmetrisation mechanism as in Qiu et al. (2010). Finally, VRWs emanating from the eyewall are able to survive the filamentation zone outside of the eyewall (Abarca and Corbosiero, 2011) so may provide a means of generating vorticity and AAM near the stagnation radius in a case where outer rainband activity is weak.

The boundary layer can also contribute to SEF by invoking the unbalanced spin-up mechanism first described in Smith et al. (2009) which notes how an air parcel within the unbalanced sub-gradient boundary layer can increase its AAM if the loss in AAM from frictional dissipation is more than compensated for by the rapid

decrease in the parcel's radial distance from the centre. This unbalanced spin-up mechanism allows for an initially subgradient tangential wind at some height in the boundary layer to become supergradient. A supergradient wind, in turn, leads to the parcel experiencing an outward gradient force which can lead to convergence and forced ascent promoting convection. Unbalanced spin-up occurring at a radial distance much greater than the radial distance of the eyewall has, therefore, been hypothesised to be a cause of SEF (e.g. Wang et al., 2016).

Wang et al. (2016) describe how unbalanced spin-up can promote SEF. First, an acceleration of the tangential wind occurs in the prospective SEF region as a balanced response to outer rainband convection. The increased tangential wind increases the friction, which in turn enhances the unbalanced inflow and can lead to tangential wind acceleration in the boundary layer by the unbalanced spin-up mechanism. Wang et al. (2016) also emphasises the role of eddy AAM convergence as a result of the increased boundary layer inflow. Sun et al. (2013) note the cooperative interplay of balanced and unbalanced dynamics in SEF with the balanced response from the diabatic heating of outer rainbands above the boundary layer being a prerequisite for the development of the supergradient wind within the boundary layer. Kepert (2018) was able to show that, even in a dry, idealized framework, adding a spiral vorticity band (to simulate rainband activity) lead to strong boundary layer convergence and tangential acceleration.

One ubiquitous feature in all the described SEF mechanisms is the presence of strong outer rainband activity which is likely a necessary prerequisite. Zhu and Zhu (2014) were able to identify, using a SE analysis of WRF simulations, a critical threshold where the outer convection must be at least a tenth as strong as the eyewall convection in order to initiate a secondary wind maximum and cause SEF to occur. Additionally the same SE analysis showed that no SEF event was possible, as a balanced response, without heating from outer convection. By creating composites of many aircraft observations Wunsch and Didlake (2018) were able to find features associated with SEF. Notably this included a broadening tangential wind field followed by the axisymmetrisation of an outer rainband complex. The importance of outer rainband activity is further highlighted in experiments performed by Wang

and Tan (2020) which showed inner rainband activity is unable to act as a substitute to drive the unbalanced processes in SEF, nor does SEF occur in experiments with suppressed outer rainband activity.

Another example of SEF not completing as expected is the so called partial eyewall replacement cycles modelled in Zhang et al. (2017) where outer convection initially develops a region of ascent at a radius much greater than the RMW, which gradually descends as in the case of a full eyewall replacement cycle. However, instead of forming a coherent secondary updraught separated by a moat region it merges with the primary eyewall. Wang and Tan (2020) describe, what is likely, a similar phenomenon with a ‘fake’ SEF event driven by inner rainband activity in one of their experiments. The ‘fake’ SEF has a secondary updraught but with no associated local tangential wind maximum and located much closer to the primary eyewall. The reason that the secondary updraught is so close to the inner eyewall, is that the induced boundary layer convergence from the inner rainbands are insufficient to increase the local vorticity enough to produce a secondary tangential wind maximum and hence the storm does not benefit from positive feedback associated with the unbalanced SEF mechanism (faster tangential wind means greater frictional induced inflow which leads to more spin-up and so on).

In an eyewall replacement cycle the two eyewalls are separated by a moat region, characterised by suppressed convection, descent and low equivalent potential temperature. The moat region is important to understand the replacement phase of the eyewall replacement cycle. Zhou and Wang (2011) show that during the eyewall replacement cycle the low entropy reservoir of the moat region interrupts the supply of moist entropy to the inner eyewall and hence weakening of the inner eyewall occurs. In addition, when the moat region is large, cold dry air is imported into the eye causing a strong weakening, whereas the intensity fluctuation is more subtle when the moat region is narrower and not well defined.

2.5 Intensity fluctuations

In addition to eyewall replacement cycles there are also other forms of intensity fluctuations that are less well studied. One example is vacillation cycles, a form of intensity fluctuations that sometimes occur during RI. Nguyen et al. (2011) showed that, during RI, Hurricane Katrina (2005) exhibited structural changes that caused the storm to ‘vacillate’ between monopolar and ringlike states which also led to short term intensity changes with the more monopolar states associated with acceleration of the tangential wind well inside the RMW and little intensification near the eyewall. The monopolar and the ring-like states were termed ‘symmetric’ and ‘asymmetric’ respectively because the former was associated with a smaller azimuthal standard deviation of PV and the latter a higher azimuthal standard deviation of PV. It should be noted that monopolar vs. ring-like and symmetric vs. asymmetric are independent metrics but are, in this case, correlated. Reif et al. (2014) showed that the asymmetric states were associated with radially inward moving isolated PV anomalies. The cause of the asymmetric states is further examined in Hankinson et al. (2014) which related asymmetric periods to both convective and barotropic instability. Hardy et al. (2021) showed similar processes occurring during the RI of Typhoon Nepartak (2016) with monopolar states associated with near stagnant tangential wind tendency and weaker eyewall updrafts than in the ring-like phase.

Similar changes in structure have been identified in observational data, notably in Kossin and Eastin (2001) who identified two regimes with a monopolar and ringlike angular velocity distribution which also have concomitant monopolar and ringlike equivalent potential temperature distributions.

Diurnal cycles have also been known to induce intensity fluctuations in TC structure during RI (Lee et al., 2020; Dunion et al., 2014) although these fluctuations can be explicitly linked to the external environment and have an imposed period of 24 hours.

2.6 Intensity fluctuations in Hurricane Irma

Intensity fluctuations have been observed in the case of Hurricane Irma during its second period of RI between 04 September and 06 September. Fischer et al. (2020) used observational data to identify two periods of weakening, on the afternoon of 04 September and the morning of 05 September, during RI where the RMW suddenly increased and described as “rapidly evolving eyewall replacement cycles” which was considered to be “antithetical” to the normal behaviour of eyewall replacement cycles that cause a TC to stop intensifying. The two periods of weakening were hypothesised to have different causes but were both linked to lower tropospheric convergence and vortex Rossby wave activity. These intensity fluctuation in Fischer et al. (2020) occurring during the RI of Hurricane Irma were subtle (relatively small intensity changes compared to most eyewall replacement cycles), but did involve an expansion of the RMW which, as in the case of a full eyewall replacement cycle, can increase the radius of gale force winds and increase the probability of storm surge, hence motivating a need to be able to understand and predict these forms of fluctuations. As the fluctuations occur over a short time period and involve subtle changes in the TC structure a modelling study is best suited to try and understand the dynamics at work.

2.7 Summary and unanswered questions

Over the last few decades there have been great strides made in understanding why and how TCs intensify. From an initial concept of a secondary circulation as a balanced response to a heat source, to fully fledged axisymmetric balanced paradigms such as the extended cooperative intensification paradigm, the TC is well understood from a balanced axisymmetric perspective. More recently TC understanding has been extended beyond the limitations of balanced axisymmetric dynamics to include unbalanced and asymmetric processes such as vortex Rossby waves. This improved understanding has been applied to better understand RI and eyewall replacement cycles which are two examples of still poorly predicted phenomena in TCs. There are however, even less well studied forms of intensity changes such

as intensity fluctuations that occur during RI. There is a paucity of research on these types of intensity fluctuations (which have been termed vacillation cycles) and nearly all of the previous analysis has been focused on a single storm (Hurricane Katrina (2005)). As such there is an incentive to perform further research on another storm such as Hurricane Irma (2017). Hurricane Irma displayed unusual intensity fluctuations during its RI. There has been a single observational study on these intensity fluctuations which ascribed them to a never seen before new form of eyewall replacement cycles. Therefore there is the need to conduct a modelling study into these fluctuations in order to investigate whether the intensity fluctuations in Hurricane Irma are similar to eyewall replacement cycles or more similar to vacillation cycles as in Hurricane Katrina (2005). A further advantage of Hurricane Irma is that a full eyewall replacement cycle occurred shortly after these intensity fluctuations giving scope for a direct comparison between both types of intensity fluctuations.

Chapter 3

Methodology

The thesis focuses on understanding intensity fluctuations in Hurricane Irma (2017) during a period of RI that occurred between 04 September and 06 September. In order to understand these fluctuations, a combination of flight observations, dropsondes, satellite and radar as well as model output from NWP forecasts performed with the MetUM were used. This chapter describes in detail the observational data used as well as the technical details of the MetUM model setup, including a description of the diabatic tracers which form part of the analysis. In addition, there is a section on how the centre of the storm is determined in the model data. Accurately determining the storm centre is important when azimuthally averaging the model data for subsequent analysis.

3.1 Observational data

The National Oceanic and Atmospheric Administration (NOAA) made multiple flights through Hurricane Irma (2017). The flyovers were performed by the NOAA aircraft operations centre (OMAO, 2020) and the 53rd Weather Reconnaissance Squadron (WRS, 2011). Observations used from these flights include in-situ wind speed and pressure measurements, dropsondes and airborne radar. Dropsondes measure many meteorological fields including temperature, pressure, windspeed and wind direction.

Visible Satellite, infra-red satellite (IR) and morphed integrated microwave imagery

(MIMIC) (Wimmers and Velden, 2007) provide additional information. Intensity estimates from the Satellite Consensus (SATCON) algorithm (Velden and Herndon, 2020) are used in conjunction with the lower temporal resolution best track data (HURDAT2) (Landsea and Franklin, 2013).

The SATCON intensity estimates are derived from the structure of the TC with heavy usage of microwave and satellite IR imagery, so relating structural changes to intensity changes would be a circular argument. Where possible, therefore, MSLP data from flights and dropsondes is used for short periods where there are a large number of flyovers such as in the afternoon of 05 September. MSLP data as an intensity proxy is preferable to flight-level tangential wind data which is strongly dependent on the direction of the flight into the eyewall and the height of the aircraft.

The dropsonde data is available in a quality controlled post processed format (in some cases due to lack of availability raw data was used). In addition some of the NOAA aircraft are equipped with C-band and doppler radars on the nose, lower fuselage and tail. The processed lower fuselage and tail radar data is used in the analysis and shows precipitation reflectivity in dBZ. The processed dropsonde, flight-level, satellite and radar data used in this thesis is available from the Hurricane Research Division ¹.

3.2 Numerical model setup

This model study is based on simulations conducted using the MetUM. The MetUM is a finite-difference NWP model with a dynamical core capable of solving the fully compressible, non-hydrostatic, deep atmosphere dynamical primitive equations using a semi-implicit semi-Lagrangian time integration scheme (Davies et al., 2005). Its vertical coordinate system is a terrain following height coordinates. The model variables are configured to a vertically staggered Charney-Phillips grid (Charney and Phillips, 1953) and a horizontally staggered Arakawa-C grid (Arakawa and Lamb, 1977). The MetUM has a comprehensive set of parametrisations for dealing

¹URL: https://www.aoml.noaa.gov/hrd/Storm_pages/irma2017/

with sub-grid level processes which includes a two-stream radiation scheme (Edwards and Slingo, 1996), a scale-aware warm rain scheme (Boutle et al., 2014), a diagnostic cloud scheme (Smith, 1990), a flow blocking and mountain wave drag scheme (Webster et al., 2003), a blended boundary layer scheme (Lock et al., 2000) and the Joint UK Land Environment Simulator (JULES) land surface scheme (Best et al., 2011). The parametrizations have been updated over the years. Full details of this are available in (Bush et al., 2020).

The MetUM has been setup in the regional tropical (RAL1-T) science configuration (Bush et al., 2020) which is designed for high resolution forecasts in tropical regions. The regional model domain used in the majority of the analysis is shown in Fig. 3.1a. The grid spacing for the regional model was 0.04 degrees latitude, 0.04 degrees longitude (approximately $4.4\text{ km} \times 4.4\text{ km}$), and 80 vertical levels which have a 38.5 km domain top and a first level of 5 m for horizontal flow. The model timestep is 75 s. The RAL1-T configuration has also been modified to reduce the drag coefficient for high wind speeds (Powell et al., 2003) such that it more closely matches observational data (Black et al., 2007).

The Met Office Global and Regional Ensemble Prediction System (MOGREPS-G) is used to run 18 ensemble forecasts in both the global configuration and the regional configuration. The global model, used to initialize the regional model is setup in the Global Atmosphere 6.1 configuration (GA6.1) (Bowler et al., 2008). The global configuration has a coarse 0.1875 degree meridional, 0.2815 degree zonal grid spacing (approximately $21\text{ km meridional} \times 30\text{ km zonal}$ at 17° N), and 70 vertical levels. The global ensemble member initial conditions are generated using an Ensemble Transform Kalman Filter (Heming et al., 2019) with schemes such as the Random Parameter v2 used to perturb uncertain parameters within physics parametrizations (Sanchez et al., 2016). Sea surface temperatures in each global ensemble are constant throughout the forecasts but may be different between members. The global ensemble model is used to generate the lateral boundary conditions for the regional configuration which is done at hourly intervals. There is no additional stochastic physics used within the regional model nor any regional model data assimilation or vortex specification schemes. As a result it is necessary to wait for at least fifteen

hours (which was determined by checking the large scale precipitation field until it stabilized) for the regional model to spin-up.

The main part of the analysis (including Chapters 4, 5, and 6) used a set of ensemble forecasts initialized on 03 September 00 UTC running for 96 hours with the regional model domain shown in Fig. 3.1a. An ensemble of forecasts initialized on 05 September 12 UTC was also used to analyse a full eyewall replacement cycle (see Chapter 7). Apart from these two ensembles, forecasts were also initialized on 02 September 12 UTC, 04 September 00 UTC, 05 September 12 UTC, 06 September 00 UTC and 06 September 12 UTC with the aim of determining how common intensity fluctuations or full eyewall replacement cycles are in MetUM forecasts.

3.3 Diabatic tracers

Incorporated into the MetUM are two sets of tracers (PV and potential temperature) capable of diagnosing diabatic contributions from various parametrisations within the model (Saffin et al., 2016). Examples of tracers being applied in extratropical cyclones include Chagnon et al. (2013). The PV is diagnosed in a semi-Lagrangian way by the tracer such that:

$$\frac{D(PV)}{Dt} = \sum_{phy} \frac{D(PV)}{Dt} + \sum_{dyn} \frac{D(PV)}{Dt} + \varepsilon. \quad (3.1)$$

The change in PV is given by the sum of increments from all physical processes in the first term represented by the subscript *phy* (namely radiation, micro-physics, gravity wave drag, boundary layer diabatic heating and friction and cloud pressure rebalancing). There are also dynamical processes in the second term represented by the subscript *dyn* which include the dynamical solver and mass conservation tracers. Ideally these tracers would be zero and preserve the material conservation of PV. However, this will not be the case in reality due to approximations made in the dynamical core of the model, and processes such as explicit diffusion, for example. The ε term represents residuals in the PV budget which may come from truncation errors or non linear effects between the various physical tracers. The

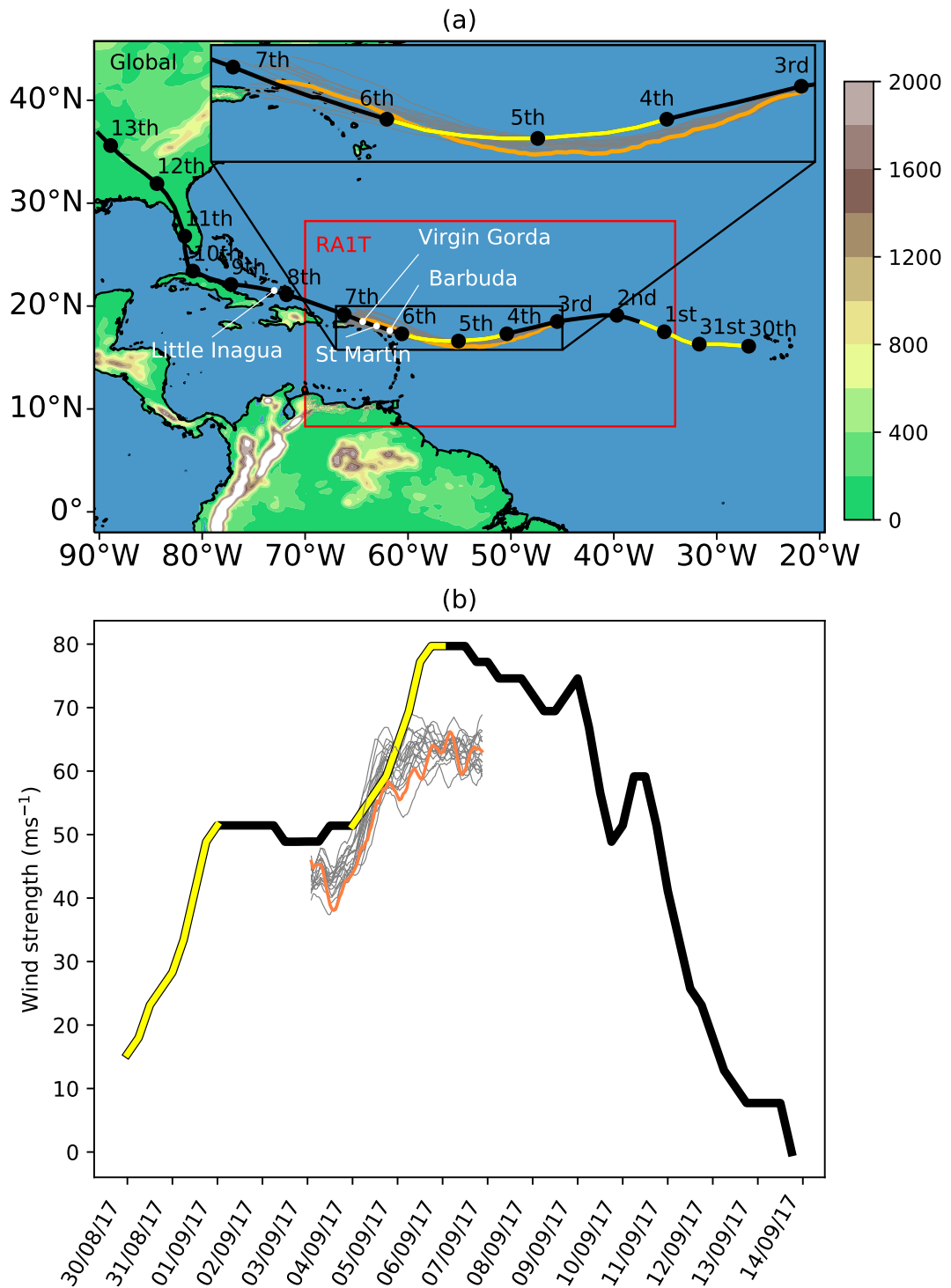


Figure 3.1: (a) Best track of Irma (black line) with points corresponding to the position of Irma on each date from 30 August 2017 to 13 September 2017. Orography (m) is shown in shading. The domain of the RA1T model is shown with the red rectangle. The two periods of RI are shown in yellow. The 18-ensemble tracks are displayed in grey with ensemble e15 shown in orange. Islands where landfall occurred are indicated by white dots and labels. (b) best track wind speed (black), the maximum surface wind of the ensembles initialised on 03 September 00 UTC with e15 highlighted in orange. Yellow lines indicate the two periods of RI.

tracer used most in this analysis is the “initial PV advected” tracer, PV_{adv} , which can be applied to work out what portion of the change in PV at a particular grid point is due to advection only (i.e. ignoring any change in PV generated by diabatic processes). Every hour the PV_{adv} tracer is reset to the diagnosed PV. The change in PV due to advection at a grid point (x,y,z) over the course of an hour is then given by:

$$PV_{adv}(x, y, z, t + 1) - PV(x, yz, t). \quad (3.2)$$

3.4 TC centre and track finding methods

It is important to ensure, when comparing observations to model data, that the observed TC centre over time is accurately and precisely determined especially when any comparisons are done in cylindrical storm relative coordinates.

3.4.1 Simplex

Much of the analysis is done from an axisymmetric perspective in storm–relative cylindrical coordinates. Calculations such as this can be highly sensitive to the location of the storm centre. The simplest way to find the TC centre in the model simulation is to find the coordinates that minimize the MSLP field. However, meso–vortices within the eyewall often lead to the MSLP being displaced from the geometric centre of the eye into the inner eyewall which can cause the tangential flow within the eye to be overestimated and the tangential flow outside the eye to be underestimated. Several more robust methods have been proposed, each with their own advantages and disadvantages. These include finding PV centroids (e.g. Riemer et al., 2010), geopotential height minima (e.g. Stern and Zhang, 2013) or finding the point that maximises tangential wind speed in cylindrical coordinates at its RMW (e.g. Ryglicki and Hart, 2015).

The method used in this analysis balances the need for a consistent and reliable method for finding the location of a TC centre to an appropriate degree of precision, while considering the computational cost of doing so for 18 ensembles over a 4 day

simulation period. The method used here is similar to the one used by Reasor et al. (2013) for flight radar data which can also be applied to model fields and uses a simplex algorithm to find the point that maximises the average tangential wind within an annulus with the radius of the midpoint equal to the RMW. The iterative simplex process is summarised in Figure 3.2. The Simplex Method (Nelder and Mead, 1965) is a method to find the minimum coordinate in an n variable function (in this case the average value of the RMW annulus in latitude/longitude space) by performing geometric transformations on a $(n + 1)$ coordinate object (the simplex) without the need to evaluate function derivatives. In the case of a two-dimensional model field ($n = 2$) the simplex will be a triangle (3 point object) of coordinate latitude, longitude points.

An initial simplex is created using the MSLP centre of the model field (black cross in Figure 3.2) and then taking points in an approximately equilateral triangle $1/2$ of a degree from that point (blue crosses in Figure 3.2). For each point in the initial simplex the radius of maximum tangential wind speed, around that point, is calculated and then the average value of tangential wind speed is found in an annulus 15 km wide around that radius of maximum tangential wind (e.g. black annulus around black cross in Figure 3.2). The annulus is composed of three rings of points with the middle ring corresponding to the maximum tangential wind speed. Similar annuluses are constructed around the other points in the simplex (same blue crosses in Figure 3.2). Based on the point in the simplex which maximises the value of the tangential wind a new simplex is created using a geometric transformation (simplex $i+1$ in Figure 3.2 which includes the black cross and two green crosses). With the new simplex the process is repeated until the convergence criteria are met (red cross and circle).

The convergence criteria for the algorithm are: no more than 50 function evaluations, an absolute change between iterations of no more than 0.5 m s^{-1} (of the value of the tangential wind within the RMW annulus) for the function evaluation, and an absolute error of no more than 0.5 km between points inside a simplex (well under the grid spacing of the model at 4.4 km). Some studies (e.g. Bell and Lee, 2012) average an ensemble of solutions based on different initial simplexes; however, it

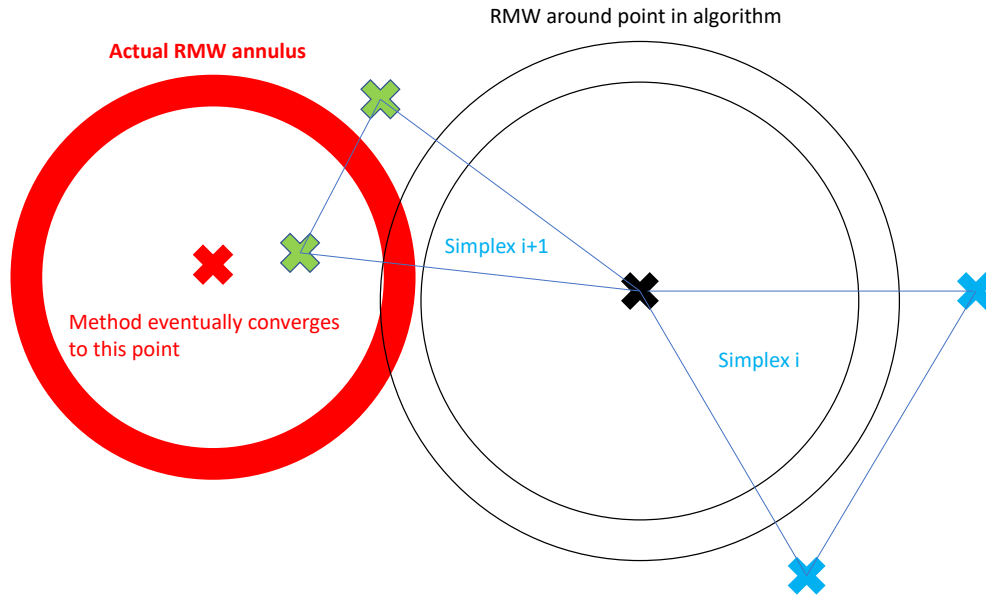


Figure 3.2: Schematic of the simplex TC centre finding method used.

was found that changing the location of the initial simplex did not result in a significantly different TC centre and so a single solution method was used throughout this work.

Figure 3.3 shows an example of the algorithm finding a more intuitive TC centre. In this case a random first guess, away from the minimum pressure centre was chosen for demonstration purposes. The three grey points surrounding the first guess represent the initial simplex. The final scatterpoint in red shows the method converges to produce a solution much closer to the middle of the eye implied by the maximum surface wind shading. The minimum pressure centre, in this case, was close to the inner eyewall in a mesovortex with only 2 hPa closed isobars.

Figure 3.4 shows that using the TC centre implied by the MSLP causes the underestimation of tangential flow in the eyewall and overestimation in the eye due to some of the eyewall flow being falsely 'averaged into' the eye when a MSLP centre is used. A similar effect causes radial inflow to be underestimated within the eyewall and overestimated within the eye. However, the error caused by the displaced TC centre reduces, as expected, as the radius from storm centre increases. Ensuring the TC centre is sensible, therefore, is particularly important for later analysis on

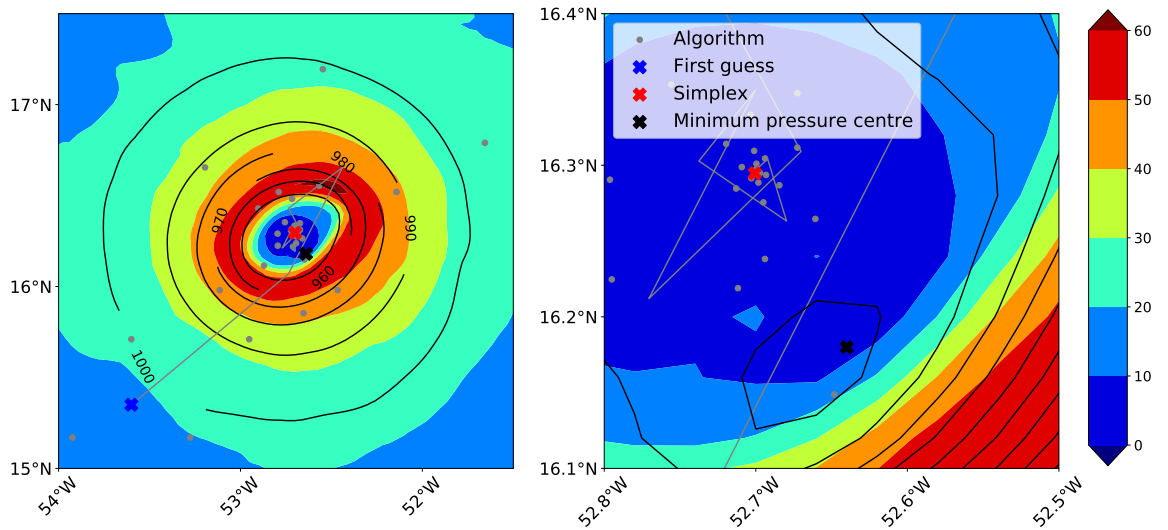


Figure 3.3: Ensemble member 0, T+36h, 10 m wind speed (shading) and MSLP (black contours) with scatter points showing an initial first guess for the algorithm (blue cross), MSLP (black cross), each point in the algorithm (grey dots) and the final point (red cross). A grey line shows the path centre of each simplex. The right panel shows a zoomed in version of the first. Contour intervals are 10 hPa for the left panel and 2 hPa for the right panel.

inner core processes.

Figure 3.5 shows a comparison between the track of the 0 ensemble of the regional model with TC centres using MSLP and the simplex method. The track using the simplex method can be seen to be a lot smoother whereas the track using minimum surface level pressure is highly perturbed and noisy especially on the 4th September. The more intense storm on the 5th and 6th September has a similar track for both methods implying the storm became more symmetric with the MSLP coinciding more with the geometric centre of the eye.

3.4.2 Track finding methods

NOAA provides ‘best track’ data; however, this dataset has a low spatial and temporal resolution. Wind centre fixes, a method to pinpoint the storm centre location in real time using flight directional wind data are also provided with a high spatial and temporal precision based on the method described by Willoughby and Chel-mow (1982). This involves constructing lines perpendicular to the wind direction along the flight track and comparing with the line drawn when the wind speed

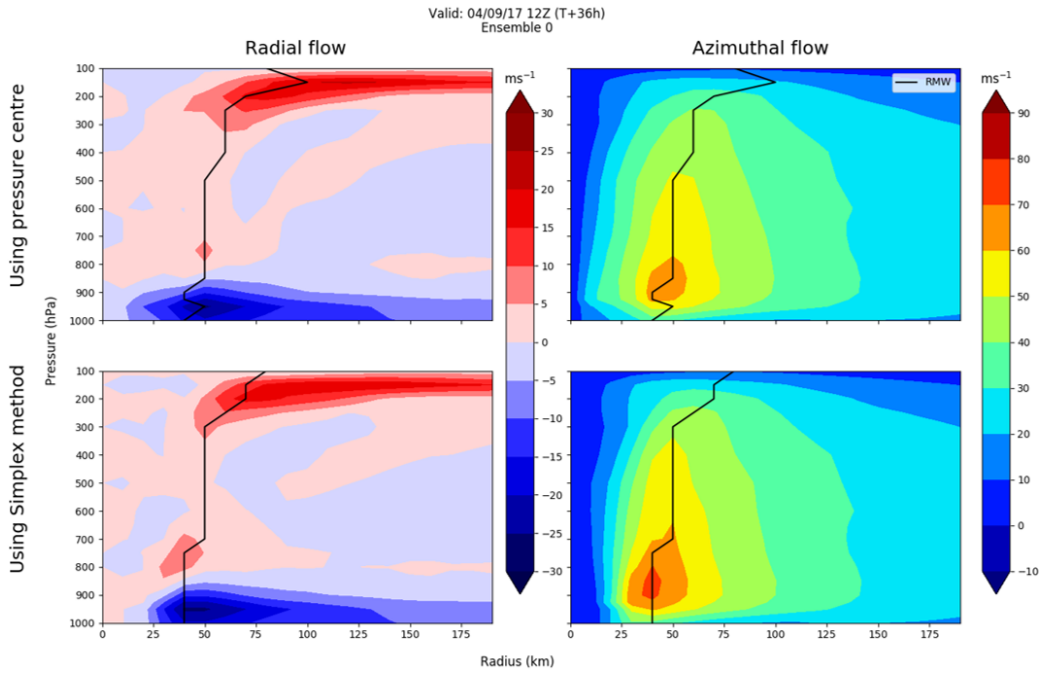


Figure 3.4: Comparison for the same time period and ensemble as Fig. 3.3 showing the difference between the storm–relative radial flow and the tangential flow in cylindrical coordinates using the MSLP centre (top) and the centre derived using the simplex method (bottom).

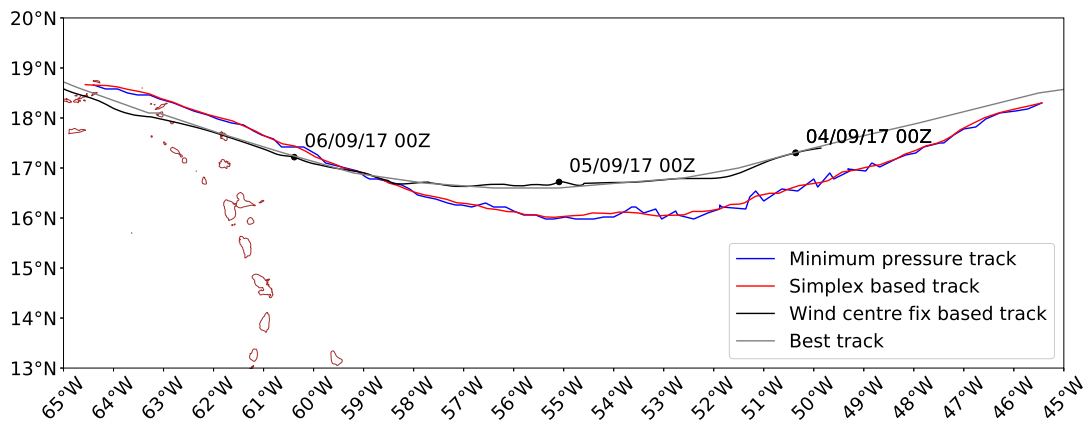


Figure 3.5: Comparison of the regional model ensemble member 0 track using MSLP and track derived with the simplex method.

reverses direction and minimising the squares of all the distances to intersect with this wind speed reversal line. To ascertain whether this wind centre fix track data is an accurate representation of the storm track it has been checked against another, more modern, method: the translating pressure fit (TPF) technique described by Kepert (2005) which involves fitting an analytic Holland-B function (Holland, 1980) to dropsonde or flight pressure data and performing a least squares regression analysis to minimize a cost function using the Levenberg-Marquadt algorithm. This method was first attempted using dropsonde data. The explicit form of equation 6 in Kepert (2005) is given in equation 3.3.

$$J = \sum_{i=1}^{n_{obs}} \left\{ \frac{p_i - p_{hol}}{\sigma} \right\}^2, \quad (3.3)$$

$$p_{hol} = p_e - \Delta p \left(1 - \exp \left(\left(\frac{RMW}{Hav(x_i + ut_i, y_i + vt_i, x_c, y_c)} \right)^b \right) \right),$$

where x_i, y_i, t, p_i are the dropsonde longitudinal, latitudinal, time coordinate and surface dropsonde pressure defining the observed data. J is the cost function to be minimized with 8 degrees of freedom corresponding to the following 8 parameters. $p_e, \Delta p, RMW, x_c, y_c, u, v, b$ are the environmental pressure, TC pressure drop, radius of maximum wind speed, longitudinal TC centre coordinate, latitudinal TC centre coordinate, zonal translational TC velocity component, meridonal TC velocity component, Holland B parameter (storm shape) respectively. $Hav(x_1, y_1, x_2, y_2)$ is the haversine formula for calculating distances on a sphere (Earth constant radius is assumed). Given the relative paucity of dropsonde measurements, the need for a small time window (to preserve a storm's characteristics) has to be balanced with the need for enough observations for the least squares analysis to be robust with an absolute minimum of more than the 8 degrees of freedom, where any function can be guaranteed to perfectly match the data given the right, and often wildly unrealistic, parameters. Adding additional parameters for storm acceleration or deepening/weakening does not solve the issue as it increases the number of degrees of freedom. On balance, a window of approximately 6 hours was used. The time dependence in a storm's intensity can be partly rectified by choosing σ to be of the form $0.1hPa + ct$. c was chosen to have a value of 1 hPa h^{-1} which is a reason-

able level of deepening that might be expected during a RI period. Given all the caveats about the regression analysis, there will be some conditions as to whether a TPF based centre is considered: all the parameters should have reasonable values (b should not be less than 1 or more than 2.5, the RMW should be between 20 and 100 km, p_e should be within 10 hPa of 1010 hPa and the pressure drop should be between 60 and 90 hPa); all their errors should be reasonably small (especially in the case of x_c and y_c which should have a standard error of less than 0.1 degrees, a greater error is allowed on the other parameters), and the standard errors should also not be zero.

Figures 3.6 and 3.7 show an implementation of the TPF method for dropsondes from a flight on 03 September and 05 September (the $t=0$ time was set at 2222 UTC and 1235 UTC respectively). Both the x and y coordinate of the wind fix derived centre are within the standard error of the TPF derived centre. The centres are 3.7 km apart which is less than the regional model resolution. All of the other parameters are reasonable except the meridional velocity component which has the wrong size and magnitude (and also the largest standard error). The conditions described above were not met for 04 September; no sensible cost function could be determined so there is no analysis for this date. This may also be due to the intensity fluctuations that would have caused a rapid variation in RMW and made a function even more difficult to fit.

3.5 Vortex Rossby wave identification

As part of the model analysis, it will be necessary to determine if there are any VRWs present. This section gives details about how to verify where a PV anomaly is moving in the correct speed and direction to be consistent with the behaviour of VRWs. Analysis method is applied both in Chapters 5 and 7.

In order to determine whether the wavenumber-2 PV activity is as a result of VRWs, the VRW dispersion relation (equation 3.4), originally derived in Montgomery and Kallenbach (1997), can be evaluated:

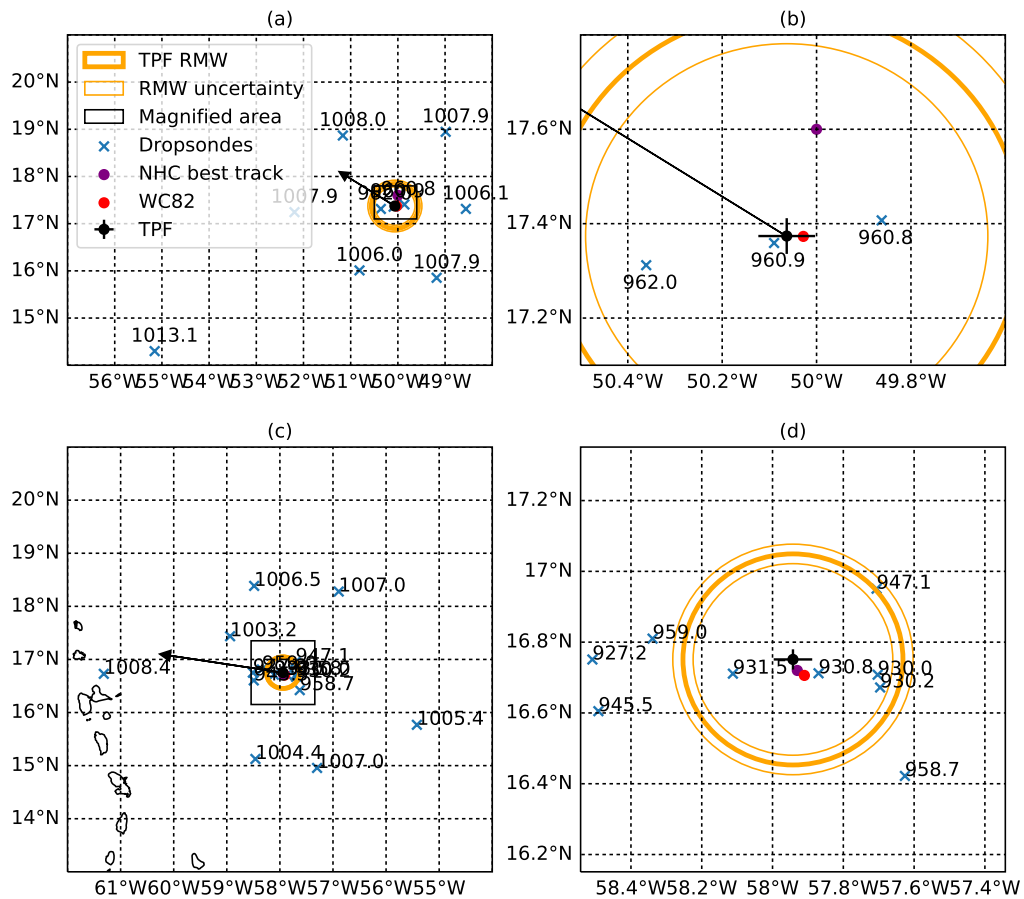


Figure 3.6: Dropsondes (blue crosses), NHC interpolated best track (purple points), WC82 TC centre, TPF TC centre (black point with uncertainty cross), TPF implied RMW (thick orange line) and its standard error (thin orange lines) and TPF implied translation velocity (black arrow). Flights shown are (a,b): NOAA42 (01111A) flight occurring between 1911–0230UTC on 03 September $t=0$ is arbitrarily taken to be 22:22:52 the time at which dropsonde 4 hits the surface. (c,d): NOAA42 (01111A) flight occurring between 0959–1453 UTC on 05 September. $t=0$ is arbitrarily taken to be 12:35:10 roughly the time at which a dropsonde hits the surface and to coincide with a WC82 point.

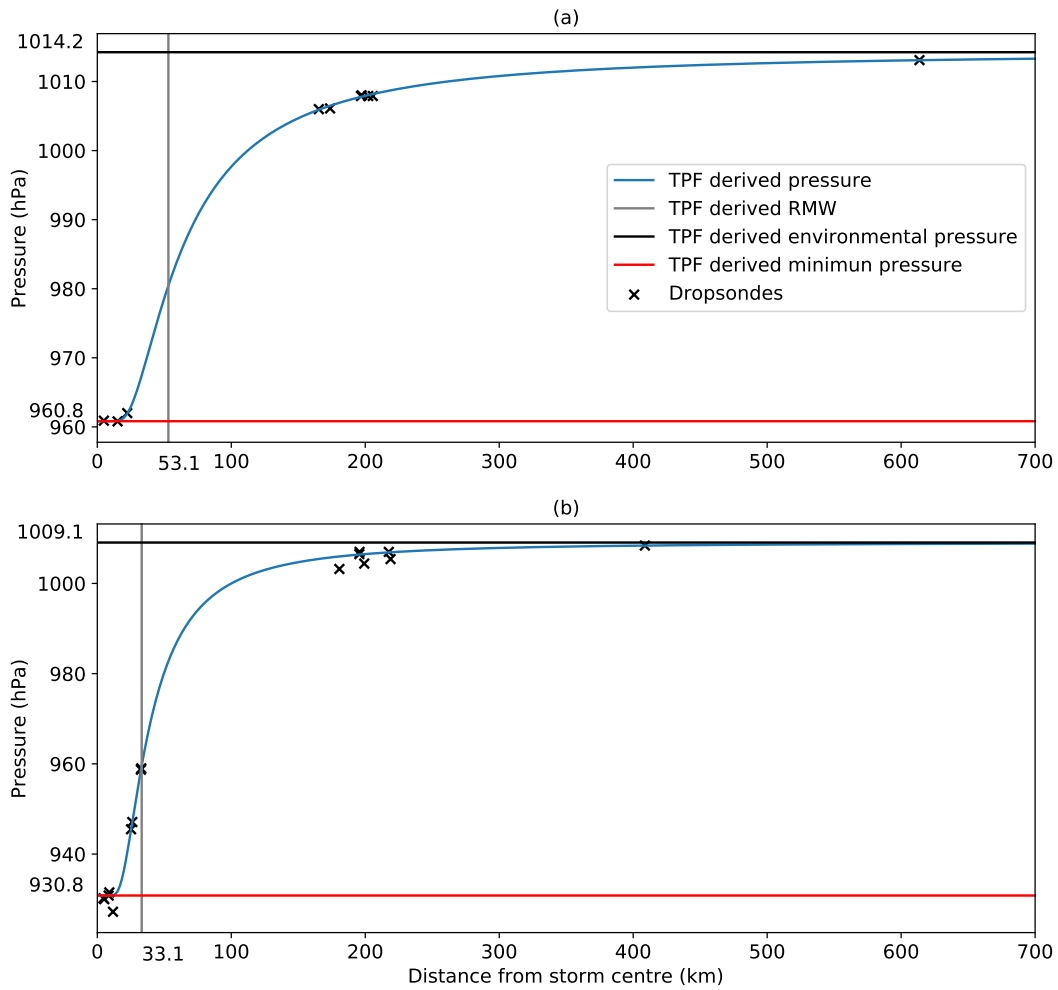


Figure 3.7: Plot of p_{hol} showing p_e , RMW parameters as well as the implied pressure at the TC centre. Valid for (a): the NOAA42 (01111A) flight occurring between 19:11-02:30 UTC on 03 September (b): NOAA42 (01111A) flight occurring between 0959-1453 UTC on 05 September.

$$\omega = n\Omega + \frac{n\bar{\xi} \frac{\partial \overline{PV}}{\partial r}}{R\overline{PV} \left[k^2 + \frac{n^2}{R^2} + \frac{\bar{\eta} \bar{\xi} m^2}{N^2} \right]}, \quad (3.4)$$

where ω is the angular frequency of the VRW, \overline{PV} is the mean state PV, R is the reference radius the dispersion relation is evaluated at, $\Omega = v/R$ is the azimuthal angular frequency, $\bar{\xi} = 2v/R + f$ is the inertial parameter (f is the Coriolis frequency), N^2 is the static stability, and $k = k(r, z, t)$ and $m = m(r, z, t)$ are the radial and vertical wavenumbers of the VRWs respectively, n is the azimuthal wavenumber which in this case is 2. From equation 3.4 the azimuthal phase velocity ($C_{\rho\lambda} = R\omega/n$) can then be calculated. It is possible to evaluate most of the terms in this equation from simple manipulation of the model fields or their gradients.

The radial and vertical wave numbers are more difficult to calculate. These wave numbers were calculated using an empirical mode decomposition and Hilbert transformation described in Huang et al. (1998). Essentially the wavenumber-2 PV structure is decomposed into radial or vertical wave components called empirical mode decompositions (EMD). The mode with the highest amplitude is then Hilbert transformed which allows an ‘instantaneous frequency’ to be identified by differentiating the unwrapped phase change in the analytical (Hilbert transformed) wave. The algorithm to calculate this instantaneous phase is available here <https://pypi.org/project/EMD-signal/> and was developed by Dawid Laszuk. The method is stochastic as it evaluates an ensemble of signals which are perturbed by random variations. This stochastic method is necessary to produce a single EMD with a relatively high amplitude compared to the other EMDs. Because the method is stochastic and occasionally also produces unphysical negative frequencies it is necessary to average the result over several azimuths to make it more robust. The advantage of this method is that it allows the motion of VRWs to be fully, quantitatively, diagnosed (if they exist) as a function of time, radius and height as opposed to selecting just one reference radius and height with estimates for m and k . Further details of the method are available in Chapter 5.

In addition to the azimuthal phase speed, the radial phase speed can be calculated

as follows:

$$C_{phase,r} = \frac{\omega}{k}, \quad (3.5)$$

which allows the outward propagation speed of the VRWs to also be verified.

3.6 Calculation of equivalent potential temperature (θ_e)

Equivalent potential temperature provides useful information about the thermodynamic structure of the storm and functions as a sensible proxy for entropy. θ_e is used to analyse the effect of the secondary eyewall on the inner eyewall and understand why the inner eyewall dissipates from a thermodynamic perspective (Chapter 7).

The MetUM does not output the θ_e field; therefore, the variable had to be calculated.

The mathematical formulation of θ_e as given in Bryan (2008) is:

$$\theta_e = T \left(\frac{p_0}{p} \right)^{R_d/(c_p+r_t c_{pl})} RH^{-r R_v/(c_p+r_t c_{pl})} \exp \left[\frac{L_v r}{(c_p + r_t c_{pl}) T} \right], \quad (3.6)$$

where RH is the relative humidity, T is the temperature, p is the pressure, p_0 is the reference pressure (1000 hPa), r is the water vapour mixing ratio, r_t is the total water vapour mixing ratio, c_p is the dry specific heat capacity at constant pressure, c_{pl} is the specific heat capacity of liquid water at constant pressure.

This equation involves both the variable relative humidity (raised to an exponent), which also has to be calculated, and a function involving an exponent of a temperature dependant latent heat of vapourisation. The large errors associated with exponents of these inexact quantities make this formulation undesirable as a means to calculate θ_e . Instead the following method based on equation 39 in Bolton (1980) was used:

$$\theta_e = \theta_L \exp \left(\left(\frac{3036}{T_L} - 1.78 \right) r (1 + 0.448r) \right), \quad (3.7)$$

where θ_L is the potential temperature at the lifting condensation level, T_L is the

temperature at the lifting condensation level. In order to determine θ_L and T_L the expression for the temperature and potential temperature at the lifting condensation level was used from Romps (2017) which gives equations for θ_L and T_L as:

$$\begin{aligned} T_L &= c \left[W_{-1} \left(RH^{\frac{1}{a}} c e^c \right) \right]^{-1} T, \\ a &= \frac{c_{pm}}{R_m} + \frac{c_{vl} - c_{pv}}{R_v}, \\ c &= \frac{-E_{0v} - (c_{vv} - c_{vl}) T_{trip}}{a R_v T}, \end{aligned} \quad (3.8)$$

$$\theta_L = T_L \left(\frac{p_0}{p \left(\frac{T_L}{T} \right)^{\frac{c_{pm}}{R_m}}} \right)^{R/c_p}, \quad (3.9)$$

where W_{-1} is the negative one branch of the Lambert-W function, c_{pm} is the moist specific heat capacity at constant pressure, R_m is the moist specific gas constant, c_{vl} is the specific heat capacity of liquid water, c_{pv} is the moist specific heat capacity at constant volume, R_v is the specific gas constant for water vapour, E_{0v} is the difference in specific internal energy between liquid and solid at the triple point of water, c_{vv} is the specific heat capacity of water vapour at constant volume, T_{trip} is the temperature of the triple point of water, R is the dry specific gas constant. All of these quantities are known prognostic variables or constants (see Romps (2017) for values used) except the relative humidity which also has to be calculated. The relative humidity was output at the surface level which was used to check the calculated value was reasonable.

The relative humidity is given by the ratio of the vapour mixing ratio (prognostic variable) to the saturated vapour mixing ratio:

$$RH = \frac{r}{r_s}. \quad (3.10)$$

In order to calculate the saturated vapour mixing ratio the following formula is used,

$$r_s = \frac{R p_s}{R_v p}, \quad (3.11)$$

where p_s is the saturation vapour pressure. It is important to obtain the maximum possible accuracy for the relative humidity over a sensible temperature range. Consequently the empirical Arden–Buck equation is used (Buck, 1981) to calculate the saturation vapour pressure which has good accuracy in the meteorologically relevant temperature range (-50 to 30°C):

$$p_s = \begin{cases} 6.1121 \exp \left(\left(18.678 - \frac{T}{234.5} \right) \left(\frac{T}{257.14+T} \right) \right), & T > 0^\circ C \\ 6.1115 \exp \left(\left(23.036 - \frac{T}{333.7} \right) \left(\frac{T}{279.82+T} \right) \right), & T < 0^\circ C. \end{cases} \quad (3.12)$$

3.7 Summary

In summary this chapter describes the observational data, namely flight-level, dropsonde, satellite, microwave and radar which are used to evaluate the MetUM model performance in Chapter 4 and analyse intensity fluctuations in Chapter 5. The details of the model setup for the MetUM is examined which forms the bulk of the analysis in this thesis. This also included the novel tracer system which was used to look at PV transport in Chapter 5. The method for finding the tropical cyclone centre for azimuthally averaged model output is also described along with how the observed track is determined, which is important for any analysis that involves working in cylindrically symmetric coordinates.

Chapter 4

Model Evaluation

4.1 Synoptic overview

Hurricane Irma was the first major hurricane of the 2017 North Atlantic hurricane season. Irma peaked at an intensity of 80 m s^{-1} (1-minute sustained surface wind speed) with a central surface pressure estimate of 914 hPa early on 06 September before making landfall in Barbuda (Cangialosi and Berg, 2018). A summary of the track of Irma is shown in Fig. 3.1 along with the best track surface wind speed. Irma underwent two periods of rapid intensification (RI): firstly, between 30 August 00 UTC and 01 September 2017 00 UTC where Irma intensified from a tropical storm to a category 3 hurricane on the Saffir-Simpson scale, and secondly, during a period of RI where Irma intensified from a category 3 storm (945 hPa , 50 m s^{-1}) at 00 UTC on 04 September to a category 5 storm (914 hPa , 80 m s^{-1}) at 00 UTC on 06 September (Cangialosi and Berg, 2018). The focus of the analysis here is the period of RI between 04 and 06 September.

Irma formed from an African Easterly wave off the west coast of Africa at around 30°W , 17°N on 30 August. By 21 UTC on 30 August Irma was a coherent area of low pressure situated under an upper-level anticyclone in a low shear environment moving westward. On 31 August Irma began an initial period of RI reaching hurricane strength and a clearing eye structure, moving in a north westerly direction. This first period of RI terminated early on 01 September with an intensity of

51m s^{-1} at 03 UTC. Irma remained in a slightly weakened state during the period from 01 September to 02 September due to a combination of marginal sea surface temperatures and an influx of dry air (Cangialosi and Berg, 2018). Irma's eyewall was noted to be rather small. Irma's track also became more southwestward due to the increasing influence of a subtropical ridge to the north.

The second period of RI began on 04 September with Irma reaching an intensity of 60 m s^{-1} by 03 UTC on 05 September. At this time, Irma was in a low wind shear environment with sufficient mid-level tropospheric moisture for intensification and high sea surface temperatures. The influence of the subtropical anticyclone to the north of Irma pushed the storm in a westward direction with a translational velocity of about 5 m s^{-1} . Irma reached category 5 intensity by 12 UTC on 05 September and peak intensity of 80 m s^{-1} by 06 September. Irma made landfall in Barbuda at near peak intensity at 0536 UTC with a minimum recorded mean sea level pressure (MSLP) of 915.9 hPa. During the course of 06 September Irma maintained its intensity and landfall occurred later that day at St. Martin at 1115 UTC and Virgin Gorda at 1630 UTC.

Despite favourable environmental conditions Irma weakened to category 4 during 07 September due to the start of an eyewall replacement cycle. Irma passed over Little Inagua at 05 UTC on the same day. The eyewall became distorted and elliptical by 03 UTC on 08 September with an eyewall replacement cycle underway, causing the storm to weaken to category 4. Irma also passed over Little Inagua at 05 UTC. An interaction with the orography of Cuba on 09 September caused further weakening to an intensity of 57 m s^{-1} by 21 UTC, although there was a brief period of intensification that occurred around 03 UTC on 09 September despite Irma's close proximity to land. A concentric eyewall structure was also observed early on 10 September.

Thereafter, apart from a brief period of intensification that occurred around 03 UTC on the 09 September, Irma gradually weakened due to increasing vertical wind shear and eventually land interaction after making landfall in Florida on 11 September. Irma finally dissipated inland on 13 September. Further details on the synoptic overview of Hurricane Irma (2017) are available in Cangialosi and Berg

(2018).

4.2 Intensity and tracks

A key way of evaluating the model performance is to check that the storm track and intensity are similar to the observations. The global and regional model ensemble tracks for Hurricane Irma, initialised on 03 September 2017 at 00 UTC, are shown in Fig 4.1. The model tracks are calculated using a simplex algorithm described in detail in section 3.4.1. These tracks are compared with the wind centre fix (WCF) based track which is based on flight measurements (described in section 3.4.2). Also shown is the ‘best track’ which uses IBTrACS data (Knapp et al., 2010) to derive the storm centre location from satellite measurements.

The track of Irma (denoted by the ‘best track’ and wind centre fix based track) is accurately predicted by the model with deviations of typically less than 50 km from the centre of the storm. The global model has a slightly more southward track initially than the regional model. Towards the end of the simulation, most of the global and the regional model ensembles position the storm slightly too far north. Figure 4.2 shows that the track error increases greatly with forecast lead time for the global model which is due to the modelled translational speed being too slow in the global model compared to the actual track. It is worth noting that there is little evidence that there is any relationship between the intensity of the TC in each ensemble and the track of the storm.

The MSLP of the storm was represented well by the regional model. Figure 4.3 shows all the ensembles closely followed the National Hurricane Centre’s MSLP estimates (Cangialosi and Berg, 2018) albeit with a slightly faster rate of RI between the first and second day of the simulation and a slightly weaker rate of intensification thereafter. The global model was incapable of adequately intensifying the TC. Most of the ensembles only intensified the TC by around 10 hPa over the entire simulation period (not including an initial spin up where the storm was initialized too deep). A similar pattern to the MSLP can be seen in the maximum surface wind speeds shown in Fig. 4.3. The regional model captures the RI well with the ensembles

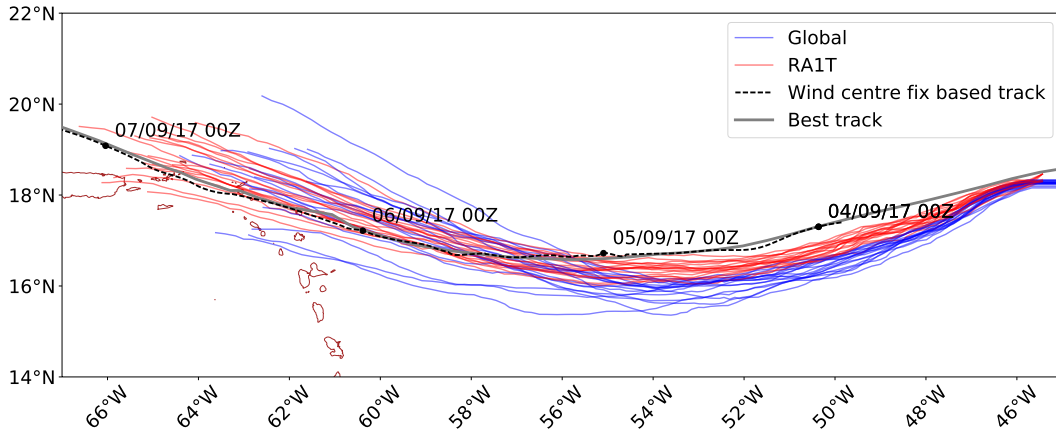


Figure 4.1: Storm tracks for Hurricane Irma (2017). The RA1T model (initialized 03 September 00 UTC) storm tracks are shown in red and the tracks from the global model are shown in blue. The grey line shows the IBTrACS best track and the black line shows the wind centre fix based track.

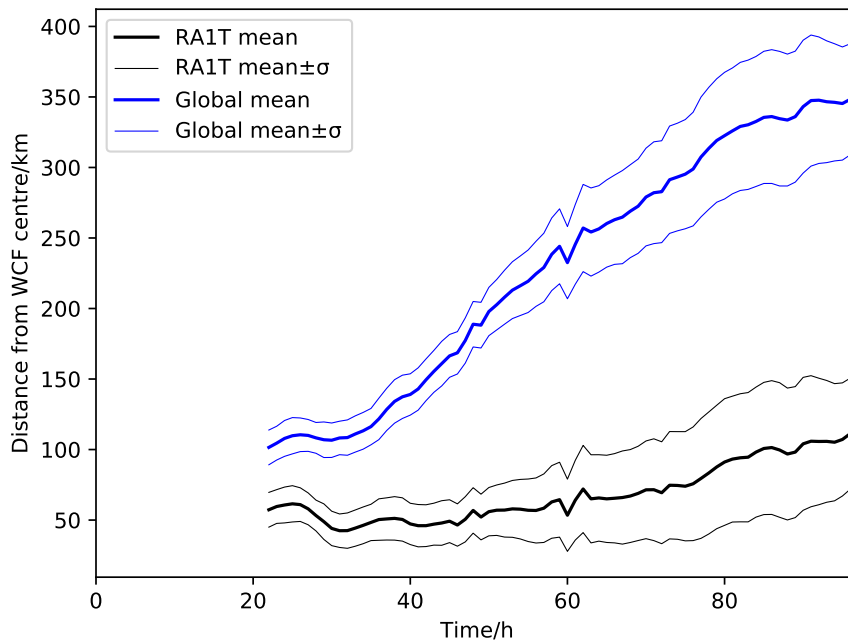


Figure 4.2: Average storm centre difference from the actual storm centre (wind centre fix centre) for both the global and regional model. The wind centre fix data was not available for the first 24 hours and, therefore, is not shown. One standard deviation either side of the mean is also shown. WCF data is unavailable before +21hours due to a paucity in dropsonde and flight data at this time.

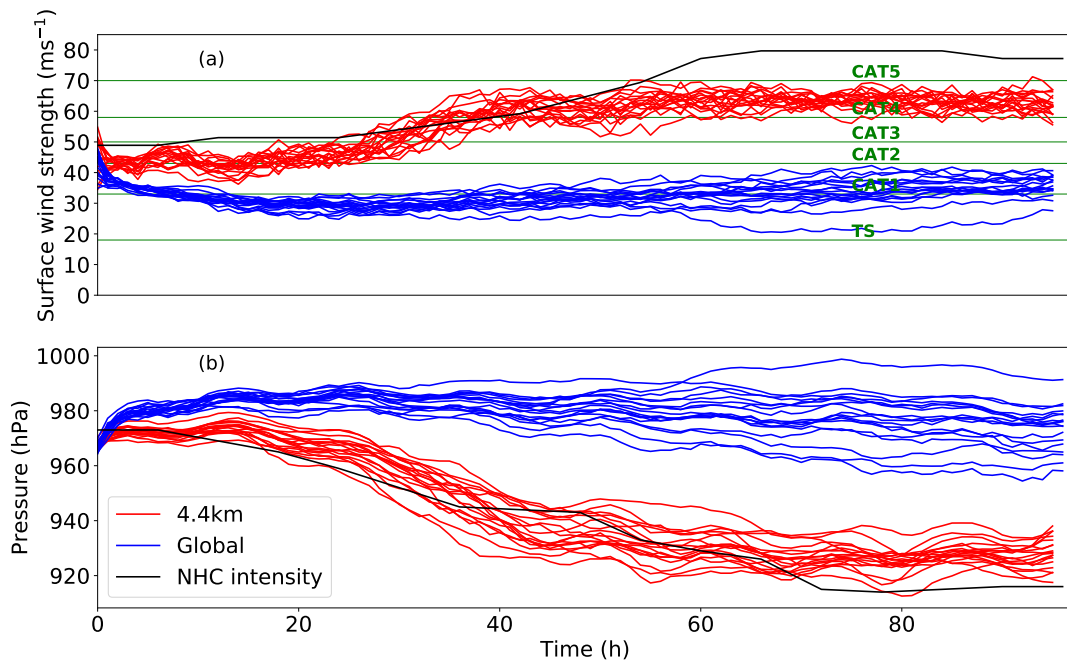


Figure 4.3: (a) MSLP and (b) maximum surface wind speed as a function of run time for both the global (blue lines) and regional (red lines) simulations and NHC intensity (black line).

following the NHC intensity closely, albeit with intensification occurring slightly too rapidly up until day two where the intensification levels off too quickly with most of the ensembles ending the simulation as a category 4 storm. The global model only weakly intensifies the TC with most ensembles only producing a category 1 storm by the end of the simulation which is unsurprising given that TC intensity is sensitive to horizontal resolution particularly around the resolution where convection can be resolved Gentry and Lackmann (2010). Both the regional and global models exhibit an initial model spin-up period in which there is an unphysical rapid weakening of the storm in the first few hours.

The MetUM has had a long standing issue with a wind speed bias in strong TCs (Short and Petch, 2018). The bias is examined by plotting the MSLP for each simulated storm against the maximum surface wind speed. The regional model agrees well with the NHC wind-pressure relation for the storm (Fig. 4.4) during the first two days of the simulation after which the regional model produces a storm which is too deep for its respective wind speed. This behaviour is consistent with previous studies where the regional MetUM model diverges from the wind-pressure relationship at higher intensities. The global model performs worse than the regional model with over-deepening occurring at relatively weak intensities. Two notable features of the observed wind and pressure relation are the initial step decline in

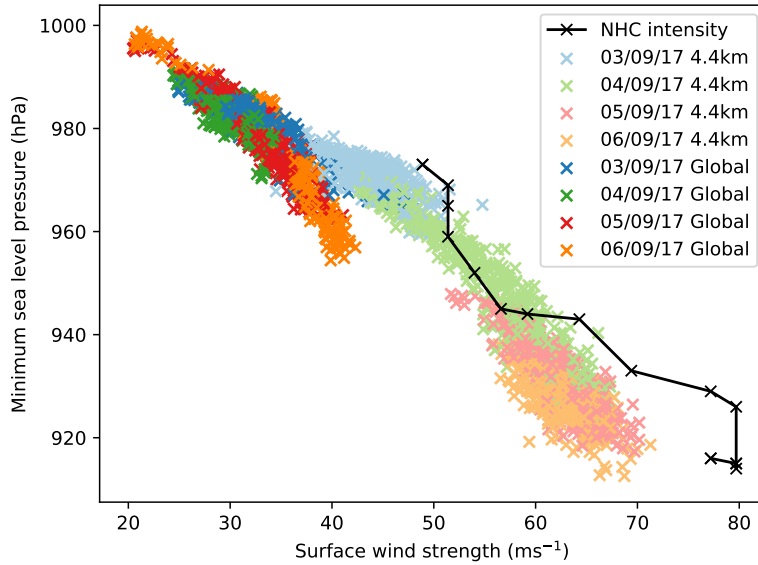


Figure 4.4: MSLP as a function of maximum surface wind speed for both the global and regional models, and NHC intensity for the simulation initialized on 03 September 00 UTC.

pressure with only a weak increase in wind speed late on 03 September and early on 04 September, and a more rapidly decreasing wind than pressure at the end of the simulation. These paths through pressure–wind phase space are interpreted in the same manner as Kossin (2015). The NHC intensity path shows an initial steep decline in pressure relative to surface wind strength which would indicate a weak eyewall replacement cycle (although the observational evidence for this is unclear), while a decrease in wind strength at constant pressure implies a strong eyewall replacement cycle. The model does not capture the start of the eyewall replacement cycle at the end of 06 September; however, it should be noted that the secondary eyewall formation does not happen until 07 September (past the simulation period for the 03 September 00 UTC initialized forecast).

4.3 Selection of a representative ensemble

The deviations between the different ensemble members are subtle and variations in intensity, shape and structure are small. All of the ensembles in the regional model suffer from systematic biases. In general they tend to produce TCs that have an overly large eyewall and RMW. The eyewall also tends to be too weak at all

levels except in a layer around 1000 m above the surface where the wind strength can sometimes be stronger than expected. There is also an issue regarding all the ensembles intensifying the storm too quickly on 04 September and too slowly thereafter. The most representative ensemble will have a lower bias in as many of these points as possible.

A compelling case could be made for ensemble members 0, 3, 15 or 16. Each one of these ensembles has a lower bias in most of these metrics. Ensemble members 0, 3 and 15 have amongst the smallest eyewalls and RMWs (averaged over the entire simulation the 6th, 2nd and 1st lowest, respectively) although this still only means RMWs on the order of less than 5 km lower than average. Ensemble 0, 3 and 15 also have one of the most accurate storm tracks from 36 hours onwards, although they are slightly too far south (as are most of the ensembles) prior to this. Ensemble 16 is slightly more accurate prior to 36 hours but less accurate by the end of the simulation ending up too far north. Despite these shortcomings, ensemble 16 does have one of the best time dependant intensification profiles. Ensemble members 0, 3 and 15 intensify and finish intensifying too early.

Taking everything into account ensemble member 15 was selected as the most representative ensemble for further analysis. This is partly due to its more accurate tangential wind strength towards the end of the simulation (particularly on 05 September) when many of the other ensembles were too weak. Also the RMW of this ensemble was small compared to the other ensemble members which makes it the most accurate in terms of the radial position of the eyewall.

4.4 Satellite observations

4.4.1 Comparison between model output and satellite imagery

Figures 4.5, 4.6, and 4.7 show regional model outgoing long wave radiation for all 18 ensemble members which can be qualitatively compared with the visible and infrared satellite imagery. All subplots are centred on the storm so will have slightly different longitude and latitude axes. Each subplot has an area of 10 degrees longitude by 10 degrees latitude. The development of Irma is consistent with Fig. 4.3,

in that the development was too rapid. Figure 4.5 shows that by 14 UTC on 03 September the eye of Irma was only beginning to clear out. However, the model outgoing long wave radiation plots imply a more mature eye structure. Some of the ensembles manage to correctly identify the orientation of the two main spiral bands to the southwest and northeast of the TC centre. In particular, ensemble 17 has trailing thunderstorms to the southwest of the TC and a band visible to the northeast (Fig. 4.5). Ensemble 8 seems to be an outlier with a less developed structure and ragged eye. By 04 September (Fig. 4.6) all ensembles have developed a large clear eye with a symmetrical central dense overcast region. Again, this does appear to be a more coherent structure than implied by the visible satellite and IR imagery. By the 05 September at 14 UTC the structure of the storm seems to be better represented with both the satellite imagery and the model outgoing long wave radiation implying a large clear eye with a large central dense overcast. The structure on 06 September is also adequately modelled (not shown). 11 out of 18 ensembles correctly show thunderstorm activity to the south east with most of the ensembles appearing to show the outflow channel to the north of the storm centre.

4.5 Radar imagery

Radar data was collected from NOAA's P3 aircraft radars during flights into Hurricane Irma (see chapter 3 section 3.1). The flight-level radar data can be qualitatively compared to the regional model large scale rain output to give indications about how well the model is performing with regards to the TC convective structure such as the shape and size of the eyewall, existence of outer rainbands or isolated thunderstorms. Figure 4.8 shows a comparison of the regional model ensembles' surface radar reflectivity (calculated using diagnosed large scale rain rate model data) compared to the flight-level radar at T+33 h. The difference in level of the radar and model output makes any quantitative comparison impossible; however, it is possible to point out some broad structural differences. Firstly, the implied reflectivity in the model output is excessively high which may be a parametrization issue. Secondly, the double eyewall structure is only captured in some of the ensembles

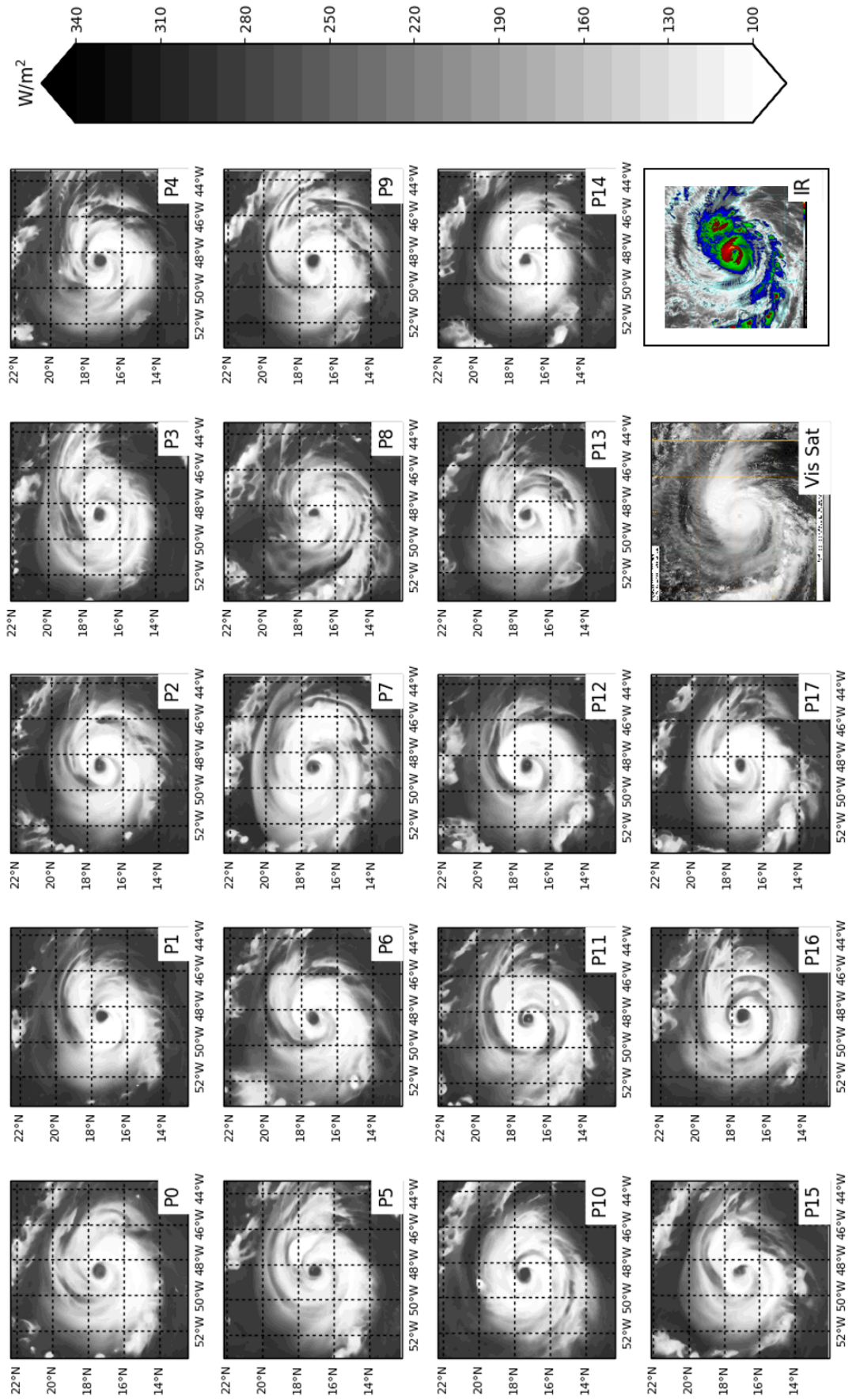


Figure 4.5: Regional model outgoing long wave radiation for 03 September 14 UTC (T+14h) with visible/IR satellite for comparison.

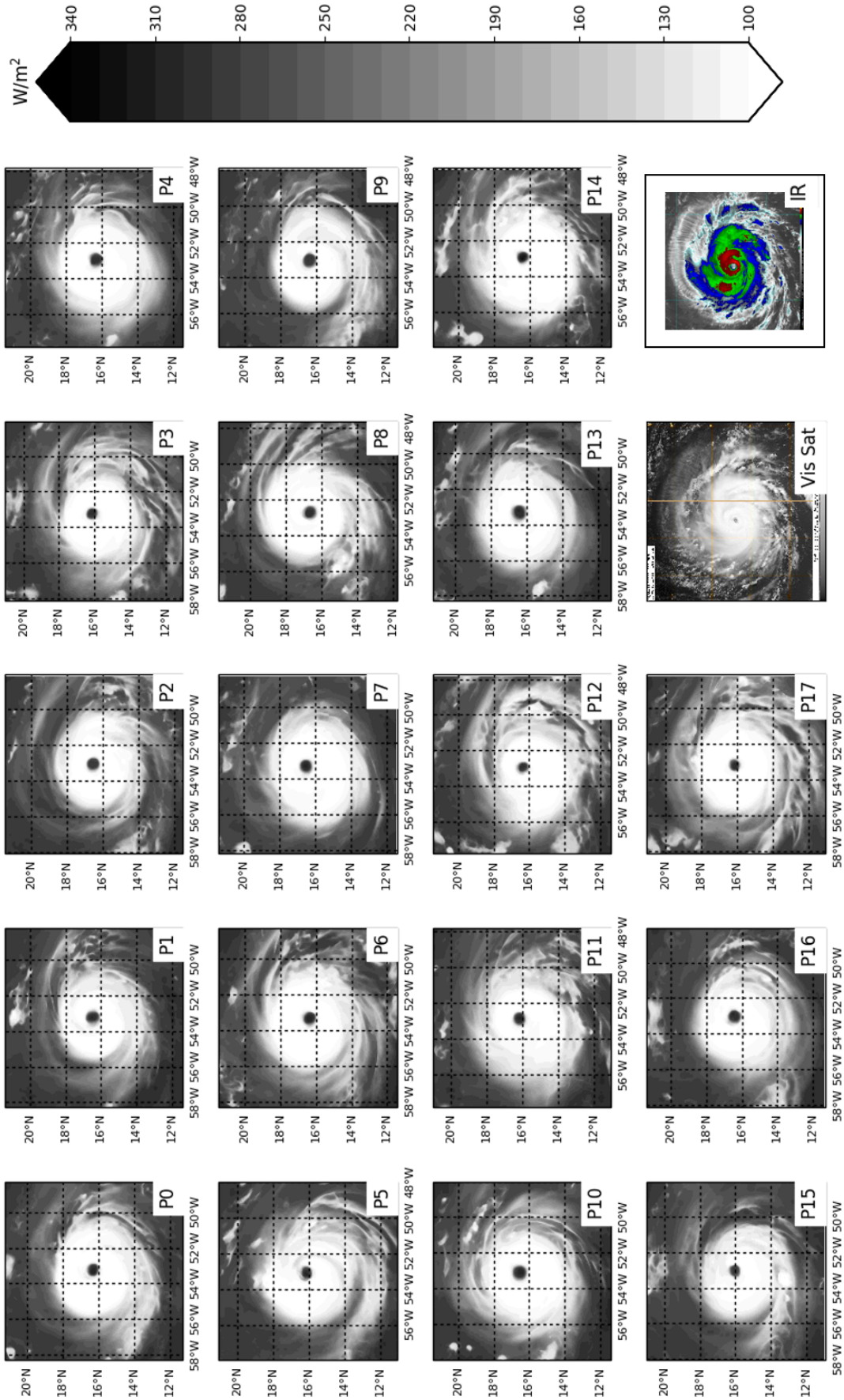


Figure 4.6: Regional model outgoing long wave radiation for 04 September 14UTC (T+38 h) with visible/IR satellite for comparison.

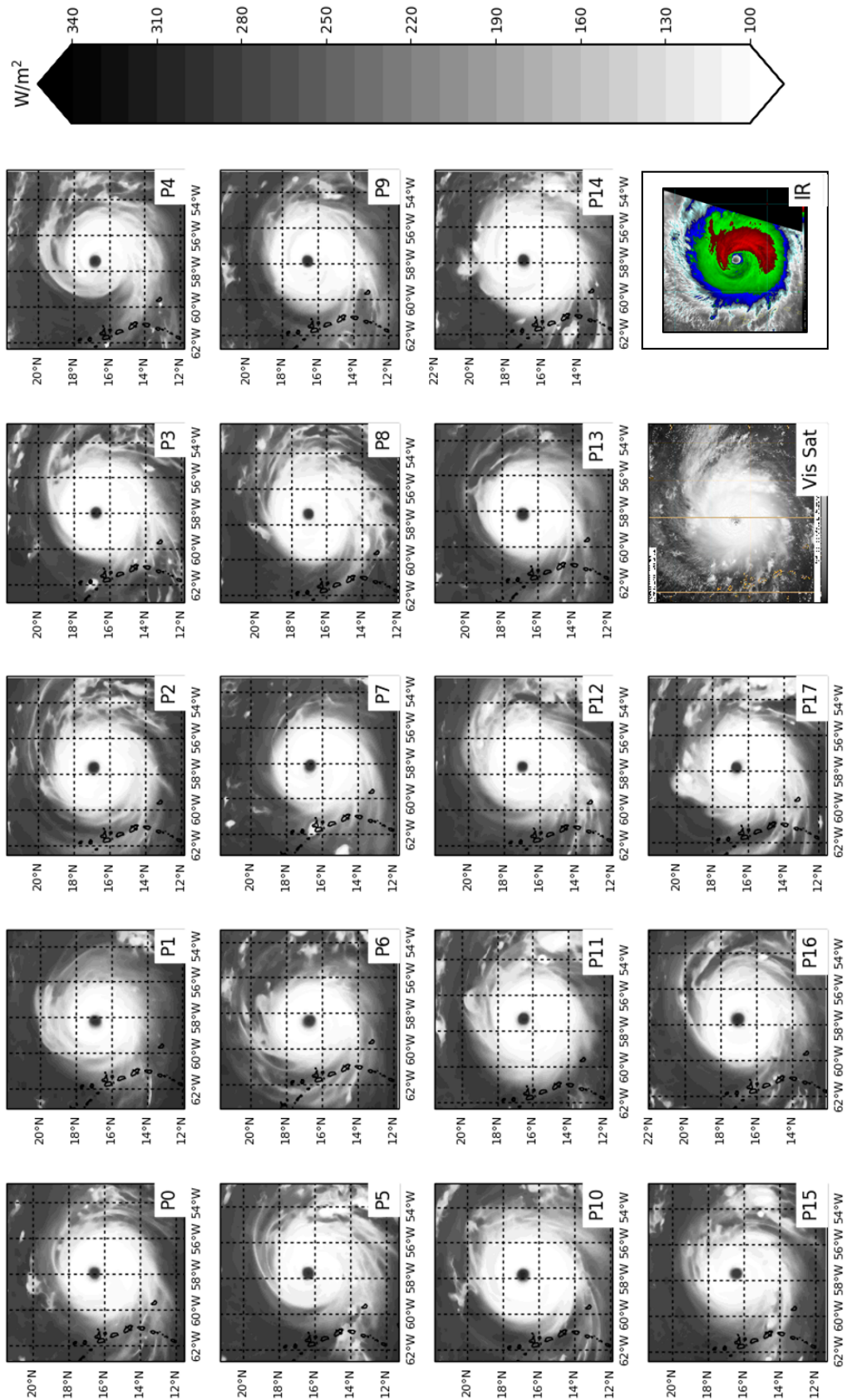


Figure 4.7: Regional model outgoing long wave radiation for 05 September 14 UTC (T+62 h) with visible/IR satellite for comparison.

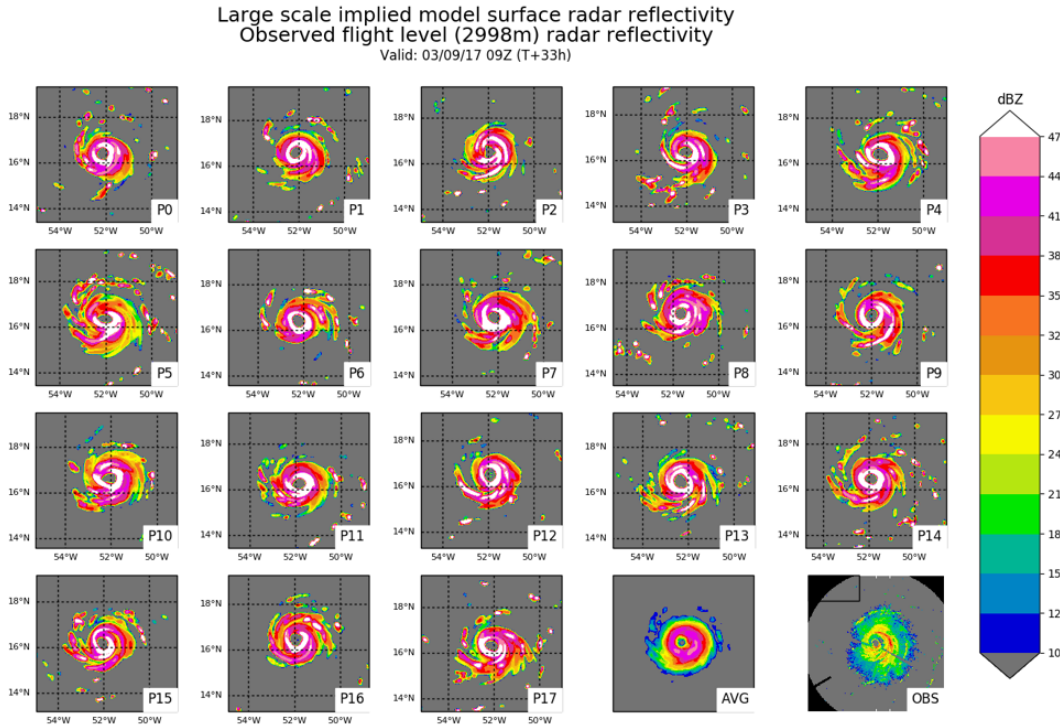


Figure 4.8: Surface radar reflectivity (calculated from large scale rain rate) from the regional model initialized at 03 September 00 UTC. and flight level radar imagery for T+33h.

(notably ensemble members 2, P8 and 15 in Fig. 4.8). Another comparison between surface radar reflectivity and ground radar at T+71,h (not shown) shows similar agreement with ensemble member 15, in particular, also capturing key features such as the eyewall structure and spiral rainbands. The ability of this ensemble member to represent the storm structure well is a motivation for it to be used in a more detailed analysis (see section 4.3).

4.5.1 Radar fractional skill score comparison

A method to perform model verification using radar data is described in Roberts and Lean (2008): the fractional skill score (FSS) which, when applied to binary data such as rainfall thresholds, can provide a metric which describes the resolution to which the data has a specified skill. Although used mostly for rainfall data, it can, in principle, apply to any threshold from the radar data available including relative vorticity and windspeed fields, which are also derived from radar data. The fractional skill score for the radar windspeed data was performed using a convolution

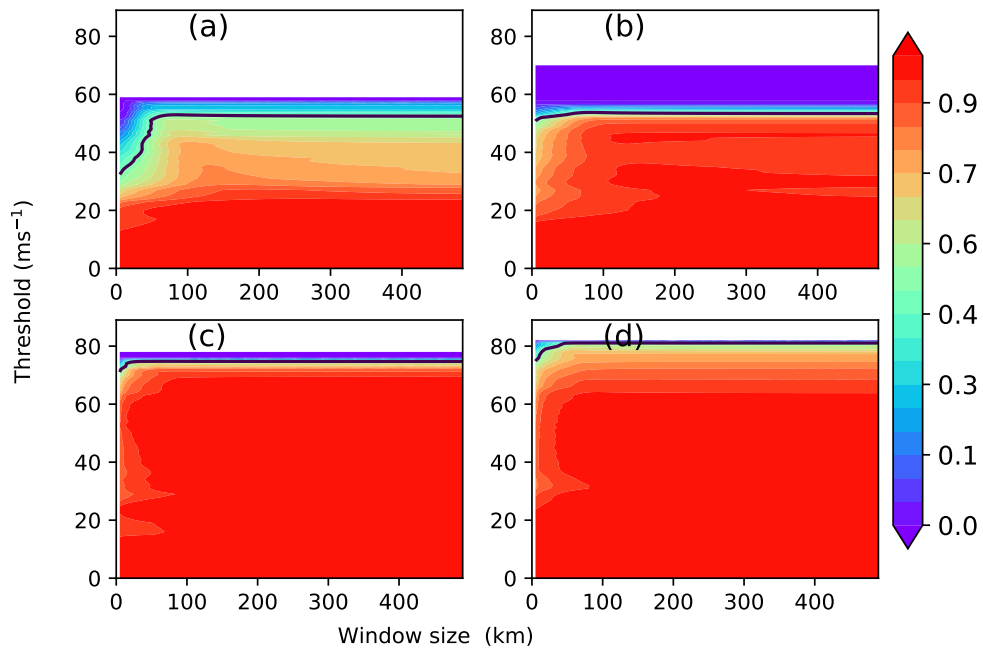


Figure 4.9: Fractional skill score composite for ensemble 15 valid for (a): T+9 h – T+24.3 h, (b) T+32.7 h – T+36.6 h, (c) T+57.3 h–T+61.1 h, (d) T+69.1 h–T+73.3 h.

method as described in Faggian et al. (2015).

Fractional skill scores were calculated for a height of 500 m for derived radar wind data and compared to ensemble member 15. The radar wind data is averaged over a period of typically several hours so the fractional skill scores are weighted average composites of these hours. For example if the radar composite starts at 0930 UTC the model output corresponding to 0900 UTC would receive a weighting of 0.5. A fractional skill score of at least 0.5 has been used as a general benchmark for a ‘useful’ forecast (Skok and Roberts, 2016). The forecasts on 05 September (Fig. 4.9c,d) are considered to be significantly more skilful than forecasts from 03 or 04 September (Fig. 4.9a,b). On the 05 September there is skill for eyewall type wind speeds of 50 m s^{-1} for all resolutions, whilst for 03 September and 04 September skill is less than 0.5 for resolutions less than 50km for thresholds greater than eyewall type speeds of 40 m s^{-1} . This shows that the tangential wind structure of the TC is modelled better later in the simulation as the skill score increases for all wind speeds, particularly on 05 September.

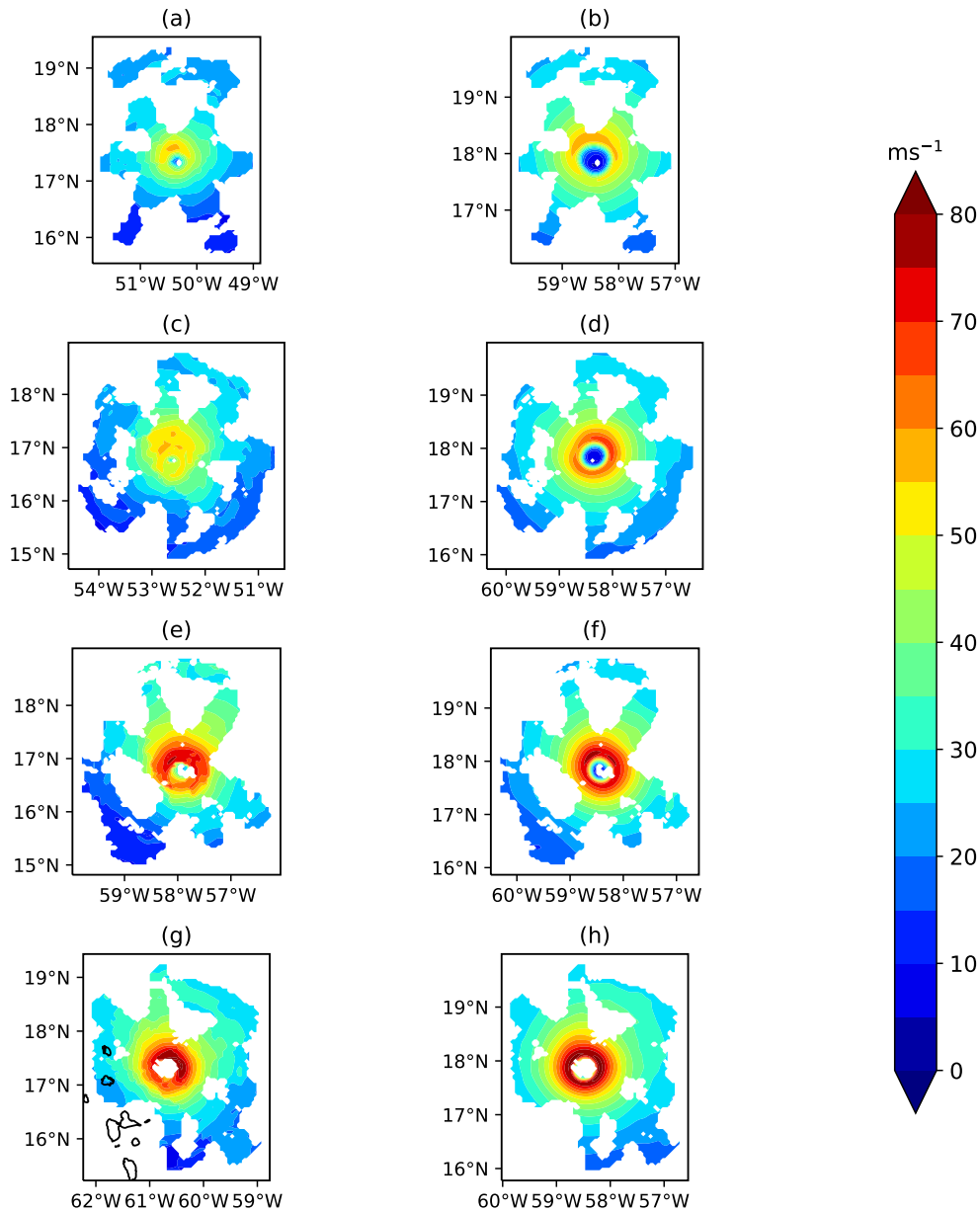


Figure 4.10: Radar composite (left column) and model composite (right column) windspeed at 500 m height for ensemble 15 valid for (a),(b): $T+21\text{ h} - T+24.3\text{ h}$, (c),(d) $T+32.7\text{ h} - T+37.6\text{ h}$, (e),(f) $T+57.3\text{ h} - T+61.1\text{ h}$, (g),(h) $T+69.1\text{ h} - T+73.3\text{ h}$.

4.5.2 Radar RMW comparison

Composite flight-level radar data was used to directly validate the modelled RMW. In the case of the composite radar data a simplex method as described in section 3.4.1 was used to find the centre of the storm from which an RMW could be determined.

Figure 4.11 shows the structure of the storm's wind field during the storm's RI from the flight-level radar data (Fig. 4.11 b,d,f,h) and compared to the regional model ensemble mean (Fig. 4.11 a,c,e,g). On the morning of 04 September the radar wind speed cross section shows high wind speeds near the centre of the storm (Fig. 4.11d). This is likely due to intensity fluctuations that were occurring during that time (see Chapter 5). One other issue is that wind speed is averaged over a five hour period where the RMW may be contracting which may cause artificial smoothing of the wind field in the eyewall and eye. The structure of the storm for the other three time periods is better represented, although the eyewall is stronger in the model particularly early on. Figure 4.11e,f shows that by midday on 05 September the model and radar wind speed are more similar.

Figure 4.12 shows the RMWs from the model ensemble members as a function of height in comparison to the RMW implied from the radar. The RMW is overestimated by the model on 04 September although this may be due to the issues associated with flight-level radar data composites during an intensity fluctuation. The RMWs at lower heights in particular are also overestimated by the model during the other time periods except for the morning of 05 September where the radar implied the RMW is only slightly greater than the calculated ensemble mean. The tendency for the model to produce larger eyewall structures compared to observations is corroborated by satellite data.

4.6 Flight-level wind analysis

One of the most intuitive ways to compare the flight-level data with the model data is to use linear interpolation to create a virtual flight path through the regional model. A correction is also applied to take into account the differing model and

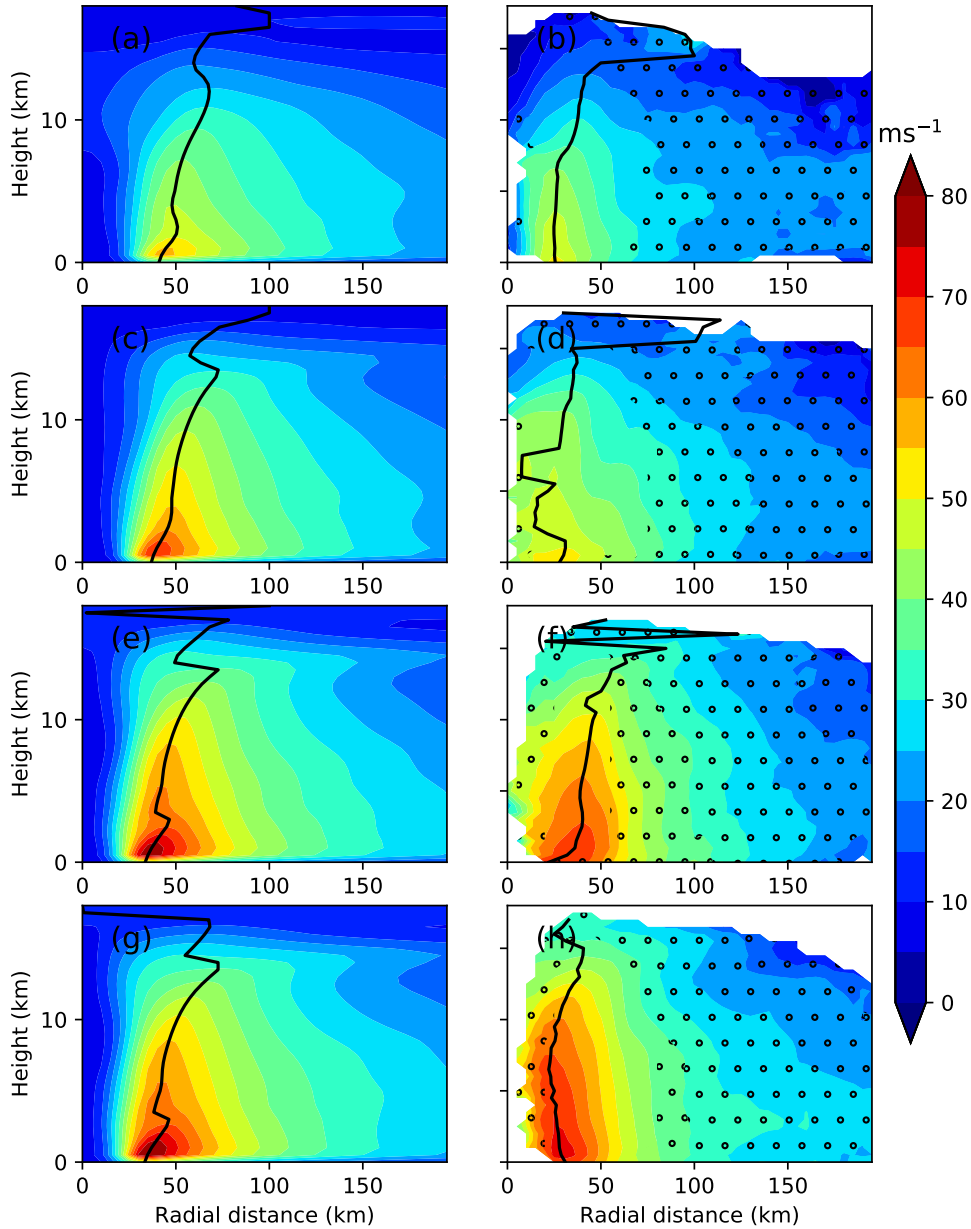


Figure 4.11: Comparison of the ensemble mean (left column) of wind speed to radar derived wind speed composite (right). Black lines show the height dependent RMW, black stipples show incomplete radar data (i.e. there is not data for all azimuthal angles). Valid for (a,b) T+21 h – T+24.3 h (c,d) T+32.7 h – T+37.6 h, (e,f) T+57.3 h–T+61.1 h, and (g,h) T+69.1 h–T+73.3 h.

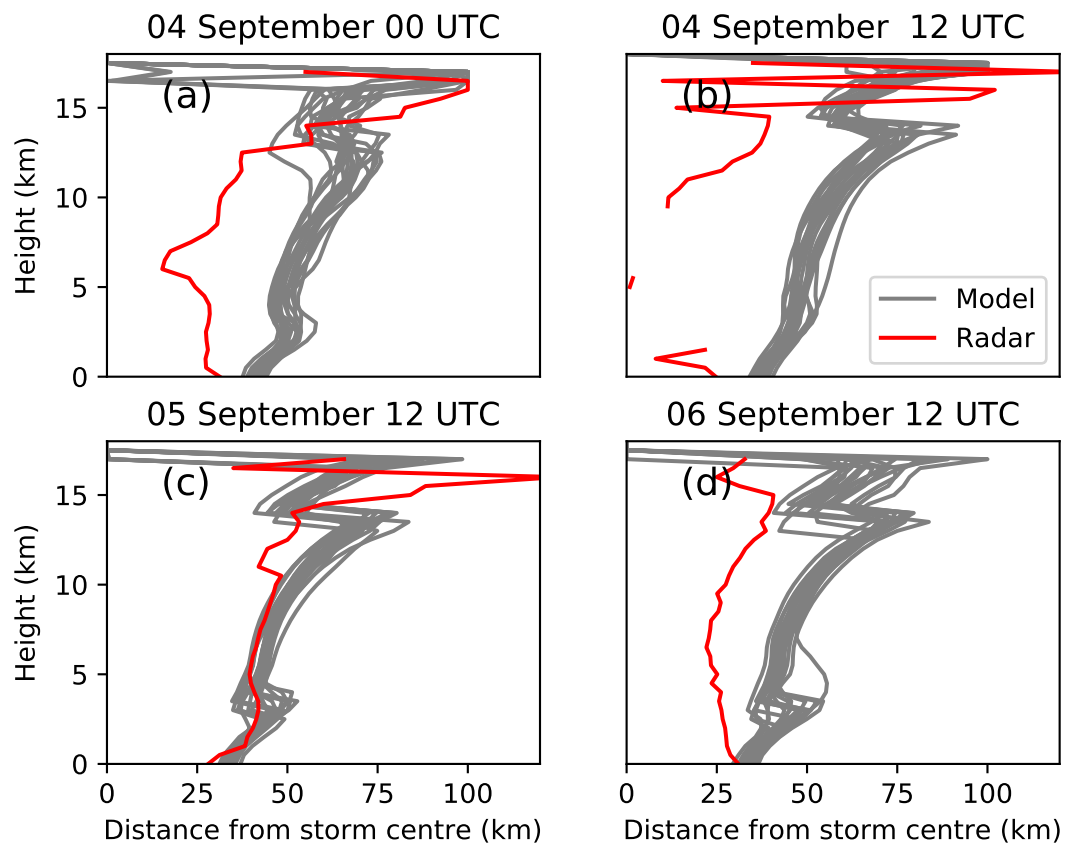


Figure 4.12: Radar derived composite RMW (red line) as a function of height and regional model ensemble composite RMWs (grey lines) as a function of height for four different times.

observed TC centres such that the virtual flight path is storm–relative.

In general, the flight–level data confirms that the model handles the intensification of Hurricane Irma well, with the azimuthal and radial winds being objectively similar in the model compared to the flight–level data. There are some differences, notably the model tendency to overestimate the size of the eyewall and the RMW which is evident particularly early on in the model simulation.

An example of this can be seen in Fig. 4.13a which shows that the radial azimuthal wind distribution at the flight–level is well captured but with the model RMW being too large. However, during the course of 04 and 05 September the size of the RMW is represented better which can be seen in, for example, Fig. 4.13b.

The azimuthal wind speed, by contrast, which starts off very accurate at flight–level becomes less accurate with the azimuthal wind speed being underestimated on 05 September in particular (e.g. Fig 4.13c). By 06 September the tangential wind intensities in the eyewall are more similar to flight–level data but the RMW is also overestimated in size by the model likely due to a contraction in the eyewall.

Another apparent difference between the model and the observation which can be seen particularly in Fig. 4.13 is the systematic underestimate of the azimuthal wind speed in the eye region, which ties into the notion that the model produces a larger calmer, less disrupted eye.

A feature not picked up by the model is a double wind maximum that appears briefly on 04 September and can be seen in Fig. 4.14. The double wind maxima occurs around the time just prior to the start of a weakening period (see Chapter 5 for additional details of the intensity fluctuations). This double wind maximum is not seen in the flight–level data later on in the afternoon on 04 September.

4.7 Dropsonde data analysis

4.7.1 Preparing dropsonde data for comparison to model data

The premise of the dropsonde analysis is to directly compare dropsonde observations with the regional model output. For the purposes of this analysis the focus will be

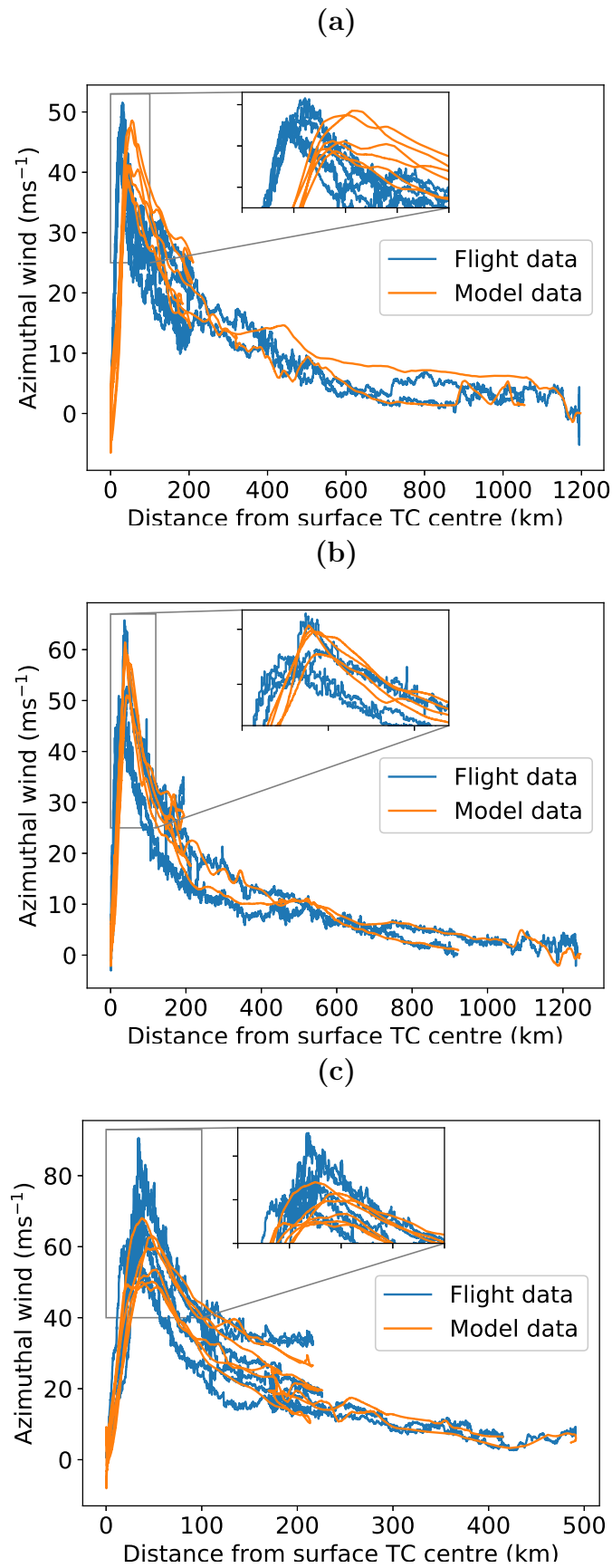


Figure 4.13: Flight azimuthal wind (ms^{-1}) and virtual model flight azimuthal wind (calculated using interpolation from the relative TC centre) (ms^{-1}) as a function of distance from the storm centre for: (a) flight NOAA 42 (0111A) valid 19:11-02:30 UTC 03 September, (b) flight USAF 309 (0311A) valid 14:15-20:24 UTC 04 September, (c) flight NOAA 42 (0711A) valid 07:54-13:54 UTC 05 September.

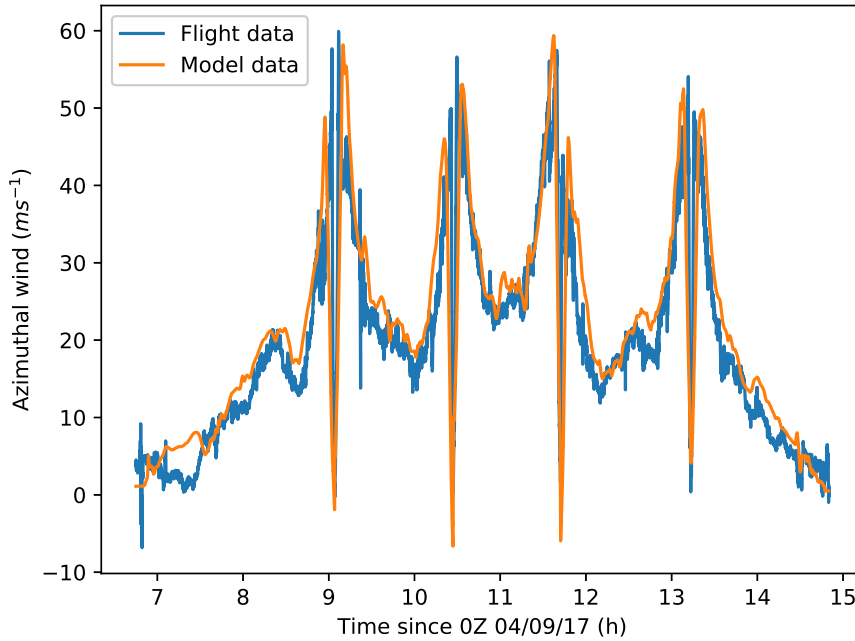


Figure 4.14: Flight azimuthal wind speed (m s^{-1}) and virtual model flight azimuthal wind speed (m s^{-1}) for NOAA 42 (0211A).

the comparison between dropsonde observations and ensemble member 15 (4.3)

Each dropsonde is categorized, by its position relative to the storm centre, into one of four categories: ‘Eye’, ‘Eyewall’, ‘Outer’ (larger radii outside of the inner core) and ‘Environment’. Depending on the category the dropsonde falls into will determine how it is handled in the analysis. Dropsondes in either the ‘Eye’ or ‘Outer’ category are handled in a storm–relative sense. Additional corrections are performed on the ‘Eyewall’ category to account for differing RMWs. The analysis of the ‘Environment’ is not done from a storm–relative perspective since the dropsondes are far from the influence of the TC. The dropsonde locations in real space are translated in accordance with the deviation of the location of the storm model centre compared to the actual storm centre. Therefore, dropsondes that fall into the ‘Eye’ or ‘Outer’ category will be the same distance from the model storm centre in model space as the dropsondes are to the real centre in real space. This will ensure any deviations between observations and model output will not be caused by the storm centres simply being misaligned.

In the case of the ‘Eyewall’ category it was found that differences in the size of the

RMW are responsible for most of the deviation between the observed and modelled tangential and radial wind. To account for the model's systematic bias for producing an overly high RMW an additional correction (on top of the storm relative correction) was applied to all the dropsondes in this category whereby the distance of the dropsonde to the centre of the storm in virtual model space was extended (or in theory shortened) so it coincides with the modelled RMW (but preserving the angle of the dropsonde with respect to the storm centre). The implicit assumption made is that the dropsonde was dropped at the surface RMW. Although this is unlikely to be always true, dropsondes in the 'Eyewall' category are typically dropped within the middle of the eyewall region.

The principle is demonstrated in Fig. 4.15a and 4.15b. Figure 4.15a shows an 'Eyewall' dropsonde on 04 September in virtual model space (after adjusting for the deviation in model and real storm centres). Due to the model overestimating the size of the RMW the dropsonde is incorrectly located within the eye region. After applying the correction, Fig. 4.15b shows the dropsonde is now within a high wind speed region in model space which is consistent with the dropsonde being dropped into the eyewall. Figure 4.16a and b show the difference the adjustment makes to wind speed. The virtual dropsonde before the correction is applied shows a strong negative bias associated with the model exaggerating the size of the RMW. However, after the correction the model and observed vertical profiles match up well.

For the fourth category, the 'Environment', no correction is applied. For dropsondes far from the storm centre the environmental winds are assumed to dominate so no account is made for the differences in modelled storm centre compared to the actual storm centre.

The conditions defining the first two categories are determined by the flight reports written during the flight. For the vast majority of flights there are several eyewall and eye drops and this is made clear in the logs along with the quadrant for the eyewall drops. For dropsondes that are not clearly labelled 'eyewall' or 'eye' in the logs they will occur outside of the eyewall region. In order to determine whether or not the dropsonde is considered to be in the outer region of the storm or in the environment an estimate for the storm size using model data the method described

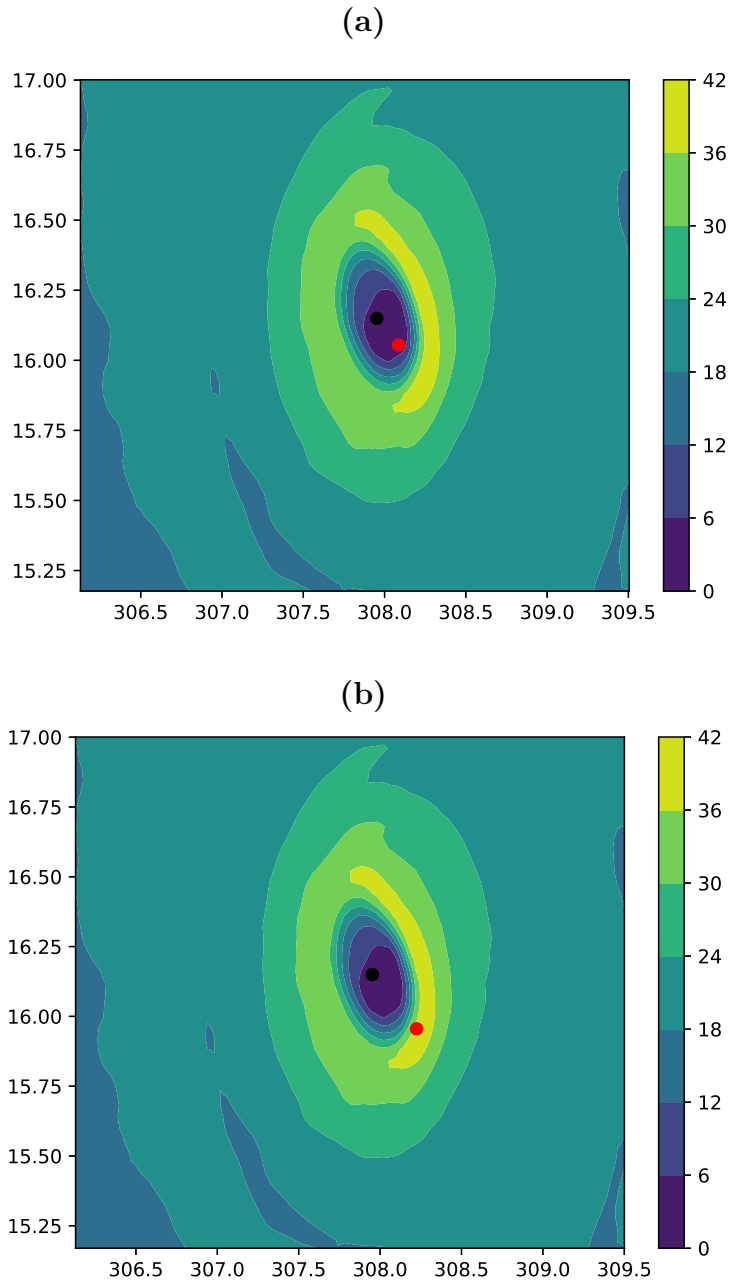


Figure 4.15: Wind speed contour plot (m s^{-1}) with model storm centre (black point) and (a) original dropsonde location (point) and (b) adjusted dropsonde location.

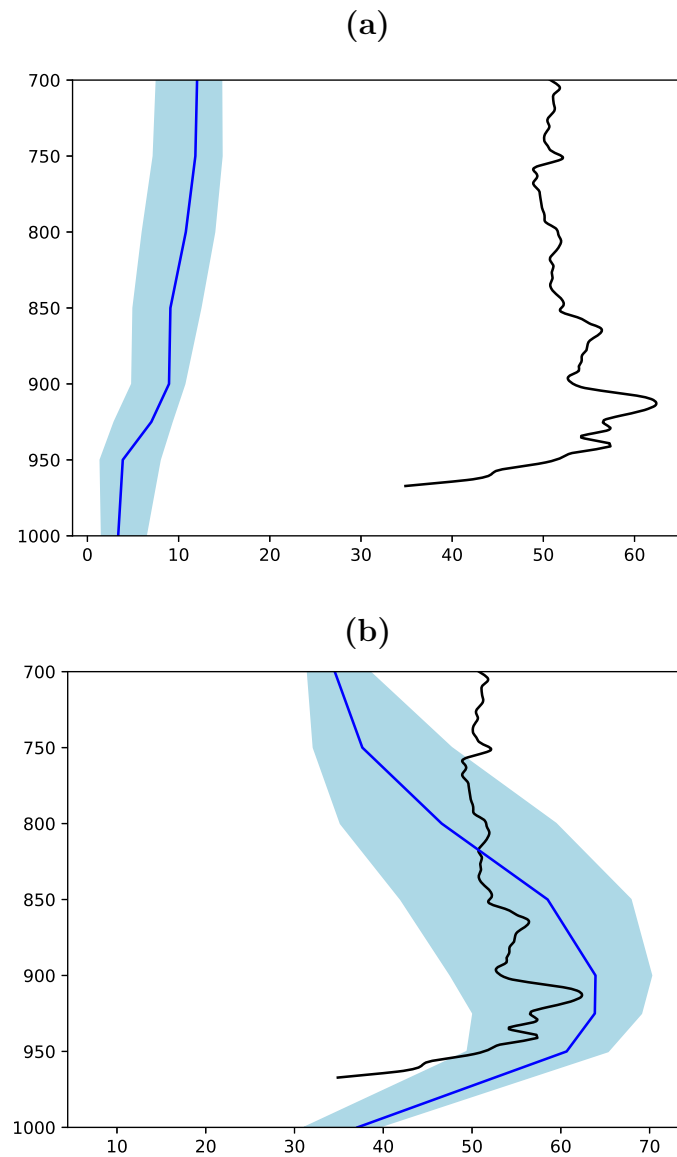


Figure 4.16: Wind speed (ms^{-1}) vs pressure (hPa) for dropsonde (black) and (a) virtual dropsonde in MetUM (blue) with the standard deviation of neighbourhood points in the MetUM (pale blue). (a) Uncorrected virtual dropsonde, (b) virtual dropsonde corrected for the differing MetUM and observed RMW.

in Dean et al. (2009) is used. From their equation 8 the storm size, r_0 , is given as:

$$r_0 = \sqrt{r_{34}^2 + \frac{262184.5045r_{34}}{\sin \varphi} \cdot (1 \text{ metre})}, \quad (4.1)$$

where r_{34} is the radius of the 17.5 m s^{-1} wind and φ is the latitude.

Equation 4.1 is used to determine whether the dropsonde is considered to be in the outer region of the storm or in the environment. In most cases this is obvious with reconnaissance flights usually only containing ‘Environment’ type dropsondes and most other flights containing no ‘Environment’ type dropsondes at all. However, in a few cases it may be difficult to determine whether a dropsonde is considered to be in the outer region or the environment. Therefore, it is necessary to create a radial wind profile of the TC to determine the 17.5 m s^{-1} wind radius and, from that, determine the radius of zero winds defining the boundary between the storm and the environment. The method to create the wind profile was developed by Holland et al. (2010). The advantage of the method is that it can be used for wind speed or azimuthal wind speed at any level and there does not need to be any assumption of gradient wind balance. Therefore, for dropsonde data where there is limited information about the wind structure of the storm this function is ideal.

$$v = v_{max} \left\{ \left(\frac{RMW}{r} \right)^{b_s} e^{(1 - (\frac{RMW}{r})^{b_s})} \right\}^x \quad (4.2)$$

The functional form of the modified wind profile (equation 4.2) where v is the wind (can be azimuthal, total, and any height above the surface), v_{max} is the maximum wind (in the RMW), r is the radial distance from the storm centre, RMW is the radius of maximum wind speed, $b_s = \frac{v_{max}^2 \rho e}{\Delta p}$ is the modified Holland B shape parameter, $x = 0.5 + a(r - RMW)H(r - RMW)$ is an arbitrary exponent, a is the linear gradient of x , H is the heaviside step function, Δp is the pressure change from the centre of the storm to the environment, $\rho = \frac{p_{RMW}}{RT_{s_{RMW}}(1+0.61)} \left(\frac{RH_{s_{RMW}}}{p_{RMW}} \frac{3.802}{p_{RMW}} \right) e^{\frac{17.67(T_{s_{RMW}} - 273.15K)}{T_{s_{RMW}} - 29.65K}}$ is the density of air at the RMW, and $p_{RMW} = p_{min} + \Delta p e^{-1}$ is the surface pressure at the RMW,

$RH_{s_{RMW}}$ is the relative surface humidity at the RMW, $T_{s_{RMW}}$ is the surface temperature at the RMW, p_{min} is the minimum surface pressure. The multivariable function is then solved using a least squares method similar as the TPF. a , v_{max} , RMW , Δp are taken as parameters (values are outputted in the combination which produces the best fit). The surface RMW temperature is approximated using eyewall temperature dropsonde observations; the minimum pressure is approximated using the best NHC estimate; relative humidity at the surface of the RMW is also approximated using the eyewall dropsonde observations. These four parameters were chosen because there is either high sensitivity to them or they are difficult to infer from observations. By using derived azimuthal wind observations from the dropsondes (calculated using WCF fix centres) and equation 4.1 the storm size can therefore be calculated.

For the analysis a ‘neighbourhood’ of points was used. Usually the dropsonde vertical profile was compared to a range of vertical profiles created from the virtual dropsonde location in model space and the eight surrounding points. If the model can accurately reproduce a variable (such as azimuthal wind) within this range then it will have done so with an uncertainty comparable to the model resolution and therefore can be assumed to be an accurate representation of reality. Sometimes the ‘neighbourhood’ of points are more than nine to account for spatial drift as the dropsonde falls (usually this is only significant within the eyewall). In this case the vertical profiles in model space of all the points within the dropsonde drift and their surrounding points are considered. For example if the dropsonde drifts 4.4 km east as it falls then the neighbourhood of points includes two points for the drift and an additional ten points for those that surround them. A dropsonde typically falls to the ground within five minutes. The effect of this elapsed time is assumed to be negligible and the real storm centre is taken to be the wind centre fix at the time the sonde is dropped. In model space the time is rounded to the nearest hour and compared with the hourly output.

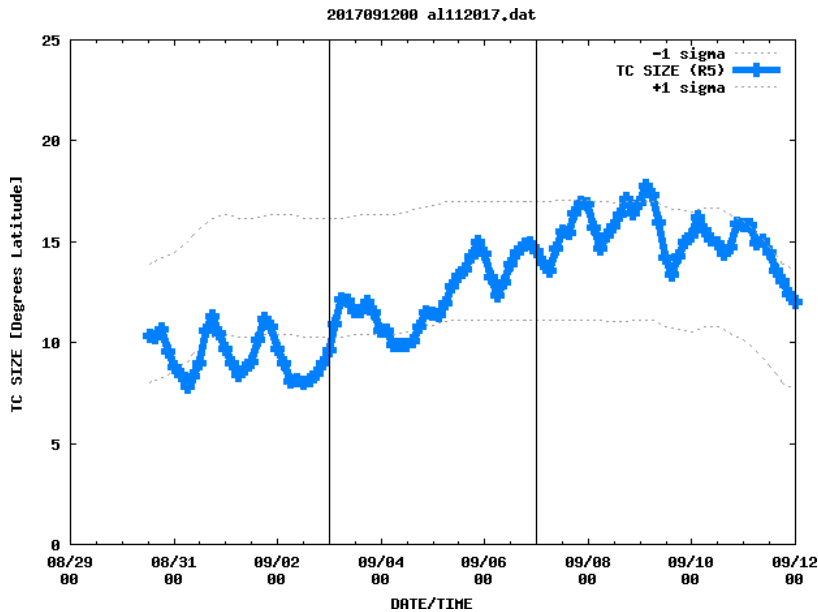


Figure 4.17: IR satellite derived TC size. Image produced by NOAA. Vertical lines added indicate the time period modelled.

4.7.2 Storm size comparison

One quantitative use of the satellite data is determining the storm size. NOAA produces operational storm size data (defined as when the wind field of the storm becomes indistinguishable from the environmental wind) from IR satellite imagery. This is shown in Fig. 4.17. This can be compared to the MetUM using equation 4.1.

4.7.3 Neighbourhood point analysis

An analysis of the dropsondes shows many of the major features of the primary and secondary circulation were replicated accurately by the model.

An example of this is shown in Fig. 4.18 which shows selected eyewall dropsondes from an afternoon flight on 04 September with both the radial and azimuthal wind reasonably well replicated. The model is able to capture key features including the inflow layer near the surface and the outflow jet above the boundary layer. The height of the maximum azimuthal wind is also well replicated with both the model and the dropsondes showing a maximum azimuthal wind at around 300 m.

One feature the model is not able to replicate are mesoscale features. An example of this is shown in Fig. 4.19 (left panel) where there is anticyclonic motion in that

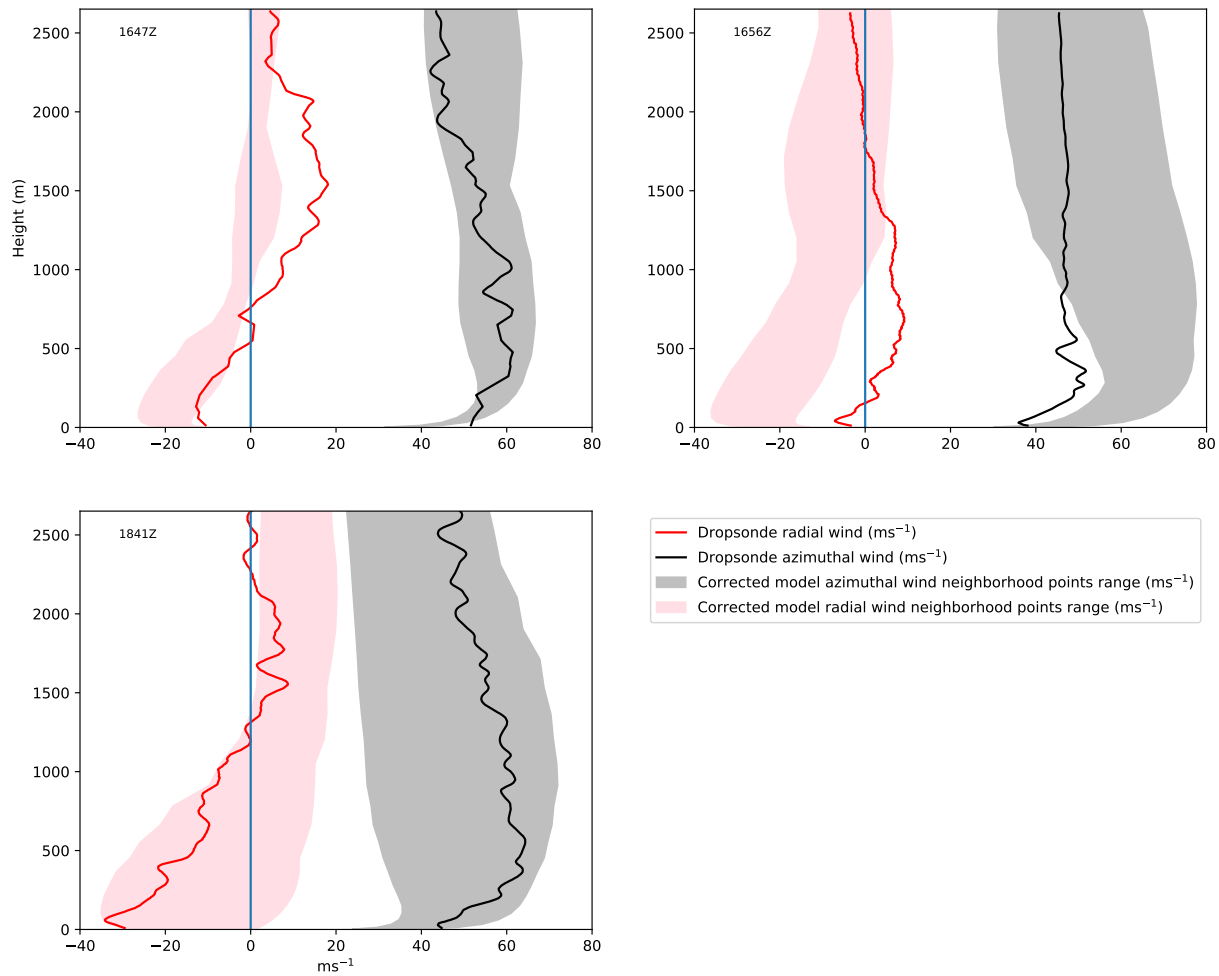


Figure 4.18: 'Eyewall' category on 04 September showing the dropsonde azimuthal (black line) and radial (red) wind with model neighbourhood (average of surrounding grid points) displaying the azimuthal (grey shading) and radial (red shading) wind.

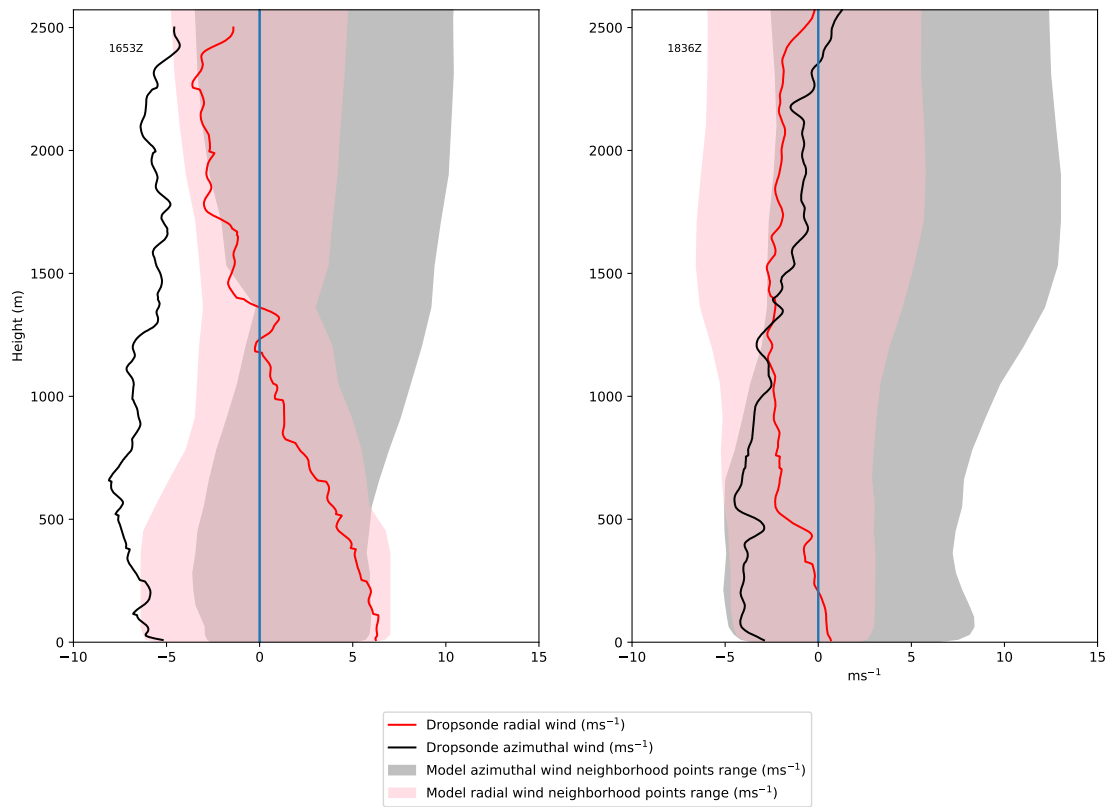


Figure 4.19: As Fig. 4.18 with ‘Eye’ category dropsondes on 04 September.

is measured in 1653 UTC dropsonde that is not replicated by the model. In general, the model does do a good job of replicating the weak airflow within the eye.

Figure 4.20 shows some dropsondes from 05 September. It is apparent that the inflow is sometimes weaker in the boundary layer compared to the dropsonde measurements. There is a consistent negative bias in the azimuthal wind. This bias tends to be strongest at the top of the boundary layer typically within the 500 m–1500 m range. The model underestimating the azimuthal flow is also evident on 06 September, particularly within the boundary layer.

The model agrees well with the dropsondes in the outer regions of the storm and the ‘Environment’ category. One example is shown in Fig. 4.21 where the dropsondes were at different azimuths to the storm centre.

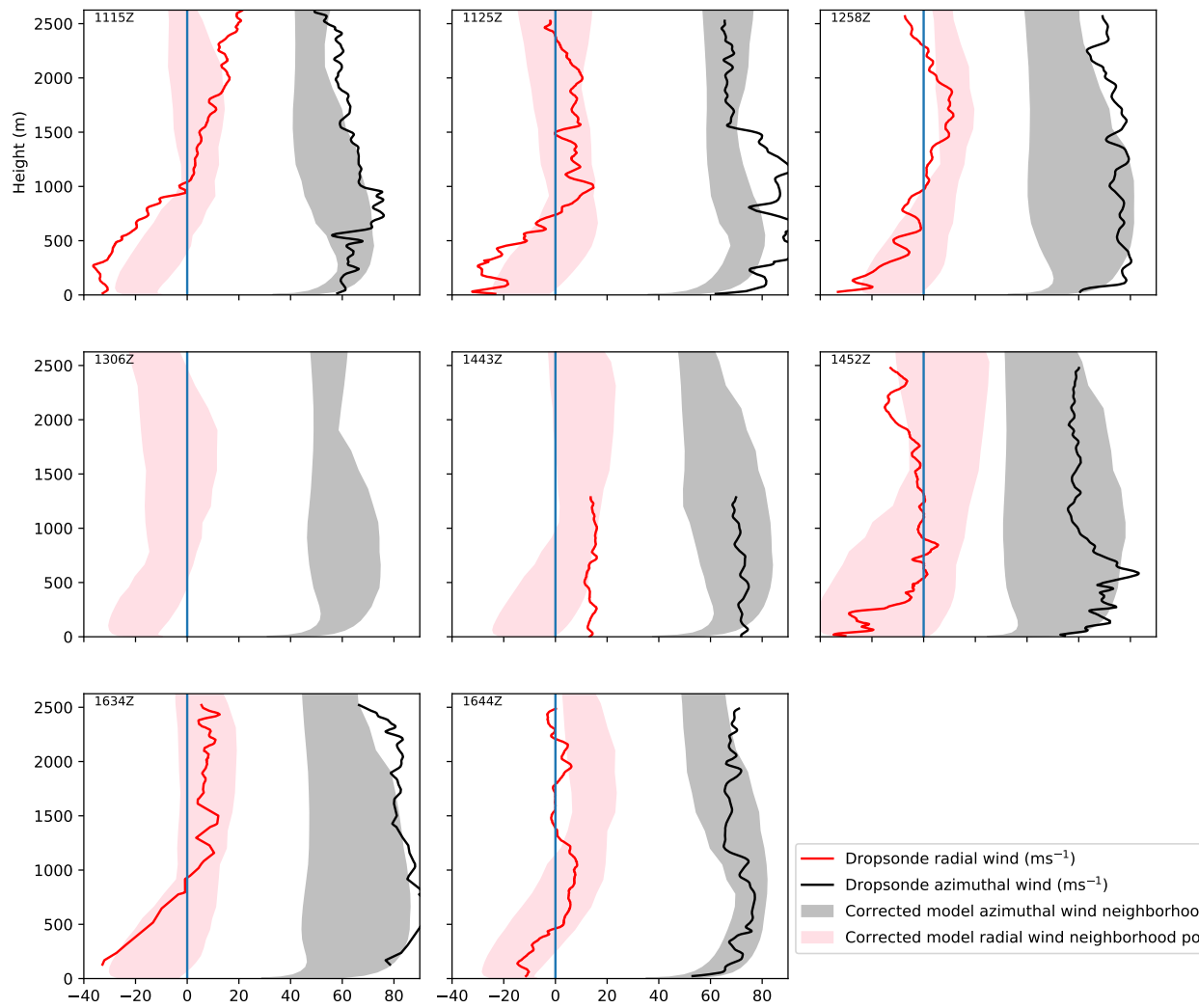


Figure 4.20: As Fig. 4.18 with 'Eyewall' category dropsondes on 05 September.

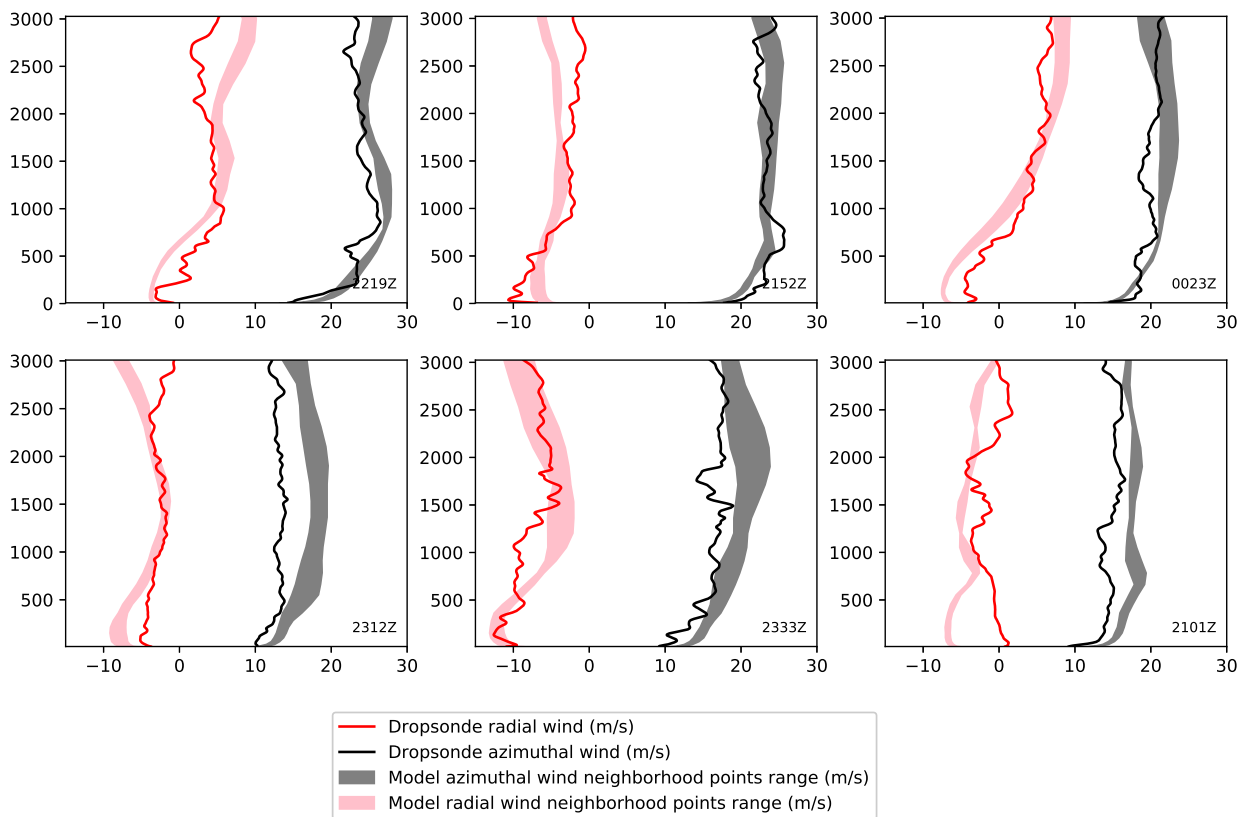


Figure 4.21: As Fig. 4.18 with ‘Outer’ category dropsondes on 03 September.

4.8 Summary

A variety of techniques was used to evaluate the MetUM regional 4 km convection permitting ensemble simulations in representing a period of RI in from 03 September 00 UTC to 07 September 00 UTC in Hurricane Irma. During this period Irma's central dense overcast structure became more coherent and symmetrical especially by 05 September, but there were some notable changes in structure on 04 September with double eyewall structures sometimes present.

Several techniques were used to evaluate the MetUM model performance. Satellite data provided useful qualitative comparisons of storm structure but was limited in its utility. Storm vertical cross sections could be compared between the regional model and radar data from which windspeeds were derived. However, averaging of radar data over several hours introduced errors particularly if the storm structure changed during the averaging time period. As a result, fractional skill score tests confirmed that the radar data did not usually have a useful skill for most eyewall windspeeds at the regional model resolution on 04 September.

One issue throughout the analysis was to derive accurate storm centre coordinates in reality as well as to determine the storm centre within the model given the sensitivity of any analysis in storm centred radial coordinates to the position of the storm centre. To determine the real storm centre position, the WCF method which had already been implemented by NOAA, was used.

Dropsonde and flight data was also used to validate the model tangential, radial and total wind fields. One limitation was the model systematically overestimating the RMW which had to be accounted for. Attempting to distinguish the environment from the storm wind field was also difficult and relied on the relatively small number of dropsondes.

In a broad sense the model performed well with representing the azimuthal wind and MSLP. The convection-permitting model simulations, however, did seem to struggle to resolve structural changes that occurred on 04 September. On the 03 September and 04 September in particular the model produced a much more coherent and, likely, more intense storm (the flight-level data suggests this may not

be true at the flight-level of around 3000m) with a cloud free eye and noticeably smaller RMW than in the convection-permitting ensemble members. However, the modelled RMW seems to be more similar to the actual RMW by 05 September. With regards to intensity it seems that by the 05 September the model TC is overall weaker than the real TC with reduced azimuthal winds in the eyewall, reduced flight-level winds and eventually a higher surface level pressure and maximum wind-speed. The radar data implies that at the top of the boundary layer the model storm is still overly intense. The satellite and radar data also continue to suggest that the storm remains too tightly bound and coherent (although the storm's presentation on 05 and 06 September is more similar to reality than 03 and 04 September).

One notable feature captured in the flight and radar data was a double eyewall structure on 04 September. Although not all the ensembles developed this structure, some did and the change in the TC structure to become more coherent, symmetrical and stronger by late on 05 September, was correctly modelled.

Of all the ensembles, ensemble 15 seemed to agree with the observational data the most closely so this will be the focus of more in depth analysis in future chapters. The double eyewall structure and intensity fluctuations on 04 September are also examined in detail in Chapter 5. Given the evidence the MetUM simulation (particularly ensemble member 15) performs well for its resolution and appears to be similar enough to reality, its use in investigating the RI phase can be justified even if the RI phase occurs slightly too early in the model.

Chapter 5

Intensity fluctuations in Hurricane Irma (2017)

5.1 Introduction

Intensity fluctuations have been observed in the case of Hurricane Irma during its second period of rapid intensification (second yellow line in Fig. 3.1b). Fischer et al. (2020) used observational data to identify two periods of weakening during rapid intensification where the RMW suddenly increased. The two periods of weakening were hypothesised to have different causes but were both linked to lower tropospheric convergence and vortex Rossby wave activity. These intensity fluctuations in Fischer et al. (2020) occurring during the rapid intensification of Hurricane Irma were subtle (relatively small) intensity changes compared to most eyewall replacement cycles. However, they did involve an expansion of the RMW. As in the case of a full eyewall replacement cycle, they can increase the radius of gale force winds and the probability of storm surge, hence motivating a need to be able to understand and predict these forms of fluctuations. As the fluctuations occur over a short time period and involve subtle changes in the TC structure, a modelling study is best suited to try and understand the dynamics at work.

An analysis was conducted into the intensity fluctuations of Hurricane Irma using both observations and convection-permitting simulations to help to understand

whether or not the inner core intensity fluctuations are a previously unknown phenomenon or exist on a spectrum that may include vacillation cycles, eyewall replacement cycles or other structural changes that occur during rapid intensification. The purpose of this chapter is to investigate the cause of the intensity fluctuations and understand the structural and dynamical changes of the TC in the transition between a strengthening and weakening phase. In particular, we ask the following questions: (i) Is the PV structure generated by the latent heating, associated with convection, barotropically stable? and (ii) Does barotropic instability lead to a breakdown of the ring-like structure during weakening phases? (iii) What role does the boundary layer play in the fluctuations, and are they caused by unbalanced dynamical processes. The convective structure is examined to attempt to understand the cause of the fluctuations. The focus is on inner rainband diabatic contributions and how these act to spin up or spin down the primary circulation through balanced mechanisms.

The chapter is organised in the following way: Some of the calculations used in the analysis are described in section 5.2. The results are introduced in section 5.3.1 with model intensity fluctuations defined in terms of mean sea level pressure (MSLP), tangential wind speed and RMW. Section 5.3.2 contextualises the storm's development in terms of environmental factors. Diurnal cycles are also discussed as a possible explanation. Section 5.3.3 looks at the Fourier decomposition of the PV structure with the aim of determining whether barotropic instability or vortex Rossby waves play a role in the fluctuations. Section 5.3.4 analyses the modelled PV structural changes that occur during the intensity fluctuations. Section 5.3.5 examines the diabatic heating distribution and how this changes during weakening and strengthening periods. Section 5.3.6 investigates the role of the boundary layer during the intensity fluctuations. In order to demonstrate the robustness of the results, section 5.3.7 generalizes some of the key results from previous sub-sections by investigating composites of strengthening and weakening phases based on several ensemble member forecasts. Section 5.4 brings together the results and explains the cause of the fluctuations. Concluding remarks are given in Section 5.5.

5.2 Methodology

5.2.1 Calculation of agradient wind

During the analysis of the intensity fluctuations agradient wind is used as part of the analysis and is not outputted as a diagnostic variable from the MetUM. Consequently, it has been calculated, and the details of this calculation are given below.

The agradient wind is determined by taking the gradient wind balance, where the pressure force is balanced by the sum of the Coriolis and centrifugal forces: $\frac{1}{\rho} \frac{\partial p}{\partial r} = \frac{v_g^2}{r} + f v_g$, where ρ is the dry density, p the pressure, v_g is the gradient wind, f the Coriolis parameter and r the radial distance from the centre. Substituting in the ideal gas law: $p = \rho R T$, where R the ideal gas constant and T the temperature, and then noting that the agradient wind is given by the deviation of the tangential wind from the balanced tangential wind: $v_{ag} = v - v_g$ where v_{ag} is the agradient wind we arrive at,

$$v_{ag} = v - \frac{1}{2} \left(\sqrt{\frac{4RrT}{p} \frac{\partial p}{\partial r} + f^2 r^2} - fr \right). \quad (5.1)$$

5.2.2 Calculation of maximum potential intensity

As part of the analysis a maximum potential intensity calculation was undertaken in order to determine the effect of the environmental conditions on the intensity fluctuations.

Maximum potential intensity (minimum central pressure and maximum surface wind speed respectively) was calculated using the average vertical profiles of water vapour mixing ratio, pressure and temperature in an annulus between 350km and 550km from the centre of the storm. This was to ensure that the maximum potential intensity (MPI) calculated represents the thermodynamic potential of the environment sufficiently removed from the storm. The algorithm used to calculate the MPI is available here (<ftp://texmex.mit.edu/pub/emanuel/TCMAX/>).

5.2.3 Slab boundary layer model setup.

As part of the analysis on the unbalanced spin-up mechanism MetUM results were compared to a slab boundary layer model. A brief description of the model is given here.

The model used was based on the setup in Smith and Vogl (2008). This considers a boundary layer to have a constant depth and be governed by radial momentum, azimuthal momentum and mass continuity equations which describe the boundary layer inflow, tangential wind, vertical velocity and gradient wind.

These sets of ordinary differential equations can be solved by integrating inwards from an arbitrarily large reference radius (in this case 568 km). At the reference radius initial conditions can be determined by making some assumptions which include a steady flow above the boundary layer in geostrophic balance, momentum transport from above is zero and there is a constant level of moisture, given sensible values for the surface temperature, Coriolis parameter, surface drag coefficient, mass flux of shallow convection, and specific humidities in and above the boundary layer at this radius.

Once the initial conditions at the reference radius have been determined the radial and tangential boundary layer wind and the vertical velocity can be determined at any smaller radius and only depend on the radially dependent gradient wind. The gradient wind is taken to be equal to the tangential wind at the top of the boundary layer which is diagnosed from the MetUM. An appropriate height of the boundary layer was determined from examining the height of the inflow layer in the MetUM over a wide range of times and radii and chosen to be the 1202 m model level.

The slab boundary layer model is run with a time resolution of one hour for the full 96 hours and allowed to take a time varying Coriolis parameter (f) which is determined from the storm centre latitude from the MetUM. Full details of the model setup are available in Smith and Vogl (2008).

5.2.4 Intensity fluctuations in observations

The focus of the analysis is on the second period of rapid intensification which starts on 04 September at around 00 UTC and finishes around 00 UTC on 06 September (Fig. 3.1b, Fig. 5.1). During rapid intensification the MSLP decreases from around 970 hPa to its minimum value of 914 hPa. This rapid deepening is interrupted by two periods of stagnation or slight weakening where the MSLP does not continue to decrease. These periods of weakening are marked by blue bands in Fig. 5.1. The first weakening period starts around 13 UTC on 04 September and lasts for about 12 hours and is followed by a strengthening period from 01 UTC on 05 September until 11 UTC on 05 September. The second weakening period starts around 11 UTC on 05 September and lasts for about 4 hours.

Figure 5.2 shows observations, from in-flight radar and satellite imagery, of the structural changes just before and after the start of the second weakening period. The convection during the weakening period appears more azimuthally symmetric and continuous as shown in Fig. 5.2b compared to Fig. 5.2a where two regions in the north-west and south-east eyewall have relatively high rainrates. The convection is shallower in the weakening period as indicated by warming cloud tops shown in Fig. 5.2d compared to Fig. 5.2c. The shallower nature of the convection is also evident in the microwave imagery in Fig. 5.2e and Fig. 5.2f. A similar structural change occurs during the first weakening period (not shown) with banded features within the eyewall giving way to broader but shallower convection compared to prior to the weakening period.

5.3 Results

The section begins by outlining how the fluctuations have been identified in terms of wind strength and MSLP. Then the environmental factors are considered, to try and understand if they have any impact on the intensity fluctuations. The barotropic structure of the storm is examined to compare these fluctuations with the ring-to-monopole transition observed in vacillation cycles (e.g. Nguyen et al., 2011) while the convective structure is examined to determine the effect of the

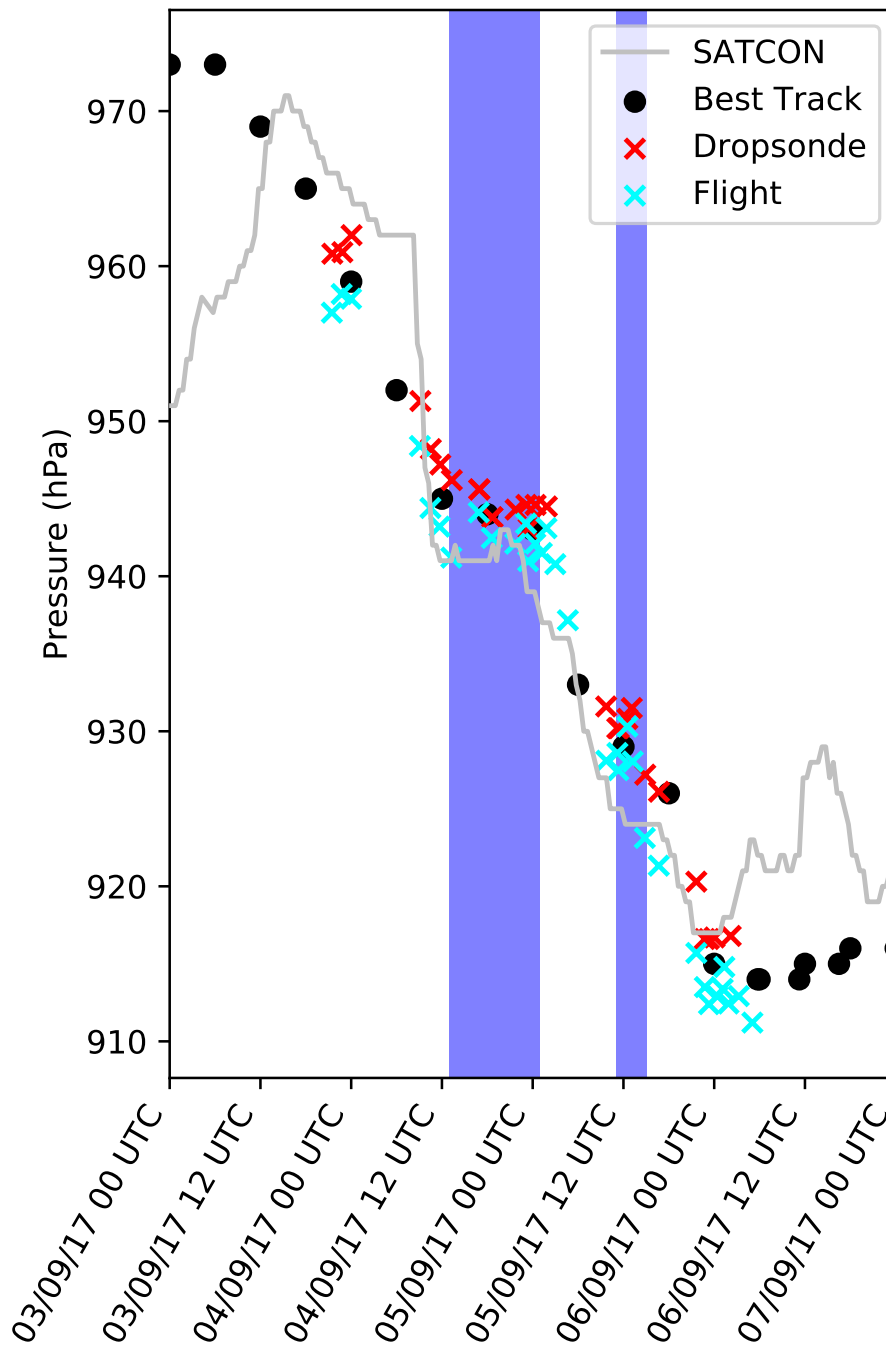


Figure 5.1: Observed sea level pressure as a function of time based on SATCON, NHC forecaster assessed Best Track as well as direct dropsonde and flight measurements. The 96-hour period shown is the same as the simulation initialized on 03 September 00 UTC. Two notable weakening/stagnation periods during the rapid intensification are highlighted with the blue bands.

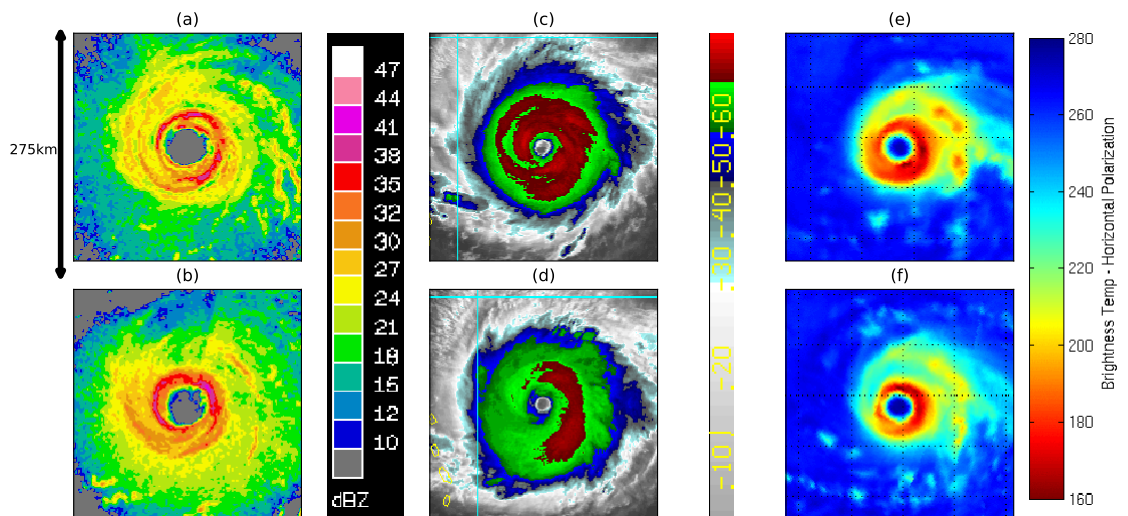


Figure 5.2: NOAA P3 flight radar (in dBZ) on (a) 05 September 0943 UTC and (b) 05 September 1232 UTC, colour enhanced infrared (IR) imagery (in $^{\circ}$ C) on (c) 05 September 0945 UTC and (d) 05 September 1245 UTC and MIMIC microwave imagery (brightness temperature in K) for (e) 05 September 0945 UTC, (f) 05 September 1245 UTC. Upper row just before the start of the second blue bar in Fig. 5.1, lower row just after the start of the second blue bar in Fig. 5.1

diabatic heating distributions on the fluctuations. Studying the boundary layer is important to investigate the effect of unbalanced dynamics as described by Smith and Montgomery (2015) particularly since Fischer et al. (2020) highlighted the possible importance of lower tropospheric convergence in causing these fluctuations. The importance of any gradient wind changes during the intensity fluctuations and their effect on the outflow jet are discussed.

5.3.1 Model simulation of intensity fluctuations

The MetUM is capable of capturing the second period of rapid intensification in Hurricane Irma. One of the ensemble members (ensemble member 15) was analysed in detail as it was judged to be most representative in terms of the size of the RMW, the surface wind speed, mean sea level pressure and track, in comparison to the observations. Fig. 5.3 shows how the MSLP and surface wind speed change for ensemble member 15 for the simulation initialized at 00 UTC on 03 September. The modelled MSLP is slightly higher than the NOAA best track values but the rate of deepening is captured well with the rapid intensification occurring at the correct

time. Even with the reduced drag at high wind speeds the wind–pressure relation in the model is too steep (wind speeds are weaker than expected compared to observations but MSLP is reasonable) and consequently the wind–speed is underestimated after rapid intensification. However, the timing of the rapid intensification and its cessation is accurate. The track of this forecast and the other ensemble members are shown in Fig. 3.1 and all agree well with the best track.

Figure 5.3 shows how the maximum surface total wind speed, pressure and RMW vary over the course of the simulation. Based on these fields the development of the TC has been split into distinct phases. The pre–fluctuation rapid intensification phase covers the first 45 hours of the simulation. During this time, after an initial model spin–up period, the storm intensifies nearly monotonically; the wind speed increases rapidly at all levels, the MSLP decreases and the RMW contracts (Fig. 5.3).

During weakening phases (blue bands in Fig. 5.3) the MSLP stagnates or increases, the maximum surface total wind speed decreases and the RMW expands. The opposite occurs in the strengthening phases (red bands in Fig. 5.3).

The maximum tangential wind, particularly near the top or just above the boundary layer (e.g. at 1532 m) also exhibits these fluctuations but does lag behind compared to higher levels (e.g. at 3002 m) where the maximum tangential wind follows a similar pattern to the surface total wind speed. This is also true of the expansion of the RMW, with the increase in the RMW happening at 1532 m (dark green line) prior to the increase in the surface RMW (aqua line). At the surface, the signal in the tangential wind speed is weaker compared to at higher levels. The role the radial flow plays in the total surface windspeed during the fluctuations, and the reason for the tangential wind spin–down preceding a weakening phase is explored in detail in Section 5.3.6.

The simulation shows four weakening periods and three strengthening periods which are defined in terms of surface wind speed, surface RMW and MSLP. There is also an uninterrupted period of intensification prior to these fluctuations. During the period of intensity fluctuations from 45 hours to 84 hours Irma is still rapidly intensifying

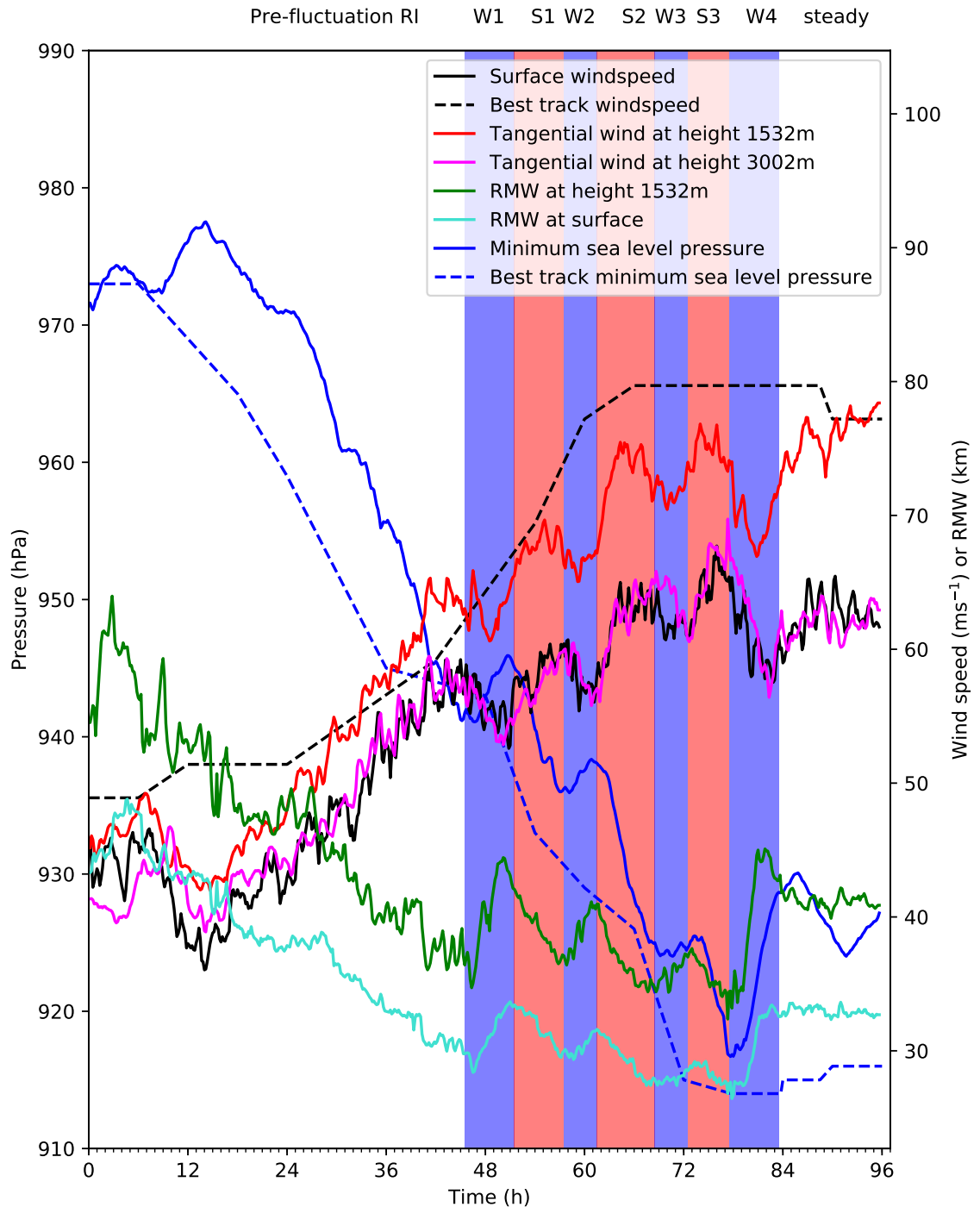


Figure 5.3: Various model parameters (solid lines) and corresponding observations (dotted lines, where available) as a function of time. Details are given in the legend. Phases have been subjectively identified. Blue bands indicate weakening phases, and red bands indicate strengthening phases during the rapid intensification period. The individual strengthening and weakening phases have also been labelled (see top of plot). W stands for ‘weakening’, S stands for ‘strengthening’.

overall, so the brief interruptions in intensification do not stop rapid intensification from happening. The main aim of the analysis is to determine why these intensity fluctuations happen during this period of rapid intensification, the mechanisms behind them and any structural changes with which they are associated.

5.3.2 Environmental factors

In order to focus on the dynamics and internal processes of the storm's development during rapid intensification (RI) it is important to also consider the effect of the environment. Irma is considered to be an axisymmetric storm in an environment highly conducive to tropical cyclone development and intensification. The purpose of this section, therefore, is to justify the assertion that the environment is not directly responsible for intensity fluctuations or weakening phases during the rapid intensification of the tropical cyclone. However, environmental effects are still important and may still indirectly affect development or have subsidiary impacts on development and intensity.

Vertical wind shear

One of the most important environmental factors governing tropical cyclone development is vertical wind shear, i.e., the variation in the magnitude of the strength of the environmental flow in the vertical direction. Prior studies have shown that vertical wind shear is one of the most important metrics to predict the future intensity of a developing TC. Fitzpatrick (1997), for example, incorporates vertical wind shear into one of four parameters that can best predict the ultimate strength of a TC. The mechanism for wind shear to disrupt TC intensification has also been well studied through its impact to the inner core structure e.g. Frank and Ritchie (2001) or DeMaria (1996). In order to determine the shear of the modelled storm a method similar to that of Park et al. (2012) was implemented where the vertical shear was averaged between the 850mb and 200mb levels in an annulus between three and five degrees from the storm centre; the thresholds shown for the vertical wind shear were also based on those used in Park et al. (2012).

Figure 5.4 shows the vertical shear for the duration of the simulation. For the ma-

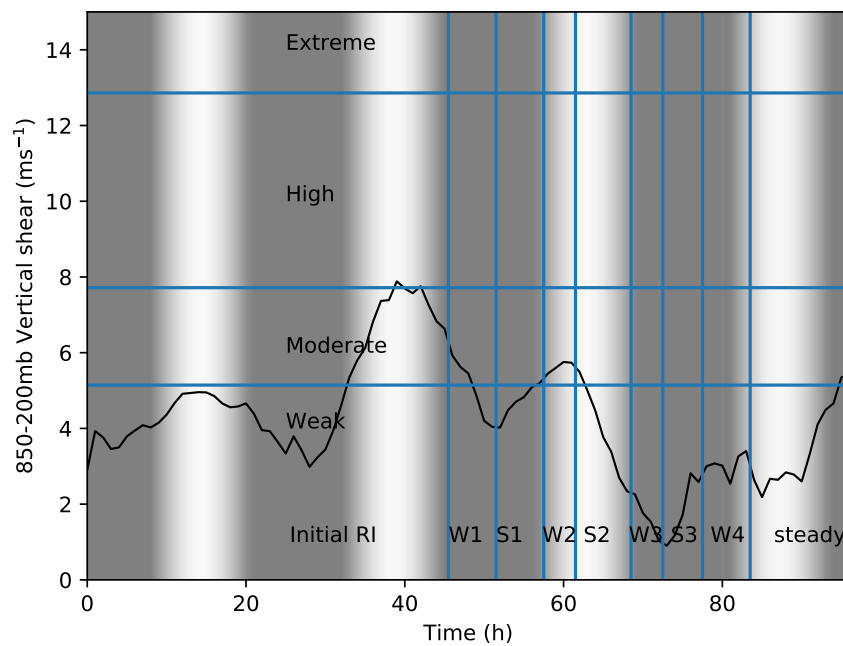


Figure 5.4: 850–200mb vertical wind shear in 3 to 5 degree annulus from model TC centre as a function of time. Colour shading is total incoming short-wave radiation which allows easy identification of daytime (pale grey or white) or nighttime (darker grey). Thresholds defining weak, moderate, high or extreme (where TC development is impossible) are also based on Park et al. (2012).

jority of the simulation the vertical shear is weak and unlikely to have a detrimental effect on storm development. The exception to this is around the 40 hour mark when (likely due to the presence of a weak upper level trough increasing a high level northerly flow), during the initial RI phase, the simulated TC briefly experiences moderate vertical shear. A wind shear in the $6\text{--}8\text{ ms}^{-1}$ range is not usually enough to cause a major hurricane to weaken (Wong and Chan, 2004) but may be considered too high to sustain rapid intensification (Paterson et al., 2005). From the middle of W1 onwards the wind shear remains weak and any variation between around 1ms^{-1} and 4ms^{-1} would not be expected to have any effect on the storm development (Tao and Zhang, 2015). The variation in the shear also appears to be uncorrelated to the development phase. During S1 the shear is relatively high (though still weak) and increasing, during S2 it is relatively high and decreasing and during S3 it is relatively low and increasing. Similarly, both increasing and decreasing shear were observed during all of the weakening phases. It is worth noting that it is not possible to completely decouple the environment from the inner core dynamics. For example, a moderate shear may be capable of inducing instability in the eyewall region which could have some long lasting effect on the subsequent development and structure even after the shear subsides, including the development of vortex Rossby waves (Reasor and Montgomery, 2015). So, while these intensity fluctuations may not be directly related to changes in wind shear, an increase in vertical wind shear prior to the W1 phase cannot be ruled out as a trigger.

Translation speed

One way the environment can influence the intensification of a tropical cyclone is through its effect on the storm translation speed. A tropical cyclone moving too slowly will have to contend with lower SSTs as a result of cold water upwelling which is exacerbated by a slow translation speed (Mei et al., 2012). At the other extreme, a fast moving TC may also be negatively affected, not only because stronger steering flows often come in conjunction with higher wind shear but also potentially due to direct effects such as the induction of wave 1 asymmetries (Sun et al., 2019).

Figure 5.5 shows the translation speed of the storm as a function of time. Through-

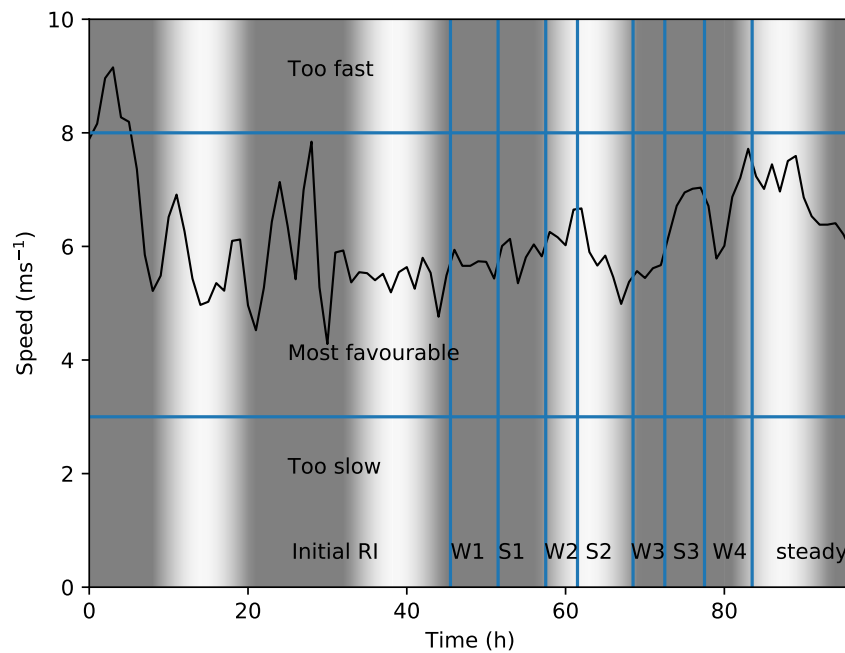


Figure 5.5: Translation speed of the TC centre. Colour shading is total incoming short-wave radiation which allows easy identification of daytime (pale grey or white) or nighttime (darker grey). Thresholds defining the ideal development speed are based on Michaels et al. (2006).

out the simulation, after the model spin up period, the TC has a translation speed which is similar to the average seen in the strongest tropical cyclones (Zeng et al., 2007). The variation during the intensity fluctuations is small and not correlated with the weakening and strengthening phases. There is also no evidence that a change in translation speed contributed to triggering the intensity fluctuations.

Sea Surface Temperature

It is well known (e.g. Zeng et al., 2007) that high sea surface temperatures (SSTs) and oceanic heat content play a critical role in the intensification of tropical cyclones and warm SSTs can help promote rapid intensification.

Throughout the simulation the SST was favourably high with a gradual increase during the initial RI period followed by a rather rapid increase at around 60 hours (not shown). There is no relationship between the intensity phases and the sea surface temperature with a nearly entirely monotonic rise throughout the simulation.

The SST after around 40h passes the threshold beyond which there is no clear relationship between SST and final intensity according to Michaels et al. (2006).

Maximum potential intensity

It is possible to generalize the SST information to build up a more complete picture of how conducive the environment is to TC intensification. The method, developed by Emanuel (Emanuel, 1986) equated the mechanical dissipation with the energy available to do work. Emanuel also derived expressions for maximum surface wind speed and from there derived the minimum possible centre sea level pressure. The maximum potential intensity depends only on environmental factors: the SST, the outflow temperature and factors influencing the energy transfer from the surface which include the boundary layer moisture.

The MPI increases throughout the simulation until around 80 hours where there is a slight decrease thereafter. Unsurprisingly, as the tropical cyclone intensifies, its central pressure and wind speed become closer to the MPI. With the intensity never quite reaching the MPI, the environment remains conducive to intensification throughout the simulation. The intensity fluctuations do not seem to correlate to the MPI, in general, although, notably, the MPI does increase rapidly at the onset of both S3 and S1, although not all the intensification is accounted for by the change in the MPI.

This is exemplified in Figure 5.6 which shows the difference between the storm intensity (in terms of SLP and surface maximum wind speed) and the MPI. In both cases the weakening phases show the storm becoming weaker relative to the MPI (typically by 5–10hPa or 5–20 ms^{-1}) and during the strengthening phases becoming stronger relative to the MPI (by similar sorts of values). The W3 phase may be a slight exception where the SLP decreases slightly faster than the MPI SLP although the W3 phase is the least impressive of all the weakening phases.

It is possible to see some periodicity in the MPI which seems to be related to the diurnal cycles (which are discussed in the next section). This is likely due to outflow temperatures being lower in the early morning leading to higher Carnot efficiencies.

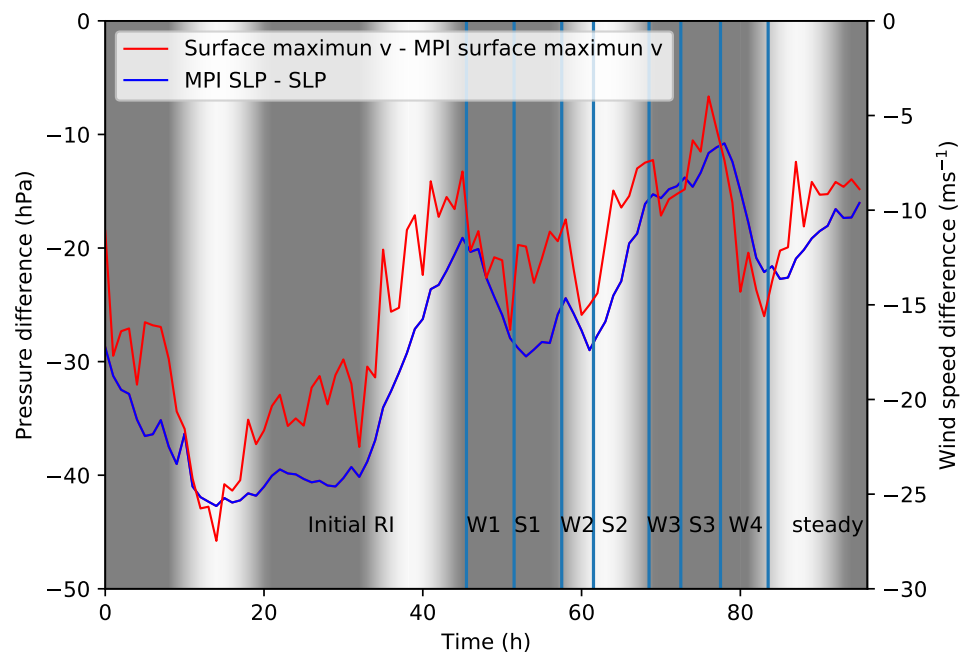


Figure 5.6: Difference between MPI and actual minimum sea level pressure (left scale) and maximum surface wind speed (right scale). In both cases negative values represent actual storm intensities less than the MPI (i.e. higher SLP or lower wind speed) and the zero line represents an intensity equal to the MPI. Colour shading is total incoming short-wave radiation which allows easy identification of daytime (pale grey or white) or nighttime (darker grey).

Diurnal Cycles

The diurnal cycle has been known to create intensity fluctuations so it is a plausible explanation that needs to be explored. Dunion et al. (2014) showed that pulses of convection in the inner core of the tropical cyclone tended to develop shortly after sunset and then proceed to propagate outwards during the night time period. These outward propagating pulses of convection after nightfall were also shown in Ditchek et al. (2019). The effect of this outward propagating, radiation induced convection was even shown to be potentially a necessary condition for an eyewall replacement cycle. Tang and Zhang (2016) showed that, without a diurnal cycle, eyewall replacement cycles are not simulated. Given that the intensity fluctuations in this current storm might be understood as existing on a spectrum that includes eyewall replacement cycles, the importance of diurnal effects on the storm cannot be neglected without first investigating them.

Figures 5.4 and 5.6 show the incoming shortwave radiation and the phases such that the diurnal cycles may be identified. Both W1 and W3 occurred around or after sunset (when it would be expected that the intensity of the TC should increase) while W2 occurred during the morning after sunrise. The strengthening phases all happened at different points during the diurnal cycle. S1 occurred prior to and during sunrise, S2 occurred during the middle of the day and lasted throughout most of the afternoon and S3 happened during the middle of the night. The periodicity of the intensity fluctuations did not match what would be expected for a diurnal cycle either with each phase lasting between 4–7 hours rather than the 12 hours that would be expected for a diurnal variation.

5.3.3 PV Fourier decompositions

One possible cause of the intensity fluctuations are vortex Rossby waves. In order to investigate this possible cause a Fourier decomposition of the PV was performed which allows vortex Rossby wave activity to be seen as counter propagating inward and outward moving PV anomalies.

Figure 5.7 shows the mean PV field and Fourier transformed components above the boundary layer. The change from a monopole type structure with high PV in the

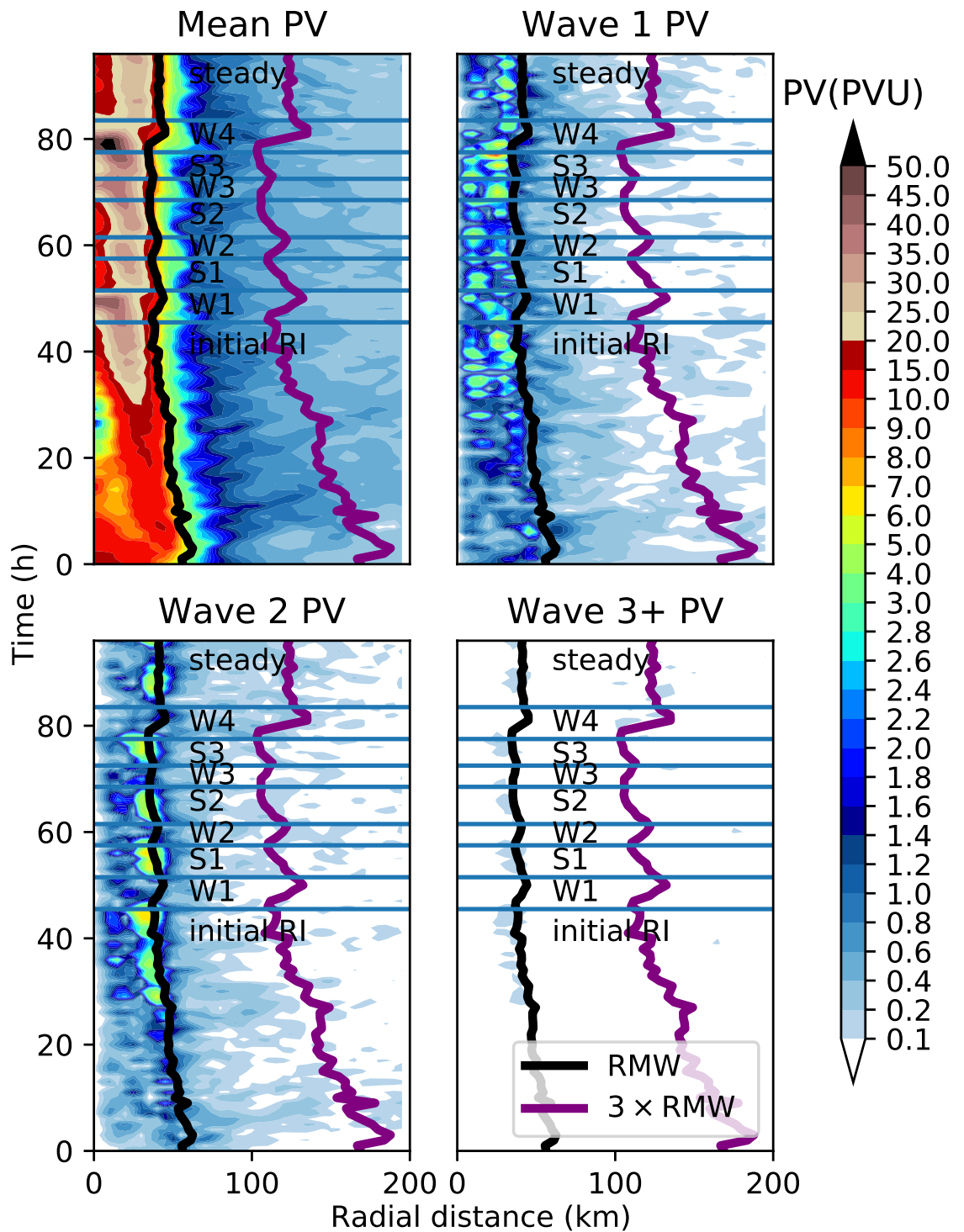


Figure 5.7: Mean PV field and azimuthal Wave 1, Wave 2 and Wave3+ frequency components for 1532m height level. Also shown are the intensity fluctuation phases, the RMW and $3 \times \text{RMW}$ (the approximate theoretical stagnation radius).

eye during weakening phases (particularly W1, W3 and W4) to a ring like structure with the PV maximum closer to 0.5 RMW is clearly evident. The magnitude of the PV maximum also tends to increase and be higher during the weakening phases compared to the strengthening phases. For example, the maximum PV during W1 decreases from above 30PVU to less than 20PVU during S1. Another notable feature of the mean PV field is the expansion of a 'skirt' of high PV outside of the eyewall during weakening phases.

The wave-1 component of PV shows little relation to the intensity fluctuations, although there is an increase in the amplitude in the later part of the initial RI. This may be related to the moderate increase in vertical wind shear (see Fig. 5.4) which is known to affect this PV (Reasor et al., 2000). The higher wave components of PV (3+) have an extremely low amplitude and are unlikely to matter significantly.

The wave-2 component of PV does seem to be associated with the intensity phases. During the Initial RI phase and each strengthening phase the wave-2 PV gradually increases around and just inside the RMW reaching a maximum at the transition point between a strengthening and weakening phase wherein the wave-2 PV then rapidly decreases. There is limited evidence, however, that this fluctuation in wave-2 PV is due to the development of VRWs since there is no sign of any outward propagation of the wave-2 PV anomalies nor is there any evidence (with the possible exception of the W4 period) of a drop in wave-2 PV around the stagnation radius.

It was checked whether or not the change in wave-2 activity was caused by vortex Rossby waves and was found VRW emission events do not seem to be associated with the intensity phases. However the phases are still associated with a change in the wave-2 PV structure within the eye-wall which may be a consequence of a more dramatic barotropic breakdown in the eyewall.

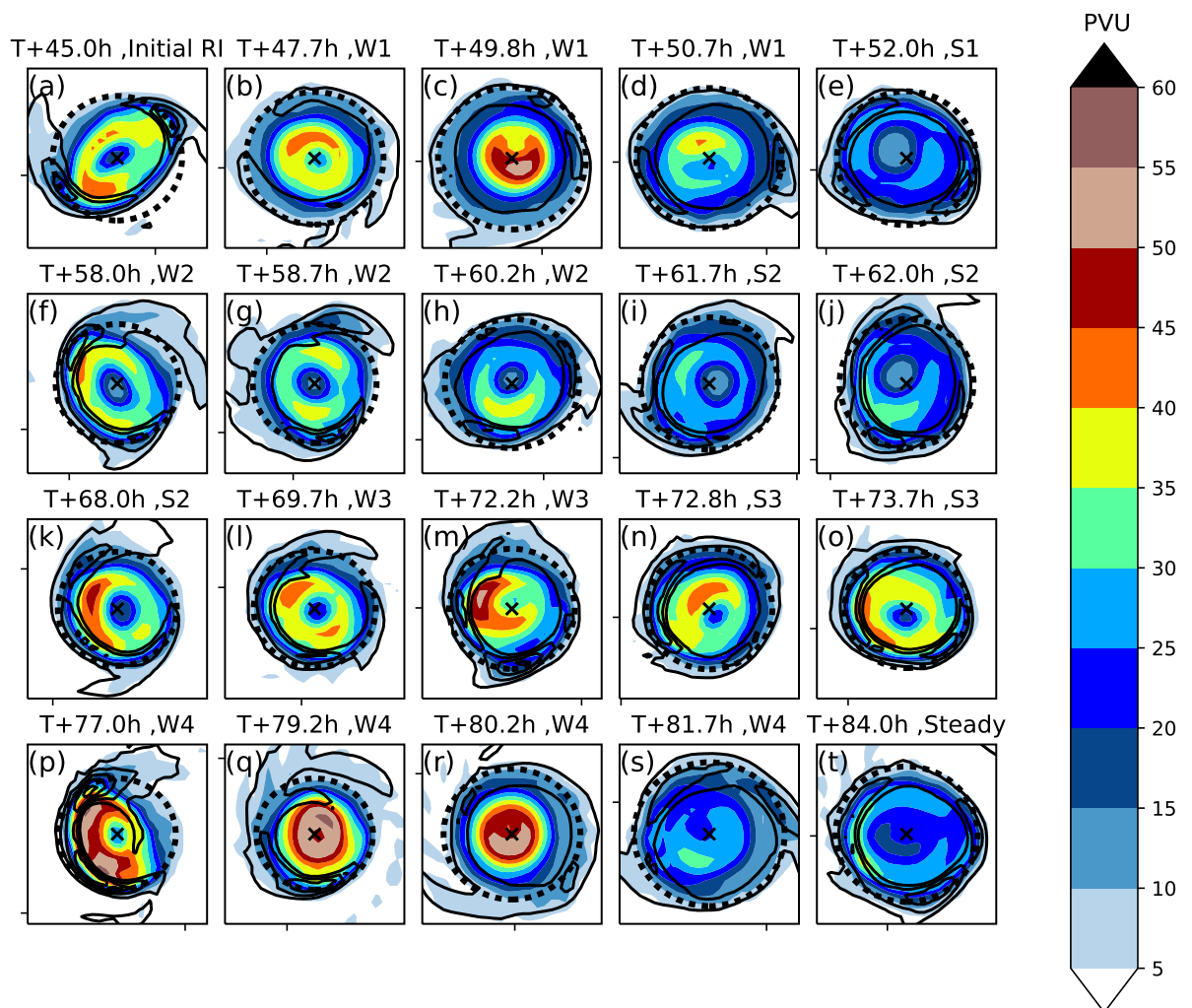


Figure 5.8: PV (PVU, shaded) at 1532m height for selected times and vertical velocity (1 m s^{-1} , black contour). The RMW is indicated by the dashed black line. A cross marks the centre of the TC. The data is output in 10-minute intervals, times are given to the nearest 0.1 hours.

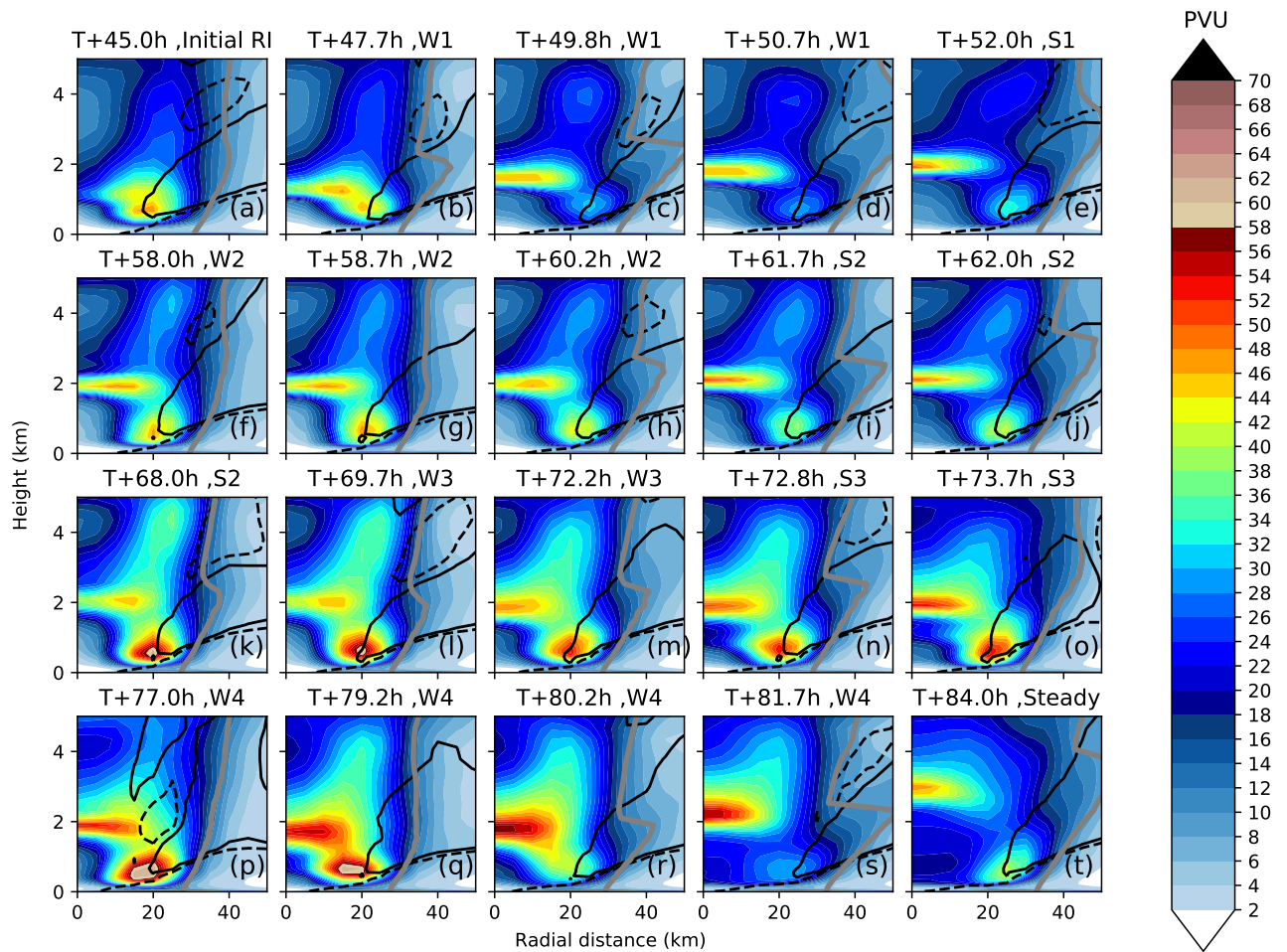


Figure 5.9: Azimuthally averaged PV (PVU, shaded) as a function of radial distance and height for selected times. The RMW is indicated by the grey line. Also shown are the 1 m s^{-1} (black lines) and -1 m s^{-1} (dashed black lines) radial wind contours.

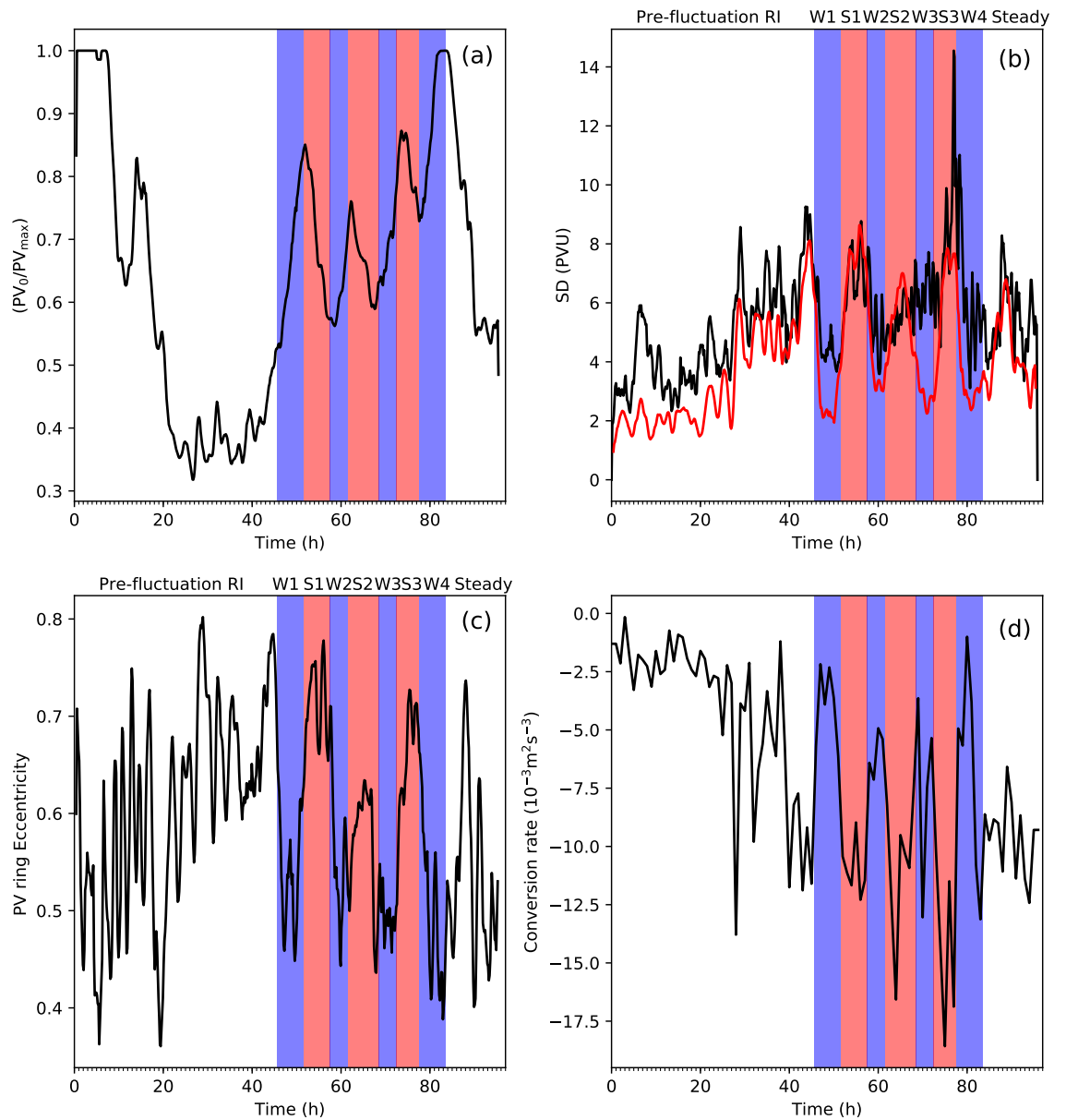


Figure 5.10: (a) Ratio of the low-level PV (depth averaged between 1052 m and 4062 m) at the centre of the TC to the maximum azimuthally averaged low level PV. (b) Maximum standard deviation of PV at 1532 m (black) and standard deviation of PV at 1532 m at the RMW (red). (c) Eccentricity of the ring fitted to the PV distribution at 1532 m. (d) Average barotropic conversion rate from the surface to 4062m averaged between 5 km and 70 km as a function of time. To smooth out high frequency noise a 1-h running mean is applied to 10-minute data. Weakening (blue) and strengthening (red) phases are also shown.

5.3.4 Barotropic structural changes

PV symmetry and structure

Distinct structural changes took place during the strengthening and weakening phases of Hurricane Irma. Fig. 5.8 and Fig. 5.9 show the PV field from a horizontal (just above the boundary layer where the change is most visible) and azimuthally-averaged perspective with times selected to best illustrate the evolution of the PV from just prior to the start of a weakening phase to the end of the weakening phase and start of the next strengthening phase. The evolution during the strengthening phases is less dramatic and is not shown. Prior to each weakening phase the PV field is ring-like and elliptical (Fig. 5.8a, f, k, p). This elliptical PV field becomes more circular at the start of each weakening phase (Fig. 5.8b,g,l,q). The PV field also becomes more monopolar during a weakening phase with higher PV in the centre of the storm and lower PV in the eyewall. A comparison of Fig. 5.9a,f,k,p with Fig. 5.9b,g,l,q shows that the transition from a ringlike to a more monopolar PV structure at the start of the weakening phase occurs primarily just above the boundary layer especially between 1 km and 2 km height. The trend towards a more monopolar distribution continues to the middle of the weakening phases where a ‘C’ shaped ring of high PV (Fig. 5.8c,h,m,r) develops near the TC centre above the boundary layer (Fig. 5.9c,h,m,r). The PV within the boundary layer also declines but maintains a more ringlike structure. The end of the weakening phase is characterised by the upward movement of the high PV zone at around 2 km height in the eye (Fig. 5.9d,i,n,s), and re-formation of a weak, circular, PV ring above the boundary layer (Fig. 5.8d,i,n,s). The start of the strengthening phase roughly coincides with the strengthening of this new PV ring (Fig. 5.8e,j,o,t) which becomes increasingly elliptical during the strengthening phase. The elliptical to circular transitions are particularly prominent in W1 and W4 which are more pronounced weakening phases than W2 and W3.

Figure 5.10a summarises these PV structure changes throughout the simulation with an index that describes how monopolar or ring-like the PV distribution is above the boundary layer (Hardy et al., 2021). Higher values of the PV ratio PV_0/PV_{\max} index, where PV_0 is the layer averaged PV at the centre of the storm, and PV_{\max} is

the maximum layer averaged PV, imply the vorticity structure is more monopole-like while lower values imply the structure is more ring-like.

During the weakening phases there is a trend for the PV structure to become more monopolar. At the end of each weakening phase the trend suddenly reverses and the vorticity structure becomes more ring-like. The change in the tendency of the vorticity structure is very sudden and coincides with the start and end of each phase. However, as indicated by Fig. 5.9 the PV distribution does not change uniformly at all heights. At lower levels closer to the boundary layer the PV field is more monopolar at the beginning of the weakening phase, while at higher levels it lags behind and is more monopolar at the start of the next strengthening phase. Unlike fluctuations associated with vacillation cycles (Hardy et al., 2021) the storm is continually transitioning away from or towards a ring-like structure. It should be noted that the more dramatic weakening phases, W1 and W4 shown in Fig. 5.8a–e,p–t and Fig. 5.9a–e,p–t are associated with a more pronounced realignment of PV both in terms of the ring becoming more monopolar and an overall decrease in PV between Fig. 5.8c,r and Fig. 5.8d,s. Fig. 5.10a shows a much bigger increase in PV_0/PV_{\max} for W1 and W4 compared to W2 and W3 (this is also seen in Hardy et al. (2021) with a greater change in PV_0/PV_{\max} associated with a more dramatic intensity fluctuation). It is well understood that annular vorticity rings can only be maintained by constant diabatic forcing and that without this the rings will be unstable and the vorticity will be redistributed into a monopole like structure (e.g. Prieto et al., 2001; Nguyen et al., 2011). The change in this PV distribution is likely due to PV being transported from the eyewall into the eye.

Figure 5.11 shows the PV tendency due to radial and vertical advection only over the previous hour. The start of the weakening phase shows PV transported to the eye at T+45 (Fig. 5.11a). At T+48 (Fig. 5.11b) the PV transport occurs above the boundary layer including at the 1532–m level shown in Fig. 5.8. At T+45 the transport of PV into the eye at this level is weak with different azimuthal starting points in the trajectories leading to rather different end points. Therefore, the gain of PV within the eye is due to eddies transporting more PV inwards than outwards. By T+48 there is a more distinct vertical transport of PV in the eye

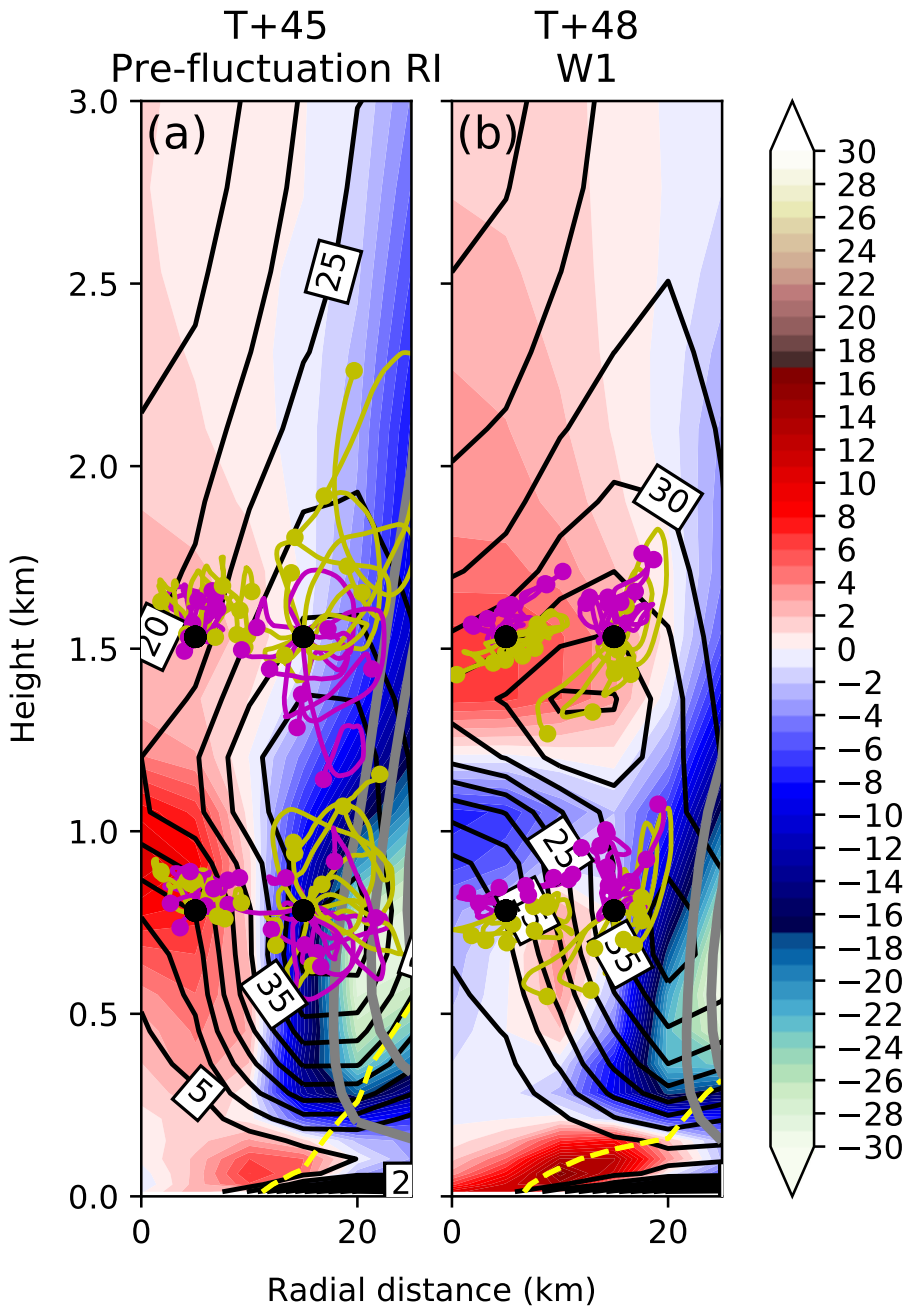


Figure 5.11: Change in PV over the past hour due to advection only (shaded PVU h^{-1}). Black line contours show the PV field in intervals of 5 PVU. Additionally, four sets of trajectories are shown for the following (r,z) points (black scatter points): (5 km, 1532 m), (15 km, 1532 m), (5 km, 782 m), and (15 km, 782 m). Purple lines and end scatter points represent the forward trajectory over the next hour while mustard lines and scatter points represent the backward trajectory over the previous hour. Each set of trajectories contains 8 points going back or forward with the same radial distance from the storm centre but with different azimuthal angles around the storm centre: from the east, northeast, north, northwest, west, southwest, south and southeast. The grey contours show vertical velocity in 0.25 m s^{-1} intervals indicating the location of the inner eyewall. Yellow dashed line shows the -1 m s^{-1} inflow contour.

from the boundary layer. So, the change to a more monopole structure can be explained by an initial inward asymmetric radial transport of PV within the eye followed by the development of a very weak (on the order of 0.02 m s^{-1}), deep ascent layer, transporting PV slowly upward. PV is also transported radially inward in the eye although the radial transport is weak. The weak ascent that develops within the eye originates within the eyewall and gradually extends inwards into the eye (not shown). The upward vertical motion is weak and inconsistent, only becoming apparent when 10-minute data is averaged over an hour. The PV contribution from diabatic processes is negative indicating the entire positive PV tendency is linked to movement of PV into the eye. The negative PV tendency regions in Fig. 5.11 are caused by the loss of PV through the updraft in the eyewall. There is also a gain of PV advected near the surface particularly in Figure 5.11 which can be linked to an increase in the inflow within the eye region and transport of frictionally generated PV from greater radii.

In addition to the radial PV structure the PV also varies azimuthally with the intensity fluctuations. One way of describing the azimuthal PV symmetry is the method of Nguyen et al. (2011) and Reif et al. (2014), where the azimuthal standard deviation of PV is calculated at each radius and the maximum value is taken. A high standard deviation of PV implies a less azimuthally symmetrical storm. It should be emphasised that this is a separate metric not related to the radial distribution of PV (i.e. monopolar and ringlike distributions). In the case of Nguyen et al. (2011) for example, the radial and azimuthal measures of PV were used interchangeably to describe ‘symmetric’ or ‘asymmetric’ states (the ringlike PV distribution in Nguyen et al. (2011) was correlated to an azimuthally symmetric state which is not the case here). In this study, references to symmetry only refer explicitly to variations in the azimuthal distribution of PV.

Figure 5.10b shows how this metric varies throughout the simulation. The red curve shows that the change in the variation of azimuthal PV at the RMW follows a similar pattern to the maximum azimuthal PV (black line). At the start of a weakening phase the maximum azimuthal standard deviation of PV decreases rapidly or becomes more azimuthally ‘symmetrical’ with the inverse happening dur-

ing strengthening phases. The weakening phases are, therefore, characterised by more azimuthally symmetric, more monopolar PV fields while the strengthening phases are characterised by a less azimuthally symmetric, more ring-like PV distribution. The azimuthal symmetrisation of the PV field occurs at approximately the same time that the field becomes more monopolar. This contrasts with prior work on vacillation cycles (e.g. Nguyen et al., 2011) where a more azimuthally symmetric PV field in Hurricane Katrina (2005) was associated with a ring-like distribution of PV. The change in the azimuthal symmetry is also described in Fig. 5.10c which shows that during the strengthening phases the initially circular PV rings become increasingly more elliptical (higher eccentricity) confirming that the start of a weakening phase is associated with a rapid change from an elliptical PV ring to a more circular one (also seen in Fig. 5.8).

To attempt to explain the causes of the change in PV structure the barotropic conversion rate was evaluated (as in Hankinson et al., 2014). The barotropic conversion rate describes how kinetic energy is transferred between eddies and the mean flow. Hankinson et al. (2014) showed that the conversion rate, in their simulation, is always negative which implies a conversion of kinetic energy between the mean state and the eddy state.

Figure 5.10d shows the barotropic conversion rate as a function of time. The beginning of the weakening phase is accompanied by a distinct rise in the barotropic conversion rate (it becomes less negative) while the commencing of the strengthening phase is associated with a more negative conversion rate. As the strengthening phases are associated with a less symmetric PV structure more kinetic energy is transferred from the mean state to the eddy state. The start of a weakening phase is therefore associated with a rapid reduction in the amount of kinetic energy transferred away from the mean state to the eddy state.

Vortical hot towers

During the strengthening phases, VHT-like features are apparent with small-scale local regions of high vorticity and vertical velocity within the eyewall. These features resemble VHTs formally defined in Smith and Eastin (2010) with local max-

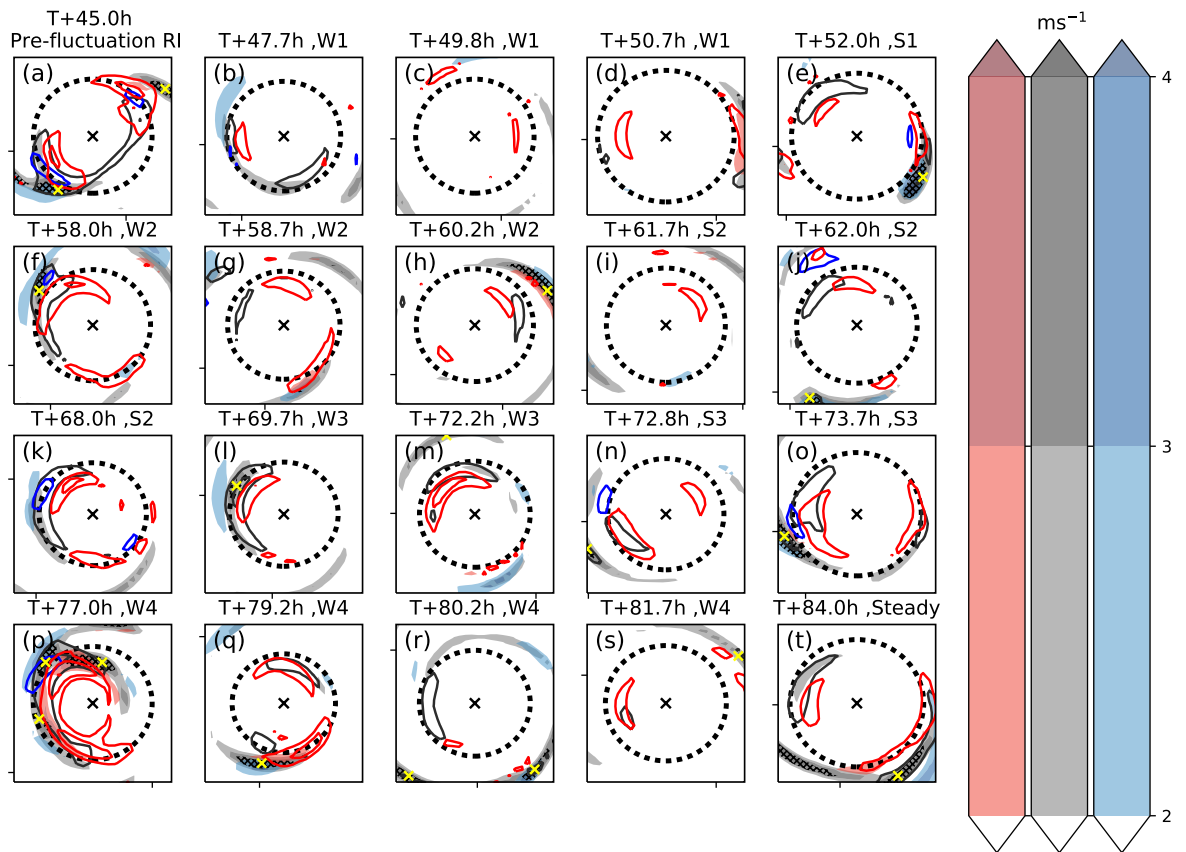


Figure 5.12: Perturbation vertical velocity (m s^{-1} shaded) (relative to the azimuthal mean), perturbation relative vorticity (10^{-3} s^{-1} coloured line contours) shown at the same times as in Fig. 5.8. Heights shown are 2532 m for the red shades/lines, 4963 m for the grey shades/lines, 9934 m for the blue shades/lines. The centre of the TC is denoted by the cross and the RMW at 4963 m is indicated by the black dashed line. Black hatches represent regions where the maximum perturbation vertical velocity at any level exceeds 5 m s^{-1} . Yellow crosses show the locations of locally high perturbation relative vorticity at 4963 m to indicate the location of VHT like structures.

irma in perturbation vertical velocity and with significant vertical depth albeit with lower values in these quantities (weaker and shallower). These structures appear frequently and may play a significant role in the development of the cyclone. Since they look like VHTs but are not strong or deep enough to meet the criteria for a VHT they will simply be described as VHT-like structures.

Figure 5.12 shows perturbation vertical velocity and relative vorticity at different heights at the same times as in Fig. 5.8. The VHT-like structures are more likely to be present during strengthening phases (particularly towards the end of the strengthening phases) and rarely form during weakening phases although an already

existing VHT-like structure may persist for a couple of hours into the weakening phase. These structures typically last on the order of an hour which is a little shorter than the lifespan of convective structures found by Yeung (2013) for the rapid intensification of Typhoon Vicente. The VHT-like structures move anticlockwise, with the flow, near the RMW. Filaments of high perturbation vertical velocity, but relatively low perturbation relative vorticity, associated with inner rain-bands, also commonly emanate outward from these VHT-like structures (see, for example Fig. 5.12p north of the RMW). It is fairly common, within the strengthening phases, to see two VHT-like structures at once which typically are 180 degrees from each other. In this case one VHT-like structure tends to be much stronger than the other. An example of this is shown in Fig. 5.12a with the VHT-like structure in the southwest quadrant being more intense and deeper than the one in the northeast quadrant.

During the weakening phases VHT-like structures rarely form such that in the middle of a weakening phase it is unusual to see one of these structures. The T+72.2 panel (Fig. 5.12 m) does show a weak, shallow, VHT-like structure in the northwest quadrant though it should be noted that W3 is the weakest weakening phase. Towards the end of a weakening phase VHT-like structures may redevelop and often form outside of the RMW. The T+50.7 panel (Fig. 5.12d) shows a VHT-like structure on the eastern side of the TC outside of the RMW that forms before moving inwards. If Fig. 5.12 is compared to Fig. 5.8 it can be seen that the VHT-like structures are typically located at the two points on the elliptical PV rings furthest away from the centre (i.e. along the semi-major axis of the PV elliptical ring). The strongest VHT-like structures tend to form just prior to a weakening phase and may last for the first few hours of the weakening phase. The VHT-like structure in Fig. 5.12a,p are examples of particularly strong VHT-like structure that occur just prior to the W1 and W4 phases respectively but are shown to very quickly dissipate during the start of W1 and W4 respectively as in Fig. 5.12b,q. The regions of locally high vertical velocity and relative vorticity associated with the VHT-like structures becomes increasingly delocalized and distributed over the entire eye-wall region resulting in a more axisymmetric structure. Any regions of high perturbation

vorticity or vertical velocity that form during the weakening phases are much weaker and shallower than the VHT-like structures that form during the strengthening phases (such as the low-level region of high relative vorticity north-west of centre in Fig. 5.12m) or occur well outside of the RMW (such as the updraught south-east of centre in Fig. 5.12r).

Tangential wind budget

The spin-up of a TC can be examined in terms of the tangential wind budget which describes contributions to the mean tangential wind tendency from radial and vertical advection of absolute angular momentum, which can be further split up into mean and eddy contributions. A form of the tangential wind budget based on Persing et al. (2013) is:

$$\frac{\partial \bar{v}}{\partial t} = -\bar{u} \overline{(f + \zeta)} - \bar{w} \frac{\partial \bar{v}}{\partial z} - \overline{(u' \zeta')} - \overline{\left(w' \frac{\partial v'}{\partial z} \right)} + F, \quad (5.2)$$

where v is the tangential wind, u is the radial wind, w is the vertical velocity, f is the Coriolis parameter, and ζ is the relative vorticity. Overbars represent azimuthal averages of these terms while primes represent perturbations from the azimuthal average. The terms on the right hand side of the equation from left to right are: mean radial vorticity flux, mean vertical advection of absolute angular momentum, eddy radial vorticity flux and vertical eddy advection of absolute angular momentum. The final term, F , represents sub-grid frictional contributions to the budget which are negligible outside of the boundary layer.

In order to understand the contribution of the VHT-like structures to the spin-up or spin-down of the TC, the eddy and mean contributions to the tangential wind budget were examined. Fig. 5.13 shows the contributions to the tangential wind budget through mean and eddy radial vorticity fluxes and vertical advection of absolute angular momentum (AAM). Fig. 5.13a,c shows that, near the eye-wall, the mean term has a positive contribution to the tangential wind in the boundary layer due to the radial inflow and a negative contribution above the boundary layer where the boundary layer outflow jet is located. The larger positive contribution to

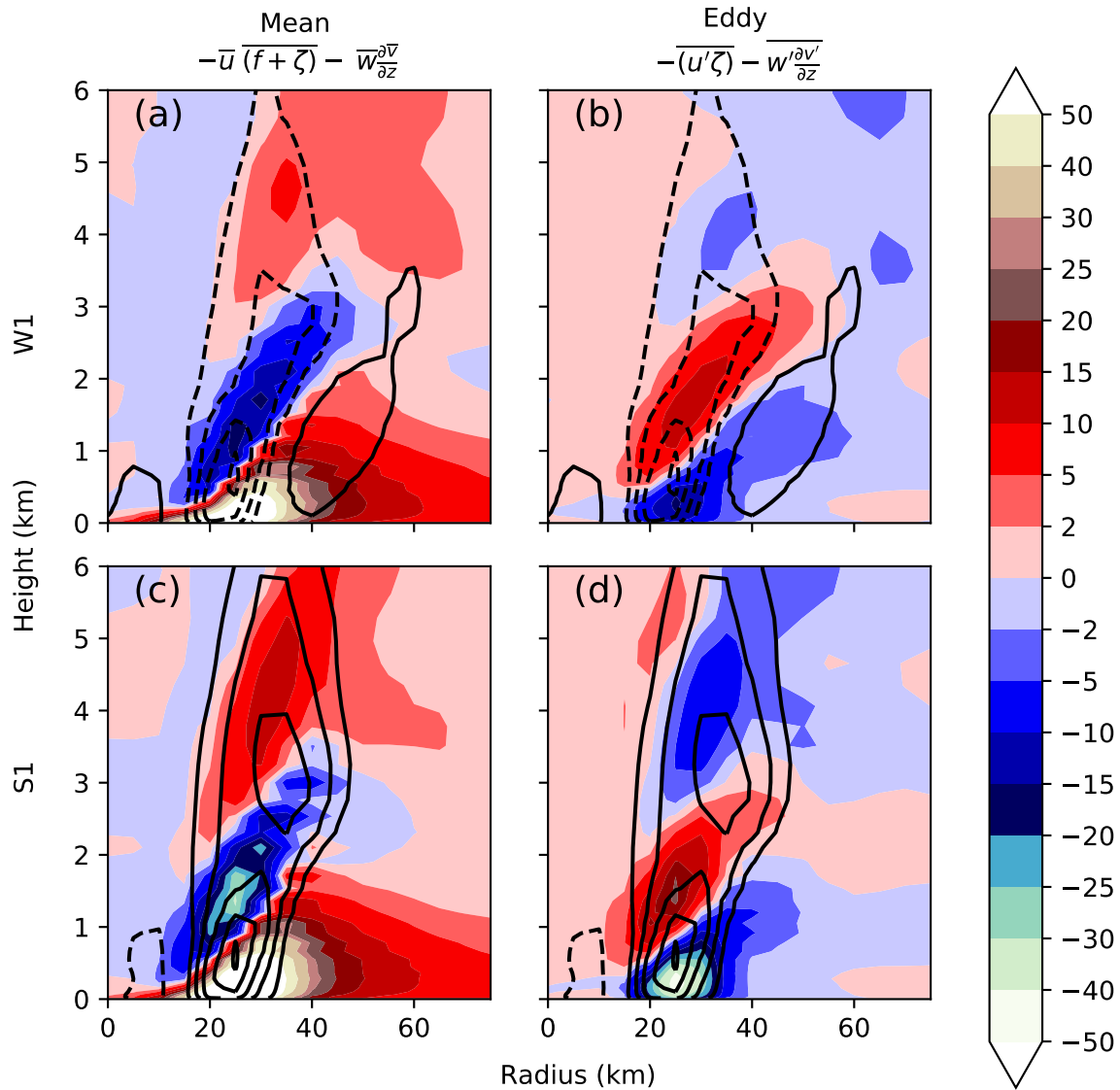


Figure 5.13: Colour shading shows the (a,c) mean and (b,d) eddy contributions to the tangential wind budget (see equation 5.2) in $\text{ms}^{-1} \text{h}^{-1}$. Line contours show the average tangential wind tendency in $2 \text{ms}^{-1} \text{h}^{-1}$ intervals with dashed contours indicating negative tendencies. The top row shows the composite for W1 (averaged over the entire W1 phase) while the bottom row shows the composite for S1. The frictional term (not shown) also contributes a large positive tangential tendency in the boundary layer.

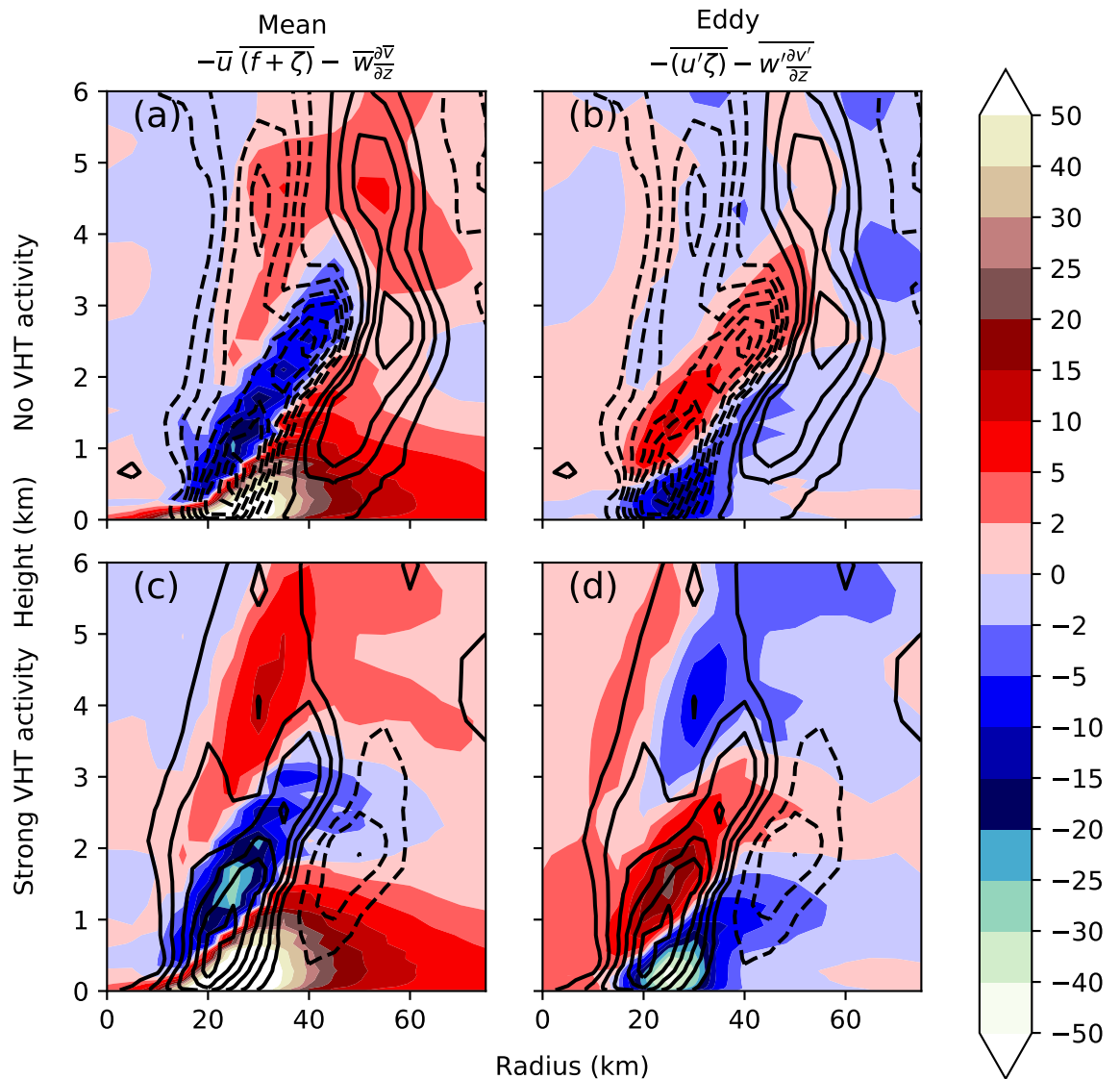


Figure 5.14: As with Fig. 5.13 but this time composites of no VHT activity (top row) and strong VHT activity (at least one VHT-like structure with ascent shading and vorticity contours at all three levels as in Fig. 5.12) (bottom row). Composites are created by averaging any times in the W1 and S1 combined period with no distinction between weakening and strengthening periods (45.5 hours to 57.5 hours) that either have no VHT activity (top row) or strong VHT activity (bottom row).

the tangential wind in the boundary layer, and larger negative contribution above the boundary layer in S1 compared to W1 is attributed to a stronger inflow and outflow in and above the boundary layer respectively.

Just above the boundary layer the eddy term has a positive contribution to the tangential wind budget in both S1 and W1 (Fig. 5.13 b,d). However, in S1 the magnitude of the positive eddy contribution above the boundary layer (around 1500 m) is larger. This finding is robust across all strengthening and weakening phases and extends generally to other ensemble members that show these intensity fluctuations (see Section 5.3.7). The greater positive contribution, to the tangential wind, of the eddies just above the boundary layer during the strengthening phases is associated with VHT-like activity. These results are illustrated in Fig. 5.14 which shows during the 45.5 hour to 57.5 hour period (comprising both W1 and S1 periods) a composite of all times where there is either no VHT activity (Fig. 5.14 a,b) or strong VHT activity (Fig. 5.14 c,d). In total there were 12 times where strong VHT activity occurred and 10 times where no VHT activity occurred during this period. This allows the effect of the VHT-like structures to be analysed more directly. As can be seen by comparing Fig. 5.14 b and d VHT-like structure activity is associated with an increased positive tangential wind tendency from the eddy terms just above the boundary layer compared to times without VHT activity. This is despite the increase in the negative contribution from the mean flow (Fig. 5.14 a,c).

However, the radial location of the VHT-like structure seems to be important, the VHT-like structure inside the RMW in Fig. 5.12p is concurrent with an eddy effect that spins down the eyewall (negative contribution to the tangential wind budget) and spins-up the eye. Likewise the VHT-like structure in Fig. 5.12t is associated with a positive eddy tangential tendency outside the eyewall and a spin down within the eyewall. VHT-like structures may have the ability to change the PV structure of the storm by stirring in higher PV into the eye which can spin up the eye (e.g. Reif et al., 2014) and induce a transition from a ring-like to monopole PV structure.

Summary of barotropic structural changes

This section analysed the barotropic structural changes that occurred during the fluctuations. It is shown that the PV structure transforms from an elliptical ring-like distribution prior to the start of a weakening phase to a more monopolar yet more azimuthally symmetrical structure. This change in the PV structure is associated with the inward and upward advection of PV within the eye and weakening of the PV maxima within the eyewall. The weakening phases were also associated with the reduction of the transfer of kinetic energy from the mean state to the eddy state which is linked to the reduction in VHT-like activity during the weakening phases and the associated convection and vorticity becoming de-localized. These VHT-like structures also likely played a role in the mixing of the PV in the eye and may also induce barotropic instability prior to a weakening phase.

5.3.5 Convective structural changes

To understand how the convective structures change with the intensity fluctuations the diabatic heating profiles are investigated, in particular, how the heating profiles change from strengthening phases transitioning to weakening phases. The diabatic heating (Fig. 5.15 and 5.16) is calculated using Eulerian potential temperature increments directly output from the MetUM.

During both weakening and strengthening phases there are some similarities, notably two separate heating maxima, one in the inflow boundary layer at around 1 km and the other in the mid-troposphere associated with the solid state microphysical processes above the freezing level in the free vortex at around 7 km. The majority of the heating occurs around the RMW in the eyewall, although small amounts of heating also occur out to 150 km associated with outer rainbands.

All of the weakening phases have a heating distribution with a greater radial extent compared to all of the strengthening phases (not shown). This can also be seen in the observations in Fig. 5.2a,b which shows the convection in the eyewall appearing to thicken with the moderately high precipitation rates occupying a greater radial extent during a weakening period than just prior to it. The overall heating rates are substantially weaker compared to the strengthening phases (e.g. a maximum

of around 30 K h^{-1} in W1 compared to around 45 K h^{-1} in S1) with substantial heating occurring outside the RMW. In the strengthening phases the heating is concentrated in a narrow band (of around 10 km width) just inside the RMW, while in the weakening phases the heating maximum is shifted outside of the RMW. Just above the boundary layer there is a heating maximum in both the strengthening and weakening phases, the heating here is stronger in the strengthening phases but is located inside the RMW during both the weakening and strengthening phases. The dominant component of diabatic heating, just above the boundary layer is from the latent heating due to cloud formation at the top of the boundary layer. The change in heating structures during the course of the strengthening phases (not shown) is much less significant with no secondary heating maximum appearing, although there is a tendency for the diabatic heating within the eyewall to become a bit stronger during the course of a strengthening phase.

The effect of eddy diabatic heating was also investigated. These results are not shown since the azimuthally averaged eddy heating was small, typically an order of magnitude smaller than the mean heating terms which is similar to the results of, for instance, Montgomery and Smith (2018). The eddy terms had the largest contribution just below the freezing level and a dipole-like structure with heating below and cooling above. No significant differences in the azimuthally averaged eddy heating distribution were detected between the strengthening and weakening phases with eddy momentum effects from the VHT-like structures playing a much more significant role in causing the intensity fluctuations than their effect on azimuthally averaged eddy diabatic heating.

In terms of how the heating structures change just prior to a weakening phase Fig. 5.15b,c shows a secondary heating maximum at around 55 km radius and 5 km height associated with the inner rainbands. Along these rainbands near their intersection with the eyewall there are regions of enhanced convection which can be seen in Fig. 5.16a T+44.5 in the northwest and southeast associated with VHT-like structures which are responsible for most of the heating. The secondary heating maximum associated with the inner rainbands becomes more distinct by T+45.5 (Fig 5.15b) which develops into a secondary updraft by T+46.5 (Fig 5.15c). A

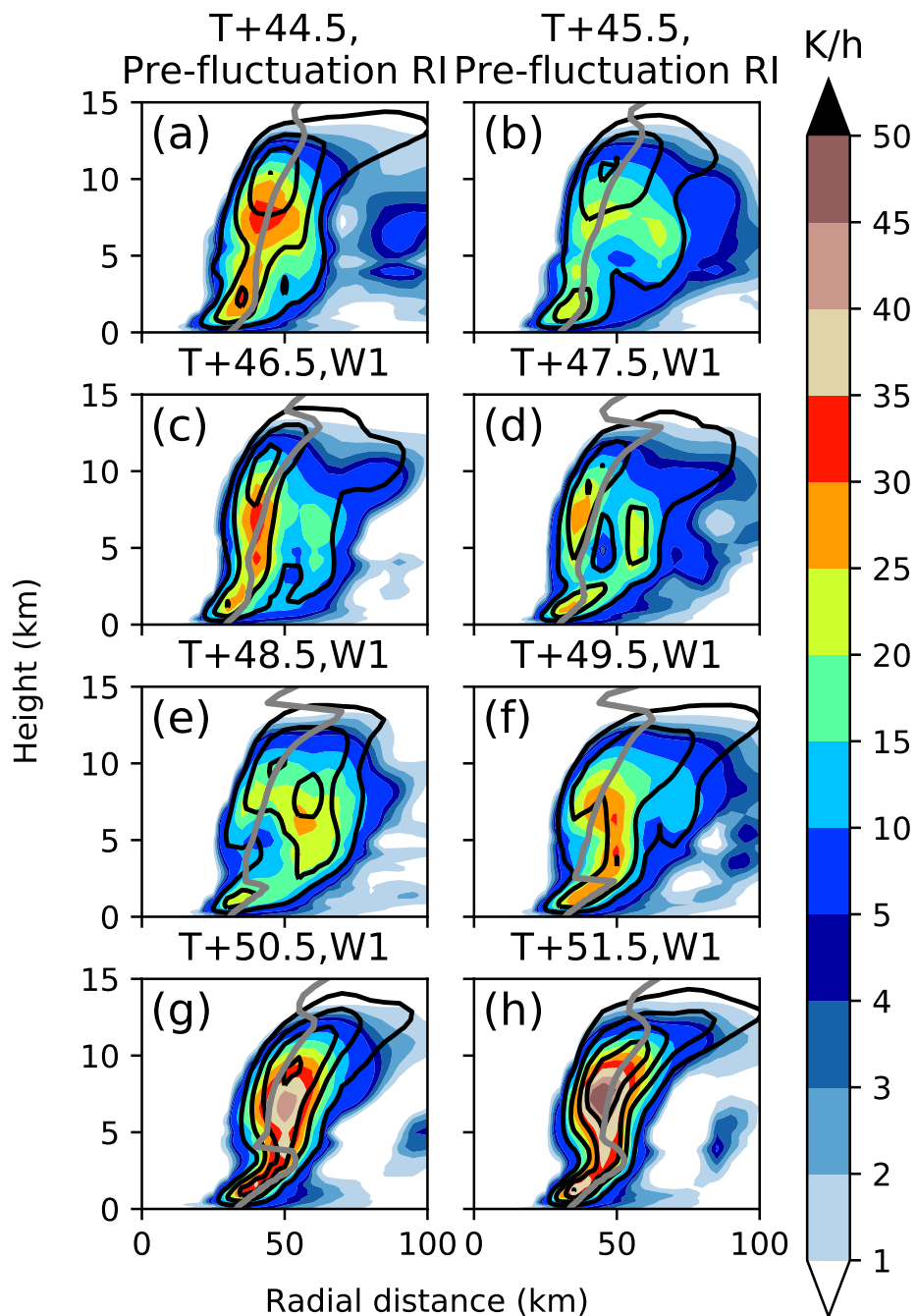


Figure 5.15: Diabatic heating (shading, K h^{-1}), vertical velocity (line contours) in intervals of 0.5 m s^{-1} before and during the first weakening phase W1. Also shown as a grey line is the RMW.

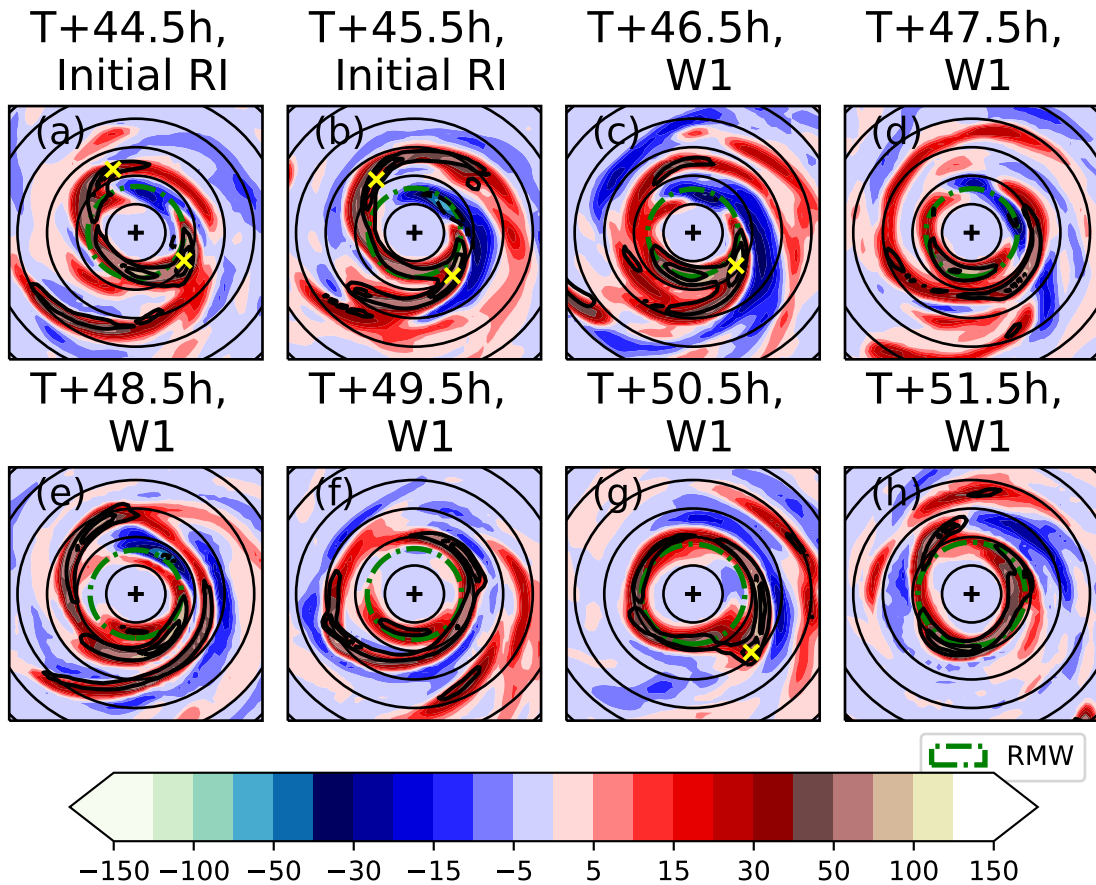


Figure 5.16: Diabatic heating (Kh^{-1}) for height 4963 m before and during the first weakening phase W1. Vertical velocity contours in intervals of 2 m s^{-1} . Yellow crosses indicate the location of the maximum local perturbation vertical velocity at the same level for any VHT like structures as determined by adapted criteria in Smith and Eastin (2010).

single VHT-like structure is still visible at T+46.5 in the southeast quadrant (Fig 5.16c). However, by T+47.5 h (Fig 5.15d) an azimuthal symmetrisation has taken place with the inner-rainband convection visible as a second ring outside the eye-wall. The heating from VHT-like structures that occur in the inner rainbands near where they intersect with the eyewall becomes less significant between T+44.5 and T+47.5 (Fig 5.15a–d), but the secondary heating maximum from the inner rainbands becomes more distinct (Fig 5.16a–d).

Over the next few hours the secondary convective ring becomes more symmetrical and the VHT-like structures continue to become less visible. Eventually by T+50.5 the secondary convective ring has replaced the first (Fig 5.16g). In the remaining hour of W1 the RMW expands out to coincide with the diabatic heating maximum. Note, the inner rainband activity and the associated VHT-like structures may be necessary conditions for a weakening phase to begin; however, it is not sufficient. For example, prior to W1 a vortex Rossby wave event at T+38h led to the development of a secondary convective ring, which subsequently weakened and did not replace the primary ring. Another particularly strong single VHT-like event that occurred around T+35, in the eye-wall region, also did not lead to an intensity fluctuation.

It was found that weakening phases were associated with weaker heating outside of the RMW compared to strengthening phases associated with stronger narrower columns of diabatic heating just inside the RMW which is consistent with a simple balanced dynamical interpretation (e.g. Smith and Montgomery, 2016) whereby convection occurring outside the RMW acts to spin-up the primary circulation outside the RMW and spin-down the primary circulation inside the RMW. The cause of the increase in convection outside the RMW was found to be related to VHT-like structures within inner rainbands which de-localized to form a symmetric diabatic heating column outside of the RMW and proceeded to become dominant over the original heating column over a period of a few hours.

5.3.6 Unbalanced dynamics and the boundary layer

If the boundary layer plays a significant role in the cause of the intensity fluctuations then it may be necessary to attempt to understand the fluctuations in terms of the boundary layer spin-up mechanism as described by Montgomery and Smith (2018). This requires air parcels within the boundary layer to gain more AAM through rapid reduction of radial distance than is lost through friction. A consequence of this is the initially subgradient tangential wind within the boundary layer becoming supergradient. Examining the agradient wind in and above the boundary layer allows the importance of the unbalanced spin-up mechanism in the intensity fluctuations to be determined.

Primary and secondary circulation in or just above the boundary layer

Figure 5.17 shows how the agradient wind, the tangential and radial wind vary throughout the simulation both at the radius of 35 km and at the RMW (such that the agradient wind can be examined both at the eyewall and at a fixed radius as during a weakening phase the RMW increases). A negative agradient wind corresponds to a subgradient flow while a positive agradient wind corresponds to a supergradient flow. The blue curve near the surface is chosen to show the subgradient boundary layer flow. The green curve shows the agradient flow a little higher up but still within the boundary layer; this is at a height where during the weakening phases the subgradient flow becomes supergradient indicated by the crossing of the zero line). The yellow curve is at a height that roughly corresponds to the middle of the outflow jet and the red curve represents a level near the top of the outflow jet where the flow has returned to near gradient wind balance.

Just prior to the weakening phase the inflow in the boundary layer at a radius of 35 km decreases (Fig. 5.17d) while the inflow at larger radii (e.g. 100 km) may increase (not shown). This decrease in inflow at small radii is followed by a marked increase in the agradient wind at all levels (Fig. 5.17a,c). The increase in the agradient wind is not accompanied by an increase in the tangential wind (Fig. 5.17b) at any level which implies the increase in the agradient wind is caused by a decrease in the pressure gradient force per unit mass (PGF) which is also shown in

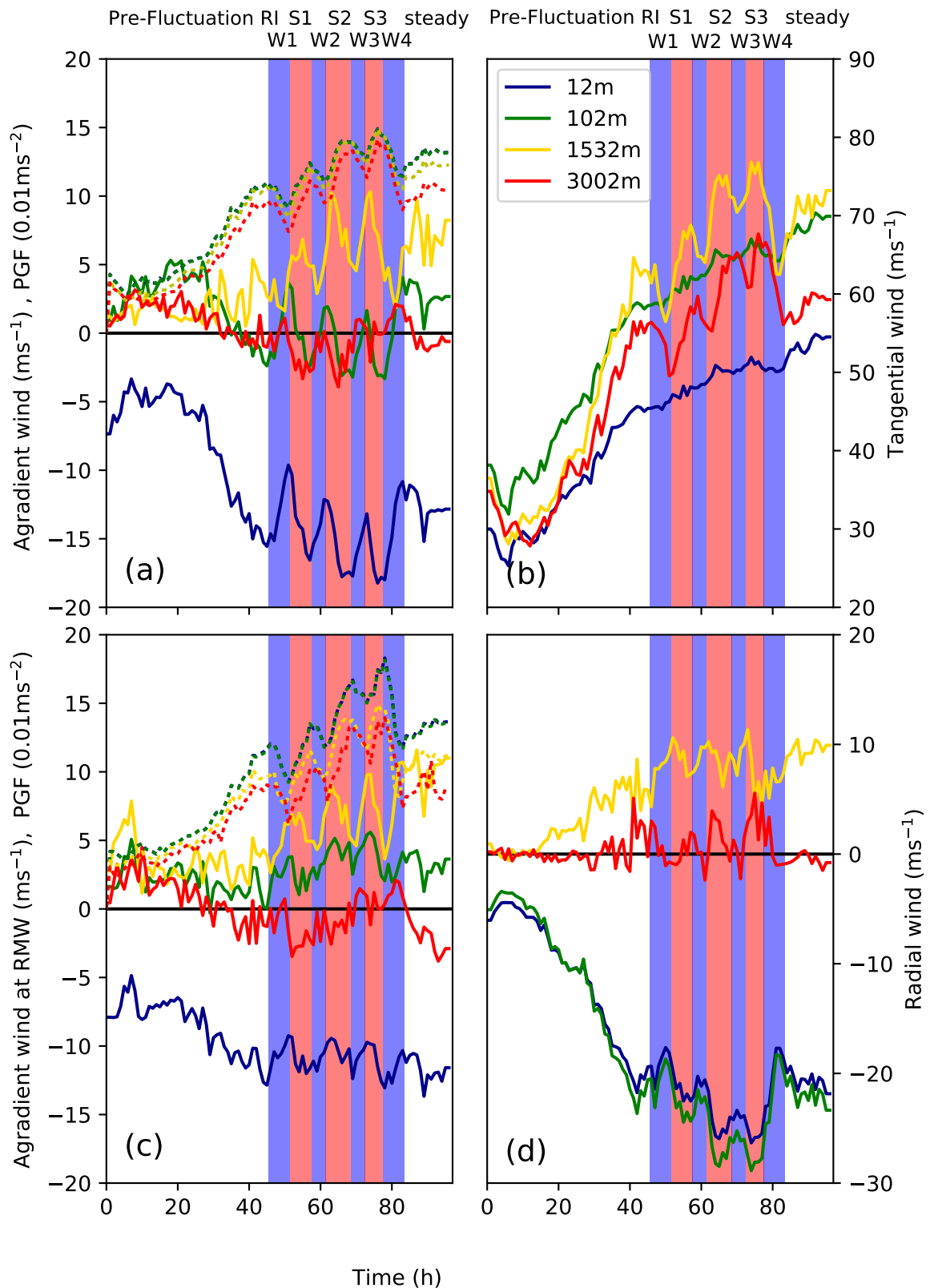


Figure 5.17: Left column shows azimuthally averaged agradiant wind as a function of time (ms^{-1}) for (a), a radius of 35 km and (c) at the RMW. The right column shows, for the 35 km radius, the azimuthally averaged (b) tangential and (d) radial winds (ms^{-1}). The height of the lines are 12 m (blue), 102 m (green), 1902 m (orange) and 3002 m (red). Panels (a) and (c) also show the pressure gradient force (0.01ms^{-2} , dashed lines) at selected levels.

Fig. 5.17 a and c. The decrease in the PGF is caused by the appearance of a convergence zone above the boundary layer where balanced inflow, enhanced by rainband convection, meets with the boundary layer outflow jet. The presence of rainband convection may also be responsible for the reduction of the inflow in the boundary layer prior to the weakening phase in the eyewall (Fig. 5.17d) which also explains why the boundary layer tangential wind (Fig. 5.17b, green curve) stops increasing before the tangential wind stops increasing at higher levels (Fig. 5.17b, red curve). The reduction in inflow, however, is not enough to spin-down the boundary layer nor prevent the boundary layer winds from becoming more agradient. Therefore, at the surface, the reduction in maximum total winds (black line in Fig. 5.3) during the weakening phases is not due to a tangential wind decrease in the boundary layer but rather a combination of a decrease in the radial inflow and an azimuthal symmetrisation of the wind field (i.e. the maximum surface wind speed decreases faster than the mean (azimuthally averaged) surface wind speed).

During the weakening phase an increase in the agradient wind is seen within the boundary layer (Fig. 5.17 a and c) which gives rise to a stronger outflow jet just above the boundary layer (Fig. 5.17d). This enhanced outflow jet continues to increase throughout the weakening phase and reaches a maximum at the start of the next strengthening phase.

The start of a strengthening phase is characterised by a strong outflow jet and a slightly subgradient ‘overshoot’ (red line in Fig. 5.17a slightly below zero near the start of the strengthening phases) i.e. as the ascending air within the super-gradient layer decelerates it overshoots to a value lower than the gradient wind.

Boundary layer slab model

Figure 5.18 shows a comparison of the boundary layer slab model with the MetUM output for the agradient and radial winds. The slab boundary layer model has only one layer and takes only the tangential wind speed above the boundary layer as an input parameter so it is not surprising that the values are quite different between the two models. However, the structures have some similarities. The decrease in radial inflow during the weakening phases and increase during the strengthening

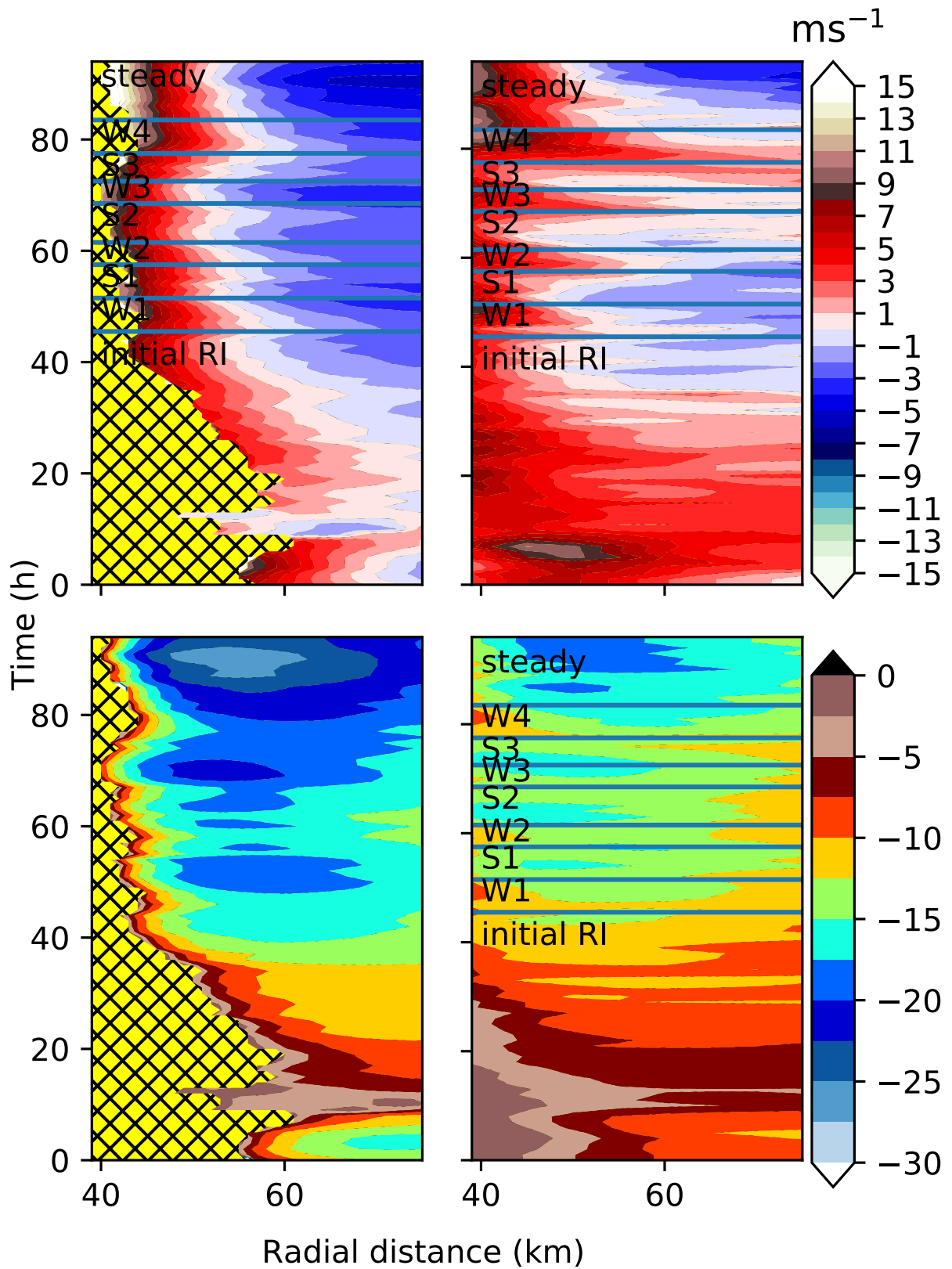


Figure 5.18: Comparison of slab boundary layer model (left) with MetUM output (right) for gradient winds (top) and radial wind (bottom). For the slab boundary layer model the depth is taken to be 1202m whilst for the MetUM output the radial and gradient winds are averaged throughout the lowest 1202m. The yellow hatched zone in the left panels represents no data where the slab boundary layer model does not converge.

phases is captured well as is the broadly strengthening trend of the inflow. The structure of the agradient wind is also similar with the slab boundary layer model showing a transition from the subgradient to supergradient wind as in the MetUM. At high radial distances (above 50km) the pattern of decreasing supergradient wind is present in both models. However, it is not possible to observe the more interesting finding of an increase in the supergradient wind near the RMW at smaller radii due to the inability of the slab boundary layer model to produce solutions for smaller radii (showed by yellow hatched zone in Fig 5.18). At the smallest radii before convergence there are some signs, in the slab boundary layer model, that the supergradient wind does increase. The ability of a simple boundary layer model to replicate such a counter-intuitive finding suggests that the boundary layer plays a very significant role in these intensity fluctuations and that a balanced dynamics interpretation alone may be inadequate. Further examination of the validity of the balanced interpretation is done in Chapter 6 where a barotropic balanced model is used to attempt to replicate the intensity fluctuations.

Tangential wind budgets

To understand how the boundary layer and outflow jet change and lead to a spin-down above the boundary layer Fig. 5.19 shows how the primary and secondary circulation change and what drives these changes by using the tangential wind budget. The times shown correspond to the times in Fig. 5.8a-c.

The increase of the agradient wind at the start of the weakening phase leading to an intensification of the outflow jet can be seen by comparing Fig. 5.19a with Fig. 5.19d with the wind becoming especially more supergradient around the RMW below the outflow jet. The main result of this comparison is a radial advection of low angular momentum (Fig. 5.19 d) which acts to cause a spin-down of the eyewall above the boundary layer (Fig. 5.19 c). The spin-down of the tangential wind just above the boundary layer pushes the RMW outwards and results in the 'kink'-like appearance of the RMW. Above the kink the tangential wind is in approximate gradient balance and the flow runs nearly parallel to the AAM surfaces. Eventually the expansion of the RMW above the boundary layer in combination with the

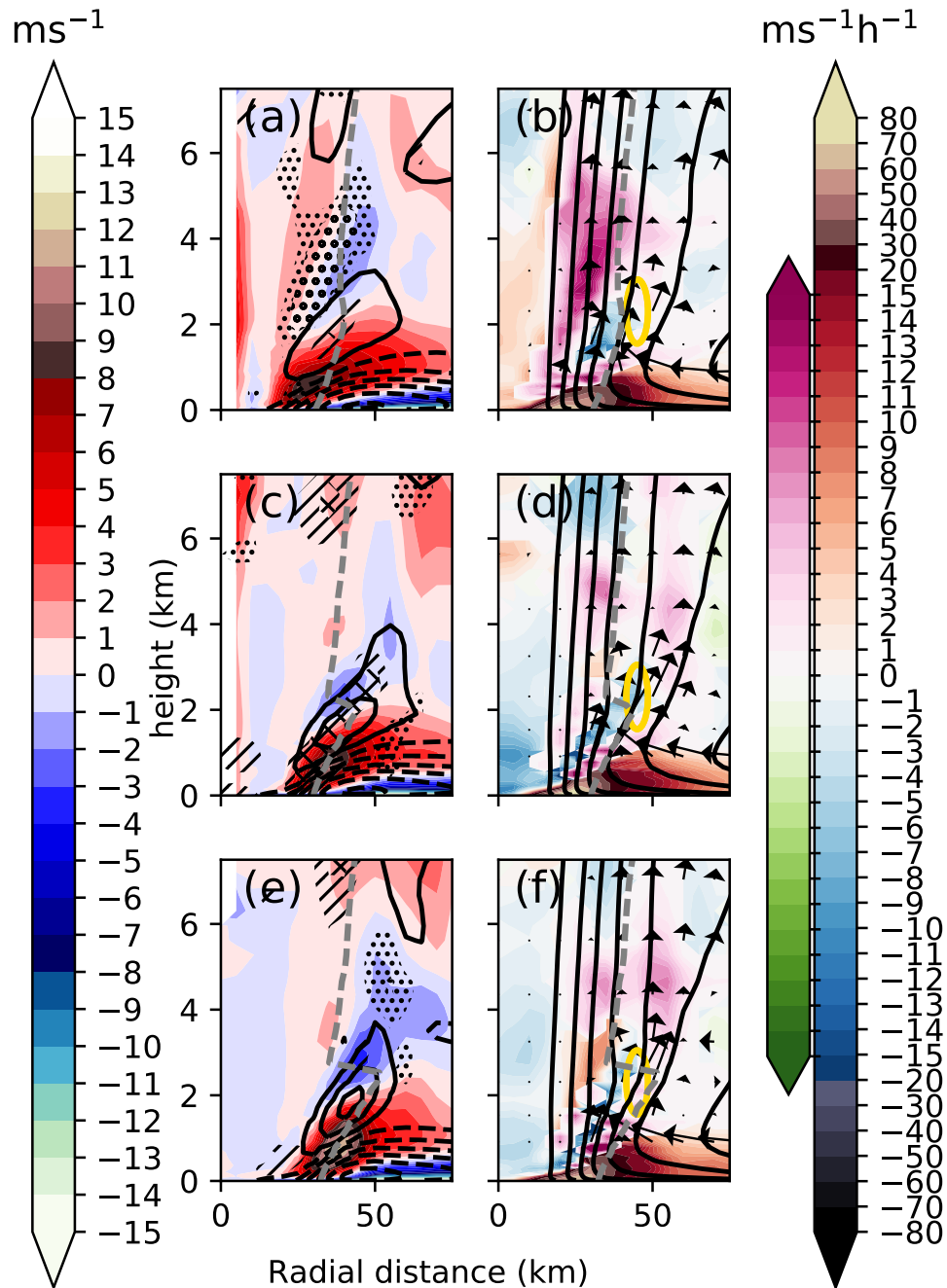


Figure 5.19: Left column shows, as a function of height and radius: the gradient wind (shading, left colourbar), the radial wind in intervals of 4 m s^{-1} with dashed lines indicating negative values, the tendency in tangential wind as small dots showing $+2 \text{ m s}^{-1}\text{h}^{-1}$, large dots showing $+4 \text{ m s}^{-1}\text{h}^{-1}$, line hatches showing $-2 \text{ m s}^{-1}\text{h}^{-1}$ and cross hatches showing $-4 \text{ m s}^{-1}\text{h}^{-1}$. Right column shows angular momentum (lines in units of $5 \times 10^{-5} \text{ m}^2 \text{ s}^{-1}$) and the secondary circulation as arrows in the plane of the cross section (with the boundary layer strong inflow omitted for clarity). The shading shows the contribution of the sum of the radial and vertical advection of angular momentum to the tangential wind budget. The colour scale used indicates which is the dominant term. If radial advection dominates over vertical advection then the blue/red shading is used and if vertical advection is dominant over radial advection then the green/purple scheme is used. For example green shading implies that the radial and vertical advection of angular momentum causes a negative tangential wind tendency and that the vertical term dominates. Also shown is RMW as the dashed grey line. The times shown in a,b are T+45, c,d, T+47.4 and e,f, T+49.8 (the first three panels in Fig. 5.12). A region of interest is denoted by the yellow ellipse.

weakening inflow within the boundary layer leads to the vertical advection of angular momentum into the low angular momentum region above the boundary layer which can be seen in the pink area near the RMW (in the highlighted yellow ellipse) in Fig. 5.19f compared to Fig. 5.19d where the same region is blue. At the increased radius, the coherent eyewall structure reforms with a spin-up as a result of the vertical advection of absolute angular momentum. The outflow jet, which previously reduced the tangential wind in the eyewall now does so within the eye which brings the TC into a strengthening phase. The PGF increases, the supergradient wind in the boundary layer becomes less supergradient, and the outflow jet weakens.

In summary the intensity fluctuations in Hurricane Irma can be understood in terms of unbalanced boundary layer dynamics. Firstly the agradient wind in the boundary layer increases as a result of a decline of the PGF (likely due to an inner rainband creating a convergence zone above the boundary layer), the rapid increase in the supergradient wind within the boundary layer leads to an intensification of the outflow jet just above the boundary layer which acts to spin down the primary circulation above the boundary layer by advecting in low angular momentum air from the eye, as well as expanding the RMW above the boundary layer. The eyewall restrengthens above the boundary layer with a higher RMW and a recoupling of the primary circulation at the higher RMW with the boundary layer signals the start of the new strengthening phase. This can be seen explicitly by looking at Fig. 5.15h; the eye-wall forms at approximately the same radius as the updraft located further from the centre of the storm in Fig. 5.15d.

5.3.7 Composites over multiple ensemble forecasts

The prior analysis has been carried out for one ensemble forecast member. To demonstrate the robustness of the analysis composites of selected key results are presented across multiple ensemble members. Five out of 18 ensemble members (including ensemble member 15), initialized on 03 September 00UTC, showed the intensity fluctuations previously discussed. A further six ensemble members also showed similar but weaker fluctuations. An additional model simulation, initialized on 02 September 12UTC, found seven out of 18 ensemble members with the same

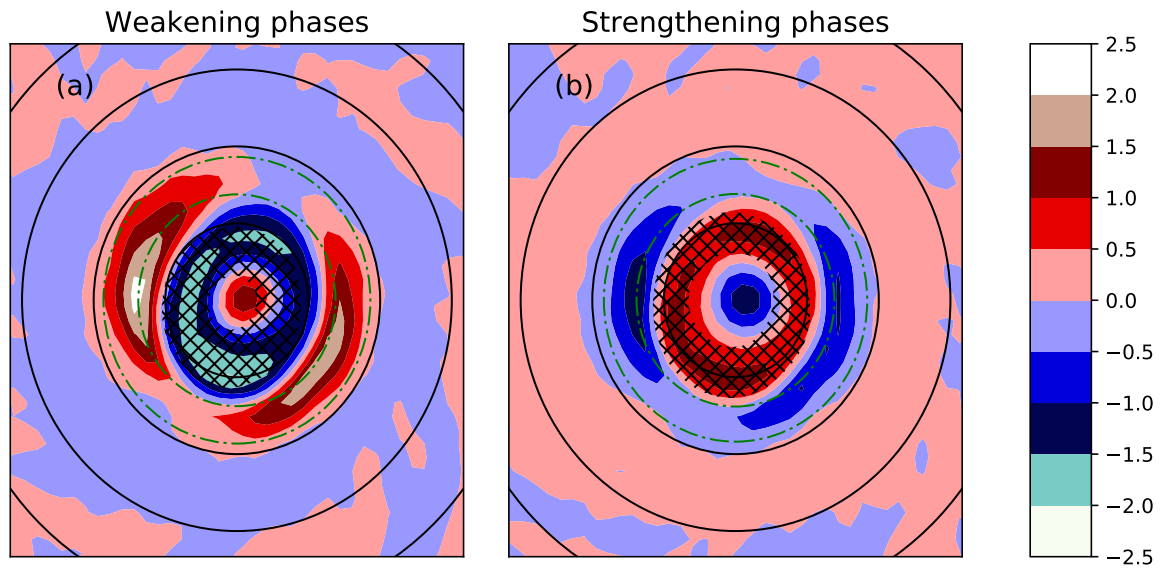


Figure 5.20: Composite PV tendencies (PVUh^{-1} , shading) at 1532 m across all weakening and strengthening phases in the six ensemble members with distinct fluctuations. Green dashed lines show the full range of RMWs at the same level. Hatching indicates regions where the average PV exceeds 30 PVU. Black circles show 25 km radial intervals.

kind of fluctuations. The following composites are based on the five ensemble members initialised on the 03 September at 00UTC that show the strongest fluctuations. The composites are over all weakening and strengthening phases in all of these five ensemble forecast members.

One of the key aspects of the analysis is the transition during weakening phases from a ring-like PV distribution at the start of the weakening phase towards a more monopolar PV distribution towards the end. Fig. 5.20 shows a PV tendency composite plot for all weakening and strengthening phases for the five ensemble members with the strongest intensity fluctuations. During the weakening phases there is a positive PV tendency within the inner eye and a negative tendency within the high PV annulus confirming the results from Section 5.3.4 for Irma's PV structure to become more monopolar in the weakening phases. The opposite is shown in the strengthening phases with PV decreasing in the inner eye and rising in the high PV annulus. Near the RMW outside the PV ring there are positive PV tendencies at the start of the strengthening phases which can also be seen in Fig. 5.8e,j,o,t to Fig. 5.8d,i,n,s near the RMW (dashed black line).

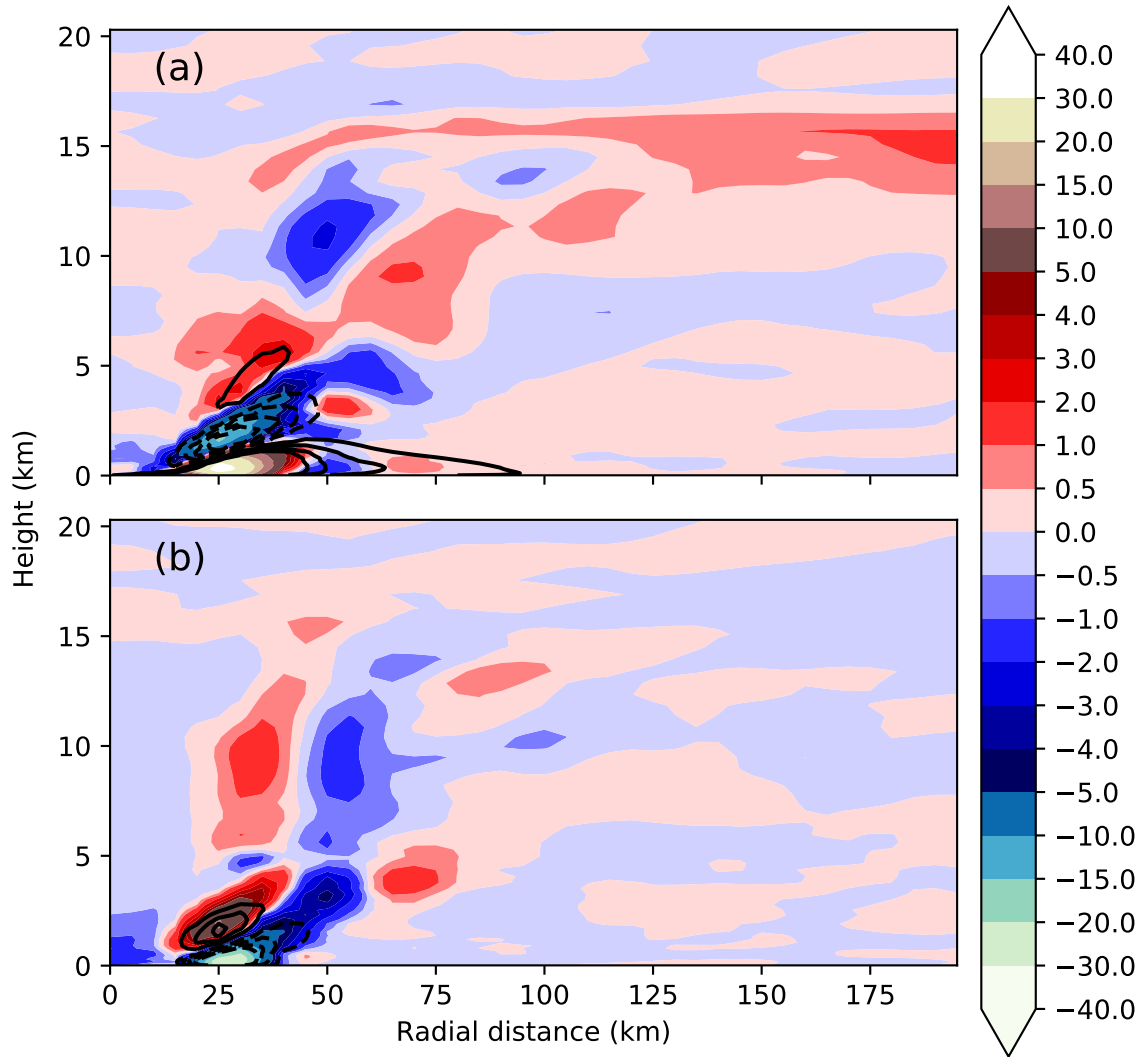


Figure 5.21: Absolute angular momentum budget composites showing: (a) mean advection of angular momentum, and (b) eddy advection of angular momentum. Colour shading shows the difference in tangential wind tendency between the strengthening phase composite and the weakening phase composite in $\text{ms}^{-1}\text{h}^{-1}$. Line contours ($5 \text{ ms}^{-1}\text{h}^{-1}$ intervals, dashed lines imply negative values) show a composite of the contribution to tangential wind budget during all the strengthening phases (for example in subplot a at around 50 km there is a strongly positive tangential wind tendency from the mean term over all the strengthening phases).

Figure 5.21 shows the contributions to the tangential wind budget through mean and eddy advection of angular momentum of the strengthening composite relative to the weakening composite (strengthening phases minus weakening phases). Above the boundary layer at a radial distance of 20 km to 35 km the eddy term plays a beneficial role in both the strengthening and weakening phases; however, in the strengthening phases the effect is distinctly greater. This comparison confirms some of the findings shown in Fig. 5.13 that the eddy momentum flux acts to cause intensification above the boundary layer particularly during strengthening phases. The effect of the mean momentum fluxes are also similar with greater tangential wind spin-up in the boundary layer in strengthening phases compared to weakening phases but also with greater spin-down above the boundary layer in the outflow jet during the strengthening phases.

The composites demonstrate that similar processes are likely occurring in the other ensemble members fluctuations in intensity during rapid intensification and are not just limited to a single ensemble member.

5.4 Discussion

During the weakening phases the RMW expanded, the wind speed decreased and the MSLP stagnated or rose, while during the strengthening phases the opposite occurred. These phases were found to be associated with different diabatic heating distributions, with weakening phases associated with broad and weak columns of heating outside the RMW and strengthening phases associated with stronger, narrower heating columns just inside the RMW. This is consistent with a simple balanced interpretation of the results; however, heating in high inertial stability environments as in Schubert and Hack (1982) was not found to be a useful predictor of the fluctuations, although inertial stability in the core region did overall increase throughout rapid intensification.

The fluctuations observed in Hurricane Irma are proposed to be the result of changes in both the barotropic and convective structure of the storm which is similar to Hankinson et al. (2014) where both convective and barotropic effects caused vacil-

lation cycles in Hurricane Katrina (2005). The start of a weakening phase during a rapid intensification period seems to be triggered by the presence of inner rainband activity, often associated with VHT-like structures, outside of the eyewall that produce significant heating and create a secondary updraft outside of the eyewall (Fig. 5.22a,b). However, unlike in the case of an eyewall replacement cycle as in Judt and Chen (2010) the rainbands are not associated with the convective generation of PV outside the eyewall, but some PV is transported into the eye instead. It has been possible to extend the work of Reif et al. (2014), using Lagrangian tracers, by showing that PV increases within the centre of the eye were caused by upward and inward advection of PV from the outer eye region. In contrast to Reif et al. (2014) this increase of PV in the eye was not associated with a pressure drop.

The effect of the secondary heating maximum is to create a balanced secondary circulation above the boundary layer which, in turn, produces a region of convergence just above the boundary layer radially outward from the outflow jet and lowers the PGF within the boundary layer. The reduced PGF results in an increased supergradient flow within the boundary layer which in turn is ventilated by an increased boundary layer outflow jet. The unbalanced spin-up mechanism as described by Smith et al. (2009) allows the wind to become supergradient within the boundary layer. The boundary layer outflow jet causes further weakening by advecting low angular momentum outwards from the eye and increasing the RMW while spinning down the flow above the boundary layer. Without a coherent heating tower the PV structure tends towards a monopole-like state with high PV from the boundary layer transported into the eye (Fig. 5.22d). This could be associated with barotropic instability causing a breakdown of the ring-like PV structure (e.g. Kuo et al., 1999; Williams, 2017).

During the weakening phase the VHT-like structures are less favoured to form which results in a more azimuthally symmetric structure (Fig. 5.22c). When the eyewall reforms at a greater radial distance this symmetric structure is initially maintained (Fig. 5.22e). However, during the strengthening phase the development of these VHT-like structures becomes increasingly favourable (Fig. 5.22a). Most of the time these VHT-like structures are not harmful to the storm's intensification

and can, through the eddy transfer of AAM, contribute to intensification. VHT-like structures that move too far inwards can have a disruptive effect and trigger a weakening phase by decelerating the tangential wind within the eyewall and accelerating it within the eye. These results seem surprising given that Kilroy and Smith (2016) suggest that an updraught in a vortex results in an increased contribution to the tangential wind budget outside of the updraught and a negative contribution inside the updraught (with more pronounced effects from updraughts further from the storm centre). Some, though probably not all, of these VHT-like structures may be related to vortex Rossby wave activity which did occur concurrently with some, but not all, of the VHT-like structures. VHTs often appear in a tropical cyclone's immature phase just prior to rapid intensification such as in Guimond et al. (2010) where their appearance precedes the rapid strengthening and increased azimuthal symmetry of the storm. Although the VHT-like structures in Hurricane Irma do precede a more azimuthally symmetric state of the storm, this is typically during a weakening phase. This suggests that VHT like structures may have different impacts on a mature storm undergoing rapid intensification compared to a much weaker storm that has not yet undergone rapid intensification.

In a study on vacillation cycles Nguyen et al. (2011) described VHT-like structures that appeared to be the result of barotropic and convective instabilities. The VHT-like structures, in Hurricane Irma here, precede the weakening phase and thus seem to be a cause of the instability rather than a symptom of it. Additionally, the mixing of PV described in Nguyen et al. (2011) causes a decrease in MSLP. However, the opposite of this occurs in the weakening phases in our simulations with MSLP increasing or stagnating during weakening phases. Another key difference between prior work on vacillation cycles is the association of azimuthal symmetry with the radial structure. In Nguyen et al. (2011) the azimuthal symmetry is positively correlated with the ring-like PV distribution, whereas here we have found it to be anti-correlated. The reasons for this are uncertain and should be investigated in future work but it may indicate the fluctuations modelled here may be different kinds of intensity fluctuations to those found in Nguyen et al. (2011).

In terms of trying to understand what these fluctuations are, there are similarities

to vacillation cycles particularly with the simulation conducted in Reif et al. (2014) which exhibits transitions from ring-like to monopolar PV distributions but with a more ring-like state than Nguyen et al. (2011). Although one significant difference compared to the vacillation cycles in Hardy et al. (2021) is that the more monopolar state during the weakening phases were transient with PV_0/PV_{\max} peaking at the end of the weakening phase before dropping rapidly. The role of barotropic and convective instability does also seem to play a role; however, the azimuthally asymmetric VHT dominated periods are not explicitly linked to strengthening phases as they are here. Fischer et al. (2020) did identify these fluctuations in the observational data of Hurricane Irma and described them as two separate eyewall replacement cycles triggered by lower-tropospheric convergence associated with a rainband and lower-tropospheric convergence associated with a super-gradient flow respectively. The fluctuations modelled here have some similarities with the second mechanism proposed in Fischer et al. (2020) with the secondary eyewall merging with the primary eyewall before dissipating. The intensity fluctuations modelled here also have some similarities to a ‘partial eyewall replacement cycle’ as described in Zhang et al. (2017) where the boundary layer updraught is unable to properly couple with a potential secondary updraught above. It is proposed that the fluctuations here are the result of the eyewall being temporarily disrupted by VHT-like structures in the inner rainbands and the resultant disruption of the coupling between the boundary layer and the free troposphere and the eventual reformation of the coherent eyewall structure. Unlike an eyewall replacement cycle there is no clear secondary eyewall formation event.

This study focuses on a single case study in Hurricane Irma (2017) so it is unclear how common this type of intensity fluctuations are in tropical cyclones. The ensemble forecasts showed no link between the likelihood of the intensity fluctuations and the environmental conditions so the causes of the fluctuations are likely stochastic in nature (in particular with respect to the radial location of VHT-like convective structures that develop). The fluctuations are shown to occur in around a third of the ensemble forecast members suggesting they may be a common feature in rapid intensification and motivating analysis of more cases.

5.5 Summary and conclusions

The main aim of this study was to determine the cause of the observed intensity fluctuations in Hurricane Irma (2017), during rapid intensification, and to identify the processes responsible. Understanding these fluctuations is important as they can affect both the intensity and size of the RMW in the short term and therefore the destructive potential of the TC. Key and novel results include the finding that intensity fluctuations are related to convective and barotropic structural changes with the asymmetric convection playing a key role in the fluctuations. Both unbalanced and balanced intensification processes were important with the balanced effect of inner rainband convection leading to an unbalanced boundary layer response which, in turn, caused a spin-down during weakening phases. Key findings from this analysis include the following:

- In Hurricane Irma, during the second period of rapid intensification, intensity fluctuations occurred, which caused short term intensification and weakening periods, although overall the storm continued to intensify.
- During strengthening phases the PV distribution was an elongated ring which became more azimuthally symmetric and monopole-like during weakening phases. Note that the azimuthal symmetry is independent of the radial PV distribution and the ring-like PV states (strengthening phases) were associated with less azimuthally symmetric distributions.
- During strengthening phases, the diabatic heating distribution had a smaller radial extent and a stronger heating maximum which is located within the RMW. During weakening phases the heating was outside the RMW and had a greater radial extent.
- VHT-like structures were stronger and more common during strengthening phases than weakening phases and contributed positively to intensification through eddy advection of angular momentum.
- Unbalanced dynamics were shown to play a role in the intensity fluctuations. During the weakening phases an unbalanced supergradient tangential flow

produced an outflow jet which acted to spin-down the flow above the boundary layer by transferring low angular momentum from the eye outwards.

In conclusion, the findings from this analysis, as summarized in Fig. 5.22, show the proposed mechanism for the intensity fluctuations observed in Hurricane Irma, and highlight the importance of both the VHT-like structures that develop on the intersection of inner rainbands with the eye-wall and of the development of the supergradient wind within the boundary layer. It was found that these intensity fluctuations appear in about 1/3 of the ensemble simulations. No link was found between the environment of the storms and the presence of these intensity fluctuations indicating they are governed by stochastic processes. In addition, the intensity of the storms at the end of the simulations with intensity fluctuations were similar to those without, indicating that the increased intensification rates during strengthening phases compensated for the weakening phases. This study gives potentially further insight to intensity fluctuations during rapid intensification, such as the vacillation cycles in Nguyen et al. (2011), and emphasises the role of the inner rainbands in causing weakening periods. It also offers an explanation to the observed intensity fluctuations in Hurricane Irma observed in Fischer et al. (2020). A future direction of this work would be to investigate the similarities between these fluctuations in rapid intensification and eyewall replacement cycles and whether they are caused by similar processes and to look at more cases to see to what extent these results can be generalized for rapid intensification.

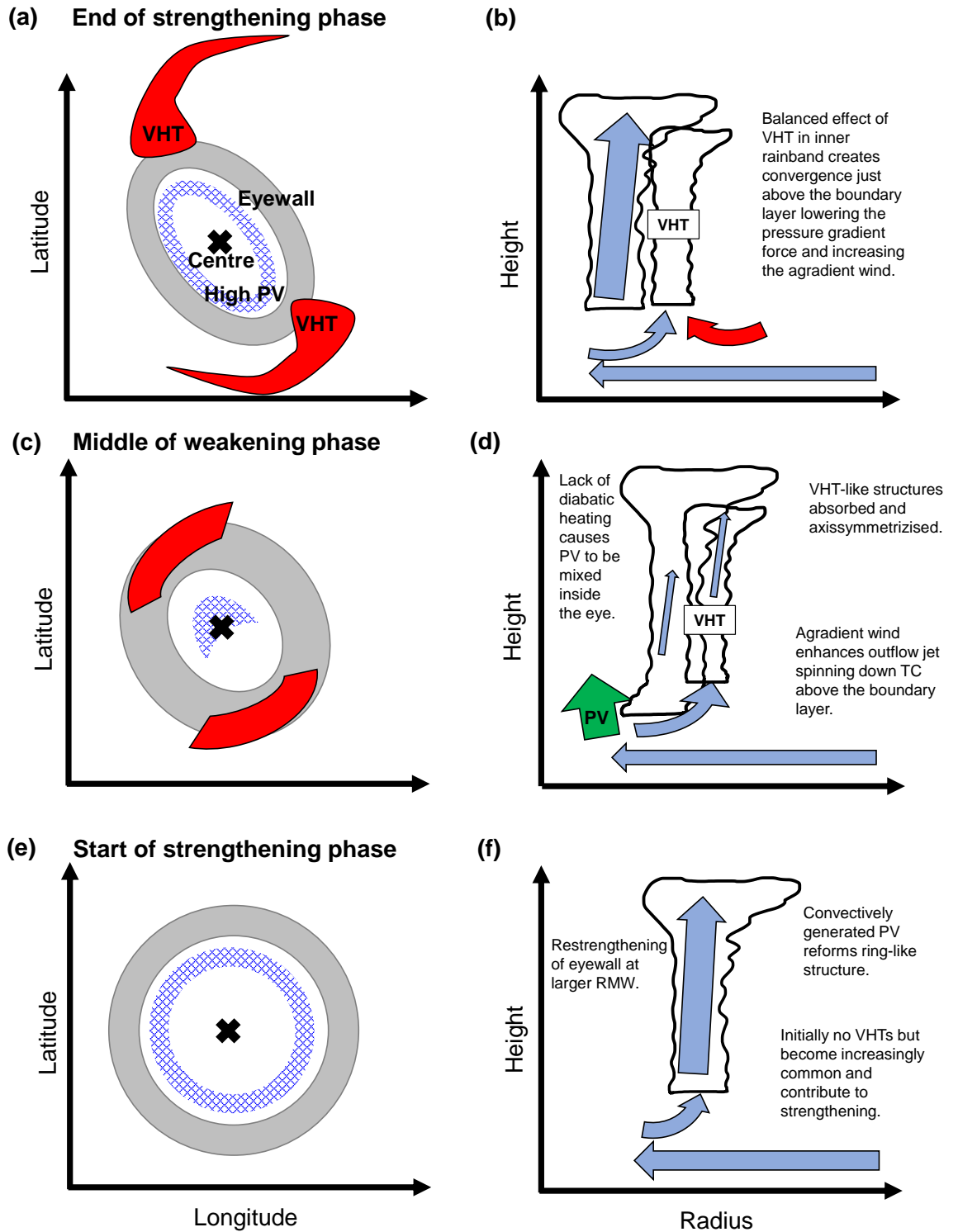


Figure 5.22: Schematic outlining the proposed mechanism for the fluctuations modelled during the rapid intensification of Hurricane Irma during: (a,b) the end of a strengthening phase, (c,d) the middle of a weakening phase and (e,f) the start of the strengthening phase. Left column shows the horizontal structure of the storm including VHT-like structures (red), eyewall convection (grey) and regions of high PV (blue hatched). Right column shows the azimuthally averaged structure of the storm at each stage with arrows indicating the direction of the secondary circulation (larger arrows imply stronger flow). A red arrow in panel b indicates that the inflow is a balanced response to the VHT-like structure. A green arrow in d shows the direction of transport of high PV. In (b,d) ~~the~~ VHT-like structure is indicated by a 2nd cloud outside of the eyewall.

Chapter 6

Intensity fluctuations: Balanced dynamics

6.1 Introduction

The use of a balanced model (in this case solving the SE equation) as a diagnostic tool has been extensive. Hendricks et al. (2004) used a balanced model to diagnose the balanced contribution of VHTs to tropical cyclogenesis. The ability for the balanced model to reproduce accurately the secondary circulation was taken as evidence that the hydrostatic and gradient balance were suitable approximations to describe tropical cyclogenesis. Given the SE equation is a linear partial differential equation (Ohno and Satoh, 2015) it is also possible to decompose the forcing heating functions given by Q and \dot{V} in equation 2.3 and analyse the contribution of each component individually. An example of the decomposition is given below:

$$\begin{aligned}\dot{V} &= -\overline{u'\zeta'} - \overline{w'\frac{\partial v'}{\partial z}} + F, \\ Q &= \dot{\theta} - \overline{u'\frac{\partial \theta'}{\partial r}} - \overline{w'\frac{\partial \theta'}{\partial z}},\end{aligned}\tag{6.1}$$

where $-\overline{u'\zeta'} - \overline{w'\frac{\partial v'}{\partial z}}$ represent sources of AAM from the eddies, F is friction, $\dot{\theta}$ is the total diabatic heating, and $-\overline{u'\frac{\partial \theta'}{\partial r}} - \overline{w'\frac{\partial \theta'}{\partial z}}$ represent eddy heat sources. Montgomery et al. (2006) used a similar decomposition to show that the total diabatic heating term dominates in the case of an intensifying tropical depression. It is also

possible to further decompose the diabatic heating $\dot{\theta}$ into heating from individual parametrizations to assess their individual contribution to the balanced response as is done in Ohno and Satoh (2015). Alternatively one can diagnose the balanced response from disparate parts of the TC such as the eyewall or rainbands as in Wang and Wang (2013).

The most important forcing after diabatic heating is friction, F . The addition of friction, near the surface, as an angular momentum sink induces an inflow as a balanced response with a weaker returning outflow above. By including friction as an angular momentum sink the solution to the SE equation will have a boundary layer where the inflow is stronger than it otherwise would be in the absence of friction. It is important to recognize that this is a balanced boundary layer which is conceptually unrealistic and leads to imperfect characterization of the inflow (Smith and Montgomery, 2008). Additionally, the effects of the unbalanced response on the primary circulation can be diagnosed by finding the residual from subtracting the overall tangential wind tendency from the balanced response as in Persing et al. (2002). It is also possible to make use of equation 2.6 to run the SE balanced model prognostically as done in Smith et al. (2018) which allows an idealized TC to be simulated governed only by strict balance dynamics.

A SE approach has been used before for diagnosing intensity fluctuations, specifically the case of eyewall replacement cycles. An example of this is in Zhu and Zhu (2014) who were able to isolate the balanced contributions from the outer-rainband and inner eyewall and were able to show that the balanced contribution from the outer-rainbands was important in initiating the secondary eyewall replacement. Another type of intensity fluctuation, the diurnal cycle, was analysed using a SE which was modified to allow for periodic heating in, Navarro et al. (2017). They were able to show that diurnal fluctuations in the intensity of the storm could be explained by balanced responses to heating in the upper and lower troposphere. Despite this, there has not yet been a SE analysis of vacillation cycles or similar fluctuations occurring during RI to determine the extent to which balanced dynamics play a role in causing them.

The aim of this chapter is to understand the intensity fluctuations in Hurricane Irma

(2017) through the framework of balanced dynamics. By solving the SE equation and comparing the results with the MetUM output during the weakening phase (see Chapter 5) the balanced response of the AAM and heating sources on the secondary circulation can be isolated and their effect on accelerating the tangential wind can be determined. This analysis will allow the following questions to be answered: (i) To what extent can the intensity fluctuations be explained by balanced dynamics? (ii) If balanced dynamics play a role, which balanced processes cause the intensity fluctuations? By running prognostic simulations it is possible to learn whether or not the intensity fluctuations can be replicated where only the prescribed diabatic heating distribution affects the intensity of the TC. It is often difficult to understand what dynamical processes contribute to phenomena like these intensity fluctuations because there are so many variables involved. By stripping down TCs to their essentials it becomes possible to effectively establish a causal link between balanced processes and their impact on TC intensification.

The chapter is organised in the following way: Section 6.2 describes the SE balanced model including its regularization. Section 6.3.1 compares the features of the secondary circulation from the MetUM output to the output from the SE solutions before and during the first weakening phase (W1). Section 6.3.2 analyses the effects of the individual components of the heating and AAM forcings given in equation 6.1 on the secondary circulation during the course of W1. The effect of these forcings on the primary circulation is analysed in section 6.3.3. A prognostic balanced SE simulation is conducted in section 6.3.4 with the aim of determining whether a purely balanced setup is capable of creating intensity fluctuations. Section 6.4 brings together the results and explains the extent to which, if any, the intensity fluctuations are caused by balanced processes and which of these processes are most important. Conclusions are given in section 6.5.

6.2 Methodology

6.2.1 Balanced Model

The script used to solve the SE equation uses the code in Smith et al. (2015) with some modifications to the regularization (described in section 6.2.2) as well as allowing for AAM sources (the form of the SE equation as in 2.3) and prognostic runs. The fields used to run the model are the density, tangential wind and forcings Q and \dot{V} which are imported from the MetUM. The density is calculated using the ideal gas equation, the tangential velocity is directly outputted. The total diabatic heating, $\dot{\theta}$, is calculated from the sum of diabatic heating terms in the Eulerian potential temperature budget. The eddy heating terms and the eddy angular momentum sources are calculated as in equation 6.1. The friction term is calculated following the method detailed in Persing et al. (2013) and is given below,

$$F = \frac{RT}{pv} \left(v_x \frac{\partial \tau_{xz}}{\partial z} + v_y \frac{\partial \tau_{yz}}{\partial z} \right), \quad (6.2)$$

where p is the pressure, R is the ideal gas constant, T is the temperature, v_x and v_y are the longitudinal and latitudinal components of the tangential wind vector, τ_{xz} and τ_{yz} are the vertical longitudinal and vertical latitudinal components of the shear stress tensor. Note, F only includes the vertical component of subgrid-scale diffusive tendency. However, the radial component is more than an order of magnitude smaller and negligible by comparison. It was found that the frictional sink in the model was unrealistic possibly due to the Courant–Friedrichs–Lewy (CFL) criterion being violated for high wind speeds in the boundary layer ($v_x \frac{\Delta t}{\Delta x} + v_y \frac{\Delta t}{\Delta x} \approx 0.8$, $w \frac{\Delta t}{\Delta x} \approx 0.45$, CFL ≈ 1.25 at around 500 m) which lead to high frequency noise being output in the shear stress components. As a result the frictional sink had an unrealistic bifurcated appearance which in turn caused a thin layer of outflow within the boundary level. A test run with a smaller time-step was undertaken to determine if this could fix the form of the frictional sink. Unfortunately, the stress tensor output was still noisy and the cause of this phenomenon is so far unknown.

As a result a more idealized form of F was created from the method described in

equation 7 of Smith et al. (2018) given by:

$$\dot{V}(r, z) = C_d |\mathbf{v}(r, 0, t)| v(r, 0, t) \exp \left[-(z/z_0)^2 \right] / H, \quad (6.3)$$

where C_d is the surface drag coefficient, $\mathbf{v}(r, 0, t)$ is the total surface wind speed at time t , z is the height above the surface, z_0 is the vertical scale length for the friction, H is the boundary layer height.

The parameters of this idealized balanced boundary layer were the same, other than the drag coefficient which was set at 0.0024 which is the same as the MetUM for wind speeds above approximately 33 ms^{-1} . Figure 6.1 shows the difference between the idealized and MetUM frictional AAM sinks. The bifurcated (two separate maxima can be seen) boundary layer in the MetUM results in a bifurcation of the balanced inflow especially between 50 km and 100 km (e.g Fig. 6.3b,e). Between these two inflow layers at around 500 m in height there is a weak outflow layer which is also apparent on plots (e.g Fig. 6.3b,e) which include the full forcing functions (eddy AAM sources and heating). The idealized boundary layer by contrast is not bifurcated and is qualitatively similar in structure to the vertical diffusive tendency for a mature TC (for example Fig. 8f in Leighton et al. (2018)). The difference in the balanced response (secondary circulation) from using the idealized frictional boundary layer versus the MetUM frictional AAM sink was found to be small with the main difference being the removal of the bifurcation which justifies using the idealized form of F .

In Smith et al. (2015) a uniform grid spacing of 5 km is used in the radial direction and 100 m in the vertical direction which is also adopted here. The fields from the MetUM are azimuthally averaged and then spline interpolated onto the balanced grid. Savitzky–Golay smoothing (Savitzky and Golay, 1964) is applied in the vertical direction to correct numerical distortion in the upper troposphere where MetUM vertical grid spacing is significantly greater than 100 m. As with Smith et al. (2015) derivatives are calculated using a central differencing method.

The potential temperature and density fields from the MetUM will not be strictly in gradient wind balance. Therefore the method described in Smith (2006) is used

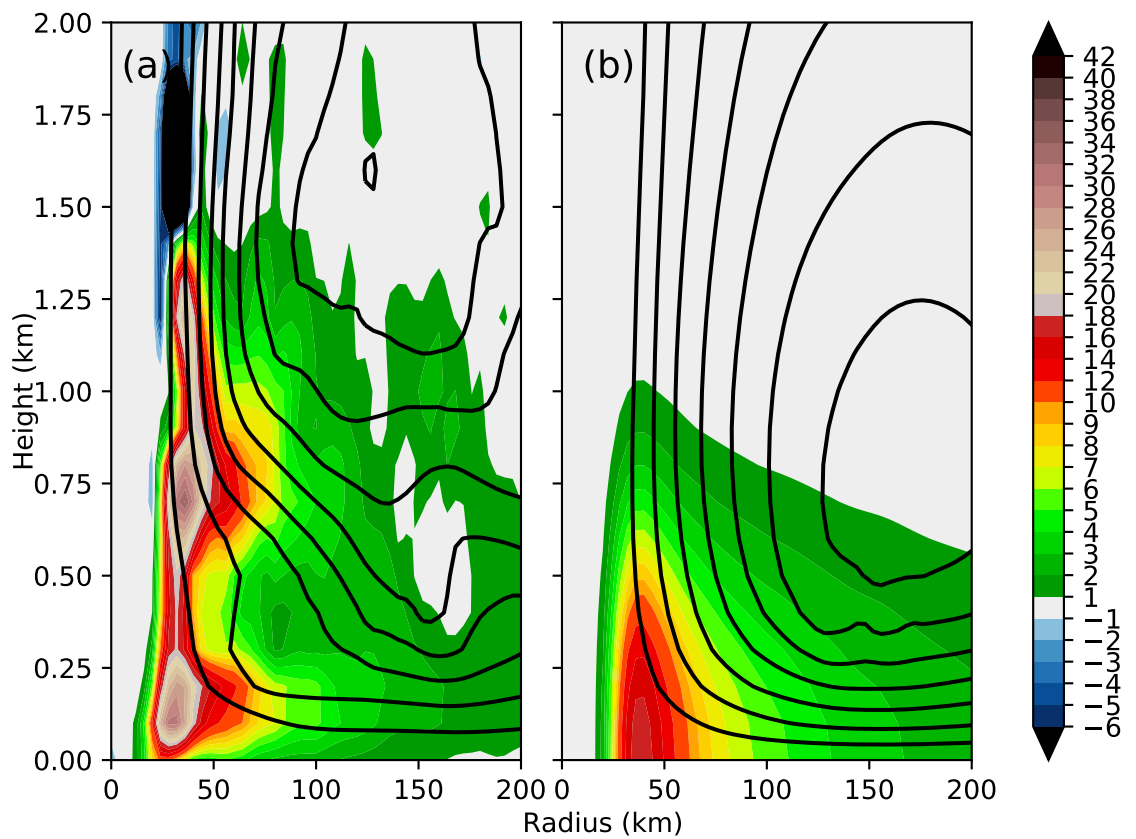


Figure 6.1: Comparison of (a) MetUM frictional AAM sink with (b) idealized mathematical AAM sink. Colour shading shows forcing in $\text{m s}^{-1}\text{h}^{-1}$ while line contours show the streamfunction of the secondary balanced response from this AAM sink only in $10^8 \text{ m}^2 \text{ s}^{-1}$.

to calculate the balanced density and potential temperature fields from the MetUM azimuthal wind field.

The model solves the SE equation using the successive over-relaxation method which involves expressing the partial differential equation as an algebraic difference equation and then iteratively updating the streamfunction until the residual (difference between the left hand side and the right hand side of equation 2.3) becomes smaller than a threshold (in this case $10^{-21} \text{ m s}^{-2}$).

6.2.2 Regularization

The balanced model is only meaningful if the solutions to the SE equation are everywhere elliptic, i.e. the discriminant of equation

$$\Delta = 4AC - B^2 \tag{6.4}$$

is always positive. If Δ is negative, as it often is where there are regions of inertial or static instability or when the baroclinicity is too high, then the balanced response cannot be found. For regions where the SE equation is not elliptic it is necessary to apply small corrections to the parameters A , B and C to ensure Δ is no longer negative, but not such large corrections that the structure of the vortex is fundamentally changed. This process is known as regularization (Wang and Smith, 2019).

There are many different methods of regularization. One of the most common is the method used in Moller and Shapiro (2002) which involves first adjusting C by adding a constant to the entire field such that the minimum global value of C is just above zero. The second step, if needed, requires setting A to a constant where the discriminant is still negative. The final step involves reducing B locally where it is too high. This method, was found by Heng et al. (2017) to produce a less accurate balanced response than their own method which involved changing the absolute vorticity in C locally to a value of one hundredth of the Coriolis parameter to ensure C overall was positive. B was then also lowered locally multiplying any grid points by 0.8 where the discriminant was negative, iteratively until the discriminant was

positive everywhere. Their balanced solution had stronger inflow near the surface which led to quantitatively different results in their tangential wind tendency.

An attempt was made to implement the regularization method in Heng et al. (2017); however, it proved ineffective at removing large non-elliptic regions near the surface largely caused by positive static instability leading A to be negative. The regularization method implemented here is similar to that of Abarca and Montgomery (2014) which is a more aggressive method that notably recalculates $\frac{\partial\theta}{\partial z}$ which helps remove the static instability near the surface. This method was found to be effective in removing nearly all non-elliptical points. It is noteworthy that the hurricane diagnosed in Abarca and Montgomery (2014) is a considerably stronger storm compared to Heng et al. (2017) with more intense diabatic heating of up to 80 K h^{-1} than in most previous studies and the more aggressive regularization method seems to be necessary to produce a convergent solution. Figure 6.2 shows the effectiveness of these three different regularization methods using the MetUM output at T+40 h. The methods of Moller and Shapiro (2002) and Heng et al. (2017) were unable to produce solutions that consistently converge with large unregularized regions in the boundary layer chiefly due to negative values of A that could not be corrected.

An additional modification did need to be made to the input tangential wind data prior to regularization. In the eye region at very small radii large negative values of C caused problems. Although the method of Abarca and Montgomery (2014) was able to produce convergent solutions, the global correction to C using these highly inertially unstable points led to unrealistic solutions with extremely high vertical velocity and extremely low radial velocity. Two solutions to this problem were investigated. Firstly, a variation of the Abarca and Montgomery (2014) method was tested with local corrections to C applying within the eye and global corrections elsewhere. Secondly, smoothing the tangential wind MetUM input field within the eye prior to regularization using a Savitzky-Golay filter (2nd order, window size of 25 points) was also tested. Both methods resulted in almost identical secondary circulations but with the smoothing method producing a slightly stronger inflow at the surface. Due to the arguments given in Heng et al. (2017) suggesting overly aggressive regularization can lead to artificially weak inflow the smoothing method

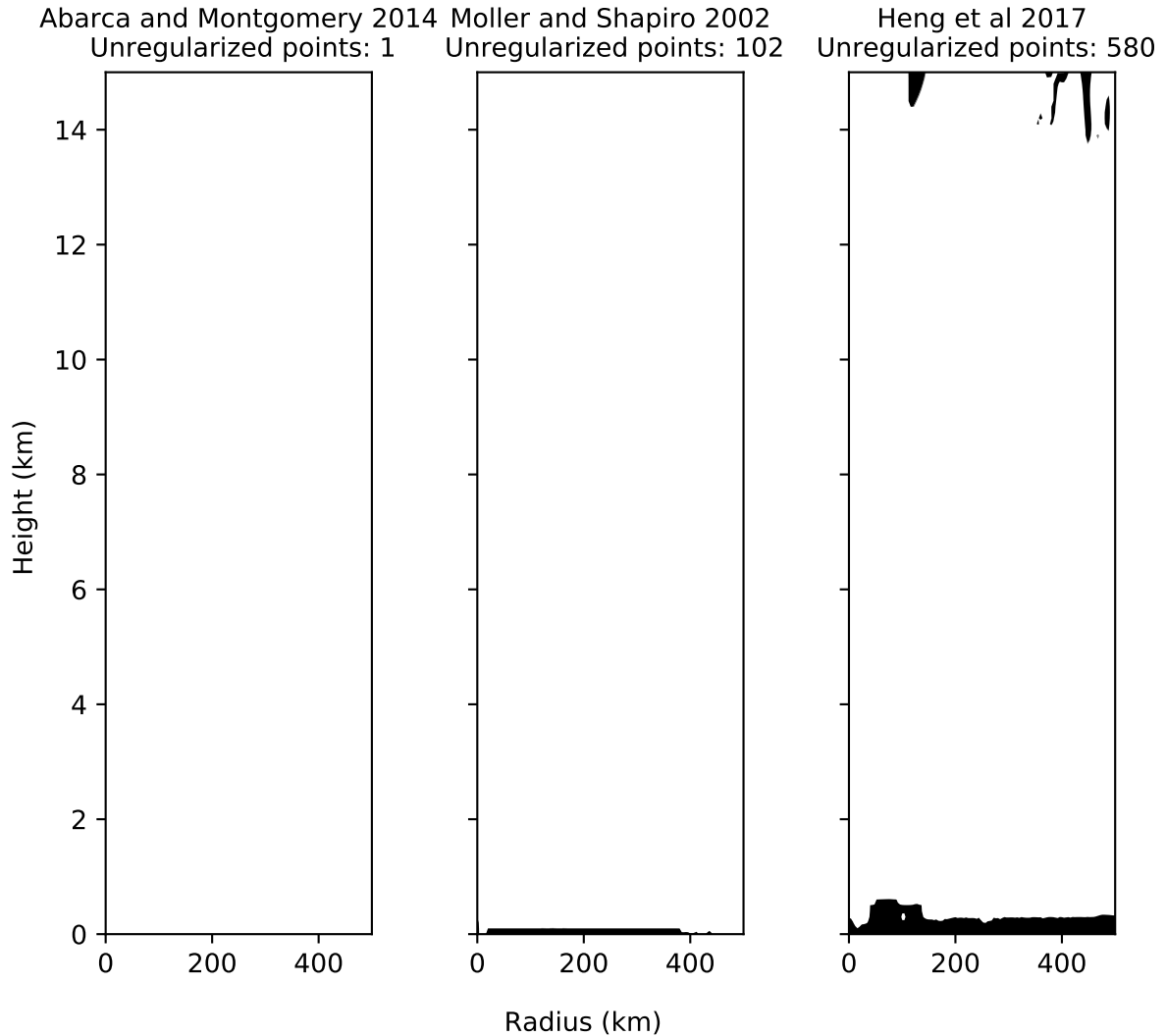


Figure 6.2: Comparison of regularization methods showing non-elliptic regions after regularization in black. White regions have been successfully regularized. Input data from the MetUM from T+40 h.

was therefore chosen.

6.2.3 Prognostic implementation of balanced model

As described in Smith et al. (2018) the SE equation can be run prognostically by making use of equation 2.6 to advance the tangential wind field. At each time step the forcing functions are still prescribed from the MetUM. In the case of running the balanced model prognostically a timestep of 1 minute (dt in equation 2.6) was chosen. The forcing functions were calculated from the MetUM 10-minute output as described in section 6.2.1 and linearly interpolated to account for the smaller than

10-minute timestep in the balanced model. The idealized form of the frictional forcing, F , was used rather than the one in equation 6.2 to prevent the potentially aberrant outflow occurring at a thin layer at 500 m.

Running the prognostic model proved to be challenging and highly sensitive to the initial tangential velocity. Because of this an initial tangential velocity that leads to long lasting stable solutions with few unregularized points was prioritized. In particular after an initial spin-up period where the AAM structure of the vortex would change rather rapidly it was assumed that AAM surfaces would become more aligned with the secondary circulation (i.e. the streamfunction contours are nearly parallel to the AAM contours) dv/dt would stay small and consistently positive and there would not be huge, local, very large positive and negative unrealistic regions of dv/dt .

A few modifications had to be made during the course of the simulation to ensure a long lasting stable evolution of the vortex. One of these is the appearance of high frequency noise that self amplified over time. The high frequency noise was mitigated completely by applying Savitzky–Golay smoothing in both the radial and vertical directions for the tangential wind field after each timestep. This smoothing had a negligible impact on the appearance of the wind field at any given time but did prevent the high frequency noise from appearing over many timesteps.

It was also found that high radial gradients in tangential velocity near the vortex centre lead to unrealistic, unstable and eventually divergent behaviour. High radial tangential velocity gradients near the centre of the TC were associated with more unregularized points, although this was not necessarily the cause of the divergence. As a result it was necessary to keep radial gradients in tangential velocity within the inner eye low. This was achieved in two ways. Firstly, both the initial tangential wind field and all prescribed forcing fields were shifted outwards by 28 km (4 grid points) with the innermost gridpoints taking a value of zero for the forcing function and the radially constant innermost initial value for the tangential wind field. This value was chosen to be as small as possible while still yielding stable solutions. Secondly, a ‘buffer’ function was used to prevent radial gradients in tangential velocity from appearing during the simulation. The velocity field was updated as

follows:

$$v_{t+1} = v_t + B(r) \frac{dv}{dt} \Delta t$$

$$B(r) = \begin{cases} \frac{1}{1 + \left(\frac{r/r_b}{1 - r/r_b}\right)^{-3}} & r < r_b \\ 1 & r > r_b \end{cases}, \quad (6.5)$$

where v_{t+1} is the updated tangential velocity, v_t is the current tangential wind, dv/dt is the balanced tangential wind tendency, Δt is the timestep (in this case one minute). $B(r)$ is the buffer function which is defined in terms of a threshold radius r_b where $B(r)$ is 1 above this radius. The mathematical form of $B(r)$ is arbitrary but was chosen as a smooth ‘S’ shaped curve (increasing from 0 in the centre and 1 at the boundary) to keep tangential velocity gradients near the centre as low as possible and to prevent artificially high gradients also occurring near the boundary. A value of r_b was chosen to be 20 km.

The combination of shifting the tangential wind field and forcing functions outwards and preventing any increase in the tangential wind field very close to the centre is effective at preventing unstable solutions. The key radial features of the MetUM forcing functions are also still preserved with the highest tangential wind speeds and heating occurring 50 km away from the buffer region. The buffer region itself is only present to prevent unstable solutions and will not be analysed; however it is not unrealistic for TCs to have very low radial velocity gradients in the centre of the eye. In addition, the Savitzky–Golay radial smoothing was not performed in the buffer region to prevent the tangential wind field from increasing.

A final correction is to forbid the tangential wind speed to update to below zero. This is particularly important in simulations involving friction which can sometimes create negative AAM layers at the surface. Negative tangential wind velocities are also associated with instability in the simulation.

It is important to note the shifting outwards of the eyewall, and other corrections, were only done for the prognostic simulations not the diagnostic analysis which did not require a stable secondary and primary circulation over a large number

of timesteps. It is true that the fundamental structure of the storm is changed by these corrections; however, this can be justified because the purpose of the prognostic simulations is not to analyse the specific case of Hurricane Irma (as it is for the diagnostic results) but to investigate whether or not any intense vortex experiences intensity fluctuations when allowed to evolve under balanced dynamics when the heating occurs outside the RMW. The size of the eye and lack of tangential acceleration within the centre of the eye are not unreasonable when compared to a generic intense TC (e.g. Weatherford and Gray, 1988).

6.3 Results

6.3.1 Secondary circulation

The secondary circulation at 40 h prior to the intensity fluctuations and at 45 h at the start of weakening phase W1 can be seen in Fig. 6.3. The balanced model is capable of qualitatively representing key features of the secondary circulation. The main deviation occurs in the boundary layer. The inflow near the surface is distinctly underestimated in the balanced model compared to the MetUM with a typical surface inflow in the MetUM of around 25 m s^{-1} at around 50 km at the surface compared to 10 m s^{-1} in the balanced model indicating that the balanced response is responsible for around half of the near surface inflow. The inflow layer in the balanced model extends to the mid troposphere with no obvious demarcation between the boundary layer inflow and the free vortex inflow as in the MetUM. This is due to the lack of outward gradient force just above the boundary layer and its associated outflow. The boundary layer itself has a similar structure in the balanced model with MetUM diagnostic friction (Fig. 6.3b,e) compared to the idealized friction (Fig. 6.3c,f) other than in a narrow layer at around 500m (the reasons for which are explained in section 6.2.1), indicating that the balanced response is not highly sensitive to the formulation of the boundary layer.

Although the balanced model is unable to capture the outflow jet above the boundary layer outside of the RMW, just inside the RMW at around 30 km radius and 1500 m height the outflow is well represented with the MetUM producing an outflow

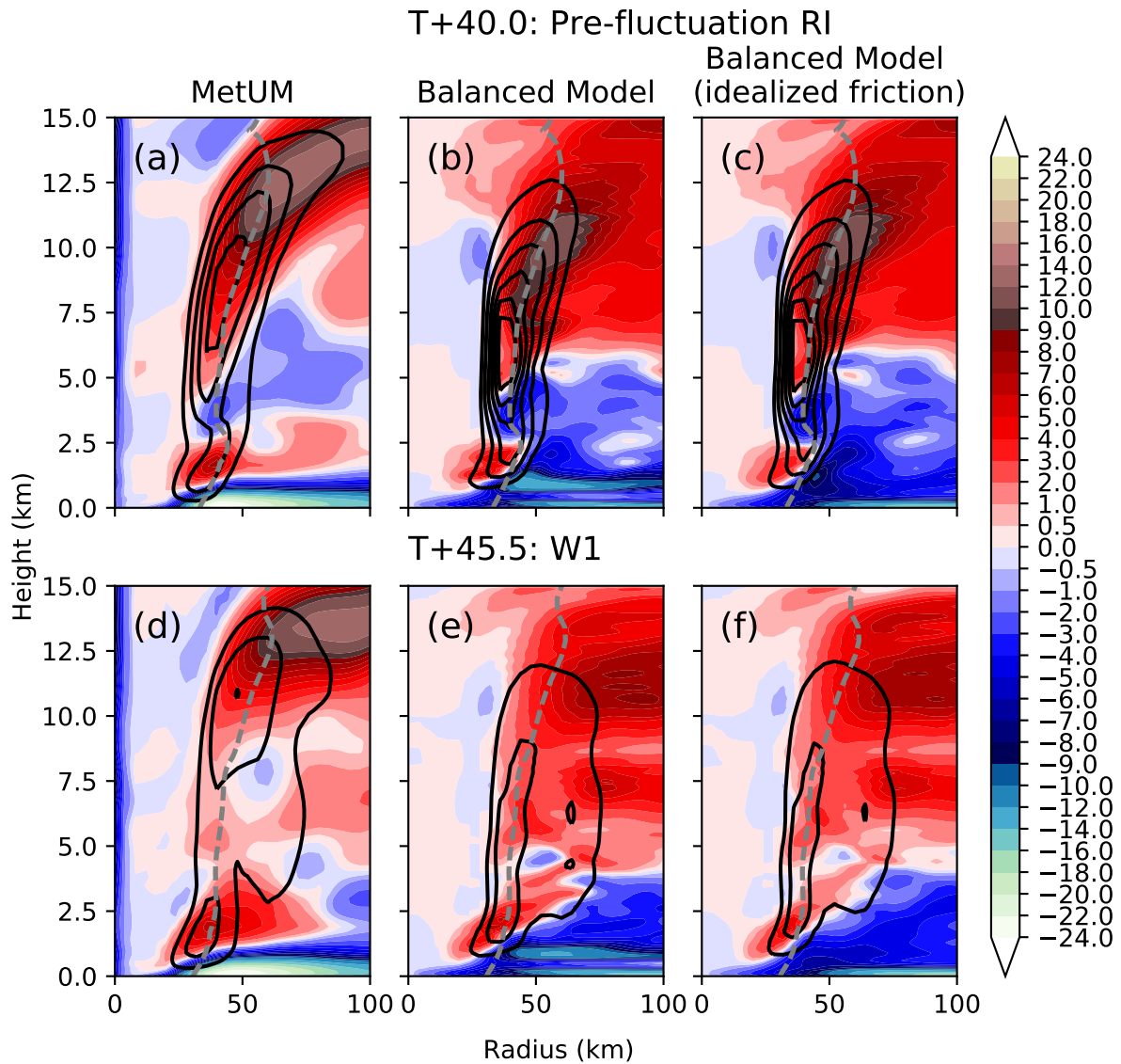


Figure 6.3: Radial wind (m s^{-1} shading) and vertical velocity (0.5 m s^{-1} , contours) from the MetUM (left column) and the balanced model (middle column, with original MetUM F , and right column, with idealized F). RMW is indicated with the dotted grey line. Top row shows results at T+40 h, bottom row shows T+45.5 h.

of around 8 m s^{-1} compared to around 5 m s^{-1} at the same radius and height. While the weaker outflow outside the RMW is an unbalanced response to a supergradient tangential wind, the frictional AAM sink is still responsible for the most of the outflow inside the RMW.

Another difference is in the vertical velocity. The balanced model produces a slightly more intense but also shallower updraught with weaker vertical velocities both near the surface and at the top of the troposphere. This behaviour can be explained by noting that the weaker balanced inflow results in a smaller mass convergence in the boundary layer compared to the stronger unbalanced inflow and therefore a deeper updraught is necessary to ventilate the converged mass. The conservation of mass requires that a stronger inflow leads to a stronger upper tropospheric outflow and thus stronger vertical ascent. Additionally, the secondary maximum in the vertical velocity at around 1500 m (a near permanent feature across the entire simulation) is not present in the balanced model which is likely a consequence of a more direct secondary circulation between 2 and 4 km height without the unbalanced outflow above the boundary layer.

Figure 6.3d–f displays the balanced output shortly after the start of the weakening phase. Comparing Fig. 6.3a–c to Fig. 6.3d–f shows that the balanced model is able to capture some key features of the secondary circulation near the start of the weakening phase.

It is notable that the secondary heating maximum associated with the inner rainbands produces a region of vertical velocity outside of the primary updraught at around 60 km as it does for the MetUM. Additionally, the main outflow in the mid and upper troposphere is split in the balanced model with a peak at around 7 km height at a radius around 75 km in addition to the main upper tropospheric outflow above 10 km as it is in the MetUM. It is also apparent that the change in the structure of the outflow jet above the boundary layer is partly caused by a balanced response to this heating structure, with outflow now being shown outside the RMW at around 3 km height and 50 km radius. However, the balanced model completely fails to capture the updraught peak at the top of the boundary layer and the peak in the upper troposphere. The split vertical velocity structure occurring at the start

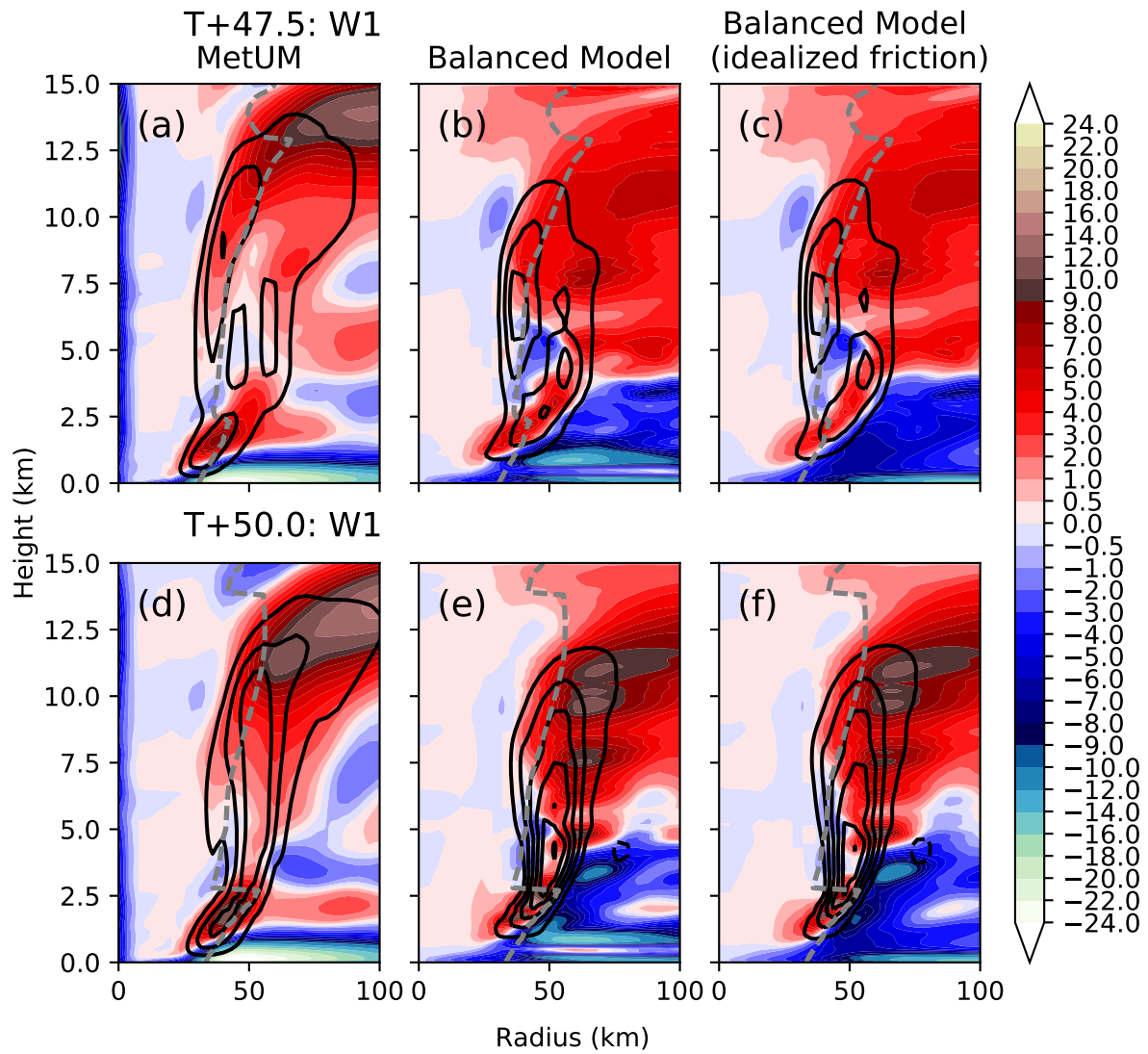


Figure 6.4: As Fig. 6.3, but with top row showing results at T+47.5 h, bottom row showing T+50 h.

of the weakening phase is, therefore, very likely an unbalanced effect.

Figure 6.4 a–c shows the balanced output at T+47.5 h in the middle of the weakening phase. The balanced model is able to capture the two separate updrafts associated with residual heating in the eyewall and the inner rain-band heating, although the vertical velocity maximum at the top of the boundary layer is not captured. The intensification of the outflow jet above the boundary layer is also captured, although the outflow at larger radii is still a mostly unbalanced effect. Another feature the balanced model is able to capture is the inflow into the eye within the region of weaker vertical velocity between the two maxima.

The balanced output near the end of the weakening phase is shown in Fig. 6.4d–f. This is the point in the weakening phase where the convection, after having weakened and split into two updrafts, has reformed into a single coherent column of vertical velocity. The salient features of the secondary circulation are still well captured. Weak outflow is evident in the balanced model above the boundary layer near 90 km radius showing the expansion of the outflow jet towards the end of the weakening phase is still a partially balanced effect. The outflow maxima seen at around 90 km radius and 5 km height in Fig. 6.3 d–f and Fig. 6.4a–c associated with the balanced response of the inner rain-band heating have disappeared.

6.3.2 Secondary circulation budget

It is possible to separate the contributions of each forcing to the balanced response to ascertain what effect each component has in accordance with equation 6.1. The components are the diabatic heating, eddy heating, eddy AAM source and frictional AAM sink.

Figures 6.5 and 6.6 show the components prior to W1 and near the end of W1. Throughout the simulation the diabatic heating dominates the balanced response. However, with the exception of the eddy heating which only seems to slightly enhance the secondary circulation associated with heating outside of the RMW, all of the other components do seem to play important roles during the prior RI and during the intensity fluctuations.

The frictional AAM sink (Fig. 6.5c) has a positive contribution to the outflow above the boundary layer (at the RMW at about 1500 m). However, it is typically only about half as strong as the balanced inflow from the diabatic heating induced inflow above the boundary layer. The ability of the TC to ventilate mass converged in the boundary layer has been described as a key requirement for intensification (e.g. Smith et al., 2017). The effect of friction on the secondary circulation is twofold. Firstly, the friction weakens the balanced induced inflow above the boundary layer at large radii. Fig. 6.5c shows that the friction induces an outflow at around 100 km radius and 3 km height where the balanced inflow is in Fig. 6.3a. Secondly, the friction plays an ever increasing role during W1 in its contribution to the outflow near the RMW just above the boundary layer and contributing to the eyewall updraught by as much as 1 m s^{-1} . The frictional contribution to the eyewall updraught may partly be explained by a change in the tangential surface wind, especially a spin-up outside of the RMW leading to a strengthened outflow. However, given that the mathematical idealized boundary layer shows a smaller and more subtle change, most of this is due to changes to the boundary layer during W1. Strictly speaking, some of these changes may be related to unbalanced processes occurring within the boundary layer changing the nature of the AAM sink. Therefore, the boundary layer formulation does play a partial role in the balanced response.

The eddy response (Fig. 6.5d) is somewhat chaotic with bands of inflow and outflow appearing at most levels. One semi-permanent feature which can be seen in Fig. 6.5d is the enhancement of the inflow within the boundary layer and outflow just above the boundary layer by around $1\text{--}2 \text{ m s}^{-1}$. These features are dependent on the VHT-like activity (small-scale local regions of high vorticity and vertical velocity) with these features almost completely disappearing by T+50 h at the end of the weakening phase (Fig. 6.6d). In effect the eddy AAM source and the frictional AAM sink work in opposite ways with the friction having a proportionally bigger contribution to the boundary layer inflow and outflow at the end of W1 and the eddies having a proportionally larger contribution at the start of W1.

The diabatic heating (Fig. 6.5a) is largely responsible for the vertical ascent in the eyewall as well as the inflow above the boundary layer. By comparing Fig. 6.5a

with 6.6a it can be seen that during the course of the weakening phase a strong region of inflow develops just outside the eyewall at around 60 km radius and 3 km height. The diabatic heating also partially contributes to the enhanced outflow above the boundary layer at the RMW. Together, the diabatic heating is responsible for the region of strong convergence above the boundary layer around the RMW that develops during the weakening phase.

The effect of the unbalanced response can be determined by considering the residual of the secondary circulation budget (which is the difference between the MetUM and total balanced terms). This is shown in Fig. 6.5g and 6.6g. During the course of W1 the unbalanced outflow and inflow become stronger by $2\text{--}4\text{ m s}^{-1}$ with a concomitant rise in the total boundary layer inflow and outflow in Fig. 6.5f and 6.6f vindicating the notion that unbalanced dynamics become increasingly important during the course of the weakening phase.

6.3.3 Balanced effect on the primary circulation

Through the use of equation 2.6 the balanced effect on the primary circulation can be analysed which allows the balanced effects of the various forcing components from equation 6.1 on the tangential wind field to be diagnosed. As described in Abarca and Montgomery (2014) the effect on the tangential circulation is highly sensitive to small changes in the balanced secondary response so only broad qualitative structural changes in the tangential wind tendency can be examined.

The diabatic heating is the largest contributing component to the tangential wind tendency. The heating occurring at a larger radius leads to increased spin-up outside of the RMW during the start of W1 and the weakening of the spin-up inside the RMW (which occurs somewhat prior to W1). Comparing Fig. 6.7a to Fig. 6.8a shows a substantial increase in the spin-up occurring at the end of W1 just outside of the RMW at 1500 m due to increased inflow. Also apparent is the negative tangential wind tendency inside the RMW which increases in magnitude during W1 at the same level.

The eddy heating in Fig. 6.7b and 6.8b is responsible only for weak secondary circulations near the eyewall (Fig. 6.3b - 6.4b) but due to the high concentration of AAM

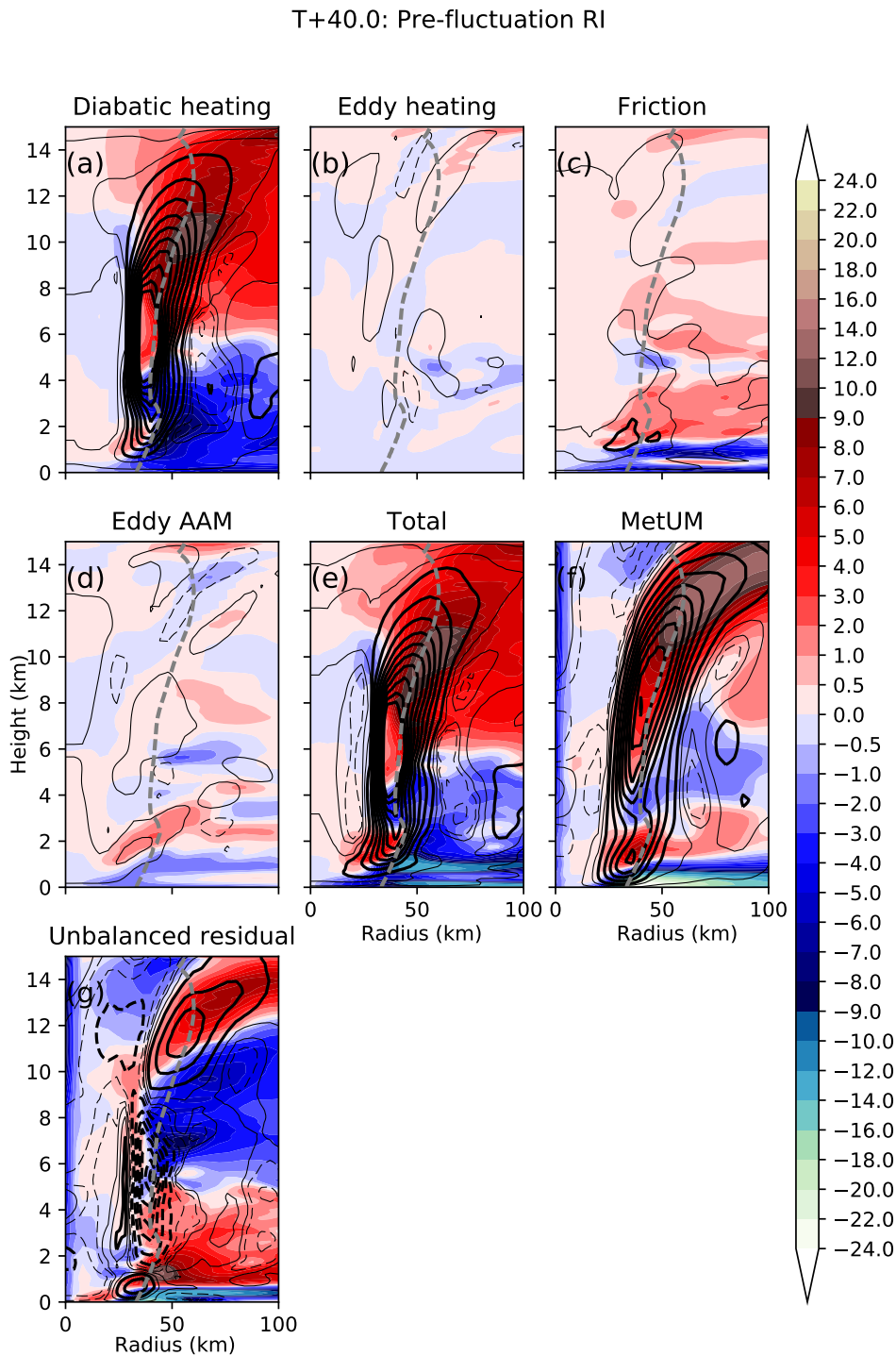


Figure 6.5: Radial wind (ms^{-1} , shading) and vertical velocity (0.5ms^{-1} , thick line contours, 0.025ms^{-1} and 0.125ms^{-1} are also shown as thin line contours. Negative values are shown as dashed contours) from (a) diabatic heating, (b) eddy heating, (c) friction, (d) eddy AAM, (e) sum of all forcings, (f) MetUM secondary circulation, (g) MetUM secondary circulation minus the total balanced response (i.e. the unbalanced residual) for T+40 h.

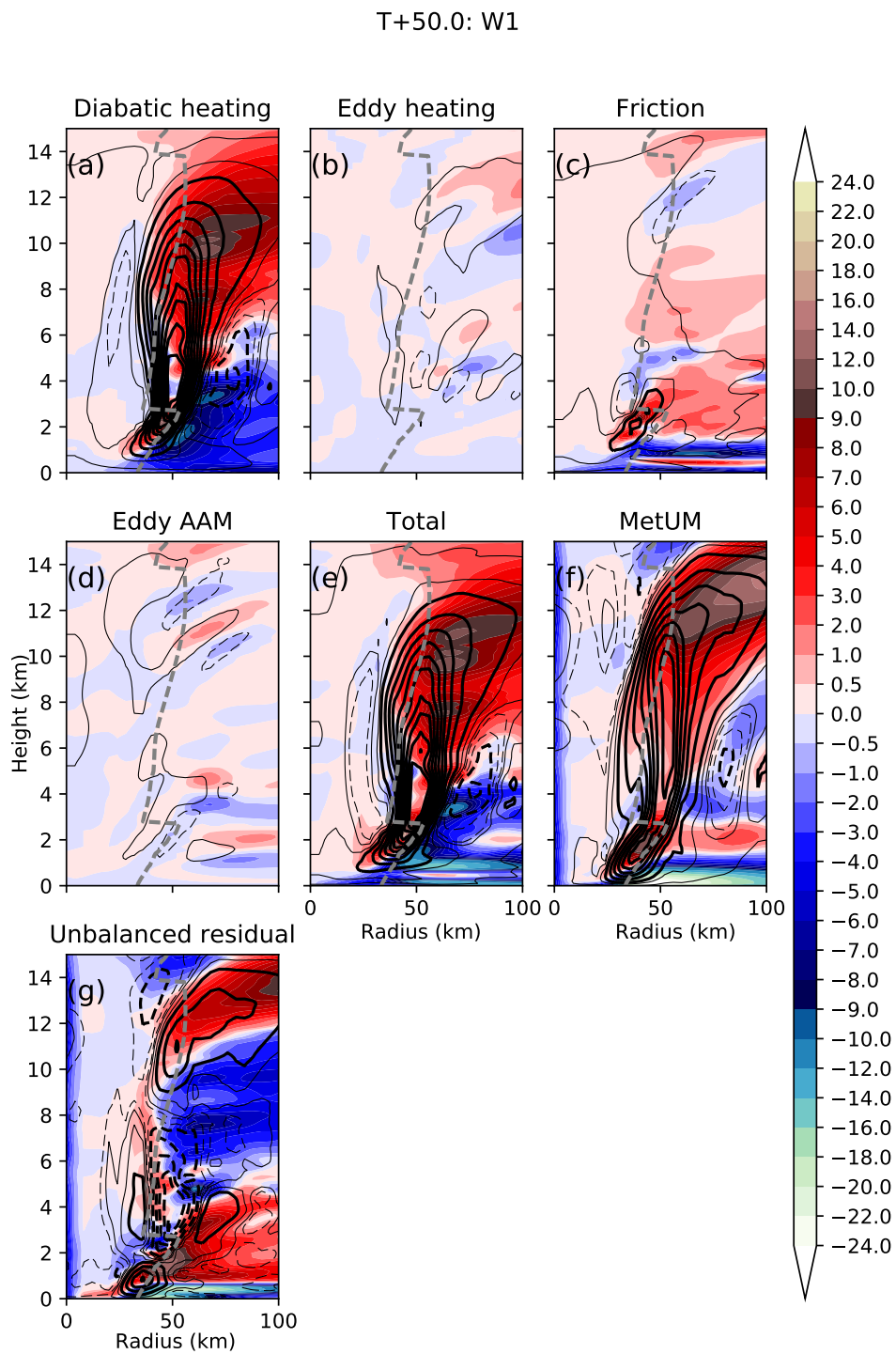


Figure 6.6: As Fig 6.5 but for T+50 h.

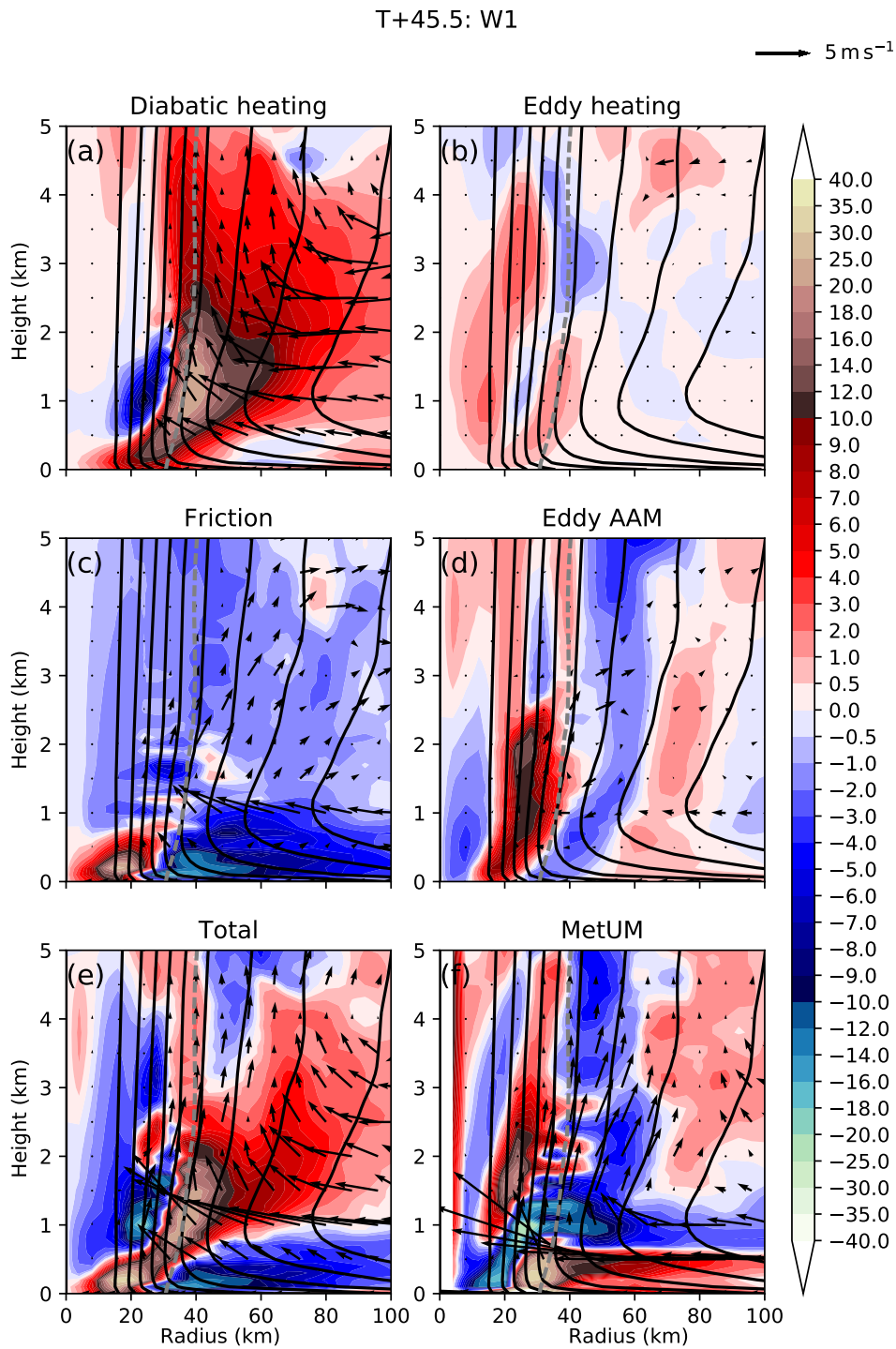


Figure 6.7: Tangential wind tendency ($\text{ms}^{-1} \text{h}^{-1}$, shading), AAM ($4 \times 10^5 \text{m}^2 \text{s}^{-1}$ contours), secondary circulation (arrows) from (a) diabatic heating, (b) eddy heating, (c) friction, (d) eddy AAM, (e) sum of all forcings, and (f) MetUM secondary circulation for T+45.5 h.

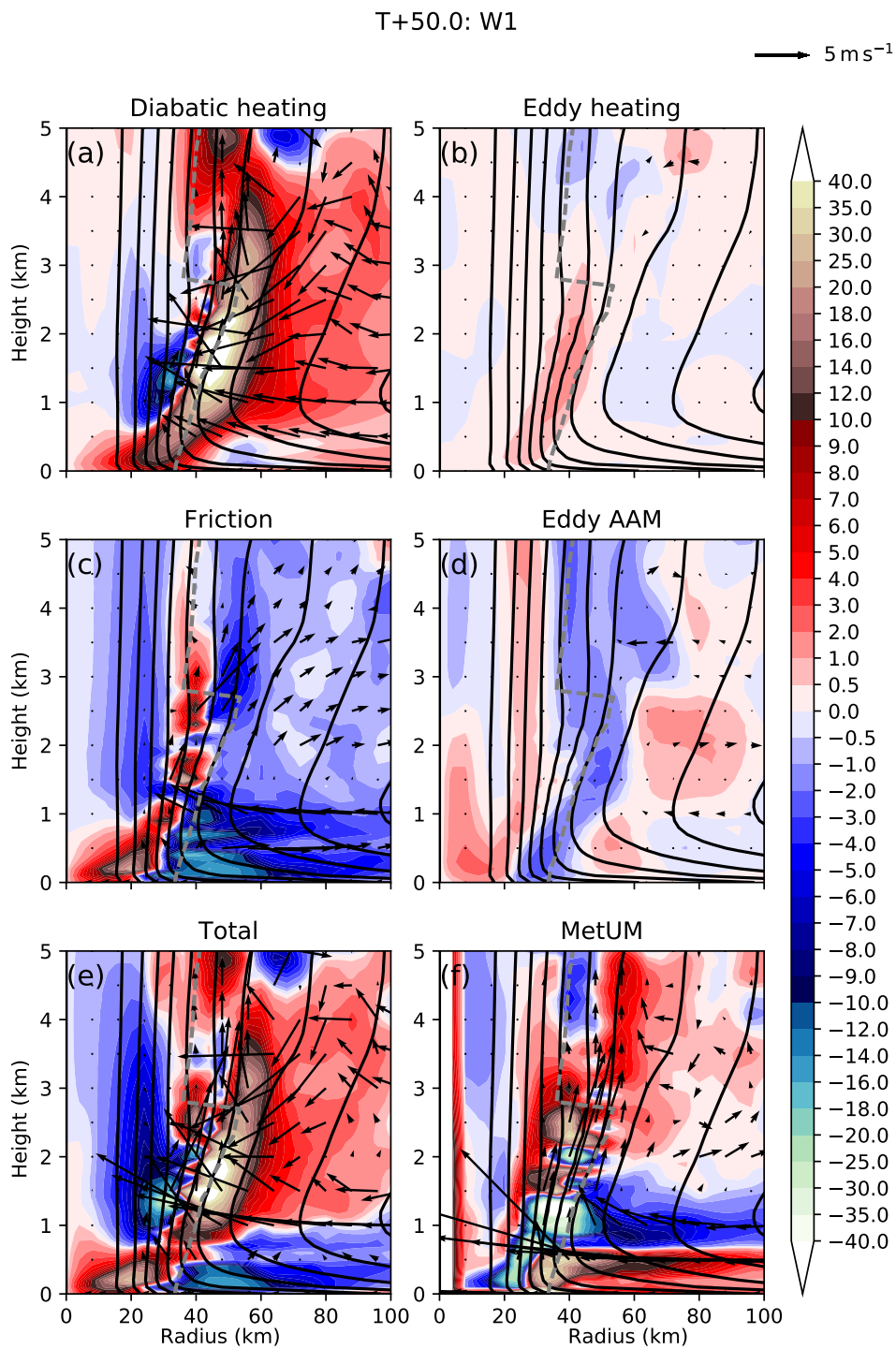


Figure 6.8: As fig. 6.7, but for T+50 h.

surfaces near the eyewall there is always a positive tangential wind tendency of typically $1\text{--}2\text{ m s}^{-1}\text{ h}^{-1}$. VHT activity is linked to slightly stronger tangential wind tendencies particularly inside the eyewall. Therefore, during W1 there is a general weakening of the eddy heating tangential wind tendencies and a restrengthening during S1.

The effect of friction (Figs. 6.7c and 6.8c) is to spin-down the TC outside the RMW. The strong frictionally induced inflow layer near the surface is not strong enough to compensate for the direct frictional loss of AAM. Inside the RMW, however, the weaker inflow is able to increase the AAM where frictional losses from a weaker tangential wind are smaller.

The effect of eddy AAM sources (Figs. 6.7d and 6.8d) is more pronounced at the start of W1 when VHT-like structures were present. Comparing Fig. 6.7d with 6.8d shows that the strong positive and negative tangential wind tendencies near the eyewall are far stronger at the start of W1 when the VHTs are stronger. The radial location of the VHTs does have a big effect on whether they cause a spin-up or spin-down near the eyewall. In some cases they lead to positive contributions to the tangential wind but inward motion of the VHTs can then lead to spin-down. The induced secondary circulations being small does mean, however, that VHTs well outside of the RMW away from the concentrated AAM surfaces have little impact on the primary circulation.

6.3.4 Prognostic runs

Diagnostically analysing the balanced response to heating and AAM sources has many advantages; however, one issue is that a hypothetical ‘balanced’ TC would naturally develop a different absolute AAM structure as it intensifies with the lack of an unbalanced inflow and boundary layer outflow jet. Consequently the diagnostic analysis does not provide a full picture of how a ‘balanced’ TC would naturally evolve under the influences of prescribed heating and AAM forcings and whether some conclusions from the diagnostic analysis simply represent a temporary restructuring of those AAM surfaces. Consequently, it is beneficial to attempt to run a prognostic simulation from an initial tangential wind field and give the TC enough

time to evolve its own AAM structure where the influence of heating regime during W1 can be studied.

The full prognostic simulation which includes the balanced frictional sink and eddy AAM sources is shown in Fig. 6.9. A key finding is that, regardless of any sensible starting wind field, including the balanced frictional AAM sink leads to a significant spin-down within the boundary layer with AAM contours becoming increasingly horizontally orientated over the course of the 6 hours. This implies that the positive tangential wind tendency induced by the balanced inflow response to the frictional AAM sink and the diabatic heating are not enough to compensate for the frictionally induced AAM loss. The initial spin-up seen inside the RMW within the boundary layer in the diagnostic results can be explained as a temporary restructuring of the AAM surfaces where higher AAM advected from the initial wind field temporarily dominates over the frictional loss. The result suggests that for the TC undergoing RI a much stronger unbalanced inflow is necessary to prevent a frictional spin-down of the boundary layer and that a TC with a ‘balanced’ boundary layer would be incapable of spinning up the storm. The spin-down of the boundary layer does not immediately cause the TC to spin-down above the boundary layer. The weakening of the frictional AAM momentum sink due to the spin-down leads to descent just outside of the RMW which prevents the low AAM from being immediately transferred vertically upwards.

To understand the effect of the differing heating distributions alone several simulations were conducted using the same initial wind field but with different initialization times for the forcings as shown in Fig. 6.10. The initial wind field is the same but the forcing from the MetUM varies with the time on the x-axis (at T+40 h for example all the simulations take the MetUM diagnosed forcing at T+40 h as the input forcing term for the balanced SE model). For the first 7 hours of each simulation the evolution of the balanced vortex depends strongly on the run-time. After this 7 hour ‘spin-up’ period the maximum tangential wind speed of each simulation evolves in a similar way, although simulations that have run longer with earlier initialization times still have stronger wind-speeds indicating that after this ‘spin-up’ period the evolution of the vortex is dependant on only the forcing.

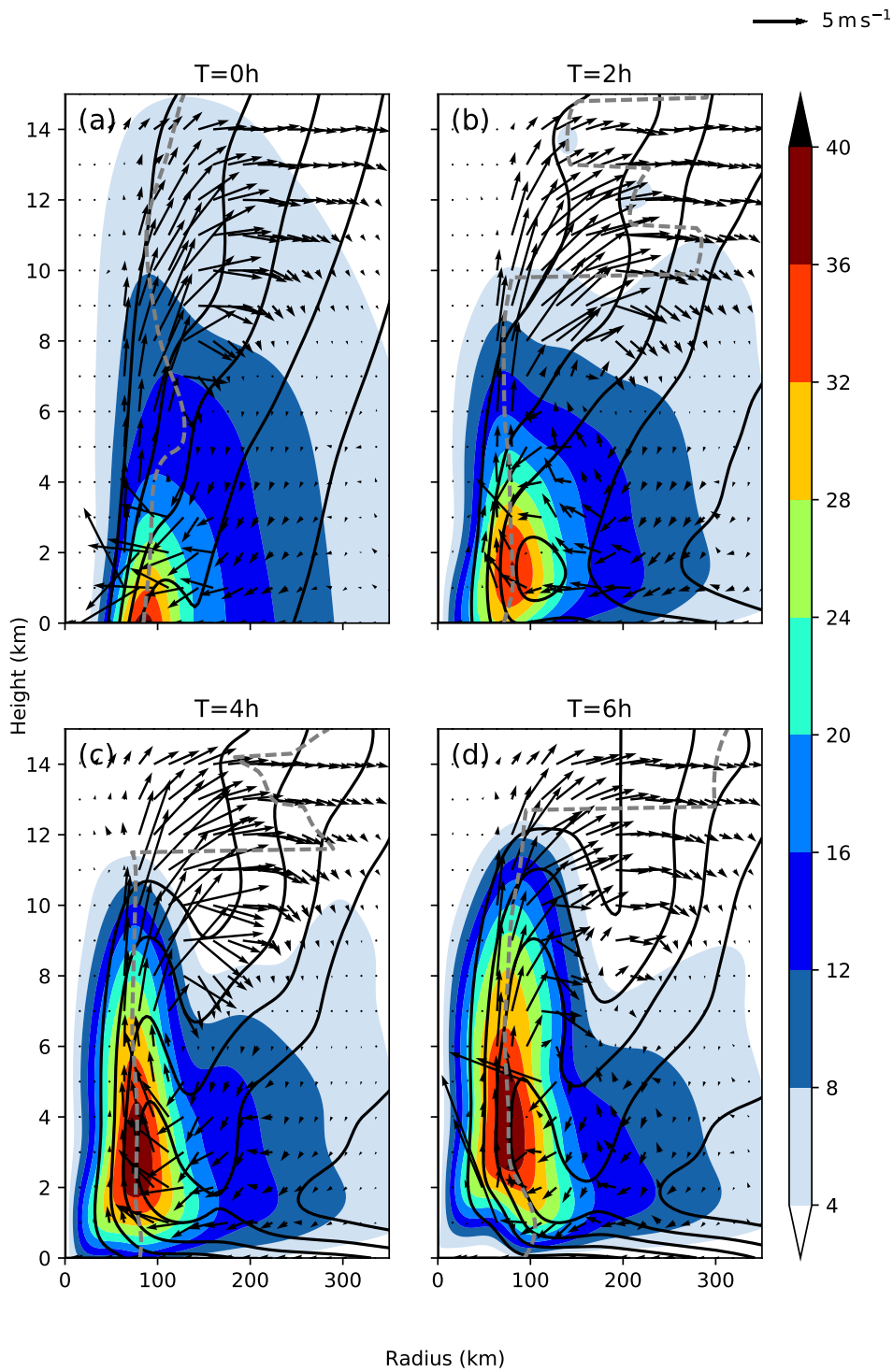


Figure 6.9: Full prognostic simulation with primary circulation (m s^{-1} , shading) and secondary circulation (arrows) with AAM ($8 \times 10^5 \text{ m}^2 \text{ s}^{-1}$, contours) at initialization and subsequent 2 hour periods. Also shown is the RMW (dashed grey line).

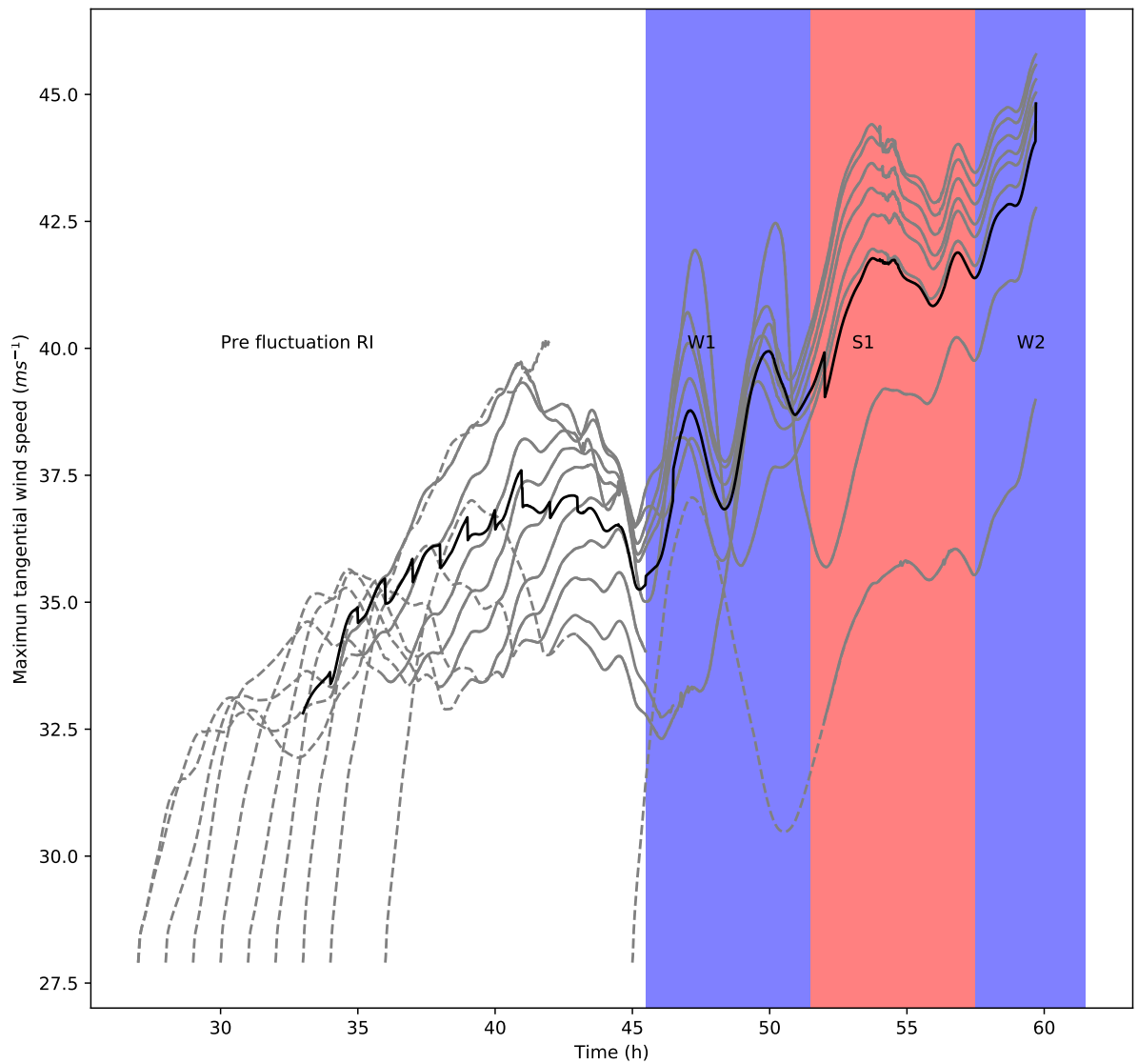


Figure 6.10: Prognostic simulations with heating forcing terms only. Lines show wind speed of simulations that have been initialized at different times (with MetUM forcings) with the same initial wind field. Dashed lines show the first 7 hours of the simulations which are deemed to be the model ‘spin-up’ period. The black solid line shows the average of all the simulations after the ‘spin-up’ period. Also indicated are the fluctuation phases which correspond to the MetUM forcings used at that time.

Figure 6.10 does not show a clear weakening of the maximum wind speed at the start of the W1 forcing period but it does show a weakening prior to W1 starting at around $T+42$ h. A similar period of weakening is shown prior to W2 at around $T+55$ h. To understand why the hypothetical balanced vortex behaves in this way panels in Fig. 6.11 show the primary circulation tendency and secondary circulation averaged over selected 2-hour periods for one of the simulations initialized at $T+28$ h. It should be noted that the vortex has developed a local maximum in AAM in the mid-troposphere at around 7 km height. This is a quite different AAM structure from a real storm such as that shown in Fig. 6.7.

Figure 6.11 shows that during the 37–39 h period the balanced inflow is causing an acceleration of the tangential wind near the surface at the RMW. Several hours prior to W1 a slight broadening in the radial extent of the heating at around 6 km leads to a subtle change in the stream function that causes greater descent near the surface outside of the RMW leading to the advection of low AAM near the RMW and an increase in the outflow within the main updraft of the eyewall. By $T+45$ h an acceleration of the tangential wind field is resumed but this is later disrupted again by another radial broadening of the diabatic heating distribution shown in Fig. 6.11e. The strengthening and radial narrowing of the diabatic heating by the start of S1 shown in Fig. 6.11f results in a weakening of the secondary circulation in the mid-troposphere and a strong tangential wind acceleration.

Although the hypothetical balanced TC without friction does not weaken in the same way as the real storm, the radial broadening of the diabatic heating distribution is disruptive to the storm's development and does lead to periods of weakening prior to and during the W1 time period.

Another way of running the prognostic simulations is to keep the heating constant at a particular time from the MetUM and then run simulations with this constant heating forcing from the same initial wind field. Figure 6.12 shows prognostic simulations with heating forcings from the MetUM at times prior to and during W1. After the model 'spin-up' period the heating forcings from W1 counter-intuitively lead to a stronger vortex; however, they also tend to undergo oscillations in intensity. In contrast, heating forcings taken several hours prior to W1 lead to more

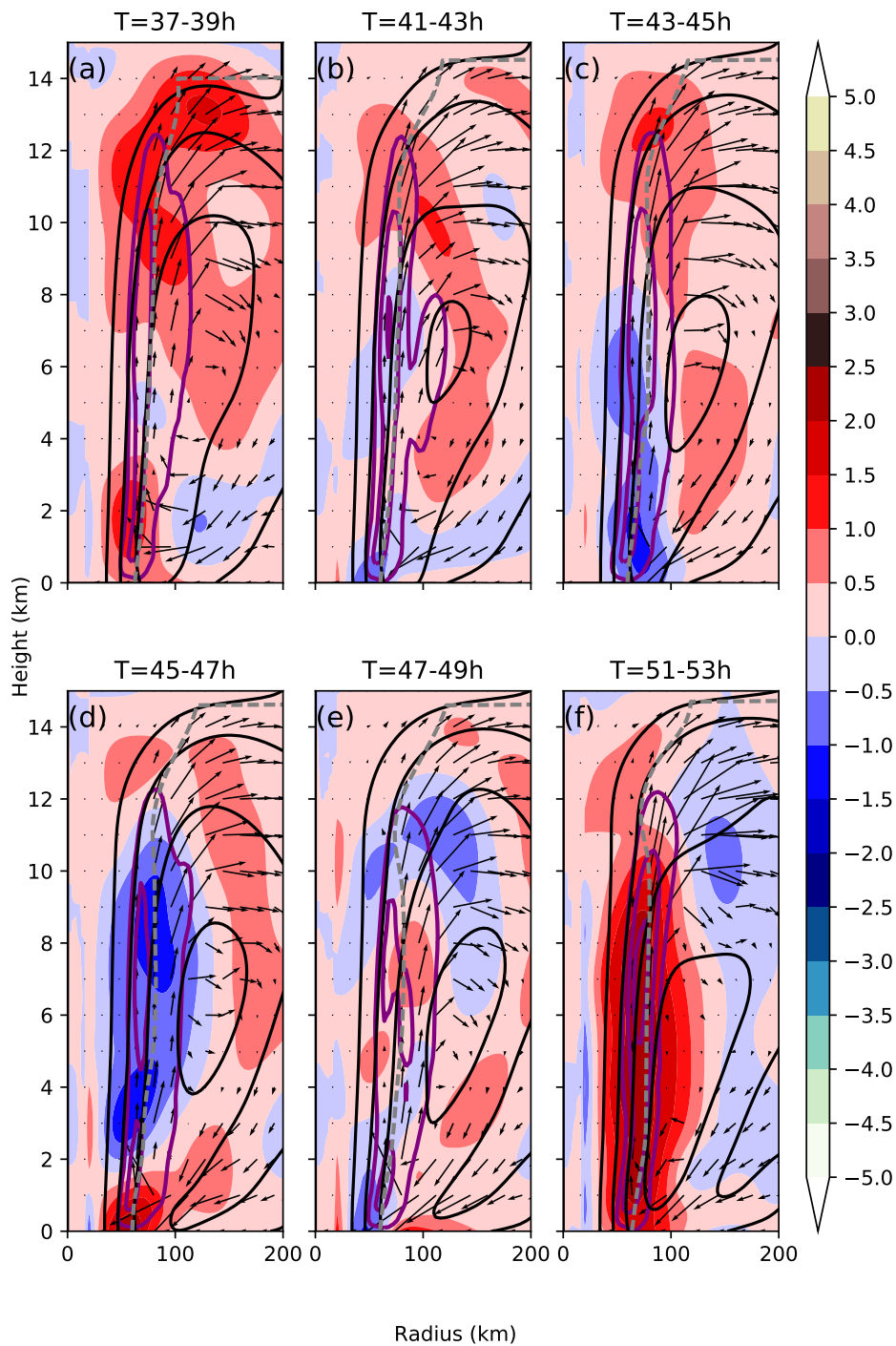


Figure 6.11: Prognostic simulation initialized with heating forcings beginning at $T+28\text{h}$. Shown are composites over selected times with tangential wind tendency ($\text{m s}^{-1}\text{h}^{-1}$, shading) and secondary circulation (arrows) with AAM ($8 \times 10^5 \text{ m}^2 \text{ s}^{-1}$, line contours). Averaged diabatic heating forcings are shown with the purple contours showing values of 5 K h^{-1} and 20 K h^{-1} . Also shown is the RMW (dashed grey line).

stable linear accelerations in the tangential wind field.

6.4 Discussion

The balanced model from Smith et al. (2015) can be run with different regularization methods. The three methods from Moller and Shapiro (2002), Heng et al. (2017) and Abarca and Montgomery (2014) were examined. It was found that only the method from Abarca and Montgomery (2014) was aggressive enough to regularize the SE equation for such strong heating forcings (maximum local value of Q in equation 6.1 in excess of 40 K h^{-1}) and tangential wind fields in the case of the diagnostic case (section 6.3.1–6.3.3). It is likely that stronger storms with larger regions of static or inertial instability are less easily represented in the axisymmetric balanced formulation compared to weaker storms. The point made in Heng et al. (2017) that balanced dynamics can better explain intensification if superior regularization methods are used may only be a robust argument for weaker storms that are known to be explained better by balanced dynamics (e.g. Miyamoto et al., 2014). The necessity of a more aggressive regularization method for stronger storms (including Hurricane Irma (2017) from 04 September onwards) could be a consequence of balance dynamics being a less appropriate model.

In terms of the results of the experiments, the balanced response prior to and during W1 was found to be consistent with results in Chapter 5. The inner rainbands and associated VHT activity at the start of W1 did have an impact on the secondary circulation as in Wang and Wang (2013). However, the balanced response is highly sensitive to the radial location of the inner rainbands. Any balanced response occurring well outside of the RMW has a smaller effect where the AAM surfaces are more spaced out. Unlike in Abarca and Montgomery (2014), there was not much evidence of the rainbands reducing inflow as in the case of a secondary eyewall formation event which may be a key difference between the two types of fluctuations (see Chapter 7). Unlike in Heng and Wang (2016) it was found that both the balanced and unbalanced contributions of friction were important both during the RI and in producing some of the features within and above the boundary layer seen within W1 such as the outflow jet at the top of the boundary layer and the surface

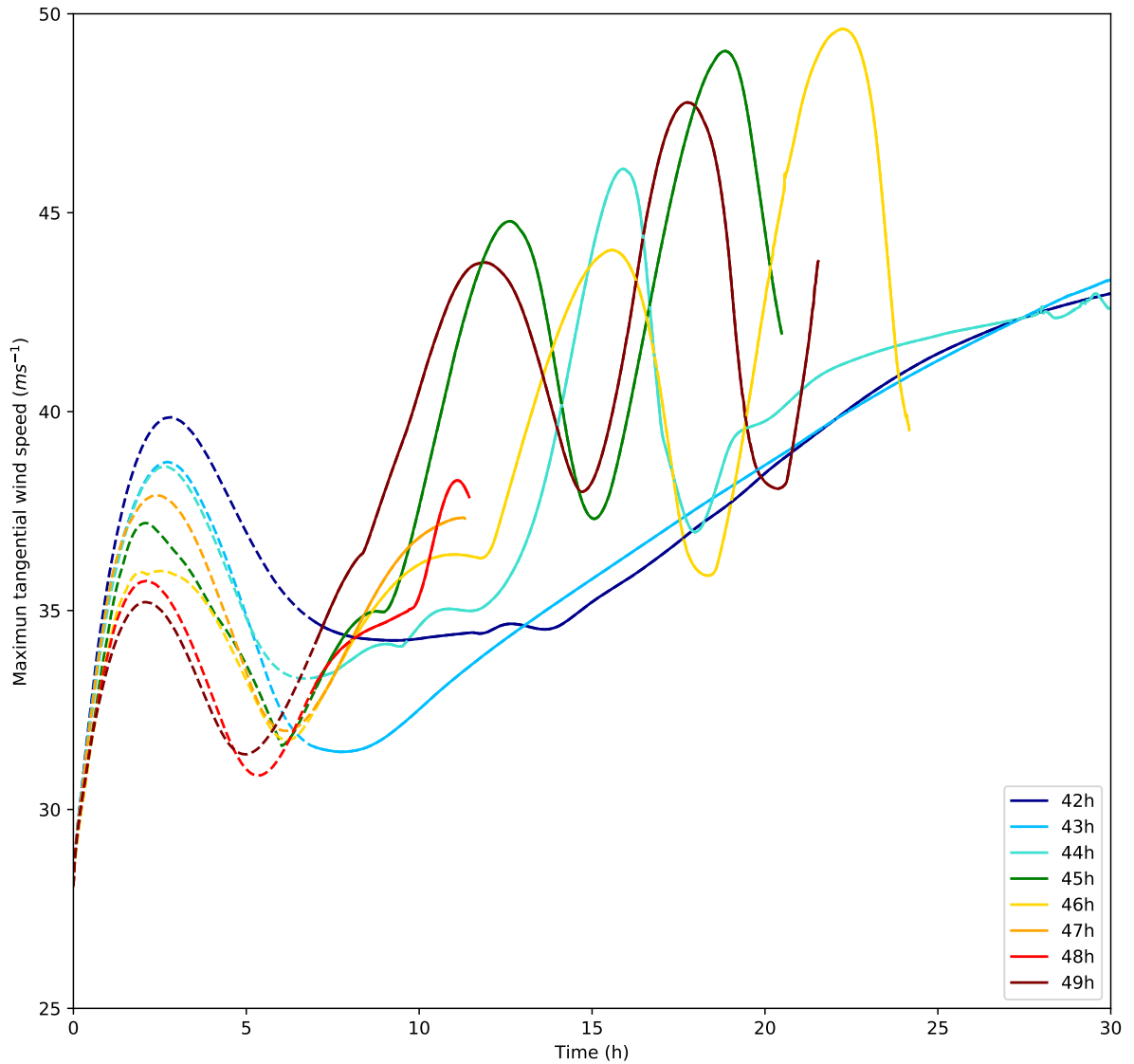


Figure 6.12: Prognostic simulations with heating forcing terms only. Lines show wind speed of simulations that have been initialized with different constant heating forcings from the MetUM at each hour between T+42 h and T+49 h starting with the same initial wind field. Dashed lines show the first 7 hours of the simulations which are deemed to be the model ‘spin-up’ period. The solid line shows the simulations after the ‘spin-up’ period.

inflow. It is likely that some of these differences can be explained by the storm being stronger compared to the storm in Heng and Wang (2016).

Prognostic simulations built on the work in Smith et al. (2018) but with heating forcings from the MetUM instead of an idealized constant heating function. It was found that stable solutions do exist with linear increases in the tangential wind-speed as in Smith et al. (2018) but with unexpected AAM surfaces after the spin-up (for example the local maxima in AAM in the eyewall in Fig 6.11). Nevertheless, the vortex is able to intensify with realistic prescribed heating from the MetUM for more than 30 hours. For the first 7 hours the evolution of the vortex is highly dependent on the initial tangential wind field but thereafter the evolution of the vortex is governed by the diabatic heating distribution. An unbalanced vortex with friction would naturally develop a different AAM structure; therefore, it may be that, if the prognostic simulations do not show any intensity fluctuations, the fluctuations may be explained by a balanced adjustment to an AAM field of an unbalanced vortex. However, if the prognostic simulations do show intensity fluctuations then that implies they can solely be explained through balanced dynamics rather than any kind of interaction between balanced and unbalanced processes. The results are somewhat inconclusive with forcings from W1 playing a distinct role in disrupting an otherwise linear intensification but with weakening occurring several hours earlier than expected. It is fair to conclude that the balanced response plays a critical role in the intensity fluctuations but the interplay between balanced and unbalanced processes is also important. The evolved AAM structure for the prognostic simulation including friction is more similar to the MetUM but crucially the unbalanced inflow is necessary to spin-up the boundary layer.

6.5 Summary and conclusions

Use of a SE balanced model has allowed the balanced mechanisms of the intensity fluctuations observed in Hurricane Irma to be separated out and their contributions assessed.

- The balanced effect of diabatic heating alone can explain both the expansion

of the RMW during W1 and the deceleration of the tangential wind inside the RMW.

- Eddy heating was shown to have a small effect on the secondary circulation but the consistently positive contribution to the tangential acceleration near the concentrated AAM surfaces during the start of W1 may be important.
- The kink structure in the RMW that develops during the later part of W1 can be partially explained by the balanced response to the frictional AAM sink.
- Eddy AAM sources (such as from VHT-like structures) have an inconsistent effect on the balanced response to the secondary circulation and can lead to both tangential deceleration and acceleration near the RMW.
- Despite the relevance of the balanced dynamics, unbalanced dynamics likely play an increasingly important role during W1 with the unbalanced residual in the secondary circulation increasing near the surface up to a few kilometres during W1.
- Prognostic experiments indicate that during the entire RI period of Irma the dissipative effect of friction is stronger than the balanced tangential acceleration from the frictional AAM sink and diabatic heating and that the boundary layer will not spin-up without the stronger unbalanced inflow.
- A hypothetical vortex governed only by balanced dynamics from prescribed heating distributions does experience intensity fluctuations but weakening lags behind the expected start of W1. During W1 the vortex fluctuates rapidly with two periods of intensification and weakening occurring.

Chapter 7

Eyewall replacement cycle and comparison with intensity fluctuations

7.1 Introduction

An eyewall replacement cycle is a common form of intensity fluctuation in intense and mature tropical cyclones. The secondary eyewall formation (SEF) has several possible mechanisms which include: vortex Rossby wave activity (e.g. Ruan et al., 2014), beta skirt axisymmetrisation (e.g. Terwey and Montgomery, 2008) and unbalanced dynamics (e.g. Wang et al., 2016). In all of the above mechanisms dynamical adjustment to outer rainband activity also plays a role with outer rainbands being a ubiquitous feature prior to SEF.

Given the many different mechanisms responsible for eyewall replacement cycles, further case studies examining the processes involved in an eyewall replacement cycle are useful. In addition, there is no known research that compares the fluctuations in eyewall replacement cycles to vacillation cycles, so trying to understand the differences and similarities between the two types of fluctuations will aid in understanding the dynamics at play in both.

The aim of this chapter is to understand the eyewall replacement cycle that occurred

between 07 and 08 September in Hurricane Irma (2017) and compare it to the intensity fluctuations that occurred between 04 September and 05 September with a view to understanding the differences and similarities between these two different forms of intensity fluctuations. Furthermore, the chapter attempts to understand whether these two different forms of intensity fluctuations are distinct and unrelated or form part of a continuous spectrum with vacillation cycles a type of eyewall replacement cycle.

The chapter is organised as follows: Section 7.2.1 compares observational data from the EWRC on 07–08 September to the model output to check that the MetUM is capable of replicating the EWRC which is then analysed in detail in section 7.2.2 and compared to established mechanisms for SEF. Once the cause and dynamical processes involved in the EWRC have been established section 7.2.2, compares these processes with the intensity fluctuations to establish similarities and differences between the two forms of fluctuations. An attempt to understand whether or not these two different types of fluctuations are manifestations of similar dynamics is given in section 7.2.3. An in–depth discussion on the causes of the EWRC and its differences to the intensity fluctuation is then presented in section 7.3. Conclusions are given in section 7.4.

7.2 Results

7.2.1 Model evaluation

Hurricane Irma (2017) underwent a full eyewall replacement cycle between 07 and 08 September. In order to understand the cause of the eyewall replacement cycle model ensemble simulations were conducted and compared to microwave data. The ensemble that best matched observations in terms of structure and development was picked for detailed analysis of the eyewall replacement cycle (ensemble member 10 from 05 September 12:00 UTC simulation). The SEF event happened earlier in reality (10:15 UTC on 07 September compared to 05:00 UTC on 08 September). Figure 7.1 shows the layer (4062–7038 m) averaged vertical velocity from the model output on the left with the concomitant microwave imagery on the right. The

T+0.0 h mark has been taken to be the approximate time of SEF occurrence.

Figure 7.1a,b shows that, prior to SEF, Irma develops a strong single outer rainband that spirals out from the eyewall. The structure of this strong outer rainband is very similar between the model output and the microwave imagery (albeit with the rainband at a different angle to the TC centre, most prominent to the south east in the model output and most prominent to the west in the microwave imagery). At smaller radii close to the eyewall the rainband presents as a continuous zone of convection whilst at greater radii the convection is disparate and consists of individual thunderstorms. However, the strong outer rainband feature does appear earlier, relative to the time when SEF occurs, compared to the model output (9 hours prior to SEF in the microwave imagery compared to 3.5 hours prior in the model output).

The structure of the TC around the time of SEF is shown in Figure 7.1c,d. The prominent outer rainband in 7.1a,b gives way to multiple outer rainband features which increasingly become apparent at all azimuthal angles and eventually begin to form a ring structure. Down-draughts associated with the many banded features also tend to axisymmetrise and form the beginnings of a moat region between the eyewall and the SEF region. Although the process takes longer in the microwave imagery compared to the model simulation, the transition from a single dominant outer rainband to multiple rainbands to a ring-like structure is similar in the model output and the microwave observation.

The convection within the SEF region takes a few hours to organise both in the model and the microwave imagery as shown in Figure 7.1e,f. Both the moat region and the SEF become stronger and more coherent rings during this period. The inner eyewall remains prominent, though in both the model simulation and microwave imagery the ring shape is broken on one side.

The transition between two concurrent eyewalls (Figure 7.1e,f) to the complete replacement of the inner eyewall (Figure 7.1g,h) takes a little over ten hours in both the microwave imagery and model output. Before this replacement occurs, both the inner and outer eyewalls in both the microwave imagery and model output

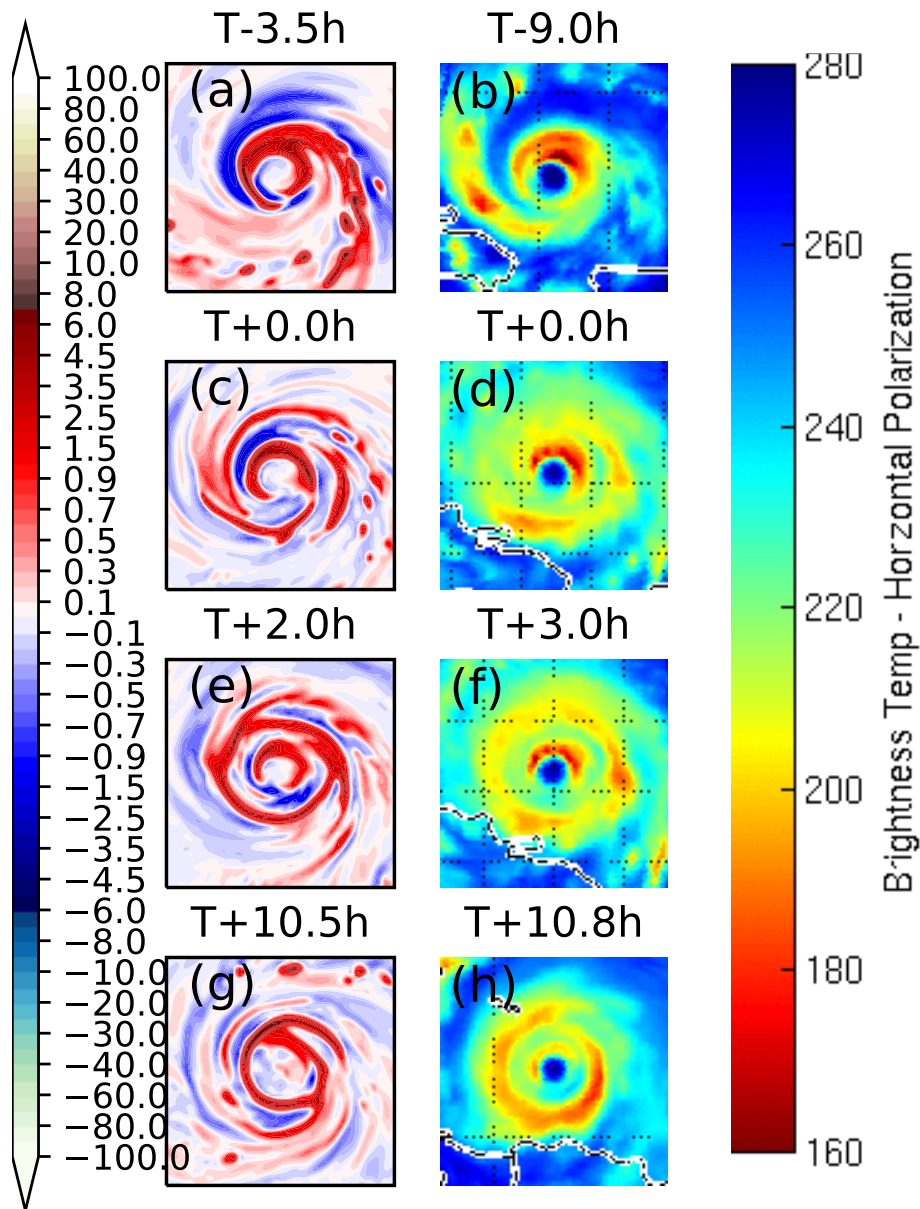


Figure 7.1: (a,c,e,g): Layer averaged (4062–7038 m) simulated vertical velocity (m s^{-1} , shading), (b,d,f,h): Microwave imagery at selected times within the eyewall replacement cycle. Times have been chosen such that they are relative to the approximate SEF stage in both the microwave and model data. These stages are: a,b Single spiral outer-rainband, c,d SEF, e,f outer eyewall becomes dominant, g,h remnant eye convection.

become less well organised and more asymmetrical with ragged and disorganised convection. The inner eyewall then dissipates and the secondary eyewall reorganises into a coherent ring structure once again. Some remnant convection from the inner eyewall is still visible in Figure 7.1g and Figure 7.1h and these remnants tend to last at least another 24 hours. This convection associated with the decaying inner eyewall slowly moves inwards into the eye and becomes weaker while it does so.

In general the full eyewall replacement cycle of Irma is captured well by the model simulation with the key structural changes taking approximately the same time. The key difference between the model simulation and the microwave data is that, in reality, it takes significantly longer for the single strong outer rainband to axisymmetrise into a coherent ring of convection.

7.2.2 Secondary eyewall formation (SEF) dynamics

The aim of this section is to understand the cause of the SEF that occurred in Hurricane Irma by analysing the ensemble simulation that captures the eyewall replacement best. Plausible mechanisms from the literature are investigated and compared to the model output to determine the role these mechanisms (if any) played in the SEF. Specifically a detailed investigation into the role of vortex Rossby waves, the beta skirt axisymmetrisation (BSA) mechanism, and unbalanced dynamics within the boundary layer as well as any dynamical adjustment from the outer rainband activity are carried out.

Vortex Rossby waves

Figure 7.2 shows the wavenumber-2 decomposed PV with a phase angle of zero degrees (eastern azimuth). A vortex Rossby wave event starts in the eyewall at T+71 h and propagates outwards to the stagnation radius by T+73.5 h. The vortex Rossby wave is convectively coupled and associated with local ascent. The azimuthal phase velocity of the VRW (not shown) was also found to be consistent with the dispersion relation (equation 3.4). There is a distinct wavenumber-2 PV anomaly from T+75 h to after SEF (around T+77 h) shown in Figure 7.2. However, these PV anomalies did not propagate in a way consistent with the dispersion relation so

many not be coherent VRWs.

In order to determine the effect of the VRW on the tangential wind field, Figure 7.3 shows the azimuthally averaged vertical velocity and tangential wind acceleration as a function of time. The vortex Rossby wave event induces a large positive tangential acceleration near the stagnation radius at around T+73 h and also leads to some slight increase in the ascent in the same region. However, it is notable that SEF does not immediately follow this VRW event and there is a slight tangential wind deceleration between T+74.5 h and T+75 h.

The mean and eddy contributions to the tangential wind budget are shown in Figure 7.4 during the VRW event and around the SEF. Comparing Figure 7.4b to Figure 7.4a shows that the VRW event led to a wave–mean interaction (energy from the VRW transferred to the mean state) above the boundary layer (around 100 km radius and 2.5 km height) and resulted in a tangential acceleration around the stagnation radius. By contrast Figure 7.4c and d show the dominant contribution during SEF was the mean term (see Chapter 5 for definition of the tangential wind budgets). The VRW event, therefore, likely contributed to the tangential acceleration near the stagnation radius prior to SEF but is unlikely to have been the direct cause of it.

Beta skirt axisymmetrisation (BSA) mechanism

In order for the BSA mechanism to occur, cumulus convection must be allowed to happen in a region where there is a mean negative gradient of vorticity. This cannot happen within the filamentation zone where convection is suppressed but also cannot happen at too large a radius where there is not a mean gradient of vorticity. Hence a ‘goldilocks’ zone must be present at some radial distance from the storm centre where convection is not suppressed and occurs within the beta skirt. The first requirement can be quantified using the filamentation time defined as:

$$\tau_{fil} = \left(\frac{-\bar{v}}{r} \frac{\partial \bar{v}}{\partial r} \right)^{-1/2}, \quad (7.1)$$

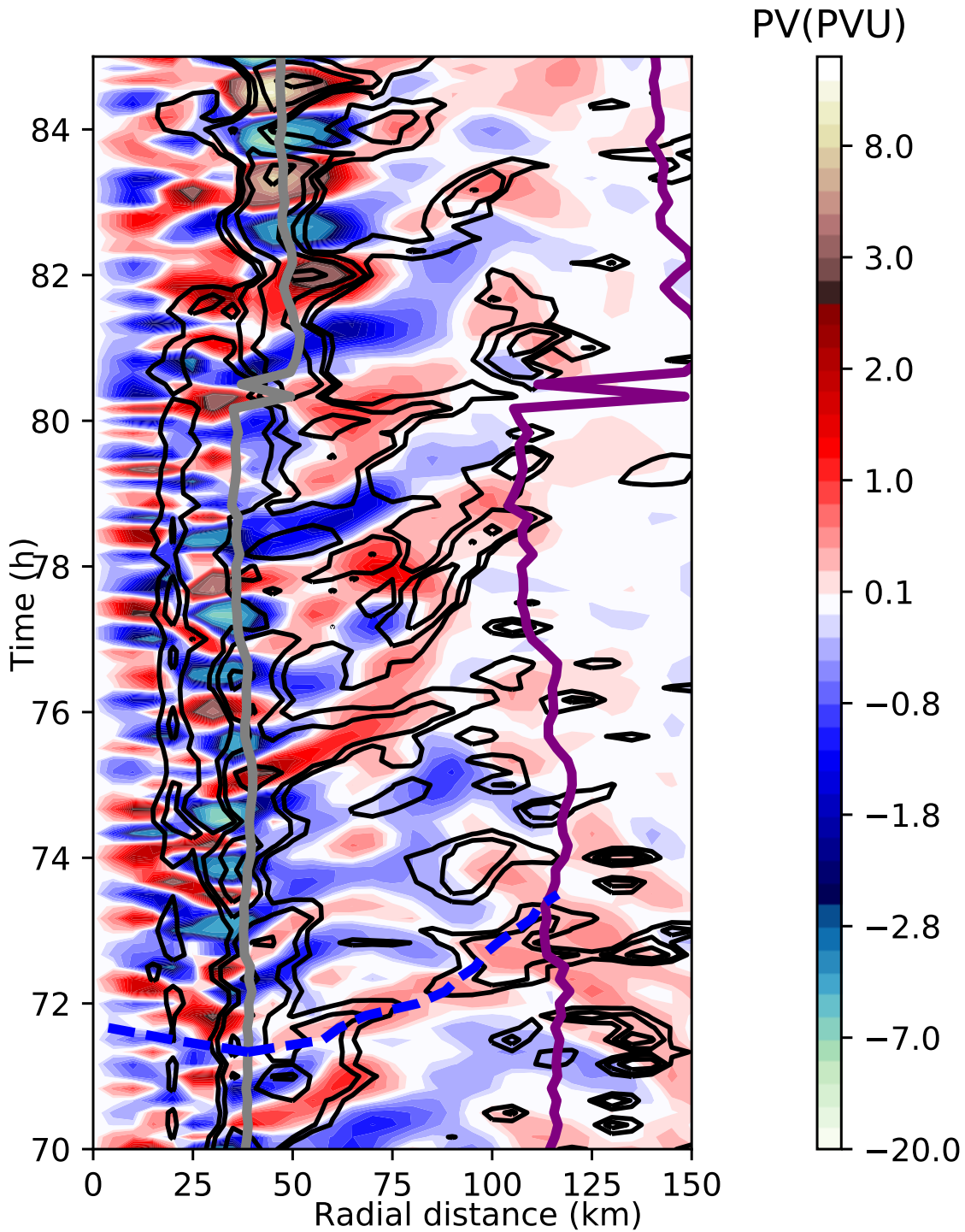


Figure 7.2: Wavenumber-2 PV for the eastern azimuth (shaded, PVU) at 1532 m. Vertical velocity (black line contours of 0.4, 0.8, 1.6, 3.2 m s⁻¹) along the same azimuthal angle and height. Also shown are the RMW for the same height (grey solid line) and 3×RMW as a proxy for the stagnation radius (purple solid line). The blue dashed line shows the trajectory of a hypothetical VRW propagating from the RMW at T+71 h using the VRW dispersion relation (equation 3.5).

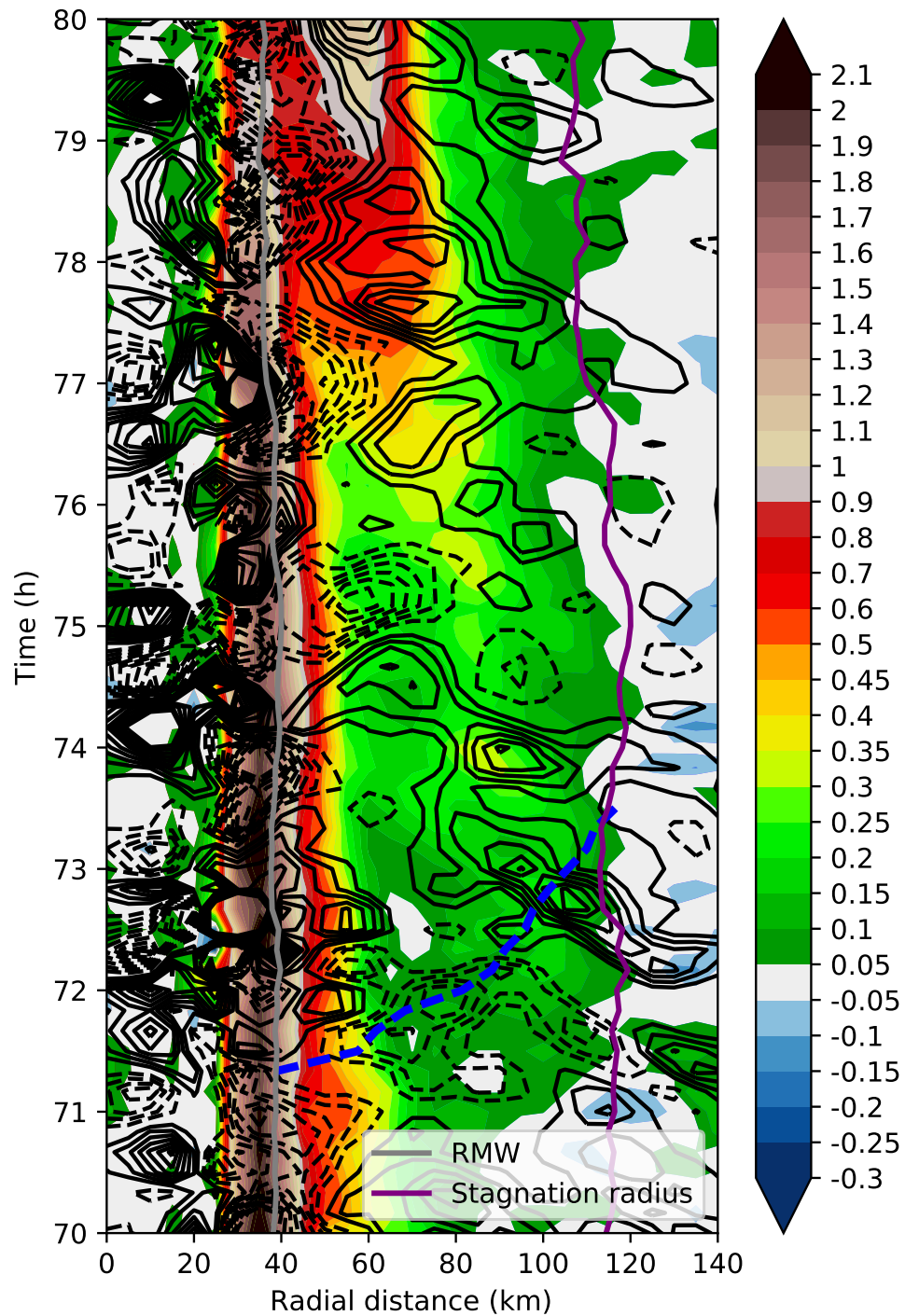


Figure 7.3: Azimuthally averaged vertical velocity at 1532 m (shaded, m s^{-1}). Azimuthally averaged tangential wind acceleration (black line contours of 0.5 m s^{-1} intervals). Also shown are the RMW for the same height (thick grey solid line) and $3 \times \text{RMW}$ as a proxy for the stagnation radius (purple solid line). The dashed blue line shows the radial, time trajectory of a hypothetical VRW propagating from the RMW at $T+71 \text{ h}$ using the VRW dispersion relation (equation 3.5).

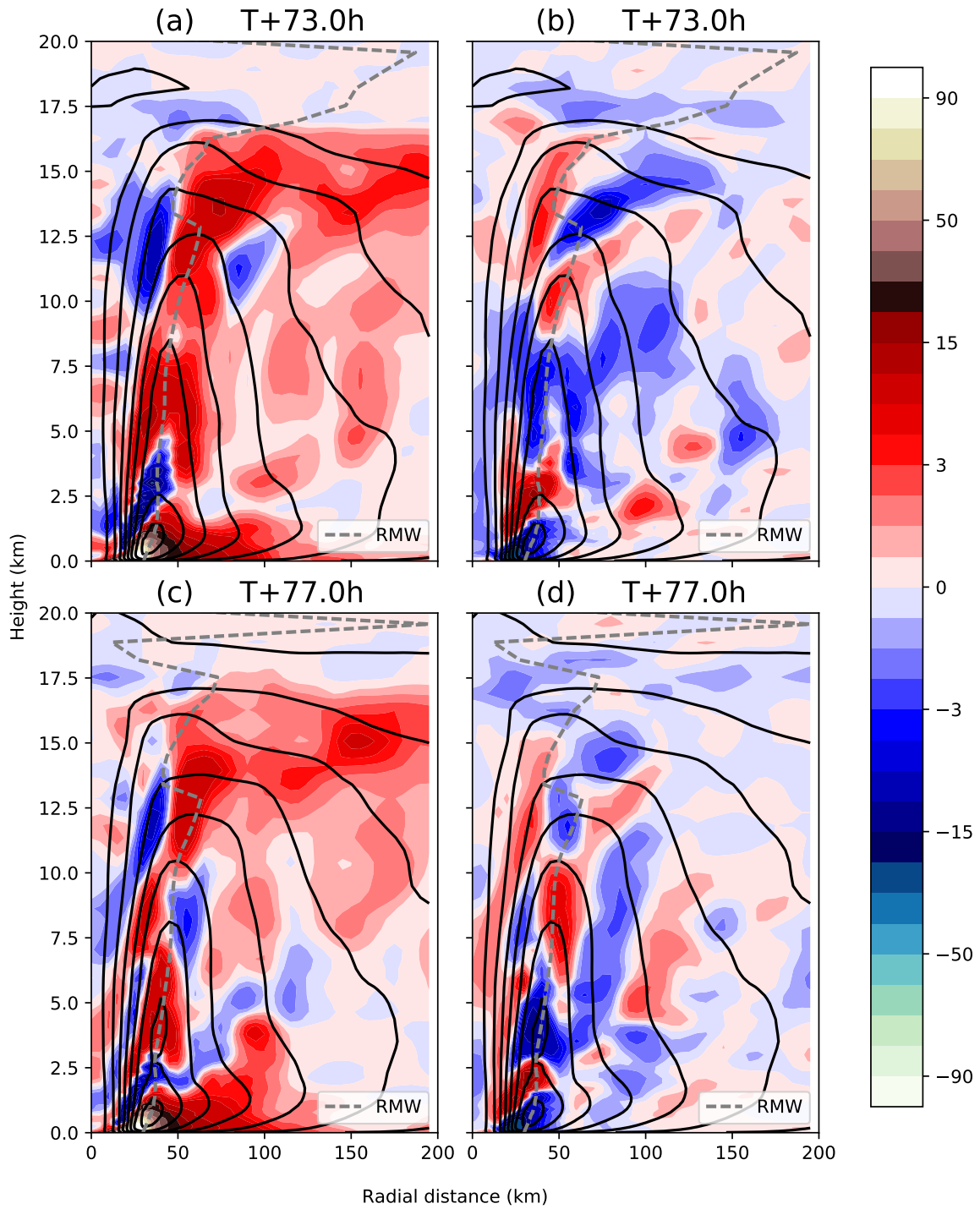


Figure 7.4: (a,c) Mean and (b,d) eddy terms (shaded, $\text{ms}^{-1}\text{h}^{-1}$) of the tangential wind budget are shown. The tangential wind (line contours, 10 ms^{-1} intervals) and the RMW (grey dashed line) are also shown.

where τ_{fil} is the filamentation time, \bar{v} is the azimuthal mean tangential wind, and r is the radial distance from the storm centre. In order for convection to occur, the filamentation time should be less than the convective lifetime of a cumulonimbus cell, usually taken to be 30 minutes or less.

The second requirement is quantified in terms of the effective beta function defined as:

$$\beta = -\frac{\partial \bar{P}V}{\partial r} \frac{\bar{\xi}}{\bar{P}V}, \quad (7.2)$$

In the SEF region β needs to be positive.

Figure 7.5 shows how the tangential wind field and the ‘goldilocks’ zone evolve prior to and after the SEF. A little after T+72 hr (Figure 7.5a) there is a region of tangential wind acceleration at around 110 km which is associated with a vortex Rossby wave event. Other than this vortex Rossby wave event the tangential wind acceleration outside of the eyewall remains weak in the hours prior to SEF. Figure 7.5b does show, however, that the ‘goldilocks’ zone does expand slightly in the hours prior to SEF with conditions met for BSA in a broad region below 2.5 km at radii higher than 70 km from 75.5 hr onwards. Despite this, a distinct increase in the tangential wind acceleration only occurs in this zone from around T+77.5 hr onwards (e.g. Figure 7.5c) by which time there is already an organised ring of convection. A secondary wind maximum does not develop until around T+80 hr (e.g. Figure 7.5d) and is only present, at first, above 2.5 km. No low-level jet is present, and the rapid strengthening of the tangential wind occurs after SEF has already occurred. It is possible that the development of the beta skirt helps develop the secondary wind maxima but it is evident that the BSA mechanism is not responsible for the SEF in this case.

Unbalanced dynamics

The unbalanced mechanism starts with a broadening of the wind field that increases the frictionally induced boundary layer inflow which in turn promotes convergence, development of the supergradient wind and further increases the tangential wind as

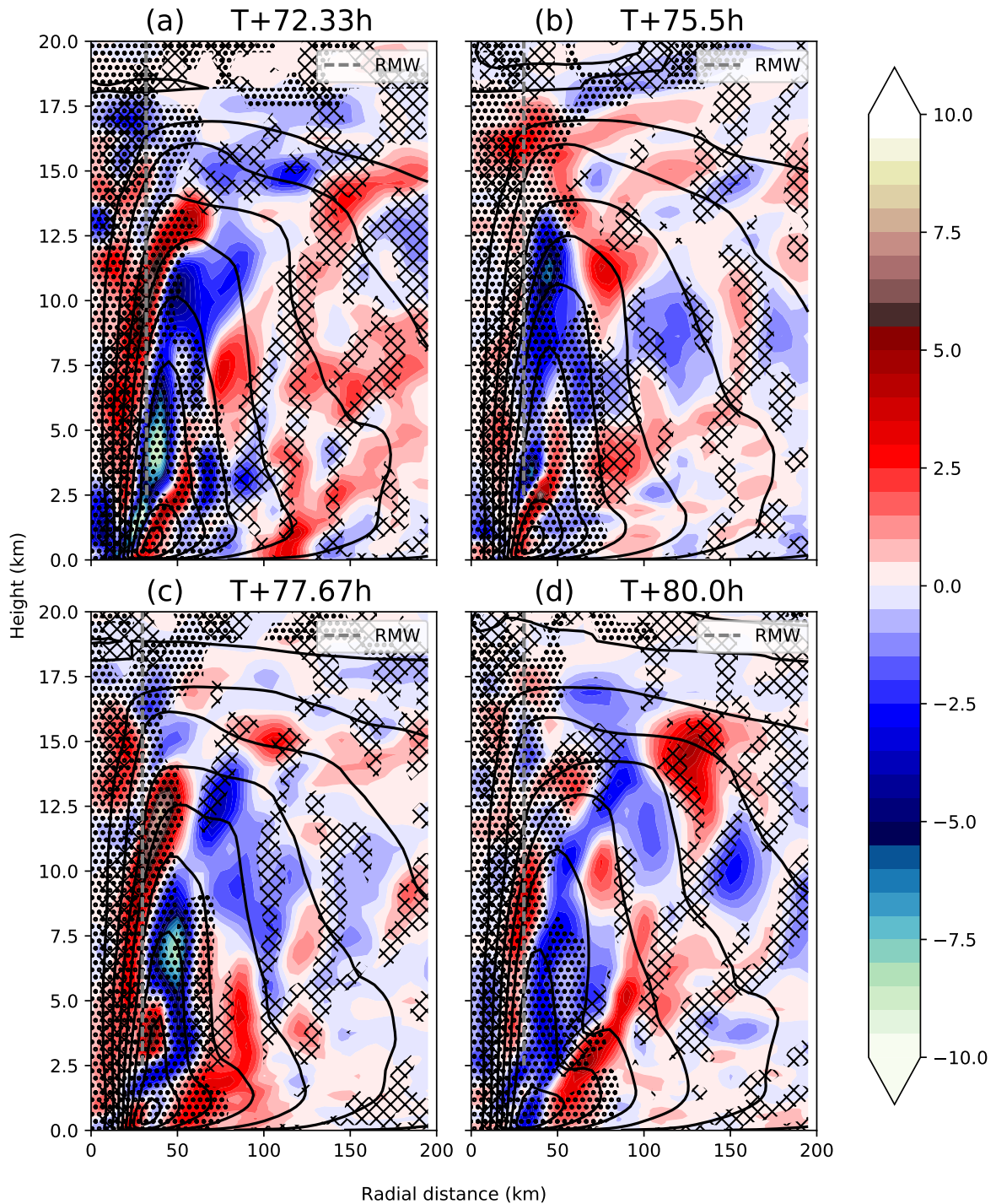


Figure 7.5: Tangential wind acceleration (shaded, m s^{-2}), tangential wind speed (line contours, 10 m s^{-1} interval) for selected times. Stippling shows regions where τ_{fil} is less than 30 minutes, and cross hatching shows regions where β is negative.

a positive feedback.

Figure 7.6a shows the development of the agradiant wind near the surface along with the tangential and radial wind fields. Figure 7.6b shows the same but for a height of 552 m where the subgradient wind becomes supergradient in the SEF region.

The main change in agradiant wind occurs at around T+77 h onwards where at around 60 km to 70 km (in the SEF region) the wind goes from marginally supergradient at 552 m to highly supergradient (Fig. 7.6b). This increase in agradiant wind occurs at approximately the same time as the rapid increase in the surface radial wind at around T+76.5 h at 60 km–70 km (Figure 7.6a) and slightly earlier for greater radii. At around 50 km the increase in the surface radial wind and 552 m height agradiant wind happens later at around T+79.5 h with the agradiant wind increasing prior to the increase in the surface radial wind.

Prior to the development of the agradiant wind and increased frictionally induced boundary layer inflow a strengthening of the tangential wind occurs above the boundary layer. Figure 7.7a shows initially before T+75 h rainbands at around 100–125 km produce a weak radial inflow above the boundary layer which is likely a balanced response to the diabatic heating. This inflow, in turn, promotes a positive tangential wind tendency in the vicinity of and at slightly greater radii than the rainbands by advecting absolute angular momentum inwards. Just before SEF (Figure 7.7b) particularly large tangential wind tendencies are seen above the boundary layer at around 2.5 km and 80 km radius. The outflow just above the boundary layer in the moat region is also enhanced by the rainband leading to increased convergence in the SEF region. By T+81 h (Figure 7.7c) coupling has clearly occurred with the boundary layer, with a maximum in vertical velocity extending from the upper troposphere to the boundary layer. By 81 h–84 h the new eyewall is completely coupled with the boundary layer and the SEF had completed.

In summary, of the mechanisms examined, the cause of the SEF is judged to be best explained by unbalanced dynamics which involve a boundary layer inflow leading to increasing agradiant outward forces that promote convection in the SEF region. The

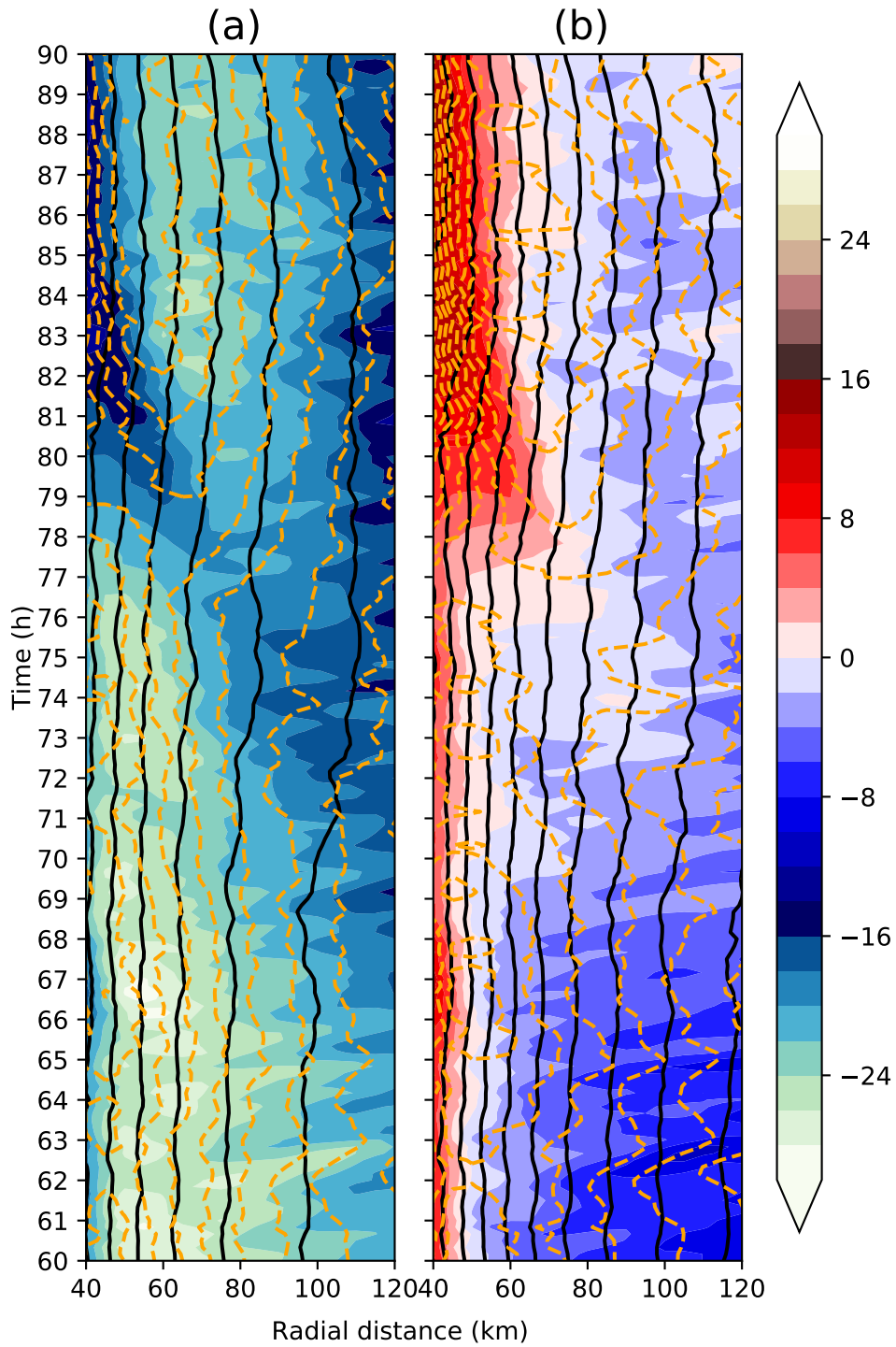


Figure 7.6: A gradient wind (shaded, m s^{-1}), tangential wind (black line contours, 5 m s^{-1} interval), and radial wind (orange line contours, 5 m s^{-1} interval, dashed lines imply an inflow) at 12 m height (a), and 552 m height (b).

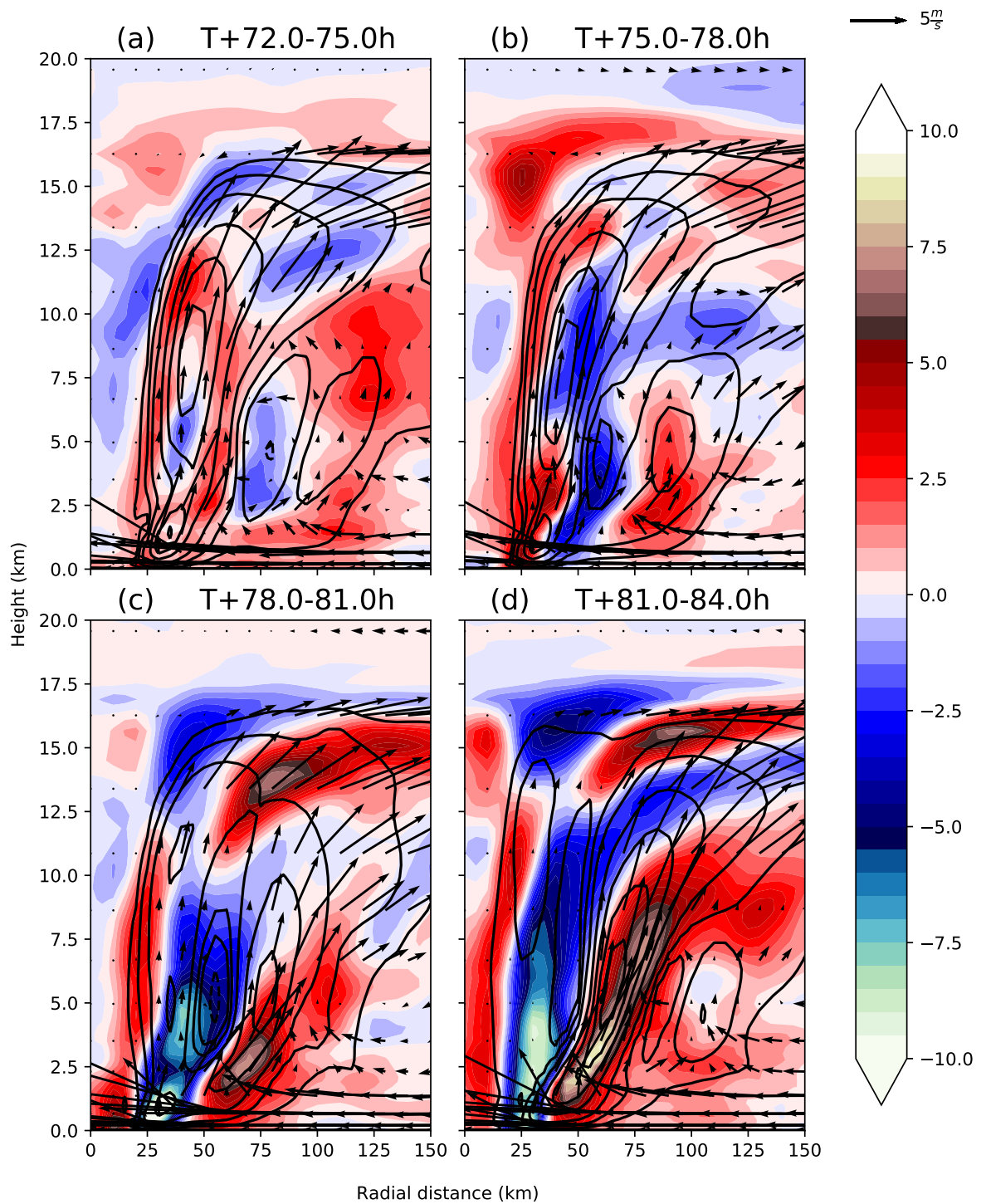


Figure 7.7: Azimuthally averaged tangential wind tendency (shaded, m s^{-1} over 3 hours), three-hourly azimuthally averaged vertical velocity (black contours, 0.25, 0.5, 1 m s^{-1} intervals and 1 m s^{-1} intervals thereafter) and wind in the plane of cross section (arrows) for selected periods prior and just after SEF. Arrow length in the vertical direction is scaled to be ten times longer than in the horizontal direction for the same flow speed.

original cause of this boundary layer inflow is likely to be due to broadening of the tangential wind occurring above the boundary layer which is primarily a result of a balanced dynamical adjustment to outer-rainband activity. Although the BSA and VRW mechanisms are not judged to directly cause SEF they do make conditions more favourable by also contributing to the broadening of the tangential wind field, above the boundary layer, prior to SEF.

7.2.3 Comparison between eyewall replacement cycle and intensity fluctuations

In order to determine whether or not the intensity fluctuations in Chapters 4–6 are caused by a similar mechanism as eyewall replacement cycles both the modelled eyewall replacement cycles discussed in section 7.2.2 and the intensity fluctuations that occurred a few days prior during RI (Chapters 4–6) were compared to one another.

Structural similarities and differences

The differences in low-level PV structure between the intensity fluctuations and the eyewall replacement cycle, above the boundary layer are encapsulated in Figure 7.8. In the full eyewall replacement cycle from about T+60 h onwards the radial PV structure becomes more ring-like as the storm gradually intensifies. The value of PV_0/PV_{\max} reaches a minimum of around 0.45 and gradually increases as the outer rainbands become more prominent after T+70 h. As the rainbands axisymmetrise there is little change in the PV structure with only a gradual tendency for the radial PV structure to become more ring-like. As discussed in Section 7.2.2 an outer ‘skirt’ of PV does form outside the eyewall around the time of SEF (Figure 7.8a at line b) but during the SEF process the PV structure within the primary eyewall and eye changes little. After the secondary eyewall becomes dominant (Figure 7.8a at line c) the PV_0/PV_{\max} metric increases rapidly and the PV structure moves from ring-like to monopolar due to PV being transported into the new, larger eye and becomes almost completely monopolar by T+88.5 h (Fig. 7.8 a at line d) where the primary eyewall has completely broken down to leave only remnant convection

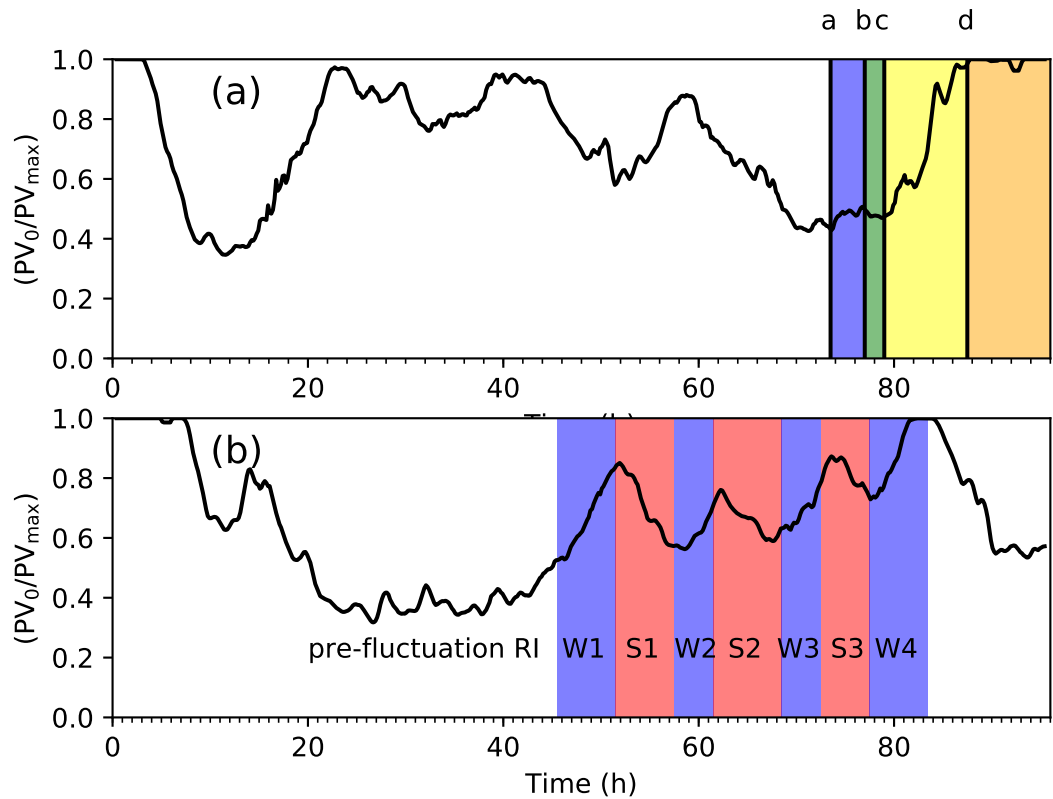


Figure 7.8: Ratio of the low-level PV (depth averaged between 1052 m and 4062 m) at the centre of the TC to the maximum azimuthally averaged low level PV for: (a) ensemble member 10 of the 05 September 12 UTC simulation showing the full eyewall replacement cycle, (b) ensemble member 15 of the 03 September 00 UTC simulation showing the intensity fluctuations. In the case of (a) the vertical lines correspond to each of the four chosen times in Figure 7.3. In the case of (b) the weakening and strengthening phases are shown.

within the eye. A secondary PV maximum appears from around T+77 h onwards corresponding to the new RMW and gradually extends upwards and outwards until merging with the larger PV column by around 85 h.

The weakening phases in the intensity fluctuations by comparison (Figure 7.8b) shows an immediate increase in the PV_0/PV_{\max} metric at the start of the weakening phase whereas during the eyewall replacement cycle the weakening of the maximum tangential wind and expansion of the RMW precedes the redistribution of PV which only occurs after the secondary eyewall has become stronger than the inner eyewall. The transport of PV into the eye in the eyewall replacement cycle causes a significant change in the PV structure and the TC does not regain its ring-like PV structure in the boundary layer until around 84 h and remains completely monopolar above the boundary layer until the end of the simulation at 96 h. For the intensity fluctuations the change in PV is temporary. During the weakening phases PV is transported into the eye and there is less diabatically generated PV in the eyewall but the ring-like PV structure quickly reforms during the start of the next strengthening phase. There is still a long term upward tendency in PV_0/PV_{\max} though with the TC overall developing a more monopolar PV structure with time.

The change in the azimuthal structure of the PV is also different in the EWRC compared to the intensity fluctuations. Figure 7.9 compares the horizontal structure of the PV during the EWRC (Figure 7.9a-d) and during the intensity fluctuations (Figure 7.9e-h). SEF is shown to have little impact on the azimuthal structure of the PV. Figure 7.9a-c shows during the SEF period there is little change in the azimuthal structure in the PV. The PV structure does, however, become much more azimuthally asymmetrical after the secondary eyewall becomes dominant with Figure 7.9d showing a more elliptical structure. This change in azimuthal PV structure is quite different to the intensity fluctuations where an initially elliptical PV ring at the start of the first weakening phase (Figure 7.9f) rapidly symmetrises into a more circular structure during the middle of the weakening phase (Fig. 7.9g). It is notable that the decrease in azimuthal symmetry after the eyewall replacement occurs at the same time as the radial PV structure becoming more monopolar (Figure 7.8) which is the opposite to what occurs during the intensity fluctuations

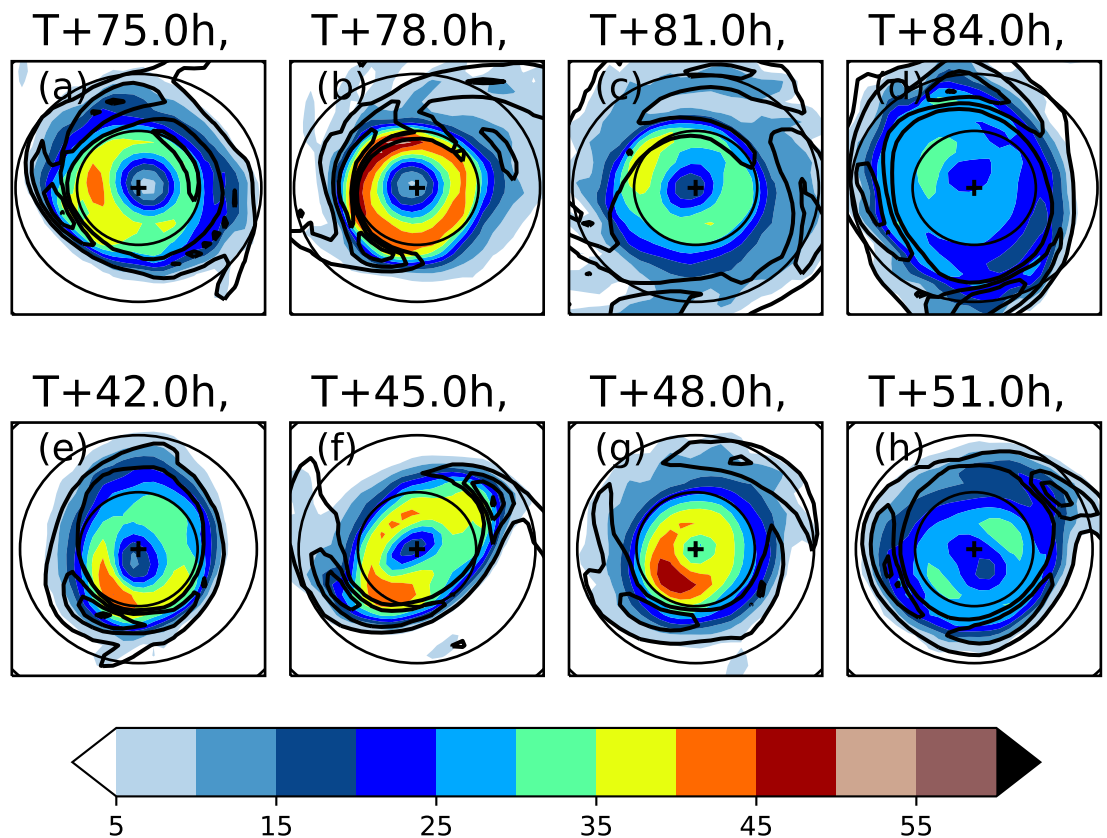


Figure 7.9: PV (PVU, shaded) at 1532 m height for selected times and vertical velocity (1 ms^{-1} , black contour). A black cross marks the centre of the TC. Black circles show radii in increments of 25 km. The data is output in 10-minute intervals, times are given to the nearest 0.1 hours. The top row is from ensemble member 10 of the 05 September 12 UTC simulation showing the full eyewall replacement cycle, the bottom row for ensemble member 15 of the 03 September 00 UTC simulation showing the intensity fluctuations.

where the PV structure becomes more ring-like and less azimuthally symmetrical. The changes in azimuthal PV symmetry during the EWRC are also less significant compared to changes in azimuthal PV symmetry during the intensity fluctuations. The maximum standard deviation of PV (not shown) does not change much during the EWRC (although there is an increase in the standard deviation of PV near the new eyewall after it becomes dominant) whereas during the intensity fluctuations there is a very rapid decrease in the standard deviation of PV during a weakening phase and a rapid increase in the standard deviation of PV during a strengthening phase.

In terms of comparing the convective structures during SEF and the intensity fluctuations, Figure 7.10 shows the secondary circulation at key times during SEF and the intensity fluctuations prior to and during W1. Prior to SEF the vertical velocity increases at a radius coinciding with the rainband region which at T+72 h is a radius of around 130 km. The updraught centre moves radially inward and slightly decreases in height over time and after SEF (Figure 7.10d) ends up merging with the boundary layer to form a coherent updraught at all levels. There is already an outflow above the boundary layer associated with the outer rainband in Figure 7.10a which develops into a full tropospheric outflow channel by T+75 h (7.10 b), during SEF (7.10 c) this new outflow channel couples to the boundary layer outflow from the primary eyewall which ends up cutting off the outflow from the primary outflow which can be seen by T+80 h in Figure 7.10 d. There is a sequence of events where the secondary circulation associated with the outer rainband gradually becomes more dominant before entirely replacing the secondary circulation of the primary eyewall. This is not seen in the intensity fluctuations. Comparing the start of W1 (Figure 7.10f) with the secondary circulation prior to the start of W1 (Fig. 7.10 e) shows that the updraught associated with the eyewall has become bifurcated; this bifurcation becomes increasingly more apparent with two separate maxima by T+47.5 h (Figure 7.10g). However, unlike in the case of the eyewall replacement cycle, there is no updraught (associated with outer rainbands) outside of the eyewall and above the boundary layer that moves radially inwards over time before merging with the boundary layer updraught associated with the newly forming secondary

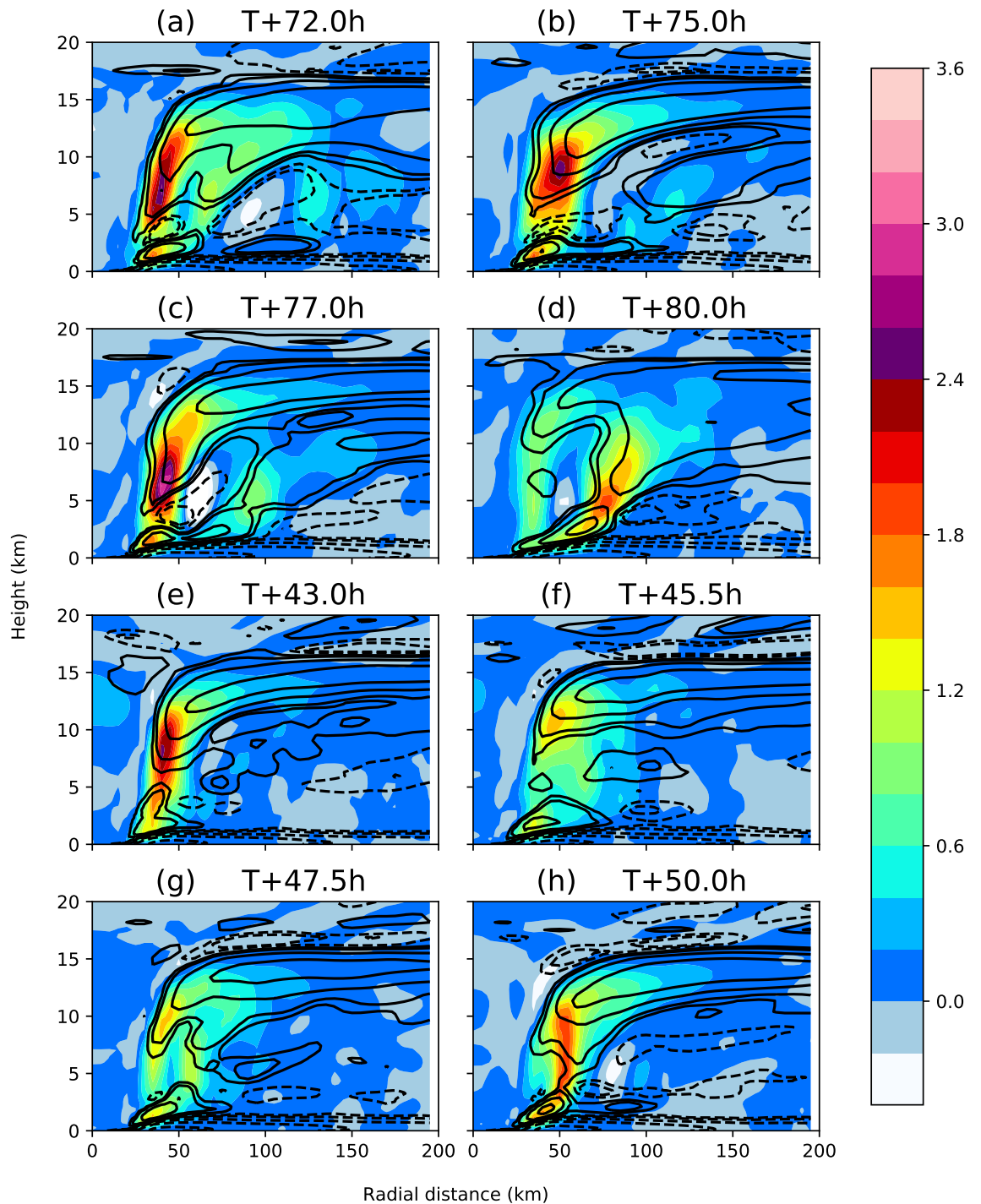


Figure 7.10: Vertical velocity (m s^{-1} , shaded) and radial wind (0.1, 0.2, 0.5, 1, 2, 5, 10, 20, 50 m s^{-1} positive (solid) and negative (dashed) black contours). Panels a-d from ensemble member 10 of the 05 September 12 UTC simulation showing the full eyewall replacement cycle, panels e-h for ensemble member 15 of the 03 September 00 UTC simulation showing the intensity fluctuations.

eyewall. In the intensity fluctuations there is a weak mid-tropospheric secondary outflow visible at $T+45.5$ h (Figure 7.10f) around 100 km radius and 7 km height but this does not subsequently merge to the boundary layer outflow as it does between $T+75$ h and $T+77$ h in the EWRC (Figure 7.10b-c).

Updraft coupling

In order to understand the differences between the eyewall replacement cycle and the intensity fluctuations it is necessary to re-examine the boundary layer and how it couples with the free vortex above in the case of both the EWRC and the intensity fluctuations.

Figure 7.11 shows how the agradient, radial and tangential wind fields change through the two types of intensity fluctuations. In the case of the EWRC, prior to SEF the agradient wind gradually increases in the top part of the boundary layer between 75 km and 100 km radius particularly where the outer rainbands are active (Figure 7.11a,b) during this time the tangential wind increases slightly above the boundary layer (at around 3.5 km height, 80 km radius) which explains the slight increase in the boundary layer inflow and increase in the agradient wind. At around $T+77$ h (Figure 7.11 c) there is a larger increase in the tangential wind above the boundary layer and an increase in the radial inflow. By 80 h (Figure 7.11d) the agradient wind has increased at all levels within the boundary layer (particularly around 60 km) and there is a rapid increase in the tangential wind above the boundary layer to form a secondary tangential wind maximum. In contrast, during the intensity fluctuations the increase in the agradient wind occurs much closer to the eye-wall which can be seen particularly between $T+47.5$ h and $T+50$ h (Figure 7.11g-h) at around 40–50 km radius within the boundary layer. There are however some similarities. The increase in the agradient wind is also associated with an increase in the boundary layer radial inflow albeit at a relatively narrow radius of around 40–60 km and there is an associated tangential acceleration at the same radius. Additionally, there is also an increase in the tangential wind prior to the weakening phase (Figure 7.11e) as there is for the EWRC (Figure 7.11b).

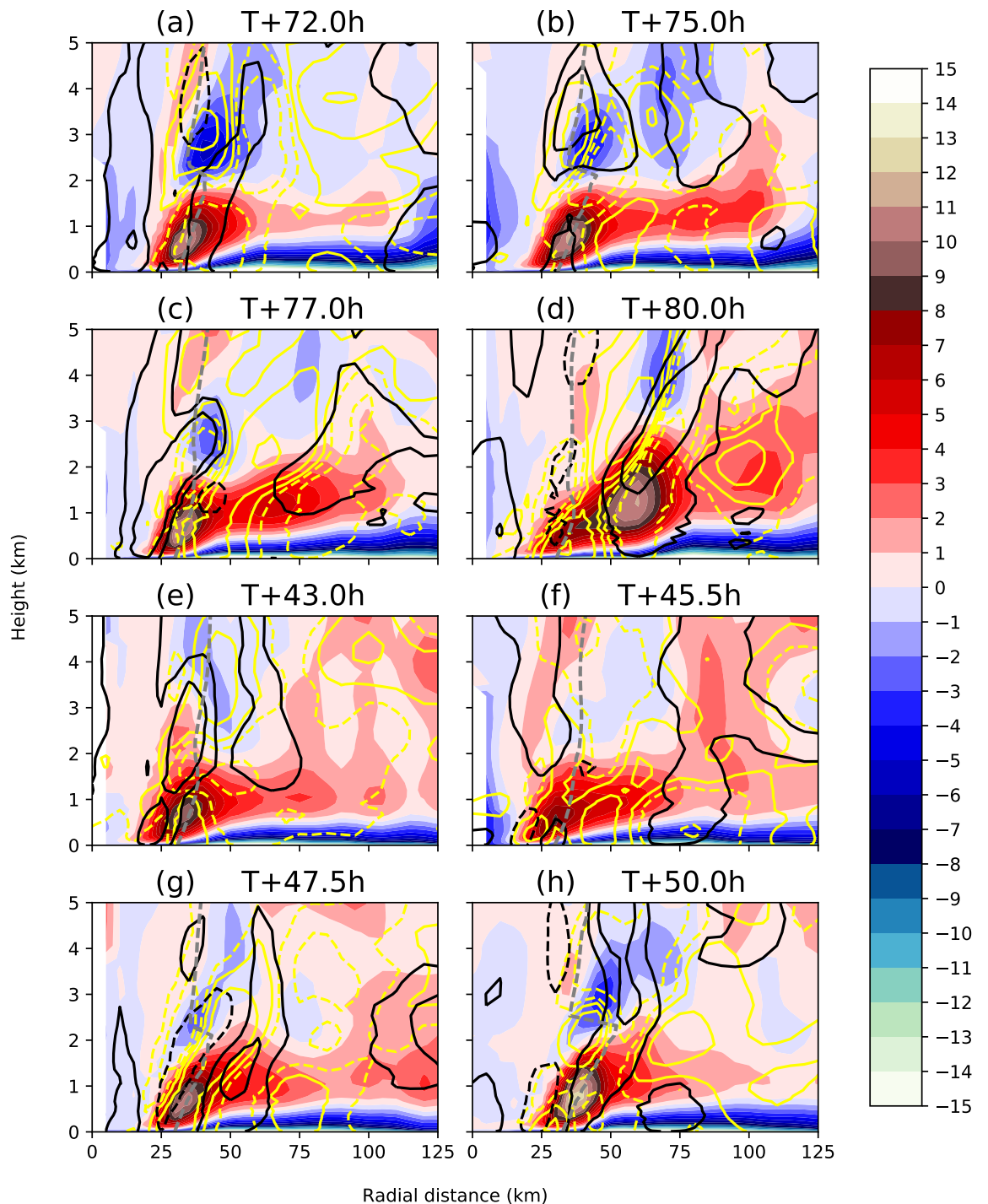


Figure 7.11: Agradient wind (m s^{-1} , shaded), hourly tendency of the radial wind ($0.5, 2, 5, 10 \text{ m s}^{-1} \text{ h}^{-1}$, positive (solid) and negative (dashed) yellow contours), tangential wind hourly tendency ($0.5, 2, 5, 10$ positive and negative $\text{m s}^{-1} \text{ h}^{-1}$, black contours). Panels a-d from ensemble member 10 of the 05 September 12 UTC simulation showing the full eyewall replacement cycle, panels e-h for ensemble member 15 of the 03 September 00 UTC simulation showing the intensity fluctuations.

Demise of the inner eyewall

It is useful to compare how the thermodynamic structure changes during the EWRC and the intensity fluctuations to determine any differences and similarities between the two kinds of intensity fluctuations. In the case of the EWRC the moat region plays an important role in the demise of the primary eyewall so it is useful to investigate whether something similar happens in the intensity fluctuations.

Figure 7.12 shows the θ_e structure during key stages of the EWRC and intensity fluctuations. In the EWRC the moat is visible especially at around T+77 h (Figure 7.12a) as a region of local descent at around 5 km height and 60 km radius and relatively low radial θ_e gradients. As the secondary eyewall updraught strengthens and becomes dominant over the inner eyewall, the moat region moves radially inwards and is visible as a region of descent and locally low θ_e at around 40 km by T+83 h (Figure 7.12c). By T+86 h (Figure 7.12d) the remnants of the moat are still visible as a region of weak descent around 30 km radius and 2.5 km height. θ_e has started to increase at this point but both the absolute value of the θ_e and the radial θ_e gradient have not recovered with both being considerably lower than they were before SEF. At around 60 km, however, the radial θ_e gradient is substantially higher than it was before SEF which is the approximate radial location of the new eyewall.

By contrast, the intensity fluctuations do not seem to have any lasting impact on the θ_e structure of the storm. During the middle of the weakening phase (Figure 7.12e) the bifurcated ascent in the eyewall is associated with a low radial θ_e gradient. However, the gradient never goes positive as it does in the moat region during the EWRC (Figure 7.12b) and no low θ_e air is imported into the eye as it is during the EWRC. Prior to SEF (for example at T+72 h, not shown) during the EWRC a parcel moving inwards would experience a large increase in θ_e from the moat region to the eyewall on the order of a 17–20 K. After SEF (Figure 7.12 c) that has declined to 10–14 K.

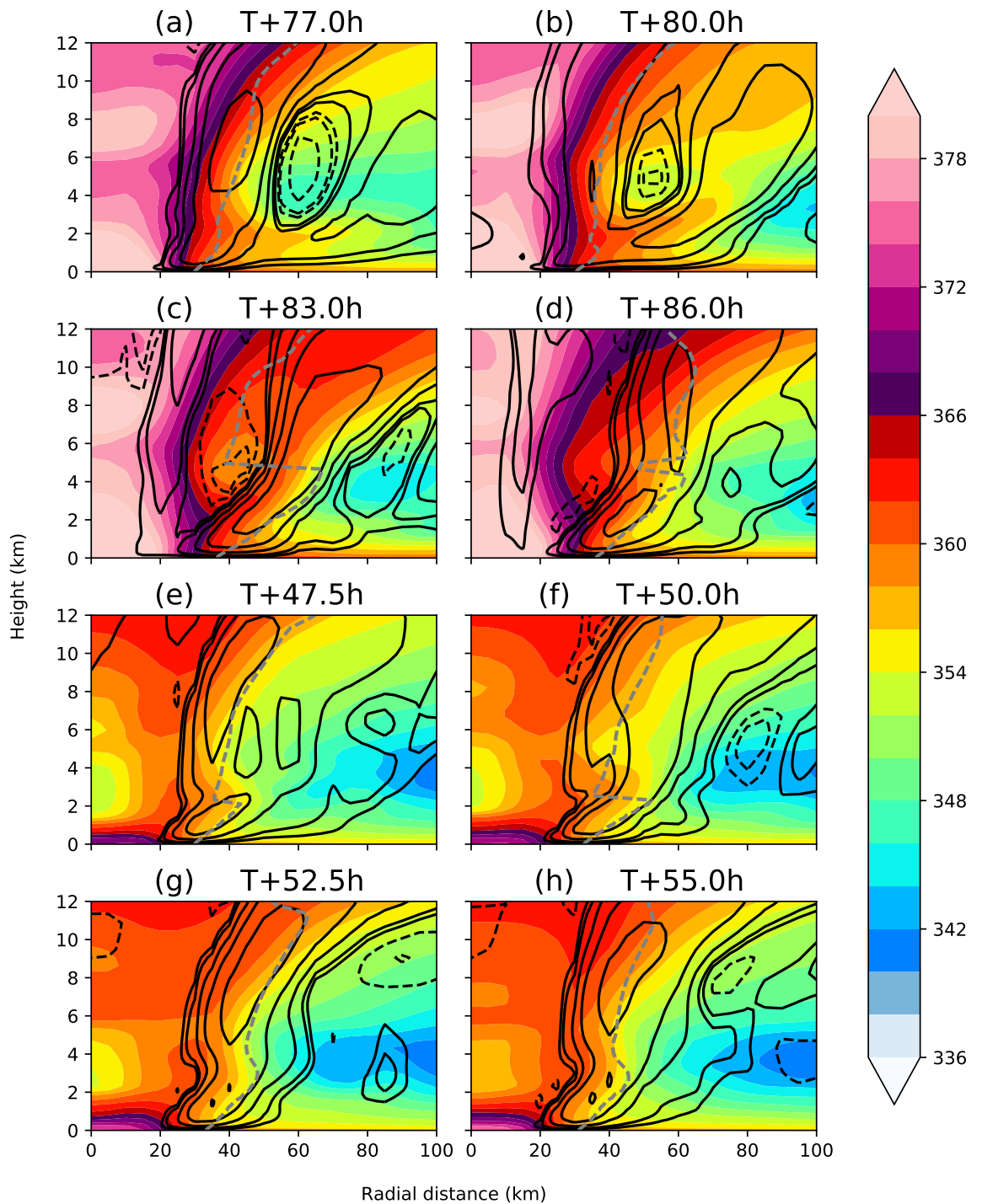


Figure 7.12: Equivalent potential temperature (K, shaded), vertical velocity (0.1, 0.2, 0.5, 2, 5, 10 m s^{-1} positive (solid) and negative (dashed) black contours). Panels a-d from ensemble member 10 of the 05 September 12 UTC simulation showing the full eyewall replacement cycle, panels e-h for ensemble member 15 of the 03 September 00 UTC simulation showing the intensity fluctuations.

7.3 Discussion

Several hypotheses were investigated in an attempt to understand the cause of the EWRC. One of those mechanisms was vortex Rossby waves. It was shown that a major vortex Rossby wave did occur at around $T+72$ hours and that it was convectively coupled (Figure 7.2) as well as showing agreement with the dispersion relation and there being evidence of a stagnation radius. The vortex Rossby wave event did have an impact on the tangential wind field, notably a wave–mean interaction (Figure 7.4b) led to an acceleration of the tangential wind around the stagnation radius at around 3 km height. However, any vortex Rossby wave events that occurred after $T+72$ h have less impact on the tangential wind field and also seem to be less convectively coupled. It is likely that the vortex Rossby wave event played an important role in broadening the tangential wind field prior to SEF but is unlikely to have been the direct cause of it.

Another mechanism investigated was the BSA. This can be ruled out as a direct cause of the SEF as a low level jet did not develop prior to the axisymmetrisation of the convection (Figure 7.5c) making a wind induced surface heat exchange feedback process impossible. Additionally, when the secondary wind maximum does develop (Figure 7.5d) it first appears above the boundary layer at around 3.5 km height. The convective updraughts associated with the new eyewall merge with the boundary layer hours earlier at around $T+77$ h (Figure 7.10c) implying that the formation of a coherent updraught effected a secondary wind maximum, not the reverse as would be the case in a BSA mechanism. Nevertheless expansion of the beta skirt did occur prior to SEF (especially after the vortex Rossby wave event at $T+72$ h which also likely played a role in enhancing the outer core vorticity) and significant tangential wind acceleration did occur in this increasingly expanding ‘goldilocks’ zone in the beta skirt outside of the filamentation zone (Figure 7.5 a-c, Figure 7.7 a-b) albeit with not enough of an acceleration to produce a low–level jet.

The most compelling mechanism for the EWRC is an unbalanced feedback process that begins with a broadening of the tangential wind field, largely above the boundary layer, that can be seen in Figure 7.7 a-b. The initial cause of this tangential

broadening is likely a balanced adjustment to the outer rainband causing increased inflow above the boundary layer which can be seen especially in Figure 7.7b at around 80 km radius. The broadening of the tangential wind in the SEF region above the boundary layer precedes a rapid increase in the agradient wind and development of a supergradient wind in the middle of the boundary layer (Figure 7.6b) that occurs between 60 km and 100 km radius after 77 h. The rapid development of the supergradient wind in the middle of the boundary layer at 77 h corresponds to the time when the rainbands axisymmetrise into a coherent tower of vertical velocity (Figure 7.10c) indicating the main cause of the spontaneous axisymmetrisation of the rainband into an eyewall structure is the outward agradient force within the boundary layer causing air to erupt out of the boundary layer and merge with the ascent associated with the rainband above.

The cause of the increased agradient wind is more difficult to determine. The mechanism to increase the agradient wind described by Tyner et al. (2018) and others is that tangential broadening above the boundary layer leads to increased frictionally induced boundary layer inflow which in turn through the unbalanced spin-up mechanism (Smith et al., 2009) leads to the increased agradient wind at some height within the boundary layer. The problem is, the surface inflow only rapidly increases after 79 h at around 65 km radius (Figure 7.6a) by which time the supergradient wind has already developed above (Figure 7.6b). At slightly higher radii (70–80 km), though, the surface inflow does increase earlier at around 76.5 h and there is an increase in the boundary layer inflow at 60–90 km radius at 552 m at around 77 h (Figure 7.6b). It is plausible that the lack of obvious causality (with increased surface radial wind preceding the increase in supergradient wind) is due to a positive feedback effect. An initial increase in the boundary inflow accelerates the tangential wind (and increases the agradient wind) in the boundary layer which in turn increases the frictionally induced inflow and further increases the supergradient wind. At the surface there is an increase in the tangential wind after T+76.5 h (Figure 7.6). Increases in the agradient wind at the 552 m level are modest between T+76 h and T+78 h on the order of $2\text{ m s}^{-1}\text{ h}^{-1}$ compared to $5\text{ m s}^{-1}\text{ h}^{-1}$ afterwards. It is noteworthy that amongst other studies that do claim

the unbalanced mechanism plays a role in SEF this apparent absence of causality is observed. For example in Huang et al. (2012) comparing their Fig. 5a with their 5c shows that between 10 September 15:00 UTC 10 September 21:00 UTC the radial inflow does not increase (and may even decrease slightly) yet the agradient wind is increasing during this time. Another example is in Chen (2018) in their Figure 11b the agradient wind increases monotonically from around T+159 h yet the radial inflow only starts to increase at around T+168 h.

It is therefore proposed that the cause of the SEF is a sequence of events that start with the development of outer-rainband activity from T+65 h onwards. Balanced dynamical adjustment to the diabatic heating from the rainband leads to increased inflow above the boundary layer which in turn accelerates the tangential wind field. The acceleration of the tangential wind field is also aided by a vortex Rossby wave event that occurs at around T+72 h. Between T+72 h and T+77 h the convection associated with the rainband continues to organise and move radially inward and the tangential wind above the boundary layer increases. Eventually the acceleration of the tangential wind above the boundary layer leads to an increased boundary layer radial inflow and concomitant development of the supergradient wind that causes the air to erupt out of the boundary layer to form the coherent secondary vertical velocity maximum. Once this updraught in the SEF region has appeared at all height levels the development of a secondary tangential wind maximum follows a few hours afterwards.

Having established the likely mechanism for the EWRC, a comparison with the intensity fluctuations can be undertaken. In Zhang et al. (2017) during the composite for a full EWRC (their Figure 6) the ascent associated with the outer rainband gradually descends and moves radially inwards until T+35 h when it merges with the boundary layer. In contrast in their ‘partial EWRC’ composite (their Figure 11) the ascent associated with the rainband does not develop and merge with the boundary layer, instead ascent beginning at around T+35 h just radially outside of the eyewall and above the boundary layer develops into a second pillar of vertical velocity by T+45 h. The differences between Figure 6 and Figure 11 in Zhang et al. (2017) are reminiscent of the differences between Figure 7.10a–d and Figure 7.10e–

h in this study suggesting that the ‘partial EWRC’ in Zhang et al. (2017) may be similar to the intensity fluctuations in Irma. An additional similarity is the lack of a coherent tropospheric outflow channel in the ‘partial EWRC’ case that does appear in the full EWRC case (as it does in this study’s EWRC example). However the intensity fluctuations did occur over a short time interval (around 6 hours) compared to the ‘partial EWRC’s in Zhang et al. (2017) which occurred over a longer time period and so the resumption of the intensification also took longer (but still shorter in ‘partial EWRC’s’ compared to the full EWRCs in Zhang et al. (2017)). A similar phenomenon to the ‘partial EWRC’ is described in Wang and Tan (2020) as a ‘fake SEF’ whereby inner rainband activity can drive boundary layer inflow, convergence and an increase in the agradient wind (as is also seen in the intensity fluctuations) but without the positive feedback associated with a ‘wind–maximum’ pathway. This lack of ‘wind–maximum’ pathway represents a plausible difference between EWRCs and the intensity fluctuations. Figure 7.12 confirms that the SEF is associated with a large tangential acceleration outside of the eyewall and results in a larger change in the agradient wind compared to the intensity fluctuations where the tangential acceleration is short lived and not big enough to result in a secondary wind maximum.

A key difference between intensity fluctuations that may be driven by inner rainband activity compared to outer rainband activity driven EWRCs is the development of a moat which can be seen in Figure 7.12. The difference between an EWRC involving a large moat compared to a smaller one is seen in Zhou and Wang (2011) in their Figure 11. With the larger moat the inner eyewall is replaced and low entropy air is imported into the eye (similar to Figure 7.12a–d) whereas with the smaller moat the low θ_e reservoir quickly dissipates and the bifurcated eyewall structure reorganises into a coherent pillar of ascent. In the case of the intensity fluctuations there is no moat at all but the radial θ_e gradient does become temporarily weaker. As such it is proposed that the thermodynamic structural differences in the EWRC and the intensity fluctuations can be explained by the absence of a moat, which in turn is caused by a balanced and unbalanced response to an inner rainband occurring radially inward of the filamentation zone. As in Zhou and Wang (2011)

a likely mechanism for the demise of the primary eyewall is the cutting off of high entropy source. As explained in Emanuel (1991) a hurricane can be considered like a Carnot cycle with the inflow leg being an isothermal expansion with air parcels picking up entropy from the environment; in the case of the EWRC the secondary eyewall reduces the length of this radial inflow to the primary eyewall, with a smaller entropy change and as a result there is less energy available to the inner eyewall during the ascending leg.

7.4 Summary and conclusions

The aim of the chapter was to understand the processes at work during a full eyewall replacement cycle in Hurricane Irma (2017) on 07 and 08 September and secondly, to compare those processes to the intensity fluctuations that occurred during RI a few days earlier. For the first aim it was determined that the EWRC was likely due to boundary layer convergence, of air, that resulted from a balanced adjustment to outer rainband activity. Vortex Rossby waves and the BSA mechanism were found to play ancillary roles but were not the main cause of the SEF. The subsequent demise of the inner eyewall is hypothesised to be caused by the interruption of the supply of warm, moist, high entropy air by the outer eyewall. In terms of comparing the EWRC with the intensity fluctuations, there were clear similarities: notably the integral role of the unbalanced spin-up mechanism in both types of fluctuation; however, there are also many differences including the changing PV structure, changing secondary circulation and the changing θ_e structure. Most significantly, the intensity fluctuations were a consequence of inner rainband activity while EWRCs are a consequence of outer rainband activity with the clear presence of a moat. Key findings from this analysis include the following:

- The SEF is largely due to unbalanced dynamics: boundary layer convergence is promoted through the development of the supergradient wind, a consequence of the broadening tangential wind field above the boundary layer.
- Vortex Rossby waves do not cause SEF in this case, but play a role in broadening the tangential wind field, an important step to SEF. Development of

a beta skirt prior to SEF likely also led to more ideal conditions for SEF to occur by promoting tangential wind acceleration in the beta skirt.

- The EWRC was characterised by a ring-like PV structure prior to and during SEF, followed by a transition to a monopolar PV structure after the secondary eyewall became dominant.
- The EWRC was characterised by an azimuthally symmetric PV structure that became more asymmetric after the secondary eyewall became dominant. Unlike in the intensity fluctuations, an azimuthally asymmetric PV structure was correlated to a more monopolar PV structure.
- Prior to SEF the convection associated with the outer rainband became increasingly intense and moved gradually inward and downwards before merging with the boundary layer during SEF. The intensity fluctuations, by contrast, had no similar SEF event and behaved more like a reorganisation of the eyewall structure rather than a replacement.
- The increase in the supergradient wind and associated boundary layer inflow was much more pronounced compared to the increase in the supergradient wind outside of the eyewall in the intensity fluctuations.
- Prior to SEF a moat region of descent and low equivalent potential temperature developed that eventually ended up in the eye after the replacement. By contrast the thermodynamic structure of the storm during the intensity fluctuations was stable.

It is proposed that the initiating mechanisms behind EWRCs and intensity fluctuations are similar, with both beginning with a dynamic, balanced response to diabatic heating. In the case of the EWRC diabatic heating is associated with outer rainbands far from the eyewall, while in the intensity fluctuations it is associated with inner rainbands and VHT-like structures emanating from the eyewall. Despite the similar initial cause, the sequence of events is quite different because in the case of the EWRC the SEF occurs far from the eyewall and is separated from it by a moat region, whereas with the intensity fluctuations the process happens at the outer edge of the eyewall itself. As a result an intensity fluctuation is a

transient weakening associated with a brief reorganisation of the eyewall, while an EWRC is a permanent substantial structural change to the storm that necessitates the complete destruction of one eyewall at the expense of building another.

Chapter 8

Discussion and Conclusions

Hurricane Irma (2017) exhibited short intensity fluctuations during RI. Brief intensity fluctuations during RI that affect a TC's structure are not well studied but could have practical implications, for example in expanding the radius of gale force winds or reducing the potential wind damage by lowering the tangential winds prior to landfall. The main objective of this study was to understand the cause of the intensity fluctuations that occurred during a period of RI in Hurricane Irma (2017) between 04 September and 06 September. These intensity fluctuations were characterized by short periods where the maximum tangential wind speed did not increase and the MSLP did not decrease. What made these fluctuations unusual is that the periods of weakening or stagnation lasted less than six hours and the storm was immediately able to resume intensification afterwards. This behaviour is in stark contrast to the most common form of intensity fluctuation, the eyewall replacement cycle which causes a major structural reorganisation of the inner-core preventing any resumption of intensification, including RI, for typically more than 24 hours (e.g. Sitkowski et al., 2011). The intensity fluctuations were similar to a phenomenon called vacillation cycles (Nguyen et al., 2011) which are also short-term fluctuations that occur during RI with weakening or strengthening phases typically lasting 2–8 hours. However, there are some notable differences between the intensity fluctuations in Hurricane Irma and vacillation cycles, notably the azimuthally asymmetric convection and the PV distribution which is associated with strengthening rather than weakening. There have been relatively few studies on vacillation cycles and

less focus on whether the conditions that give rise to these are predictable. Hence, this motivated the need for an extensive study on the intensity fluctuations with an emphasis on the initial cause of the weakening. In addition, Hurricane Irma underwent a full eyewall replacement cycle from 07 to 08 September. By simulating the eyewall replacement cycle a direct comparison was made between the two kinds of intensity fluctuations which gives new insight on both types of fluctuations. The main questions answered were:

1. What structural changes occurred during the course of a weakening and strengthening phases of the intensity fluctuations?
2. How well can a balanced dynamical paradigm explain the intensity fluctuations?
3. What caused the intensity fluctuations in Hurricane Irma (2017), to occur?
4. What are the differences and similarities between these intensity fluctuations in Hurricane Irma (2017) and vacillation cycles described in other storms?
5. What are the dynamical processes involved in the full EWRC in Hurricane Irma (2017) that occurred between 07 and 08 September?
6. Do intensity fluctuations exist on a spectrum between vacillation cycles and EWRCs?

8.1 Summary of findings

8.1.1 Model evaluation

In order to address these questions convection-permitting ensemble simulations with the MetUM were run (details of the model setup are given in Chapter 3) with different initialization times covering the second period of RI and the eyewall replacement cycle that occurred afterwards. In Chapter 4, a model evaluation was conducted to ensure that the structure of the storm was accurately represented so the model simulations could be used to investigate the dynamics of Hurricane Irma. All of the ensemble members were able to reproduce the track of the storm and the MSLP but underestimated the surface wind strength. Nevertheless, all of

the ensemble members produced a period of RI of the correct duration (around two days). A thorough analysis of the flight, dropsonde, radar and satellite data confirmed the salient features of the storm structure were accurately replicated including the radial–height distribution of the azimuthal and radial wind, as well as the boundary layer inflow, although the model did tend to overestimate the RMW slightly. Of the ensemble members, ensemble member 15 best represented Hurricane Irma (specifically by having the smallest RMW and starting RI later than the other ensemble members as well as being one of the better ensemble members at replicating the MSLP) and was therefore, the subject of much of the more in–depth analysis.

In addition to the model being able to accurately describe the RI and the track of the storm to an acceptable degree, it was also able to accurately replicate the secondary circulation, with the boundary layer inflow and outflow jet above being well captured by the model. The convective structure of Irma was also qualitatively handled well with banding features in the radar and satellite imagery matching the model output. The ability of the model to replicate the convective structure and the primary and secondary wind fields gives confidence that the results and analysis from model simulations in subsequent chapters are a fair reflection of reality.

8.1.2 Analysis of intensity fluctuations during RI

Having established the MetUM is capable of accurately simulating the development of Hurricane Irma, an in–depth investigation into the cause of the intensity fluctuations was undertaken in Chapter 5. A mechanism for the cause of the intensity fluctuations was proposed where heating associated with inner rainbands leads to an increased inflow above the boundary and convergence outside of the eyewall in turn leading to the reorganisation of the eyewall updraught through an unbalanced spin–up process.

The initial cause of the intensity fluctuations was determined to be the inner rainband activity (question 3). During the strengthening phases local regions of enhanced vorticity and vertical velocity described as ‘VHT–like’ structures became more prominent at the intersection between inner rainbands and the eyewall.

Nguyen et al. (2011) and Reif et al. (2014) also made reference to the importance of the VHT-like structures that contribute to increasing barotropic instability and the eventual breakdown of the PV ring and stirring of PV anomalies associated with the VHT-like structures into the centre. In the simulated intensity fluctuations for Hurricane Irma, it is reasonable to assume barotropic instability played a role. However, unlike in the case of Nguyen et al. (2011) and Reif et al. (2014), the weakening of the tangential wind field preceded the transport of PV into the eye and it was not found that this stirring inwards of PV was associated with a pressure drop; instead the stagnation or rise of the MSLP was concurrent with the weakening of the tangential wind field.

In Hurricane Irma, the transport of PV into the eye and the transition of the storm to a more barotropically stable state (described as more monopolar) is a consequence of a lack of diabatic heating in the eyewall during the start of the weakening phase which is a result of the heating being more concentrated outside of the eyewall in the VHT-like structures. Another difference between Nguyen et al. (2011) and Reif et al. (2014) is the association between the radial PV distribution and the azimuthal PV distribution. In contrast to the vacillation cycles, the weakening phases, which were associated with a more monopolar distribution of PV, had greater azimuthal PV symmetry and strengthening occurred when the PV was in a less symmetric state. This was because the asymmetry was caused by the VHT-like structures. During the strengthening phases the VHT-like structures became stronger and were able to contribute to the intensification of the storm above the boundary layer by the eddy advection of AAM (question 1).

It was emphasised in Chapter 5 that the radial location of the VHT-like structures was important. VHT-like structures that became too intense and moved outside of the eyewall resulted in the start of the weakening phase which was explained in terms of the unbalanced spin-up mechanism described in Montgomery and Smith (2018). The enhancement of the outflow jet above the boundary layer, combined with the inflow as a balanced response to the VHT-like structures, led to tangential wind weakening within the eyewall and strengthening outside of the eyewall. A key difference, therefore, between the intensity fluctuations and vacillation cycles is

the importance of the balanced response to the VHT-like structures and resultant disruption of the eyewall structure through unbalanced dynamics (question 4).

8.1.3 Intensity fluctuations from a balanced perspective

Having noted the importance of the inner rainbands and VHT-like structures, and hypothesised that the first step of a weakening phase involves a balanced dynamical response above the boundary layer, it was important to confirm this. Chapter 6 examines the intensity fluctuations through the lens of balanced dynamics by comparing the MetUM output with a balanced model originally used in Smith et al. (2015). The main advantage of the Sawyer–Eliassen approach is it allowed a causal link to be established between a balanced response and a tangential acceleration rather than just an association.

It was found that the balanced effect of the diabatic heating alone was capable of explaining the change in RMW during the weakening phase and the tangential wind deceleration in the eyewall which implies that the change in the diabatic heating structures analysed in Chapter 5 were capable of initiating the weakening phase. Those azimuthally averaged diabatic heating structures were known to be caused by the increased inner rainband activity and VHT-like structures, providing further confirmation that the balanced response from these structures is essential to initiating the weakening phase. The balanced effect of the eddy AAM sources was smaller than the effect of the diabatic heating, and contributed to tangential wind increase at the start of the weakening phase and tangential wind decrease by the end of the weakening phase. The most relevant balanced effect of friction was as a partial contribution to the intensification of the outflow jet which, in conjunction with the effect of the diabatic heating, lead to a weakening of the eyewall (question 2).

Another advantage of solving the Sawyer–Eliassen equation was the ability to determine the contribution of the unbalanced dynamics to the TC secondary circulation by comparing the secondary circulation from the Sawyer–Eliassen equation to that diagnosed in the MetUM. It was found that the relative contribution of unbalanced processes increased during the course of the first weakening period, which is con-

sistent with the results of the analysis in Chapter 5 that the unbalanced dynamics play an important role in reorganising the eyewall structure.

Another way to attempt to understand the relative importance of balanced dynamics was to run prognostic balanced simulations with the balanced model to try and replicate the intensity fluctuations from the balanced response to different diabatic heating distributions only. It was found that intensity fluctuations did occur but the weakening started several hours earlier than expected. So while a vortex that only evolved under the influence of the balanced dynamical response from diabatic heating did produce intensity fluctuations, they were not similar to those seen in Hurricane Irma.

8.1.4 Eyewall replacement cycle in Hurricane Irma (2017) and its link to intensity fluctuations

Intensity fluctuations in Hurricane Irma were also apparent in the detailed analysis of flight-level aircraft reconnaissance and microwave satellite observations performed by Fischer et al. (2020). It was hypothesised that the intensity fluctuations are a variant of an eyewall replacement cycle that had occurred during RI. Given that eyewall replacement cycles are not known to occur in RI and given that the associated weakening takes days rather than a few hours as observed during these intensity fluctuations it was necessary to investigate whether or not these fluctuations were a novel form of eyewall replacement cycle that occurred during RI and potentially on a spectrum that also includes vacillation cycles. This analysis was conducted in Chapter 7 which made use of the fact that a full eyewall replacement cycle occurred in Hurricane Irma between 07 September and 08 September which allowed a direct comparison between the intensity fluctuations between 04 September and 06 September and the eyewall replacement cycle between 07 September and 08 September.

The full eyewall replacement cycle was determined to have been caused by an unbalanced dynamical process caused by outer rainbands. This process can be understood as follows: outer rainband activity led to a broadening of the tangential wind field (aided by a vortex Rossby wave event and beta skirt axisymmetrisation) in the

secondary eyewall formation region which in turn led to both an increased boundary layer inflow and supergradient wind in the middle of the boundary layer. The increased supergradient wind and its associated outward gradient force led to an eruption of air from the boundary layer and development of the secondary eyewall which went on to develop a secondary wind maximum (question 5).

The intensity fluctuations analysed in Chapter 5, despite having some similarities with the full eyewall replacement cycle in Irma on 07 September, notably the involvement of unbalanced dynamics, involve a distinctly different sequences of events. The intensity fluctuations do, however, somewhat resemble so-called partial eyewall replacement cycles described in Zhang et al. (2017) where any updraughts in the mid or upper troposphere are unable to form coherent secondary eyewalls and the new eyewall develops from an outburst of ascending air from the boundary layer in the outflow jet near the eyewall. There were also similarities between the intensity fluctuations and the so called ‘fake’ secondary eyewall formation described in Wang and Tan (2020) whereby convection can develop in a coherent ring but without the positive feedback associated with a secondary wind maximum. Crucially the so called ‘fake’ secondary eyewall formation is the consequence of a balanced dynamical adjustment to inner rainband activity rather than outer rainband activity as is the case in the intensity fluctuations seen in Hurricane Irma. An equivalent potential temperature analysis of the eyewall replacement cycle showed that a moat region of low equivalent potential temperature formed, separating the inner eyewall from the secondary eyewall formation region, and eventually causing the demise of the inner eyewall when the cold dry air from the moat region was imported into the eye. However, this thermodynamic structural rearrangement does not occur in the intensity fluctuations (discussed in Chapter 7) and a moat region does not form. In Zhou and Wang (2011) a large moat resulted in a longer and more dramatic period of weakening compared to a smaller moat case which looked more similar to the intensity fluctuations indicating the lack of a moat is one distinguishing feature between intensity fluctuations and eyewall replacement cycles. One explanation could be that vacillation cycles or intensity fluctuations are eyewall replacement cycles but initiated with inner rainbands rather than outer rainbands and too close to the

eyewall to form a moat region (question 6).

To conclude, this study has provided an extensive insight into intensity fluctuations that occurred during RI in Hurricane Irma. Understanding these fluctuations extends previous work on vacillation cycles, which are another form of intensity fluctuations that occur during RI, particularly by emphasising the role of unbalanced dynamics in the reorganisation of the eyewall during the weakening phases. The analysis has also been able to determine the initial cause of the fluctuations as a balanced response to convection in inner rainbands. By comparing the intensity fluctuations with eyewall replacement cycles new light has been shed on how important the radial location of the convection is in the balance response it produces. If the convection is radially close to the eyewall it causes an intensity fluctuation by temporarily disrupting the structure of the eyewall; if it is radially far from the eyewall it gradually leads to the genesis of a secondary eyewall separated from the inner eyewall by a moat of low θ_e air, which allows the inner eyewall to remain intact during the SEF process.

8.2 Implications

Understanding the intensity fluctuations in Hurricane Irma has fundamental implications for our understanding of TC inner core dynamics, particularly how the balanced response to stochastic processes (VHT-like structures in the inner rainbands in the eyewall) can lead to several hours of weakening. This study has improved our understanding of these short-term intensity fluctuations during RI. In particular, this analysis, has extended previous research on vacillation cycles by highlighting the importance of an unbalanced spin-up process that occurs within the boundary layer. The role of barotropic instability and PV mixing in the vacillation cycles is well known, but this study adds to that by noting the role of the inner rainbands in disrupting the diabatic heating structure of the eyewall. Although it has been noted that VHT-like structures play a role it was found that many of the features associated with these intensity fluctuations can be replicated in a balanced axisymmetric perspective.

In addition to improving our understanding of the intensity fluctuations in RI, novel understanding has also been gained about eyewall replacement cycles. It has been proposed that an eyewall replacement cycle is initiated by the same balanced response as an intensity fluctuation but radially far from the eyewall. Future work could involve attempting to establish a threshold for the minimum radius for the balanced response to lead to an eyewall replacement cycle rather than an intensity fluctuation.

The implications for numerical weather forecasting are also important including the development of the MetUM. It has been shown that the intensity fluctuations are caused by stochastic processes with small differences in the radial location of convection making a large difference to the timing of weakening and strengthening phases. This emphasises the need for both convection-permitting forecasts to accurately represent convection and the use of ensembles since the fluctuations only occurred in about a third of the ensemble members. In addition, it has been shown that the boundary layer plays a crucial role in the initiation of the weakening phase, hence it is important to represent the processes in of the boundary layer adequately.

The results also have practical consequences for how TCs are observed. A first clue that a weakening phase is about to start involves changes in the tangential wind structure at the top of the boundary layer at around 1000 m to 1500 m height which is below the typical height for flight level data. Monitoring changes in the storm structure at this level could be crucial in predicting the onset of the fluctuations as well as understanding them from an observational perspective.

There have been some methodological advances made in this thesis in the process of understanding the intensity fluctuations. For example, in Chapter 5 PV tracers were used in a unique way to diagnose the advection only (non-diabatic) contributions to PV each hour by resetting the tracers each hour and comparing to the prognostic model field. This method could also be used analogously with potential temperature. In Chapter 6 a prognostic balanced simulations were run using two different approaches. Firstly, an initial tangential wind field was allowed to evolve under a constant forcing corresponding to a single output time in the MetUM. Multiple simulations could be run with different forcings corresponding to different constant

output times. Secondly, the forcing could be variable and change hour by hour, as the forcings in the MetUM would and instead different simulations could be run with different starting initial wind fields. Use of these two approaches could provide more comprehensive insight of the effect of various forcings on the balanced evolution of a TC. In Chapter 7 and Chapter 5 a new way of verifying VRW activity was proposed. By using empirical mode decompositions the radial, and vertical VRW wavenumbers could be calculated as a function of radius and height which would allow azimuthal, radial and vertical phase speed to be predicted for any radius or height which would make verification potentially much easier since it could be done for the entire TC rather than just a single radius or height. More details about some of these methods are available in Chapter 3.

There has also been some useful testing and analysis of previous methods particularly in Chapter 4 which includes a comparison between TPF and WCF storm centre finding and in Chapter 6 where different SE regularization methods are compared.

8.3 Limitations and future work

One of the main limitations of this work is that it only extended to a single storm so it is not known how common the fluctuations are or whether they are more likely in storms with certain characteristics (e.g. major hurricanes undergoing RI). Future investigations could include extending the analysis to more storms undergoing RI of differing strengths and in different basins. In the case of Hurricane Irma, 33% of the ensemble members developed distinct intensity fluctuations (and an additional 31% developed less distinct intensity fluctuations) during RI compared to 60% in Hardy et al. (2021) and 77% in Hankinson et al. (2014) suggesting that the occurrence of intensity fluctuations may be common given the right conditions. Given the similarity of the ensemble members in terms of storm intensity and structure, it is likely that what determines whether or not fluctuations occur is stochastic, for example whether the inner rainband convection is strong enough and happens to develop at the right radius. Further research on the method of perturbing ensembles and its impact on the proportion of cases showing the fluctuations may be useful

in determining what model physics the fluctuations are sensitive to. It would also be useful in attempting to understand, in more depth, why some cases have these intensity fluctuations and others do not, and whether it is possible to predict if an ensemble member will show fluctuations prior to a first weakening phase.

There are many similarities between these intensity fluctuations and vacillation cycles, such as the duration of the fluctuations. There are also considerable differences. Intensity fluctuations occurring in Hardy et al. (2021) for example, had periods where the storm was much more monopole-like in terms of its PV structure and kept its monopolar PV structure for much longer compared to the fluctuations seen here. The reasons for this are unknown and could form part of a future investigation which might involve running simulations from many different storms and cataloguing differences in any structural changes during the intensity fluctuations. In terms of the differences between vacillation cycles, eyewall replacement cycles and intensity fluctuations there may be different processes of the type observed in Hurricane Irma governing them, even if a general rule of thumb is that eyewall replacement cycles are linked to outer rainband activity and vacillation cycles are linked to inner rainband activity.

Finally, it would be prudent to run simulations with a higher grid resolution which would better capture the convection and to examine what the effect of this is on the probability of fluctuations occurring. It is still unknown how sensitive these intensity fluctuations are to the spatial resolution of the model.

To conclude, this thesis has investigated observed intensity fluctuations in Hurricane Irma (2017). These intensity fluctuations were found to be similar to vacillation cycles and were initiated by a balanced response to inner rainband activity. In addition the thesis has shown that eyewall replacement cycles have the same initial cause but lead to a radically different set of structural changes in the TC.

Bibliography

- Abarca, S. F. and Corbosiero, K. L. (2011). Secondary eyewall formation in WRF simulations of Hurricanes Rita and Katrina (2005). *Geophysical Research Letters*, 38(7). DOI:<https://doi.org/10.1029/2011GL047015>.
- Abarca, S. F. and Montgomery, M. T. (2014). Departures from axisymmetric balance dynamics during secondary eyewall formation. *Journal of the Atmospheric Sciences*, 71(10):3723 – 3738. DOI:10.1175/JAS-D-14-0018.1.
- Arakawa and Lamb (1977). Computational design of the basic dynamical processes of the ucla general circulation model. In CHANG, J., editor, *General Circulation Models of the Atmosphere*, volume 17 of *Methods in Computational Physics: Advances in Research and Applications*, pages 173–265. Elsevier. DOI:<https://doi.org/10.1016/B978-0-12-460817-7.50009-4>.
- Barnes, G. M. and Fuentes, P. (2010). Eye excess energy and the rapid intensification of Hurricane Lili (2002). *Monthly Weather Review*, 138(4):1446 – 1458. DOI:10.1175/2009MWR3145.1.
- Bell, M. M. and Lee, W.-C. (2012). Objective tropical cyclone center tracking using single-doppler radar. *Journal of Applied Meteorology and Climatology*, 51(5):878 – 896. DOI:10.1175/JAMC-D-11-0167.1.
- Best, M. J., Pryor, M., Clark, D. B., Rooney, G. G., Essery, R. L. H., Ménard, C. B., Edwards, J. M., Hendry, M. A., Porson, A., Gedney, N., Mercado, L. M., Sitch, S., Blyth, E., Boucher, O., Cox, P. M., Grimmond, C. S. B., and Harding, R. J. (2011). The joint UK land environment simulator (JULES), model description. Part 1: Energy and water fluxes. *Geoscientific Model Development*, 4(3):677–699.

- Black, P. G., D'Asaro, E. A., Drennan, W. M., French, J. R., Niiler, P. P., Sanford, T. B., Terrill, E. J., Walsh, E. J., and Zhang, J. A. (2007). Air sea exchange in hurricanes: Synthesis of observations from the coupled boundary layer air sea transfer experiment. *Bulletin of the American Meteorological Society*, 88(3):357 – 374. DOI:10.1175/BAMS-88-3-357.
- Bolton, D. (1980). The computation of equivalent potential temperature. *Monthly Weather Review*, 108(7):1046 – 1053. DOI:10.1175/1520-0493(1980)108<1046:TCOEPT>2.0.CO;2.
- Boutle, I. A., Abel, S. J., Hill, P. G., and Morcrette, C. J. (2014). Spatial variability of liquid cloud and rain: Observations and microphysical effects. *Quarterly Journal of the Royal Meteorological Society*, 140(679). DOI:<https://doi.org/10.1002/qj.2140>.
- Bowler, N. E., Arribas, A., Mylne, K. R., Robertson, K. B., and Beare, S. E. (2008). The MOGREPS short-range ensemble prediction system. *Quarterly Journal of the Royal Meteorological Society*, 134(632):703–722. DOI:<https://doi.org/10.1002/qj.234>.
- Bryan, G. H. (2008). On the computation of pseudoadiabatic entropy and equivalent potential temperature. *Monthly Weather Review*, 136(12):5239 – 5245. DOI:10.1175/2008MWR2593.1.
- Buck, A. L. (1981). New equations for computing vapor pressure and enhancement factor. *Journal of Applied Meteorology and Climatology*, 20(12):1527 – 1532. DOI:10.1175/1520-0450(1981)020<1527:NEFCVP>2.0.CO;2.
- Bui, H. H., Smith, R. K., Montgomery, M. T., and Peng, J. (2009). Balanced and unbalanced aspects of tropical cyclone intensification. *Quarterly Journal of the Royal Meteorological Society*, 135(644):1715–1731. DOI:10.1002/qj.502.
- Bush, M., Allen, T., Bain, C., Boutle, I., Edwards, J., Finnenkoetter, A., Franklin, C., Hanley, K., Lean, H., Lock, A., Manners, J., Mittermaier, M., Morcrette, C., North, R., Petch, J., Short, C., Vosper, S., Walters, D., Webster, S., Weeks, M., Wilkinson, J., Wood, N., and Zerroukat, M. (2020). The first Met Office Unified

- Model–JULES regional atmosphere and land configuration, r11. *Geoscientific Model Development*, 13(4):1999–2029.
- Callaghan, J. (2017). Asymmetric inner core convection leading to tropical cyclone intensification. *Tropical Cyclone Research and Review*, 6(3):55–66. DOI:<https://doi.org/10.6057/2017TCRRh3.02>.
- Cangialosi and Berg (2018). National Hurricane Center tropical cyclone report Hurricane Irma 20 August. <https://www.nhc.noaa.gov/data/tcr/>.
- Chagnon, J. M., Gray, S. L., and Methven, J. (2013). Diabatic processes modifying potential vorticity in a North Atlantic cyclone. *Quarterly Journal of the Royal Meteorological Society*, 139(674):1270–1282. DOI:<https://doi.org/10.1002/qj.2037>.
- Chan, K. T. F., Wang, D., Zhang, Y., Wanawong, W., He, M., and Yu, X. (2019). Does strong vertical wind shear certainly lead to the weakening of a tropical cyclone? 1(1):015002. DOI:10.1088/2515-7620/aaecac.
- Charney, J. G. and Phillips, N. A. (1953). Numerical integration of the quasi-geostrophic equations for barotropic and simple baroclinic flows. *Journal of Atmospheric Sciences*, 10(2):71 – 99. DOI:10.1175/1520-0469(1953)010<0071:NIOTQG>2.0.CO;2.
- Chen, G. (2018). Secondary eyewall formation and concentric eyewall replacement in association with increased low-level inner-core diabatic cooling. *Journal of the Atmospheric Sciences*, 75(8):2659 – 2685. DOI:10.1175/JAS-D-17-0207.1.
- Chen, H. and Gopalakrishnan, S. G. (2015). A study on the asymmetric rapid intensification of Hurricane Earl (2010) using the HWRF system. *Journal of the Atmospheric Sciences*, 72(2):531 – 550. DOI:10.1175/JAS-D-14-0097.1.
- Corbosiero, K. L., Molinari, J., Ayyer, A. R., and Black, M. L. (2006). The structure and evolution of Hurricane Elena (1985). Part II: Convective asymmetries and evidence for vortex Rossby waves. *Monthly Weather Review*, 134(11):3073 – 3091. DOI:10.1175/MWR3250.1.
- Courtney, J. B., Langlade, S., Sampson, C. R., Knaff, J. A., Birchard, T., Bar-

- low, S., Kotal, S., Kriat, T., Lee, W., Pasch, R., and Shimada, U. (2019). Operational perspectives on tropical cyclone intensity change. Part 1: recent advances in intensity guidance. *Tropical Cyclone Research and Review*, 8(3):123–133. DOI:<https://doi.org/10.1016/j.tcrr.2019.10.002>.
- Davies, T., Cullen, M. J. P., Malcolm, A. J., Mawson, M. H., Staniforth, A., White, A. A., and Wood, N. (2005). A new dynamical core for the Met Office’s global and regional modelling of the atmosphere. *Quarterly Journal of the Royal Meteorological Society*, 131(608):1759–1782. DOI:<https://doi.org/10.1256/qj.04.101>.
- Dean, L., Emanuel, K. A., and Chavas, D. R. (2009). On the size distribution of Atlantic tropical cyclones. *Geophysical Research Letters*, 36(14). DOI: 10.1029/2009g1039051.
- DeMaria, M. (1996). The effect of vertical shear on tropical cyclone intensity change. *Journal of the Atmospheric Sciences*, 53(14):2076–2088. DOI:10.1175/1520-0469(1996)053<2076:TEOVSO>2.0.CO;2.
- Ditchek, S. D., Molinari, J., Corbosiero, K. L., and Fovell, R. G. (2019). An objective climatology of tropical cyclone diurnal pulses in the Atlantic basin. *Monthly Weather Review*, 147(2):591–605. DOI:10.1175/MWR-D-18-0368.1.
- Dunion, J., Thorncroft, C., and Velden, C. (2014). The tropical cyclone diurnal cycle of mature hurricanes. *Monthly Weather Review*, 142:3900–3919. DOI:10.1175/MWR-D-13-00191.1.
- Edwards, J. M. and Slingo, A. (1996). Studies with a flexible new radiation code. Part I: choosing a configuration for a large-scale model. *Quarterly Journal of the Royal Meteorological Society*, 122(531):689–719. DOI:<https://doi.org/10.1002/qj.49712253107>.
- Eliassen, A. (1951). Slow thermally or frictionally controlled meridional circulation in a circular vortex. *Astrophisica Norvegica*, 5:19–60.
- Emanuel, K. A. (1986). An air–sea interaction theory for tropical cyclones. Part I: Steady-state maintenance. *Journal of the Atmospheric Sciences*, 43(6):585–605. DOI:10.1175/1520-0469(1986)043<0585:AASITF>2.0.CO;2.

- Emanuel, K. A. (1991). The theory of hurricanes. *Annual Review of Fluid Mechanics*, 23(1):179–196. DOI:10.1146/annurev.fl.23.010191.001143.
- Faggian, N., Roux, B., Steinle, P., and Ebert, B. (2015). Fast calculation of the fractions skill score. *Mausam*, 66(3):457–466.
- Fischer, M. S., Rogers, R. F., and Reasor, P. D. (2020). The rapid intensification and eyewall replacement cycles of Hurricane Irma (2017). *Monthly Weather Review*, 148(3):981–1004. DOI:10.1175/MWR-D-19-0185.1.
- Fitzpatrick, P. J. (1997). Understanding and forecasting tropical cyclone intensity change with the typhoon intensity prediction scheme (TIPS). *Weather and Forecasting*, 12(4):826–846. DOI:10.1175/1520-0434(1997)012<0826:UAFTCI>2.0.CO;2.
- Frank, W. M. and Ritchie, E. A. (2001). Effects of vertical wind shear on the intensity and structure of numerically simulated hurricanes. *Monthly Weather Review*, 129(9):2249–2269. DOI:10.1175/1520-0493(2001)129<2249:E0VWSO>2.0.CO;2.
- Galperin, B., Sukoriansky, S., Dikovskaya, N., Read, P. L., Yamazaki, Y. H., and Wordsworth, R. (2006). Anisotropic turbulence and zonal jets in rotating flows with a beta effect. *Nonlinear Processes in Geophysics*, 13(1):83–98.
- Gentry, M. S. and Lackmann, G. M. (2010). Sensitivity of simulated tropical cyclone structure and intensity to horizontal resolution. *Monthly Weather Review*, 138(3):688 – 704. DOI:10.1175/2009MWR2976.1.
- Guimond, S. R., Heymsfield, G. M., and Turk, F. J. (2010). Multiscale observations of Hurricane Dennis (2005): The effects of hot towers on rapid intensification. *Journal of the Atmospheric Sciences*, 67(3):633–654. DOI:10.1175/2009JAS3119.1.
- Hankinson, M. C. N., Reeder, M. J., Davidson, N. E., and Puri, K. (2014). Vacillation cycles in simulations of Hurricane Katrina. *Quarterly Journal of the Royal Meteorological Society*, 140(683):1878–1888. DOI:10.1002/qj.2275.
- Hardy, S., Schwendike, J., Smith, R. K., Short, C. J., Reeder, M. J., and Birch,

- C. E. (2021). Fluctuations in inner-core structure during the rapid intensification of super Typhoon Nepartak (2016). *Monthly Weather Review*, 149(1):221 – 243. DOI:10.1175/MWR-D-19-0415.1.
- Harnos, D. S. and Nesbitt, S. W. (2016). Varied pathways for simulated tropical cyclone rapid intensification. Part II: Vertical motion and cloud populations. *Quarterly Journal of the Royal Meteorological Society*, 142(697):1832–1846. DOI:<https://doi.org/10.1002/qj.2778>.
- Hazelton, A. T., Hart, R. E., and Rogers, R. F. (2017). Analyzing simulated convective bursts in two Atlantic hurricanes. Part II: intensity change due to bursts. *Monthly Weather Review*, 145(8):3095 – 3117. DOI:10.1175/MWR-D-16-0268.1.
- Heming, J. T. (2016). Met Office Unified Model tropical cyclone performance following major changes to the initialization scheme and a model upgrade. *Weather and Forecasting*, 31(5):1433–1449. DOI:10.1175/waf-d-16-0040.1.
- Heming, J. T., Prates, F., Bender, M. A., Bowyer, R., Cangialosi, J., Caroff, P., Coleman, T., Doyle, J. D., Dube, A., Faure, G., Fraser, J., Howell, B. C., Igarashi, Y., McTaggart-Cowan, R., Mohapatra, M., Moskaitis, J. R., Murtha, J., Rivett, R., Sharma, M., Short, C. J., Singh, A. A., Tallapragada, V., Titley, H. A., and Xiao, Y. (2019). Review of recent progress in tropical cyclone track forecasting and expression of uncertainties. *Tropical Cyclone Research and Review*, 8(4):181–218. DOI:<https://doi.org/10.1016/j.tcrr.2020.01.001>.
- Hendricks, E. A., Montgomery, M. T., and Davis, C. A. (2004). The role of vortical hot towers in the formation of Tropical Cyclone Diana (1984). *Journal of the Atmospheric Sciences*, 61(11):1209 – 1232.
- Heng, J. and Wang, Y. (2016). Nonlinear response of a tropical cyclone vortex to prescribed eyewall heating with and without surface friction in TCM4: Implications for tropical cyclone intensification. *Journal of the Atmospheric Sciences*, 73(3):1315 – 1333. DOI:10.1175/JAS-D-15-0164.1.
- Heng, J., Wang, Y., and Zhou, W. (2017). Revisiting the balanced and unbalanced

- aspects of tropical cyclone intensification. *Journal of the Atmospheric Sciences*, 74(8):2575 – 2591. DOI:10.1175/JAS-D-17-0046.1.
- Holland, G. J. (1980). An analytic model of the wind and pressure profiles in hurricanes. *Monthly Weather Review*, 108(8):1212–1218. DOI:10.1175/1520--0493(1980)108<1212:aamotw>2.0.co;2.
- Holland, G. J., Belanger, J. I., and Fritz, A. (2010). A revised model for radial profiles of hurricane winds. *Monthly Weather Review*, 138(12):4393–4401. DOI:10.1175/2010mwr3317.1.
- Huang, N. E., Shen, Z., Long, S. R., Wu, M. C., Shih, H. H., Zheng, Q., Yen, N.-C., Tung, C. C., and Liu, H. H. (1998). The empirical mode decomposition and the hilbert spectrum for nonlinear and non-stationary time series analysis. *Proceedings of the Royal Society of London. Series A: Mathematical, Physical and Engineering Sciences*, 454(1971):903–995. DOI:10.1098/rspa.1998.0193.
- Huang, Y.-H., Montgomery, M. T., and Wu, C.-C. (2012). Concentric eyewall formation in Typhoon Sinlaku (2008). Part II: Axisymmetric dynamical processes. *Journal of the Atmospheric Sciences*, 69(2):662 – 674. DOI:10.1175/JAS-D-11-0114.1.
- Irish, J. L., Resio, D. T., and Ratcliff, J. J. (2008). The influence of storm size on hurricane surge. *Journal of Physical Oceanography*, 38(9):2003 – 2013. DOI:10.1175/2008JP03727.1.
- Judt, F. and Chen, S. S. (2010). Convectively generated potential vorticity in rainbands and formation of the secondary eyewall in Hurricane Rita of 2005. *Journal of the Atmospheric Sciences*, 67(11):3581 – 3599. DOI:10.1175/2010JAS3471.1.
- Kaplan, J. and DeMaria, M. (2003). Large-scale characteristics of rapidly intensifying tropical cyclones in the North Atlantic basin. *Weather and Forecasting*, 18(6):1093 – 1108. DOI:10.1175/1520-0434(2003)018<1093:LCORIT>2.0.CO;2.
- Kaplan, J., Demaria, M., and Knaff, J. A. (2010). A revised tropical cyclone rapid

- intensification index for the Atlantic and Eastern North Pacific basins. *Weather and Forecasting*, 25(1):220–241. DOI:10.1175/2009waf2222280.1.
- Kepert, J. D. (2005). Objective analysis of tropical cyclone location and motion from high-density observations. *Monthly Weather Review*, 133(8):2406–2421. DOI:10.1175/mwr2980.1.
- Kepert, J. D. (2018). The boundary layer dynamics of tropical cyclone rainbands. *Journal of the Atmospheric Sciences*, 75(11):3777 – 3795. DOI:10.1175/JAS-D-18-0133.1.
- Kilroy, G. and Smith, R. K. (2016). A numerical study of deep convection in tropical cyclones. *Quarterly Journal of the Royal Meteorological Society*, 142(701):3138–3151. DOI:https://doi.org/10.1002/qj.2895.
- Knapp, K. R., Kruk, M. C., Levinson, D. H., Diamond, H. J., and Neumann, C. J. (2010). The international best track archive for climate stewardship (IBTrACS): Unifying tropical cyclone data. *Bulletin of the American Meteorological Society*, 91(3):363 – 376. DOI:10.1175/2009BAMS2755.1.
- Kossin, J. P. (2015). Hurricane wind pressure relationship and eyewall replacement cycles. *Weather and Forecasting*, 30(1):177–181. DOI:10.1175/waf-d-14-00121.1.
- Kossin, J. P. and Eastin, M. D. (2001). Two distinct regimes in the kinematic and thermodynamic structure of the hurricane eye and eyewall. *Journal of the Atmospheric Sciences*, 58(9):1079–1090. DOI:10.1175/1520-0469(2001)058<1079:TDRITK>2.0.CO;2.
- Kossin, J. P. and Sitkowski, M. (2009). An objective model for identifying secondary eyewall formation in hurricanes. *Monthly Weather Review*, 137(3):876 – 892. DOI:10.1175/2008MWR2701.1.
- Kuo, H.-C., Williams, R. T., and Chen, J.-H. (1999). A possible mechanism for the eye rotation of Typhoon Herb. *Journal of the Atmospheric Sciences*, 56(11):1659–1673. DOI:10.1175/1520-0469(1999)056<1659:APMFTE>2.0.CO;2.
- Landsea, C. W. and Franklin, J. L. (2013). Atlantic hurricane database uncer-

- tainty and presentation of a new database format. *Monthly Weather Review*, 141(10):3576–3592. DOI:10.1175/MWR-D-12-00254.1.
- Lee, J.-D., Wu, C.-C., and Ito, K. (2020). Diurnal variation of the convective area and eye size associated with the rapid intensification of tropical cyclones. *Monthly Weather Review*, 148(10):4061–4082. DOI:10.1175/MWR-D-19-0345.1.
- Leighton, H., Gopalakrishnan, S., Zhang, J. A., Rogers, R. F., Zhang, Z., and Tallapragada, V. (2018). Azimuthal distribution of deep convection, environmental factors, and tropical cyclone rapid intensification: A perspective from HWRF ensemble forecasts of Hurricane Edouard (2014). *Journal of the Atmospheric Sciences*, 75(1):275 – 295. DOI:10.1175/JAS-D-17-0171.1.
- Lock, A. P., Brown, A. R., Bush, M. R., Martin, G. M., and Smith, R. N. B. (2000). A new boundary layer mixing scheme. Part I: Scheme description and single-column model tests. *Monthly Weather Review*, 128(9):3187 – 3199. DOI:10.1175/1520-0493(2000)128<3187:ANBLMS>2.0.CO;2.
- McFarquhar, G. M., Jewett, B. F., Gilmore, M. S., Nesbitt, S. W., and Hsieh, T.-L. (2012). Vertical velocity and microphysical distributions related to rapid intensification in a simulation of Hurricane Dennis (2005). *Journal of the Atmospheric Sciences*, 69(12):3515 – 3534. DOI:10.1175/JAS-D-12-016.1.
- Mei, W., Pasquero, C., and Primeau, F. (2012). The effect of translation speed upon the intensity of tropical cyclones over the tropical ocean. *Geophysical Research Letters*, 39(7). DOI:10.1029/2011GL050765.
- Michaels, P. J., Knappenberger, P. C., and Davis, R. E. (2006). Sea-surface temperatures and tropical cyclones in the Atlantic basin. *Geophysical Research Letters*, 33(9). DOI:10.1029/2006GL025757.
- Miller, J. D. and Montgomery, M. T. (2000). Tropical cyclone evolution via potential vorticity anomalies in a three-dimensional balance model. *Journal of the Atmospheric Sciences*, 57(20):3366 – 3387. DOI:10.1175/1520-0469(2000)057<3366:TCEVPV>2.0.CO;2.
- Miyamoto, Y., Satoh, M., Tomita, H., Oouchi, K., Yamada, Y., Kodama, C., and

- Kinter, J. (2014). Gradient wind balance in tropical cyclones in high-resolution global experiments. *Monthly Weather Review*, 142(5):1908 – 1926. DOI:10.1175/MWR-D-13-00115.1.
- Miyamoto, Y. and Takemi, T. (2013). A transition mechanism for the spontaneous axisymmetric intensification of tropical cyclones. *Journal of the Atmospheric Sciences*, 70(1):112 – 129. DOI:10.1175/JAS-D-11-0285.1.
- Moller, J. D. and Shapiro, L. J. (2002). Balanced contributions to the intensification of Hurricane Opal as diagnosed from a GFDL model forecast. *Monthly Weather Review*, 130(7):1866 – 1881.
- Montgomery, M. and Smith, R. (2014). Paradigms for tropical cyclone intensification. *Australian Meteorological and Oceanographic Journal*, 64(1):37–66. DOI:10.22499/2.6401.005.
- Montgomery, M. T. and Kallenbach, R. J. (1997). A theory for vortex Rossby-waves and its application to spiral bands and intensity changes in hurricanes. *Quarterly Journal of the Royal Meteorological Society*, 123(538):435–465. DOI:10.1002/qj.49712353810.
- Montgomery, M. T., Nicholls, M. E., Cram, T. A., and Saunders, A. B. (2006). A vortical hot tower route to tropical cyclogenesis. *Journal of the Atmospheric Sciences*, 63(1):355 – 386. DOI:10.1175/JAS3604.1.
- Montgomery, M. T. and Smith, R. K. (2018). Comments on revisiting the balanced and unbalanced aspects of tropical cyclone intensification. *Journal of the Atmospheric Sciences*, 75(7):2491–2496. DOI:10.1175/JAS-D-17-0323.1.
- Montgomery, M. T., Zhang, J. A., and Smith, R. K. (2014). An analysis of the observed low-level structure of rapidly intensifying and mature Hurricane Earl (2010). *Quarterly Journal of the Royal Meteorological Society*, 140(684):2132–2146. DOI:<https://doi.org/10.1002/qj.2283>.
- Navarro, E. L., Hakim, G. J., and Willoughby, H. E. (2017). Balanced response of an axisymmetric tropical cyclone to periodic diurnal heating. *Journal of the Atmospheric Sciences*, 74(10):3325 – 3337. DOI:10.1175/JAS-D-16-0279.1.

- Nelder, J. A. and Mead, R. (1965). A simplex method for function minimization. *The Computer Journal*, 7(4):308–313. DOI:10.1093/comjnl/7.4.308.
- Nguyen, M. C., Reeder, M. J., Davidson, N. E., Smith, R. K., and Montgomery, M. T. (2011). Inner-core vacillation cycles during the intensification of hurricane katrina. *Quarterly Journal of the Royal Meteorological Society*, 137(657):829–844. DOI:<https://doi.org/10.1002/qj.823>.
- Ohno, T. and Satoh, M. (2015). On the warm core of a tropical cyclone formed near the tropopause. *Journal of the Atmospheric Sciences*, 72(2):551 – 571. DOI:10.1175/JAS-D-14-0078.1.
- OMAO (2020). <https://www.oma.noaa.gov/learn/aircraft-operations>. <https://www.nhc.noaa.gov/data/tcr/>.
- Ooyama, K. (1969). Numerical simulation of the life cycle of tropical cyclones. *Journal of Atmospheric Sciences*, 26(1):3 – 40. DOI:10.1175/1520-0469(1969)026<0003:NSOTLC>2.0.CO;2.
- Park, M.-S., Elsberry, R. L., and Harr, P. A. (2012). Vertical wind shear and ocean heat content as environmental modulators of western north pacific tropical cyclone intensification and decay. *Tropical Cyclone Research and Review*, 1(4):448 – 457. DOI:<https://doi.org/10.6057/2012TCRR04.03>.
- Paterson, L. A., Hanstrum, B. N., Davidson, N. E., and Weber, H. C. (2005). Influence of environmental vertical wind shear on the intensity of hurricane-strength tropical cyclones in the australian region. *Monthly Weather Review*, 133(12):3644–3660. DOI:10.1175/MWR3041.1.
- Persing, J., Montgomery, M. T., McWilliams, J. C., and Smith, R. K. (2013). Asymmetric and axisymmetric dynamics of tropical cyclones. *Atmospheric Chemistry and Physics*, 13(24):12299–12341.
- Persing, J., Montgomery, M. T., and Tuleya, R. E. (2002). Environmental interactions in the GFDL hurricane model for Hurricane Opal. *Monthly Weather Review*, 130(2):298 – 317. DOI:10.1175/1520-0493(2002)130<0298:EIITGH>2.0.CO;2.
- Powell, M. D., Vickery, P. J., and Reinhold, T. A. (2003). Reduced drag coefficient

- for high wind speeds in tropical cyclones. *Nature*, 422(6929):279–283. DOI:10.1038/nature01481.
- Prieto, R., Kossin, J. P., and Schubert, W. H. (2001). Symmetrization of lopsided vorticity monopoles and offset hurricane eyes. *Quarterly Journal of the Royal Meteorological Society*, 127(577):2307–2327. DOI:10.1002/qj.49712757706.
- Qiu, X., Tan, Z.-M., and Xiao, Q. (2010). The roles of vortex Rossby waves in hurricane secondary eyewall formation. *Monthly Weather Review*, 138(6):2092 – 2109. DOI:10.1175/2010MWR3161.1.
- Reasor, P. D., Eastin, M. D., and Gamache, J. F. (2009). Rapidly intensifying Hurricane Guillermo (1997). Part I: low-Wavenumber structure and evolution. *Monthly Weather Review*, 137(2):603 – 631. DOI:10.1175/2008MWR2487.1.
- Reasor, P. D. and Montgomery, M. T. (2015). Evaluation of a heuristic model for tropical cyclone resilience. *Journal of the Atmospheric Sciences*, 72(5):1765–1782. DOI:10.1175/JAS-D-14-0318.1.
- Reasor, P. D., Montgomery, M. T., Marks, F. D., and Gamache, J. F. (2000). Low-wavenumber structure and evolution of the hurricane inner core observed by airborne dual-doppler radar. *Monthly Weather Review*, 128(6):1653–1680. DOI:10.1175/1520-0493(2000)128<1653:LWSAEO>2.0.CO;2.
- Reasor, P. D., Rogers, R., and Lorsolo, S. (2013). Environmental flow impacts on tropical cyclone structure diagnosed from airborne doppler radar composites. *Monthly Weather Review*, 141(9):2949–2969. DOI:10.1175/mwr--d--12--00334.1.
- Reif, M., Reeder, M., and Hankinson, C. (2014). Vacillation cycles in WRF simulations of Hurricane Katrina. *Journal of Southern Hemisphere Earth Systems Science*, 64(2):123 – 131.
- Riemer, M., Montgomery, M. T., and Nicholls, M. E. (2010). A new paradigm for intensity modification of tropical cyclones: Thermodynamic impact of vertical wind shear on the inflow layer. *Atmospheric Chemistry and Physics*, 10(7):3163–3188.

- Roberts, N. M. and Lean, H. W. (2008). Scale-selective verification of rainfall accumulations from high-resolution forecasts of convective events. *Monthly Weather Review*, 136(1):78–97. DOI:10.1175/2007mwr2123.1.
- Rogers, R. (2010). Convective-scale structure and evolution during a high-resolution simulation of tropical cyclone rapid intensification. *Journal of the Atmospheric Sciences*, 67(1):44 – 70. DOI:10.1175/2009JAS3122.1.
- Rogers, R., Reasor, P., and Lorsolo, S. (2013). Airborne doppler observations of the inner-core structural differences between intensifying and steady-state tropical cyclones. *Monthly Weather Review*, 141(9):2970 – 2991. DOI:10.1175/MWR-D-12-00357.1.
- Rogers, R. F., Zhang, J. A., Zawislak, J., Jiang, H., Alvey, G. R., Zipser, E. J., and Stevenson, S. N. (2016). Observations of the structure and evolution of hurricane edouard (2014) during intensity change. Part II: Kinematic structure and the distribution of deep convection. *Monthly Weather Review*, 144(9):3355 – 3376. DOI:10.1175/MWR-D-16-0017.1.
- Romps, D. M. (2017). Exact expression for the lifting condensation level. *Journal of the Atmospheric Sciences*, 74(12):3891 – 3900. DOI:10.1175/JAS-D-17-0102.1.
- Ruan, K., Zha, Y., Huang, H., and bin Hu, Y. (2014). Contribution of vortex Rossby wave to spiral rainband formation in tropical cyclones. *Journal of Hydrodynamics, Ser. B*, 26(5):725–733. DOI:https://doi.org/10.1016/S1001-6058(14)60081-0.
- Ryglicki, D. R. and Hart, R. E. (2015). An investigation of center-finding techniques for tropical cyclones in mesoscale models. *Journal of Applied Meteorology and Climatology*, 54(4):825–846. DOI:10.1175/jamc--d--14--0106.1.
- Saffin, L., Methven, J., and Gray, S. L. (2016). The non-conservation of potential vorticity by a dynamical core compared with the effects of parametrized physical processes. *Quarterly Journal of the Royal Meteorological Society*, 142(696):1265–1275. DOI:10.1002/qj.2729.
- Sanchez, C., Williams, K. D., and Collins, M. (2016). Improved stochastic physics

- schemes for global weather and climate models. *Quarterly Journal of the Royal Meteorological Society*, 142(694):147–159. DOI:<https://doi.org/10.1002/qj.2640>.
- Savitzky, A. and Golay, M. J. E. (1964). Smoothing and differentiation of data by simplified least squares procedures. *Analytical Chemistry*, 36(8):1627–1639. DOI:[10.1021/ac60214a047](https://doi.org/10.1021/ac60214a047).
- Schubert, W. H. and Hack, J. J. (1982). Inertial stability and tropical cyclone development. *Journal of the Atmospheric Sciences*, 39(8):1687–1697. DOI:[10.1175/1520-0469\(1982\)039<1687:isatcd>2.0.co;2](https://doi.org/10.1175/1520-0469(1982)039<1687:isatcd>2.0.co;2).
- Schubert, W. H., Montgomery, M. T., Taft, R. K., Guinn, T. A., Fulton, S. R., Kossin, J. P., and Edwards, J. P. (1999). Polygonal eyewalls, asymmetric eye contraction, and potential vorticity mixing in hurricanes. *Journal of the Atmospheric Sciences*, 56(9):1197 – 1223. DOI:[10.1175/1520-0469\(1999\)056<1197:PEAECA>2.0.CO;2](https://doi.org/10.1175/1520-0469(1999)056<1197:PEAECA>2.0.CO;2).
- Shapiro, L. J. and Willoughby, H. E. (1982). The response of balanced hurricanes to local sources of heat and momentum. *Journal of Atmospheric Sciences*, 39(2):378 – 394. DOI:[10.1175/1520-0469\(1982\)039<0378:TROBHT>2.0.CO;2](https://doi.org/10.1175/1520-0469(1982)039<0378:TROBHT>2.0.CO;2).
- Short, C. J. and Petch, J. (2018). How well can the Met Office Unified Model forecast tropical cyclones in the western North Pacific? *Weather and Forecasting*, 33(1):185–201. DOI:[10.1175/waf--d--17--0069.1](https://doi.org/10.1175/waf--d--17--0069.1).
- Sitkowski, M. and Barnes, G. M. (2009). Low-level thermodynamic, kinematic, and reflectivity fields of Hurricane Guillermo (1997) during rapid intensification. *Monthly Weather Review*, 137(2):645 – 663. DOI:[10.1175/2008MWR2531.1](https://doi.org/10.1175/2008MWR2531.1).
- Sitkowski, M., Kossin, J. P., and Rozoff, C. M. (2011). Intensity and structure changes during hurricane eyewall replacement cycles. *Monthly Weather Review*, 139(12):3829 – 3847. DOI:[10.1175/MWR-D-11-00034.1](https://doi.org/10.1175/MWR-D-11-00034.1).
- Skok, G. and Roberts, N. (2016). Analysis of fractions skill score properties for random precipitation fields and ecmwf forecasts. *Quarterly Journal of the Royal Meteorological Society*, 142(700):2599–2610. DOI:[10.1002/qj.2849](https://doi.org/10.1002/qj.2849).

- Smith, K. C. and Eastin, M. D. (2010). P2.19 composite structure of vortical hot towers in Hurricane Guillermo (1997). <https://ams.confex.com/ams/pdfpapers/167821.pdf>.
- Smith, R. K. (2006). Accurate determination of a balanced axisymmetric vortex in a compressible atmosphere. *Tellus A*, 58(1):98–103. DOI:<https://doi.org/10.1111/j.1600-0870.2006.00149.x>.
- Smith, R. K., Kilroy, G., and Montgomery, M. T. (2015). Why do model tropical cyclones intensify more rapidly at low latitudes? *Journal of the Atmospheric Sciences*, 72(5):1783 – 1804. DOI:10.1175/JAS-D-14-0044.1.
- Smith, R. K. and Montgomery, M. T. (2008). Balanced boundary layers used in hurricane models. *Quarterly Journal of the Royal Meteorological Society*, 134(635):1385–1395. DOI:<https://doi.org/10.1002/qj.296>.
- Smith, R. K. and Montgomery, M. T. (2015). Toward clarity on understanding tropical cyclone intensification. *Journal of the Atmospheric Sciences*, 72(8):3020 – 3031. DOI:10.1175/JAS-D-15-0017.1.
- Smith, R. K. and Montgomery, M. T. (2016). The efficiency of diabatic heating and tropical cyclone intensification. *Quarterly Journal of the Royal Meteorological Society*, 39(142):2081–2086. DOI:10.1002/qj.2804.
- Smith, R. K., Montgomery, M. T., and Bui, H. (2018). Axisymmetric balance dynamics of tropical cyclone intensification and its breakdown revisited. *Journal of the Atmospheric Sciences*, 75(9):3169 – 3189. DOI:10.1175/JAS-D-17-0179.1.
- Smith, R. K., Montgomery, M. T., and Van Sang, N. (2009). Tropical cyclone spin-up revisited. *Quarterly Journal of the Royal Meteorological Society*, 135(642):1321–1335. DOI:<https://doi.org/10.1002/qj.428>.
- Smith, R. K., Montgomery, M. T., and Zhu, H. (2005). Buoyancy in tropical cyclones and other rapidly rotating atmospheric vortices. *Dynamics of Atmospheres and Oceans*, 40(3):189–208. DOI:<https://doi.org/10.1016/j.dynatmoce.2005.03.003>.

- Smith, R. K. and Vogl, S. (2008). A simple model of the hurricane boundary layer revisited. *Quarterly Journal of the Royal Meteorological Society*, 134(631):337–351. DOI:<https://doi.org/10.1002/qj.216>.
- Smith, R. K., Zhang, J. A., and Montgomery, M. T. (2017). The dynamics of intensification in a Hurricane Weather Research and Forecasting simulation of Hurricane Earl (2010). *Quarterly Journal of the Royal Meteorological Society*, 143(702):293–308. DOI:<https://doi.org/10.1002/qj.2922>.
- Smith, R. N. B. (1990). A scheme for predicting layer clouds and their water content in a general circulation model. *Quarterly Journal of the Royal Meteorological Society*, 116(492):435–460. DOI:<https://doi.org/10.1002/qj.49711649210>.
- Stern, D. P. and Zhang, F. (2013). How does the eye warm? Part II: sensitivity to vertical wind shear and a trajectory analysis. *Journal of the Atmospheric Sciences*, 70(7):1849–1873. DOI:10.1175/JAS-D-12-0258.1.
- Sun, Y. Q., Jiang, Y., Tan, B., and Zhang, F. (2013). The governing dynamics of the secondary eyewall formation of Typhoon Sinlaku (2008). *Journal of the Atmospheric Sciences*, 70(12):3818 – 3837. DOI:10.1175/JAS-D-13-044.1.
- Sun, Z., Zhang, B., Zhang, J. A., and Perrie, W. (2019). Examination of surface wind asymmetry in tropical cyclones over the northwest pacific ocean using smap observations. *Remote Sensing*, 11(22):2604. DOI:10.3390/rs11222604.
- Tang, X. and Zhang, F. (2016). Impacts of the diurnal radiation cycle on the formation, intensity, and structure of hurricane edouard (2014). *Journal of the Atmospheric Sciences*, 73(7):2871–2892. DOI:10.1175/JAS-D-15-0283.1.
- Tao, D. and Zhang, F. (2015). Effects of vertical wind shear on the predictability of tropical cyclones: Practical versus intrinsic limit. *Journal of Advances in Modeling Earth Systems*, 7(4):1534–1553. DOI:10.1002/2015MS000474.
- Terwey, W. D. and Montgomery, M. T. (2008). Secondary eyewall formation in two idealized, full-physics modeled hurricanes. *Journal of Geophysical Research: Atmospheres*, 113(D12). DOI:<https://doi.org/10.1029/2007JD008897>.
- Tyner, B., Zhu, P., Zhang, J. A., Gopalakrishnan, S., Marks Jr., F., and Tallapra-

- gada, V. (2018). A top-down pathway to secondary eyewall formation in simulated tropical cyclones. *Journal of Geophysical Research: Atmospheres*, 123(1):174–197. DOI:<https://doi.org/10.1002/2017JD027410>.
- Velden, C. S. and Herndon, D. (2020). A consensus approach for estimating tropical cyclone intensity from meteorological satellites: SATCON. *Weather and Forecasting*, 35(4):1645–1662. DOI:10.1175/WAF-D-20-0015.1.
- Wang, H. and Wang, Y. (2014). A numerical study of Typhoon Megi (2010). Part I: Rapid intensification. *Monthly Weather Review*, 142(1):29 – 48. DOI:10.1175/MWR-D-13-00070.1.
- Wang, H., Wu, C.-C., and Wang, Y. (2016). Secondary eyewall formation in an idealized tropical cyclone simulation: Balanced and unbalanced dynamics. *Journal of the Atmospheric Sciences*, 73(10):3911 – 3930. DOI:10.1175/JAS-D-15-0146.1.
- Wang, S. and Smith, R. K. (2019). Consequences of regularizing the sawyer eliassen equation in balance models for tropical cyclone behaviour. *Quarterly Journal of the Royal Meteorological Society*, 145(725):3766–3779. DOI:<https://doi.org/10.1002/qj.3656>.
- Wang, Y. (2002). Vortex Rossby waves in a numerically simulated tropical cyclone. Part I: Overall structure, potential vorticity, and kinetic energy budgets. *Journal of the Atmospheric Sciences*, 59(7):1213 – 1238. DOI:10.1175/1520-0469(2002)059<1213:VRWIAN>2.0.CO;2.
- Wang, Y. and Wang, H. (2013). The inner-core size increase of Typhoon Megi (2010) during its rapid intensification phase. *Tropical Cyclone Research and Review*, 2(2):65–80. DOI:<https://doi.org/10.6057/2013TCRR02.01>.
- Wang, Y.-F. and Tan, Z.-M. (2020). Outer rainbands driven secondary eyewall formation of tropical cyclones. *Journal of the Atmospheric Sciences*, 77(6):2217 – 2236. DOI:10.1175/JAS-D-19-0304.1.
- Weatherford, C. L. and Gray, W. M. (1988). Typhoon structure as revealed by aircraft reconnaissance. Part II: Structural variability. *Monthly Weather Review*,

- 116(5):1044 – 1056. DOI:10.1175/1520-0493(1988)116<1044:TSARBA>2.0.CO;2.
- Webster, S., Brown, A. R., Cameron, D. R., and Jones, C. P. (2003). Improvements to the representation of orography in the Met Office Unified Model. *Quarterly Journal of the Royal Meteorological Society*, 129(591):1989–2010. DOI:<https://doi.org/10.1256/qj.02.133>.
- Williams, G. (2017). The generation and maintenance of hollow pv towers in a forced primitive equation model. *Proceedings*, 1:156. DOI:10.3390/ecas2017-04149.
- Willoughby, H. E. (1979). Forced secondary circulations in hurricanes. *Journal of Geophysical Research: Oceans*, 84(C6):3173–3183. DOI:<https://doi.org/10.1029/JC084iC06p03173>.
- Willoughby, H. E. and Chelmon, M. B. (1982). Objective determination of hurricane tracks from aircraft observations. *Monthly Weather Review*, 110(9):1298–1305. DOI:10.1175/1520--0493(1982)110<1298:odohtf>2.0.co;2.
- Willoughby, H. E., Clos, J. A., and Shoreibah, M. G. (1982). Concentric eye walls, secondary wind maxima, and the evolution of the hurricane vortex. *Journal of Atmospheric Sciences*, 39(2):395 – 411. DOI:10.1175/1520-0469(1982)039<0395:CEWSWM>2.0.CO;2.
- Wimmers, A. J. and Velden, C. S. (2007). MIMIC: A new approach to visualizing satellite microwave imagery of tropical cyclones. *Bulletin of the American Meteorological Society*, 88(8):1187–1196. DOI:10.1175/BAMS-88-8-1187.
- Wong, M. L. M. and Chan, J. C. L. (2004). Tropical cyclone intensity in vertical wind shear. *Journal of the Atmospheric Sciences*, 61(15):1859–1876. DOI:10.1175/1520-0469(2004)061<1859:TCIIWV>2.0.CO;2.
- WRS (2011). <https://www.403wg.afrc.af.mil/about/factsheets/display/article/192529/53rd-weather-reconnaissance-squadron-hurricane-hunters/>. <https://www.nhc.noaa.gov/data/tcr/>.
- Wunsch, K. E. D. and Didlake, A. C. (2018). Analyzing tropical cyclone structures

- during secondary eyewall formation using aircraft in situ observations. *Monthly Weather Review*, 146(12):3977 – 3993. DOI:10.1175/MWR-D-18-0197.1.
- Yeung, H. (2013). Convective hot tower signatures and rapid intensification of severe Typhoon Vicente (1208). *Tropical Cyclone Research and Review*, 2(2):96–108. DOI:<https://doi.org/10.6057/2013TCRR02.03>.
- Zeng, Z., Wang, Y., and Wu, C.-C. (2007). Environmental dynamical control of tropical cyclone intensity—an observational study. *Monthly Weather Review*, 135(1):38–59. DOI:10.1175/MWR3278.1.
- Zhang, F., Tao, D., Sun, Y. Q., and Kepert, J. D. (2017). Dynamics and predictability of secondary eyewall formation in sheared tropical cyclones. *Journal of Advances in Modeling Earth Systems*, 9(1):89–112. DOI:<https://doi.org/10.1002/2016MS000729>.
- Zhou, X. and Wang, B. (2011). Mechanism of concentric eyewall replacement cycles and associated intensity change. *Journal of the Atmospheric Sciences*, 68(5):972 – 988. DOI:10.1175/2011JAS3575.1.
- Zhu, Z. and Zhu, P. (2014). The role of outer rainband convection in governing the eyewall replacement cycle in numerical simulations of tropical cyclones. *Journal of Geophysical Research: Atmospheres*, 119(13):8049–8072. DOI:<https://doi.org/10.1002/2014JD021899>.